

Exploration of Stability of 3D-Printed Steel Members

A study to buckling behaviour of wire and
arc additively manufactured stainless
steel tubular columns

G.S. van Bolderen

Exploration of Stability of 3D-Printed Steel Members

A study to buckling behaviour of wire and arc
additively manufactured stainless steel tubular
columns

by

G.S. van Bolderen

in partial fulfillment of the requirements for the degree of

Master of Science

in Civil Engineering,

Faculty of Civil Engineering and Geosciences
Delft University of Technology
The Netherlands

December 16, 2017

GRADUATION COMMITTEE

em. Prof. ir. F. S. K. Bijlaard	Faculty CiTG, Structural Engineering
Ir. P. A. de Vries	Faculty CiTG, Structural Engineering
Prof. dr. I. M. Richardson,	Faculty 3ME, Materials Science & Engineering

An electronic version of this thesis is available at <http://repository.tudelft.nl/>.

'If we knew what it was we were doing, it would not be called research, would it?'

- Albert Einstein -

Preface

I am happy to be able to present my Master's thesis to you. This thesis concludes my master's degree of Structural Engineering at the faculty of Civil Engineering and Geosciences at the Delft University of Technology.

I don't exaggerate when I say that conducting this research, together with its unavoidable challenges, but with most of all enjoyable moments, was extremely fruitful. Therefore I cannot express enough gratitude towards Gijs van der Velden and Tim Geurtjens of MX3D, the Amsterdam based 3D-printing start-up for giving me the opportunity to introduce me to this exciting new technology, and allowing me to follow the development of world's first 3D-printed metal bridge very closely. The craftsmanship of MX3D's printing experts, especially of Filippo Gilardi enabled me to study the desired test pieces and therefore deserves a special thanks.

Gratitude is extended towards the academic staff of the Stevin-II laboratory, particularly John Hermsen, and the staff of MSE-laboratory of Delft University of Technology by providing me professional assistance during the execution of tests. In addition I am very thankful for the effort and endless creativity of Bertus Naagen to let me succeed in 3D-scanning such large complex objects with an extreme accuracy.

I thank my committee members, em. Prof. ir. F.S.K. Bijlaard, Prof. dr. I.M. Richardson and ir. P.A. de Vries for providing insightful guidance throughout the research process.

I won't forget to mention my dear U-BASE friends for all the kind support and above all, the countless fun moments we had in 'office'. Axel, Carlijn, Michou, Hugo and Tanya, thanks to you I look back at this period with a big smile.

Finally I want to sincerely thank my family and parents, who supported me with love and understanding.

*G.S. van Bolderen
Delft, December 16, 2017*

Abstract

Wire and arc additive manufacturing (WAAM), a relatively new metal 3D-printing technology, allows for fabrication of shapes that were not possible to produce a few years ago. Using 6-axis industrial robots with a gas metal arc welding (GMAW)-head, Dutch start-up MX3D prints metal in every direction mid-air. By welding small parts of material at a time along a laser guided - CAD-generated path, self-supporting cross-sections of very complex shapes, such as internally reinforced non-prismatic hollow sections can be manufactured fully automatically. Unlike powder-bed based manufacturing, this technology is not bounded by size limits of a final product, which creates opportunities for fabrication of large-scale structural components and finally entire structures. It is MX3D's aim, in collaboration with key industry partners, to 3D-print world's first fully functional bridge spanning 12 metres, to be installed in the city centre of Amsterdam in the course of 2019. The bearing elements of the bridge consist of tubular shaped elements, together building up to a complex-shaped free-form steel structure. These tubular members mainly behave as axially compressed bearing elements, nonetheless it is yet not known how the stability of WAAM-members can be assessed.

Several standards for testing (and characterisation) of additively manufactured materials are published by different national and international committees, e.g. ISO/ASTM 529 and CEN-CT 438, but a comprehensive set of international standards has not been achieved yet. It is widely recognised that there is a strong link between manufacturing process parameters and material properties, which requires special attention in this research area. So far there is a lack of sufficient test results to cover a specific manufacturing process. In this research the material properties of MX3D's dot-by-dot and continuously printed members are studied.

This pioneering research provides insight in material and geometrical properties relevant for the stability of (ER)308LSi stainless steel tubular columns. A tubular column is used as existing basic structural element to assess the stability of wire and arc additively manufactured steel members. Advanced 3D-laserscanning technology is applied to characterise and analyse geometrical imperfections. A clear understanding of bending stiffness and buckling behaviour is established by performing four-point flexural bending tests and flexural buckling tests on tubular columns, diameter 33.8 mm, thickness 3.7 mm. Tensile properties of milled WAAM specimens are analysed both in - and perpendicular to - their print direction for dot-by-dot and continuously printing. It is verified whether or not the structural properties are in compliance with the existing steel standard (EC3). Additional Vickers hardness measurements and metallographical analyses are performed to examine the microstructure of column samples. Finally, a buckling design graph is proposed based on own experiments, aiming towards a safe model suitable for stability calculations of additively manufactured tubular columns.

It is concluded from experiments that the material properties of 3D-printed steel differ from that of conventionally produced steel. Following the thermal gradient of the weld pool, large columnar grain structures are detected giving rise to anisotropy. Stiffness, strength and ductility prove to be dependent on the print direction. Whereas the tensile strength top expected values, the obtained stiffness is significantly lower than that of commonly applied steel grades. Inaccuracies of the printing process result in local wall thickness variations and a relatively high out-of-straightness, both negatively affecting the buckling capacity of printed tubular columns.

Yet it should be acknowledged that due to rapid advancements in improving the printing process, the geometrical imperfections are soon expected to reduce drastically. It is recommended to apply active cooling during manufacturing to enhance mechanical properties even further. By combining topology optimisation and WAAM, an optimal material layout can be found and manufactured, consequently an excellent material efficiency can be achieved. A promising prospect for future construction projects.

Contents

Nomenclature	ix
1 Introduction	1
1.1 Problem Statement	2
1.2 Research Question & Objectives.	4
1.3 Thesis Outline	5
2 State-of-the-Art	7
2.1 Additive Manufacturing.	8
2.1.1 AM versus Traditional Manufacturing	8
2.1.2 Metal AM-Processes	10
2.1.3 Opportunities and Challenges for WAAM	14
2.2 Base Material: Stainless Steel	19
2.2.1 Base Material	19
2.2.2 Stainless Steel	20
2.2.3 Microstructure.	20
2.2.4 Mechanical Properties	31
2.3 Printing Process Parameters and Properties.	36
2.3.1 GMAW-Process Parameters	36
2.3.2 MX3D's Printing Parameters	38
2.3.3 Influence of Printing Process on Properties	39
2.4 Fundamentals of Buckling	44
2.4.1 Column Theory	44
2.4.2 European Buckling Curves (ECCS)	48
2.4.3 Buckling of Stainless Steel Columns	52
2.4.4 Buckling of Additive Manufactured Elements	56
3 Test & Measurement Methodology	59
3.1 Test Methodology.	60
3.2 Column Specimens	62
3.2.1 Specimen Choice	62
3.2.2 Specimen Printing	63
3.2.3 Specimen Overview	67
3.3 Geometry Measurements	69
3.3.1 Hand Measurements.	70
3.3.2 3D-Scans (Macro-Geometry)	71
3.3.3 Volume Measurements.	75
3.4 Mechanical Tests	76
3.4.1 Bending Tests	76
3.4.2 Buckling Tests	79
3.4.3 Compression Tests	84
3.4.4 Tensile Tests	85
3.4.5 Hardness.	86
3.5 Metallography: Tubular Columns	87
3.6 Metallographic & Mechanical Tests: Plate Material (OCAS)	91
3.6.1 Metallography	91
3.6.2 Hardness.	92
3.6.3 Toughness	92

4	Results	93
4.1	Geometry Measurement Results	94
4.1.1	3D-Scans & Hand Measurements (Initial Imperfections)	94
4.1.2	Volume Measurements.	95
4.2	Mechanical Test Results.	95
4.2.1	Bending Tests	96
4.2.2	Buckling Tests	98
4.2.3	Compression Tests	100
4.2.4	Tensile Tests	101
4.2.5	Hardness.	104
4.3	Metallography Results: Tubular Columns	106
4.4	Metallography & Mechanical Test Results: Plate Material (OCAS)	109
4.4.1	Microstructure.	109
4.4.2	Hardness.	111
4.4.3	Toughness	112
5	Analysis	113
5.1	Cross-Sectional Variations	114
5.2	Modelling of Non-Linear Stress-Strain Relation	116
5.3	Buckling Analysis	117
5.3.1	Effective Buckling Length	117
5.3.2	Proposed Buckling Curve	120
6	Conclusions & Recommendations	123
6.1	Conclusions.	124
6.2	Recommendations	129
	Appendices	133
A	General Information	133
A.1	Graduation Committee	133
A.2	Candidate.	134
A.3	Others Involved	134
B	Printing Parameters & Base Material	135
B.1	Printing Parameters.	135
B.1.1	Dot-Print Strategy	135
B.1.2	Continuous-Print Strategy	136
B.2	Base Material	136
B.2.1	Datasheet Oerlikon Welding Wire	136
B.2.2	Datasheet Ugiweld Welding Wire.	137
C	Test & Measurement Results	139
C.1	Overview Specimens	139
C.2	Mechanical Tests	141
C.2.1	Bending Tests	141
C.2.2	Buckling Tests	147
C.2.3	Tensile Tests	152
C.2.4	Hardness Tests	156
C.3	Metallography Results	158
C.3.1	Scanning Electron Microscopy.	158
	Bibliography	161

Nomenclature

List of Abbreviations

Abbreviation	Description
AM	Additive Manufacturing
bcc	body-centered cubic
BTF	Buy-To-Fly ratio
CAD	Computer-Aided Design
CNC	Computer Numerical Control
CRC	Corrosion Resistance Class
CRF	Corrosion Resistance Factor
CSC	Cross-Section Class
DMLS	Direct Metal Laser Sintering
EBSD	Electron Backscatter Diffraction
EDXRF	Energy Dispersive X-Ray Fluorescence
fcc	face-centered cubic
FMD	Fused Metal Deposition
FZ	Fusion Zone
GMAW	Gas Metal Arc Welding
GTAW	Gas Tungsten Arc Welding
HAZ	Heat-Affected Zone
hcp	hexagonal close-packed
LC	Laser Cusing
LCA	Life Cycle Assessment
LMD	Laser Metal Deposition
LVDT	Linear Variable Differential Transformer
MAM	Metal Additive Manufacturing
MIG	Metal Inert Gas
PAW	Plasma Arc Welding
RP	Rapid Prototyping
SCC	Stress Corrosion Cracking
SEM	Scanning Electron Microscope

SLM	Selective Laser Melting
SLS	Selective Laser Sintering
TIG	Tungsten Inert Gas
TO	Topology Optimization
WAAM	Wire Arc Additive Manufacturing
XRD	X-Ray Diffraction

List of Symbols

Symbol	Description	Unit
α	Column imperfection factor	–
$\bar{\lambda}$	Non-dimensional (relative) slenderness	–
$\bar{\lambda}_0$	Limiting non-dimensional (relative) slenderness	–
χ	Buckling reduction factor	–
η	Generalized column imperfection factor	–
γ_M	Partial factor	–
λ	Slenderness	–
$\sigma_{0.2}$	Proof stress (0.2%)	N/mm ²
σ_0	Resistance to dislocation movement (Hall-Petch)	N/mm ²
σ_b	Normal compressive stress	N/mm ²
σ_{cr}	Critical Euler stress	N/mm ²
σ_p	Proportionality stress	N/mm ²
σ_u	Ultimate tensile stress	N/mm ²
$\epsilon_{0.2}$	Proof strain (0.2%)	–
ϵ_f	Fracture strain	–
ϵ_u	Ultimate strain	–
ϵ_y	Yield strain	–
A	Cross-sectional area	mm ²
A_μ	Average cross-sectional area	mm ²
BHN	Brinell Hardness Number	kgf/mm ²
d	Grain diameter (Hall-Petch)	mm
D_i	Diameter of indenter	mm
d_i	Diameter of indentation	mm
E	Young's modulus / Modulus of elasticity	N/mm ²
e	Maximum amplitude of total curvature	mm
e	Non-dimensional (0.2%) proof stress	–

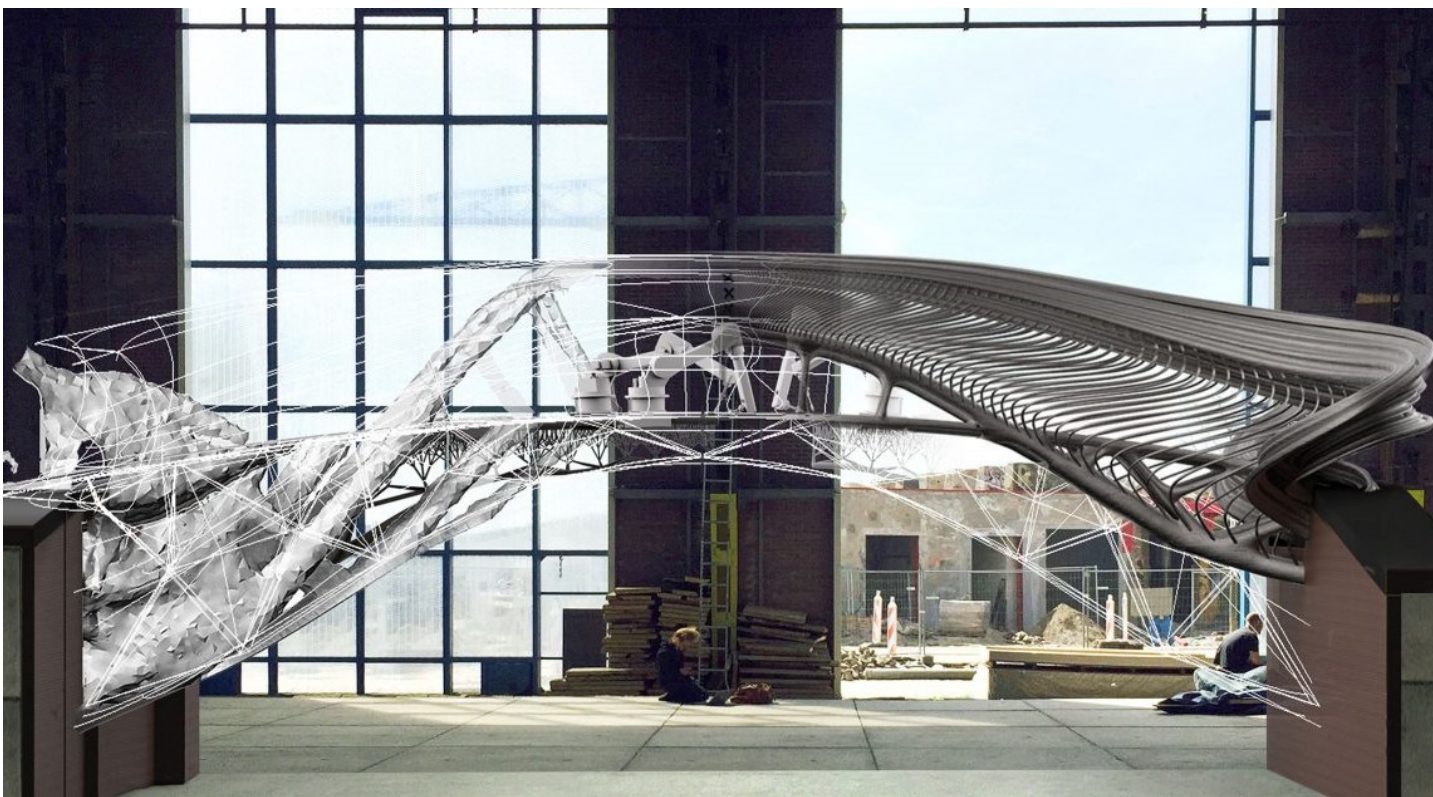
$E_{0.2}$	Tangent modulus at 0.2% proof stress	N/mm ²
E_0	Initial Young's modulus	N/mm ²
e_0	Maximum amplitude of initial curvature	mm
E_t	Tangent modulus	N/mm ²
EI	Bending stiffness	Nmm ²
F	Applied load	N
F_u	Ultimate tensile strength	N
F_{buc}	Buckling load	N
f_y	Yield stress	N/mm ²
HBW	Expression of BHN; HBW from Hardness-Brinell-indenter material: tungsten (wolfram) carbide	N/mm ²
I	Second moment of area	mm ⁴
i	Radius of gyration	mm
K	Effective length factor	–
k_y	Strengthening coefficient (Hall-Petch)	N/mm ^{3/2}
L	Length	mm
L_{cr}	(Effective) Buckling length	mm
m	Material non-linearity parameter (Rasmussen)	–
$M_{el,Rd}$	Design elastic bending moment resistance	Nmm
N	Applied load	N
n	Material non-linearity parameter (Ramberg-Osgood)	–
$N_{b,Rd}$	Design buckling resistance	N
N_{cr}	Critical Euler load	N
N_{pl}	Plastic load	N
N_t	Tangent modulus load	N
P	Applied load	N
t	Thickness column wall	mm
w	Deflection	mm
$W_{el,min}$	Minimum elastic section modulus	mm ³

Specimen Designation (\$-LL-X) or (\$-X- α)

Symbol	Description
α	Print strategy designation
\$	Test designation
LL	Specimen length in centimetres
X	Specimen designation

1

Introduction



In this section an introduction will be given to the research; first the problem statement will be presented in section 1.1, secondly the objectives and research question are described in 1.2. Lastly a contextual outline of this report is stated in section 1.3.

1.1. Problem Statement

The development of Computer-Aided-Design (CAD) as a design tool offers ultimate freedom for architects and designers to create complex free-form geometries. Additionally, the developments in CAD cannot be seen apart from the recent advancements in digital fabrication. This enables so-called ‘file-to-factory’ manufacturing of products directly from digital models, without compromise. However, most standard digital fabrication methods, such as CNC-milling are based on subtractive processes. These processes attain high buy-to-fly ratios; meaning that the material volume used to produce a product is high compared to the actual volume of the product itself. This inefficient conventional way of manufacturing results in high material usage and thus unnecessary depletion of resources. In contrast to subtractive processes, additive manufacturing does not require the removal of excessive material to obtain an end-use product, and is therefore a promising alternative for traditional manufacturing.

Additive Manufacturing (AM), also referred to as 3D-printing, is a collective term for production techniques that lays down successive layers of material from a CAD-generated model together creating a 3D-product without the necessity of removing large amounts of material. It is a relatively unexplored technology which allow direct fabrication of shapes that were not possible to produce until a few years ago. Because of the integration of CAD and robotics, the number of successful applications rose rapidly.

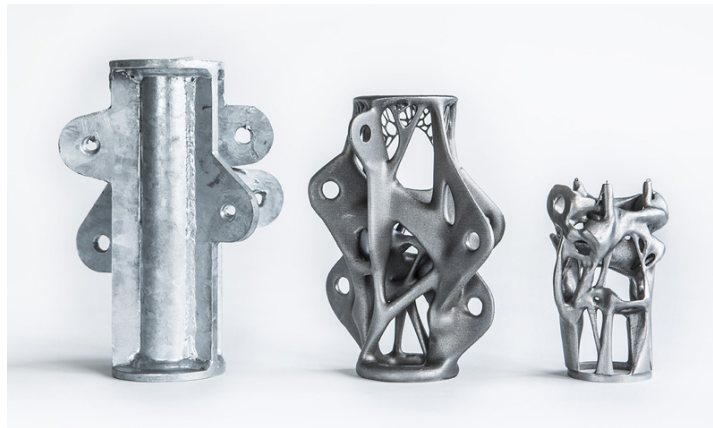


Figure 1.1: Models of the traditional node (left) and two topology optimized AM (DMLS) steel nodes [1],[2]

Furthermore by making use of Topology Optimisation (TO), an optimised material layout within a specific design space for a given set of boundary conditions; an optimal shape can be found. Combining this optimised shape and an increased fabrication accuracy for complex geometries, the full potential of both TO and AM can be exploited. Consequently reducing weight, transportation costs, labour, and (waste) material during manufacturing of the product. The European Commission therefore identified AM as one of the future key technologies for sustainable manufacturing [3].

Figure 1.1 shows an example of three steel nodes made by Direct Metal Laser Sintering (DMLS). DMLS is characterised by its high accuracy, but low deposition rates and density. At the left a traditional node can be seen, where the middle and the right are optimised and produced by AM. The most optimised node depicted at the right is an intriguing 75% lighter and half the height of the original node [1]. But where the prices per AM unit are expected to decrease rapidly [4], they are still higher for these early implementations.

Mainly because of its capability to reduce weight and material usage (buy-to-fly ratio) of expensive high-performance alloys, AM is already more commonly applied in, for example, aviation and aerospace. Whereas the ability to create personalised shapes contributes to application in medical domains; f.e. for tailor-made prosthetics and implants. Despite the rapid progress in digital fabrication and the advantages that AM offers compared to traditional ways of manufacturing, the field of structural engineering is lagging behind in adopting this promising technology. One of the main causes is a low deposition rate which limits the capacity to produce large objects. Wire and Arc Additive Manufacturing (WAAM) on the other hand cannot compete with the accuracy achieved with sintered products, but way higher deposition rates and a more dense material can be obtained.

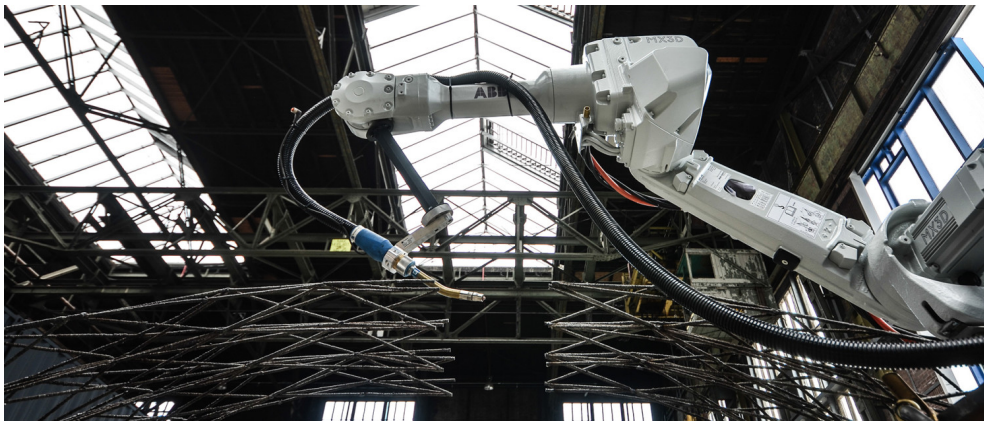


Figure 1.2: Multi-axis industrial robot with GMAW-head as used by MX3D to print metal

During this research the application of WAAM is investigated, more specifically the technique used by MX3D. Using 6-axis industrial robots with a gas metal arc welding (GMAW)-head, Joris Laarman-led Dutch start-up MX3D, is able to print metal in every direction in mid-air as can be seen in figure 1.2. By welding small parts of material at a time along a laser guided CAD-generated path, self-supporting cross-sections of very complex shapes can be manufactured fully automatically. Unlike powder-bed based manufacturing, this technique is not bounded by size limits of a final product, consequently creating opportunities for fabrication of large-scale structural components and finally entire structures. Followed by the structures shown on the images of the chapter cover pages, measuring 91x371x221 cm, the dragon bench designed by artist Joris Laarman is currently one of MX3D's largest structures. Built up from a grid of stainless steel rods it forms a self-supporting shape as shown in figure 1.3. Illustrating the endless possibilities of shapes, MX3D together with Delft University of Technology also made a bike frame by using the same technique as depicted in figure 1.4.



Figure 1.3: Dragon bench designed and printed by Joris Laarman/MX3D



Figure 1.4: WAAM steel bike frame (MX3D/TU Delft)

To demonstrate the structural possibilities of AM in an ultimate way, MX3D, together with partners aims to produce world's first 3D-printed steel footbridge in the city centre of Amsterdam begin 2019. The bridge will cross the canal parallel to the Oudezijds Achterburgwal, see figure 1.5. Its clear span will approximately be 12 metres and the structure is 4 metres wide. Because of safety and environmental reasons it is decided to print the structure at a remote location instead of on-site. An ancillary advantage of printing off-site is a better controlled working environment without potential weather implications influencing the manufacturing process.

The bearing elements of the bridge consists of tubular-shaped elements together building up a to a complex-shaped stainless steel structure. These tubular elements will mainly behave as axially compressed members. It is however not known how the stability of WAAM tubular members can be assessed. In research conducted by Joosten on (by MX3D produced) additively manufactured single-wire stainless steel rods with diameters ranging from 5.7 to 6.9 millimetres, tests have been performed to study buckling, tension and fatigue behaviour. He demonstrated that it is possible to achieve satisfying mechanical and physical properties using MX3D-technology [5]. Moreover, his recommendations opens windows for further extensive research to this material. More knowledge of the structural properties of not only rods, but especially of larger 3D-printed elements in structures is obliged to enable successful implementation of AM in structural engineering.



Figure 1.5: Early render of world's first 3D-printed steel bridge on-site in Amsterdam's city centre

Several material and testing standards for AM are published by different national and international committees, e.g. ISO/ASTM 529 and CEN-CT 438, but a comprehensive set of international standards has not been achieved yet. Although WAAM has considerable similarities with ordinary welding technologies and last-mentioned is already widely understood for stainless steels; it must however be recognised that there is a strong link between manufacturing process parameters and material properties which requires special attention in this research area. So far there is a lack of sufficient test results to cover a specific manufacturing process. The variety of materials and alloys will additionally comprise their own distinctive characteristics, and will behave different accordingly. Therefore it is important to note that each application should be considered on a case-by-case basis.

As a logical follow-up for the already investigated wire, it is chosen to study the stability of a WAAM stainless steel tubular column in this research. Consequently aiming to contribute to a better understanding of influence parameters, limitations and benefits of 3D-printed stainless steel using specifically MX3D's WAAM-technology.

1.2. Research Question & Objectives

The research question which is at the core of this report can be stated as follows:

What are relevant geometrical and material properties of 3D-printed steel to assess the stability of wire and arc additively manufactured stainless steel tubular columns?

Objectives

In order to be able to answer aforementioned research question the following objectives are formulated:

- Characterise and model the specimen's geometry;
- Determine relevant mechanical and metallurgical properties through tests;
- Identify printing process parameters and their influence on material and structural properties;
- Test and study the buckling behaviour of 3D-printed steel tubular columns and construct a corresponding design buckling curve;
- Analyse test results and assess whether the structural properties of these 3D-printed columns are in compliance with the existing steel code (EC3);
- Identify differences in material properties between dot-by-dot and continuous printing and provide advise on the application of both printing techniques for structural parts.

In this research a tubular column is used as existing basic structural element to perform a stability assessment of wire and arc additively manufactured steel members. The proposed buckling graph, based on own experiments, will be a next step towards a safe stability calculation model suitable for structural applications. During this assessment, relevant material and geometrical properties will be determined so they can be implemented in finite elements models. Since this enables modelling of complex shapes, the full potential of (topology optimised) wire and arc additively manufactured structural elements can be exploited.

1.3. Thesis Outline

To be able to answer the research question, chapter 2 provides the reader with the state-of-the-art of all topics considered in this report. More specifically this concerns additive manufacturing and stainless steel, relevant printing process parameters for WAAM and buckling theory. Chapter 3 elucidates the applied test methodology and its practical execution. The outcome of tests and measurements will be presented in chapter 4 and subsequently analysed further in chapter 5. Lastly the conclusions and recommendations will be enumerated in chapter 6. A full schematised thesis outline is provided in figure 1.6.

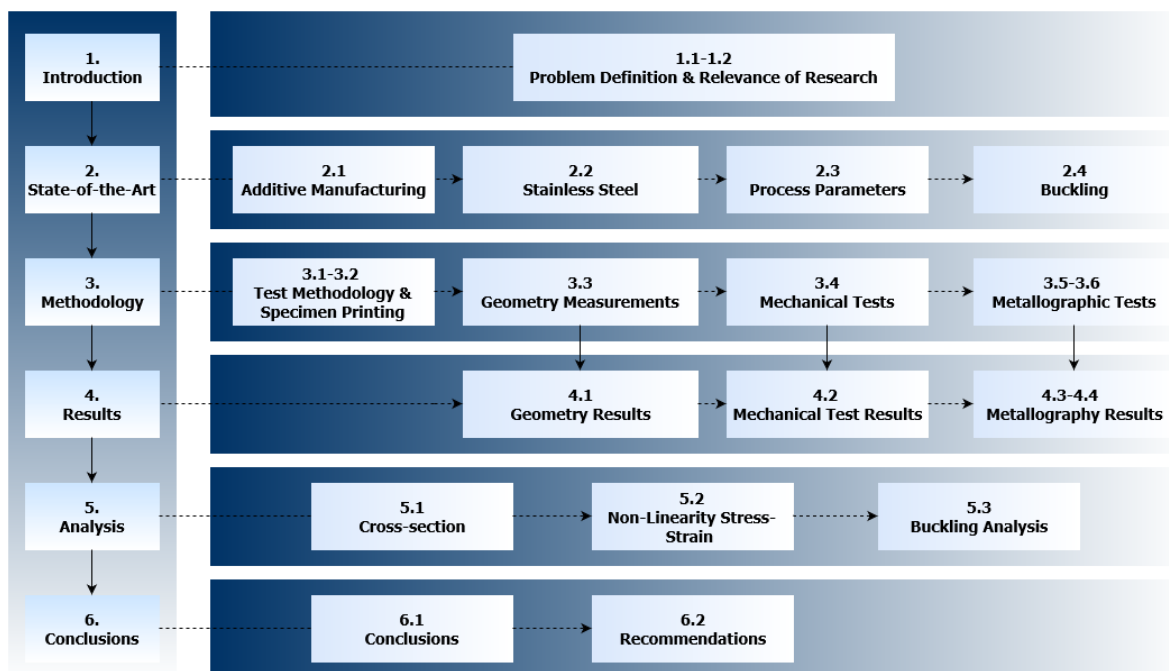


Figure 1.6: Schematic overview of the report structure

2

State-of-the-Art



Chapter 2 presents a comprehensive literature review of all the relevant subjects covered in this research. Main objective of the literature study is to get acquainted with the existing body of academic research to additive manufacturing (AM) and buckling in general.

The state-of-the-art has been subdivided in four main topics: section 2.1 presents the current state of AM. Mechanical and material characteristics of stainless steel are explained in 2.2. In section 2.3 relevant printing process parameters are identified and it is discussed how they affect properties of additively manufactured specimens. Finally, an overview of buckling theory and relevant existing standards for column stability is provided in 2.4.

2.1. Additive Manufacturing

What is additive manufacturing? What is the current state of this technology and how is it complementary to traditional manufacturing processes? These questions will, amongst others, be answered in this section. Furthermore, the various existing metal AM processes will be addressed in 2.1.2. Finally, opportunities and challenges of wire arc additive manufacturing according to existing literature are discussed in 2.1.3.

2.1.1. AM versus Traditional Manufacturing

Additive manufacturing (AM), popularly called 3D-printing, is a collective term for different production techniques capable of depositing successive thin layers of material upon each other. In this way a three dimensional object can be manufactured. A wide variety of materials can be utilized for AM, namely: plastics, resins, rubbers, ceramics, glass, concrete and, as in this research is investigated; metals. The American Society for Testing and Materials (ASTM) proposes the following definition for AM¹:

'A process of joining materials to make objects from 3D model data, usually layer upon layer, as opposed to subtractive manufacturing methodologies, such as traditional machining' [6]

The first (wire-feed) AM techniques finds its roots in a 1920-filed patent of Baker [7]. Baker claimed to have invented a new method for fabrication of 3D-metallic objects. By manually superimposing successive weld-layers using shielded metal arc welding, ornamental shapes were successfully produced as shown in figure 2.1.

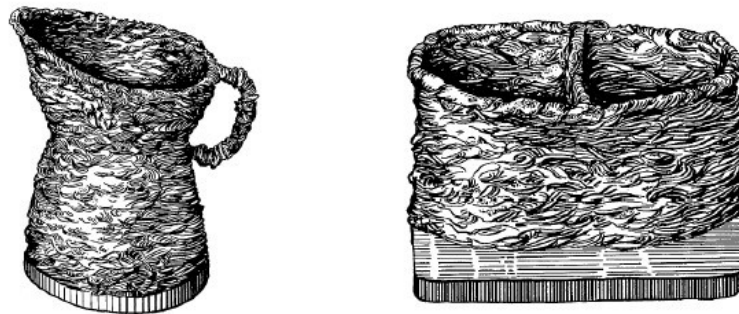


Figure 2.1: Baker's 3D-weld based components created by a layer-additive process using shielded metal arc welding [7]

At the beginning of the 1990s, metal additive manufacturing (MAM)-technologies drew increasingly commercial attention from high-tech manufacturing industries. The potential of MAM to replace traditional subtractive manufacturing was identified as such by Rolls-Royce. Their research aimed to lower the costs of aero-engine component production by reducing material usage (also referred to as buy-to-fly ratio) of expensive high-performance alloys. In this approach, similar to MX3D's process, a welding robot was used in conjunction with a GMAW-system to fabricate three-dimensional metal parts by automatically welding of successive layers. The shape metal deposition (SMD)-technology was patented by Rolls-Royce in 1999 [8].

In recent years, there has been growing interest in direct fabrication of near-net shape, fully dense and end-use components [9]. Recent advancements in digital fabrication, enabling 'file-to-factory' manufacturing directly from digital designs, aided to this growing interest. In addition, the increased adoption of topology optimization, capable of determining the optimal material distribution, has a high potential to increase the performance and efficiency of a product. A perfect example of this is the 3D-printed steel node as already shown in chapter 1. TO contributed to the popularity of AM: since AM is capable of fabricating the complex topology optimised geometries, the potential of both technologies is in this way fully utilised [10].

¹American Society for Testing and Materials (ASTM) International, Standard Terminology for Additive Manufacturing Technologies. ASTM F2792-12a, 2012.

Modern-day robotic AM evolved from rapid prototyping (RP) and aims to produce end-user parts rather than prototypes. Similar to RP, AM requires a 3D-CAD model to translate the design of the desired workpiece into a real three-dimensional object. The digital model is then (by digital means) sliced in multiple very thin cross-section profiles which instructs the 3D-printer where it should deposit the successive layers of material. The profiles are traced by a laser, electron beam, arc, or nozzle which allows accurate and automated material deposition. Once a layer has been deposited, the next layer is added. This is repeated until the whole part has been manufactured. This is just a general explanation; the variety of AM-processes are covered more extensively in section 2.1.2.

Advantages of AM

Additive manufacturing offers many advantages for the production of, especially, complex parts. At this moment, despite rapidly decreasing costs per unit of AM-production, fabrication of AM-products is costly. With the advancements of AM-technology, printing time and costs are expected to fall rapidly, see figure 2.9 [4]. Graduation research of Van der Linden (2015) [11] showed that AM in general has a 'high potential to reduce costs, cut waste and slash the carbon footprint of the construction sector'. In contrast to AM, traditional manufacturing processes involves high tooling costs; mass production is required to reduce unit costs. But there are more arguments in favour of AM as summed up in table 2.1.

Table 2.1: Overview of advantages of AM over traditional manufacturing processes for various areas of application, *based on [12]*

Areas of Application	Advantages over Traditional Manufacturing
<i>Rapid Prototyping</i>	Reduce time-to-market by accelerating prototyping Reduce the cost involved in product development Making companies more efficient and competitive at innovation
<i>Production of Spare Parts</i>	Reduce repair times Reduce labour cost Avoid costly warehousing/stock
<i>Small Volume Manufacturing</i>	Small batches can be produced cost-efficiently Eliminate investment in tooling
<i>Customised Unique Items</i>	Enable mass customisation at low cost Quick production of exact and customized replacement parts on site Eliminate penalty for redesign
<i>Machine Tool Manufacturing</i>	Reduce labour cost Avoid costly warehousing/stock Enables mass customisation at low cost
<i>Rapid Manufacturing</i>	Directly manufacturing end-use components Relatively inexpensive production of small numbers of parts
<i>Component Manufacturing</i>	Enable mass customisation at low cost Quality improvement Shorten supply chain Reduce development costs Help eliminate excess parts
<i>On-Site Manufacturing & Repair</i>	Eliminate storage and transportation costs Save money by preventing downtimes Reduces repair costs considerably Shorten supply chain The need for large inventory is reduced Allow product lifecycle leverage
<i>Rapid Repair</i>	Significant reduction in repair time Opportunity to modify repaired components to the latest design
<i>Very Complex workpieces</i>	Produce very complex work pieces at low cost

2.1.2. Metal AM-Processes

Metal AM-processes are capable of printing a wide variety of metals which all attains different properties of which the most important are:

- *Carbon-steel*: Relatively cheap [13], but one should take into account its weldability difficulties and lack of durability. A protective surface finish will be required in most environments.
- *Stainless steels*: More expensive than carbon steels, but its weldability, corrosion resistance and aesthetics are superior. Widely applied in wire and arc additive manufacturing and the material MX3D is most experienced with.
- *Aluminium*: Main advantages of aluminium is its low weight and durability. It attains however significantly lower stiffness values than structural steels.
- *Titanium*: Very expensive, but in return it exhibits excellent strength and surface smoothness while welding it. Because of its low weight and excellent mechanical properties, titanium is very popular in aerospace industry.
- *Copper alloys*: A lot of variation in alloys are applicable, such as bronze. Despite its excellent toughness, ductility and appealing aesthetics (see figure 2.2) not widely applied. Because of its excellent resistance to chloride-rich environments a good alternative for stainless steels in marine applications.



Figure 2.2: Bronze 2x3 m double curved surface named 'Butterfly Screen', exhibited at Design Miami/Basel (Joris Laarman/MX3D)

As stated in the previous section, additive manufacturing is a collective term for the variety of additive processes. The various processes are commonly subdivided according to: the heatsource used to melt or sinter the raw material; its feedstock material (wire or powder); its feedstock delivery (powder on bed or coaxial); or its system configuration [9]. This can be seen in figure 2.3 in which WAAM, the specific process adopted in this research is highlighted.

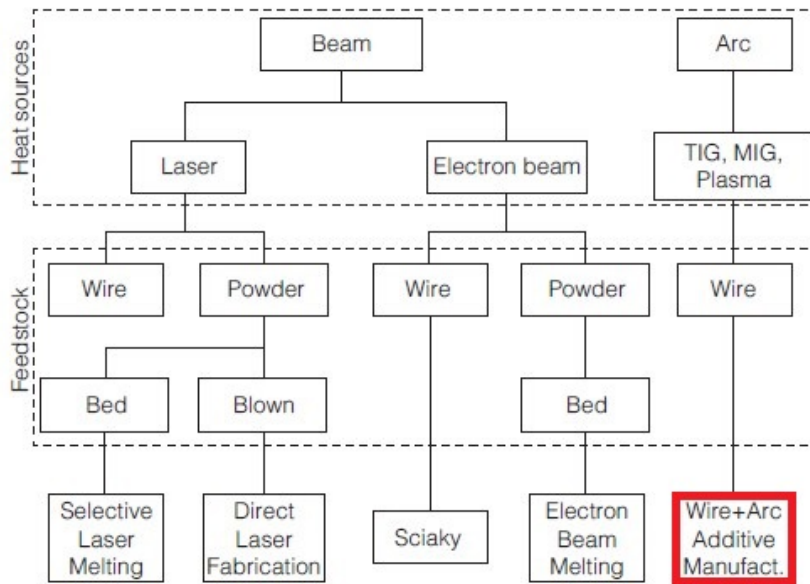


Figure 2.3: Overview of AM-processes. The considered WAAM-process has been marked in red

Whereas the processes vary widely in their details, the common denominator for all AM-processes is the ability to nearly “net-shape” manufacture complex products. At first, the most applied processes and their principles will be explained briefly.

Powder Bed Process

The collective term for powder bed processes is Selective Laser Sintering (SLS). As the name reveals, thin layers (usually 20 to 100 μm) of metal particles are spread on a processing table and subsequently fused together by sintering. A laser or electron beam (of even more than one) heats the metallic powder in the desired areas of the powder bed to just below the point of liquefaction. When solidifying, these areas become a section of the final build after which this process is repeated with a new layer. After finishing building the object, the unsintered material is removed to obtain the final product [14]. This is depicted in figure 2.4.

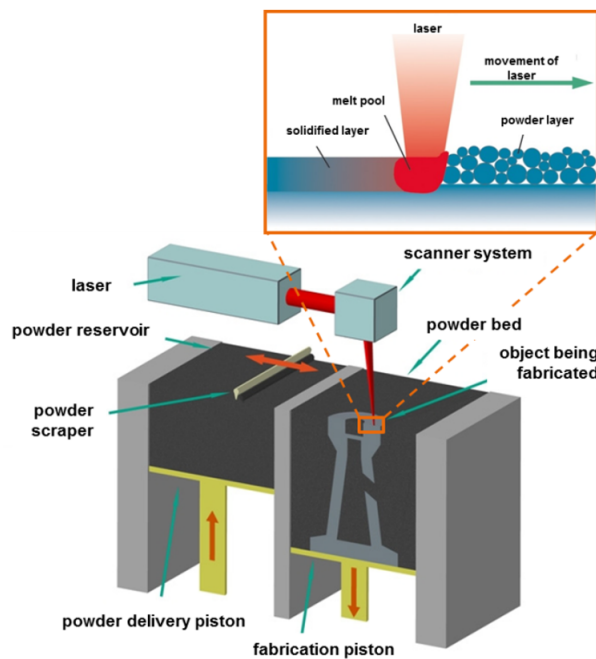


Figure 2.4: Typical powder-bed process; laser beam melting principle. Source: Fraunhofer IWU

Most powder bed processes take place in a contained building volume filled with inert gas to form a protective atmosphere. Therefore also reactive metal powders, such as aluminium and titanium can be applied. Despite the availability of many different materials, this process allows the usage of only one material at a time, in contrast to powder-fed processes. Main advantage of powder bed processes is the high accuracy which can be achieved. Different SLS technologies can be distinguished, such as:

- Selective Laser Melting (SLM)
- Laser Cusing (LC)
- Direct Metal Laser Sintering (DMLS)
- Electronic Beam Melting (EBM)

Powder-Fed or Powder-Blown Process

Powder-fed processes, also called Fused Metal Deposition (FMD), uses the same feedstock as aforementioned powder bed processes, but the method of adding subsequent layers of material differs notably. The heat source (laser or electron beam) is focused through the centre of the nozzle onto the substrate. Simultaneously, metal powder is carried by shielding gas which blows through a concentric ring towards the area being built. The nozzle moves automatically as the workpiece takes shape, as it is mounted on a multi-axis robot. This process is shown in figure 2.5. Different FMD-technologies can be distinguished, such as:

- Laser Engineered Net Scaping (LENS)
- Direct Metal Deposition (DMD)
- Laser Cladding Process / Laser Metal Deposition (LMD)

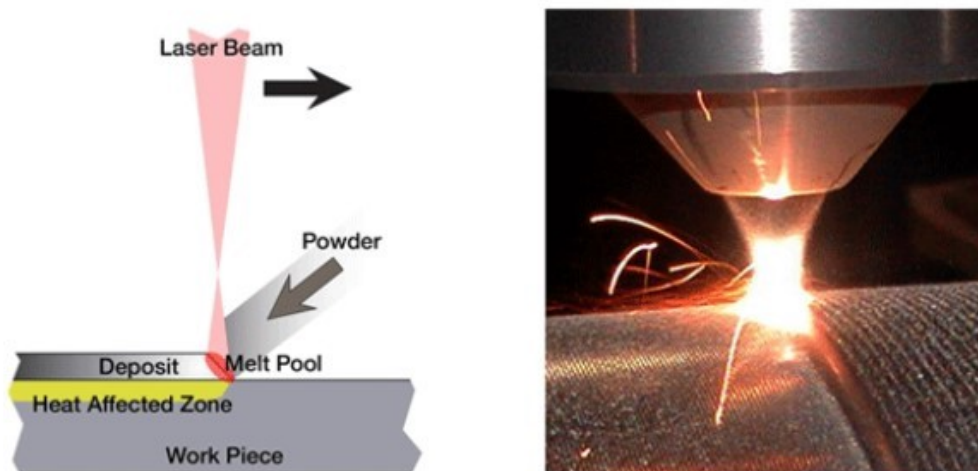


Figure 2.5: Typical powder-feed process. *Source: Sulzer Ltd, retrieved from metal-am.com*

Main advantage of this process is the possibility to produce multi-material components in one part. It is commonly used for repair of metal components. Major disadvantage is however the lack of accuracy. An extensive post-processing treatment is required to achieve a certain level of accuracy, which makes this a questionable process for complex parts. The lack of accuracy together with its low deposition rate, annihilates the advantage of tool-less manufacturing [15].

Wire-Feed Process

Wire-feed processes are actually based on systems very comparable with traditional welding. It uses a filler wire, where the heat source is used to melt the wire material in the preferable regions. The heat source can either be a laser, an electron beam or arc. Processes with an arc as heat source are generally known under the denominator of Wire and Arc Additive Manufacturing (WAAM). WAAM-processes may on their turn be subdivided in Gas Tungsten Arc Welding (GTAW), Plasma Arc Welding (PAW), or Gas Metal Arc Welding (GMAW) respectively, as depicted in figure 2.6. GMAW is the process used by MX3D, where metal is deposited from an electrode wire by creating an arc with DC-power. Meanwhile, a supply of inert gas (usually Argon and CO₂) is used to shield oxygen and other pollutants from the weld pool. The deposition is steered by a laser-guided robot path from CAD-model input. In this way MX3D is able to apply different deposition strategies while changing location or deposition order.

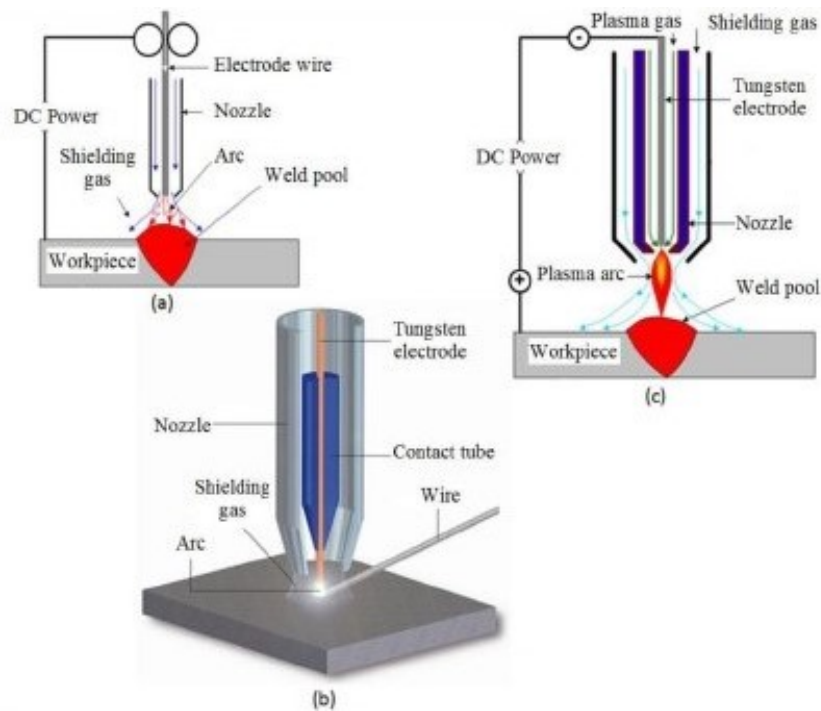


Figure 2.6: The three wire-feed processes: (a) GMAW, (b) GTAW, (c) PAW. Source: University of Wollongong

Because of their high deposition rate and relatively cheap feedstock material, wire-feed processes are especially suitable for production of medium to large-scale parts. In addition, this process is not bounded by a certain manufacturing volume as closed-powder based systems are. However, this process lacks accuracy and requires surface machining to achieve a good finish.

Table 2.2 presents an overview of properties of various AM-processes. AM-processes based on sintering, such as SLS, are significantly faster than SLM [16]. However, critical constraints for powder-based AM systems remains, namely [9]:

- Low deposition rate and processing speed leading to high specific cost
- Low alloy efficiency
- High capital cost of systems
- Cost, quality and availability of consumables
- Small build volumes
- Poor material properties with often a need for post-processing

Table 2.2: Typical properties of various AM-processes [17]

Additive materials	Process	Layer thickness (μm)	Deposition rate (g/min)	Dimensional accuracy (mm)	Surface roughness (μm)
Powder	LC	N/A	1–30	± 0.025 – ± 0.069	1–2
	SLM	20–100	N/A	± 0.04	9–10
	SLS	75	~ 0.1	± 0.05	14–16
	DLF	200	10	± 0.13	~ 20
Wire	WAAM	~ 1500	12	± 0.2	200
	EBF ³	N/A	Up to 330	Low	High

Aforementioned constraints makes powder-based processes inapplicable for printing large components such as bridge structures. Printing speed is in particular an important performance factor in AM and a key challenge that prevents it from being of practical means for manufacturing in some instances [12]. Therefore, this research focuses on an AM-process with a high deposition rate, more particularly, the WAAM-process applied by MX3D. Pros and cons of WAAM are more thoroughly discussed in 2.1.3.

2.1.3. Opportunities and Challenges for WAAM

While other AM-processes are bounded to a constraint volume, WAAM can theoretically print objects of any size as demonstrated by MX3D with their 3D-printed bridge. Research to mechanical properties of both stainless steel [5] and titanium WAAM shows promising results, with in case of titanium only a 10% strength reduction compared to extruded titanium with similar ductility values. Furthermore, the fatigue life of WAAM-titanium exceeded the fatigue life of extruded titanium for the majority of specimens [18]. The developments in post-processing WAAM-parts create even more possibilities to improve mechanical properties. Grain refinement can for instance be achieved by vertical interpass rolling, consequently enhancing yield and ultimate tensile strength [19].

Figure 2.7 shows the advantages of WAAM over other AM-processes even more clearly. Processes considered are powder bed, blown powder, WAAM and high deposition rate wire respectively. The top-right graph shows an example of a 1 meter long part of 30 kg with a BTF of 10 and a minimum feature size of 1 mm. The red-marked area shows the sweet spot of WAAM; a sharp reduction in relative part costs compared to the traditional manufacturing process of machining.

Other relations observed are the following: for a single axisymmetrical energy source at maximum melting efficiency, the build rate depends on the square of the layer height. The resolution, or accuracy, depends on the exact width-to-height ratio, usually 1.5 times the layer height at best. The surface topology (or roughness) depends linearly on the layer height [20].

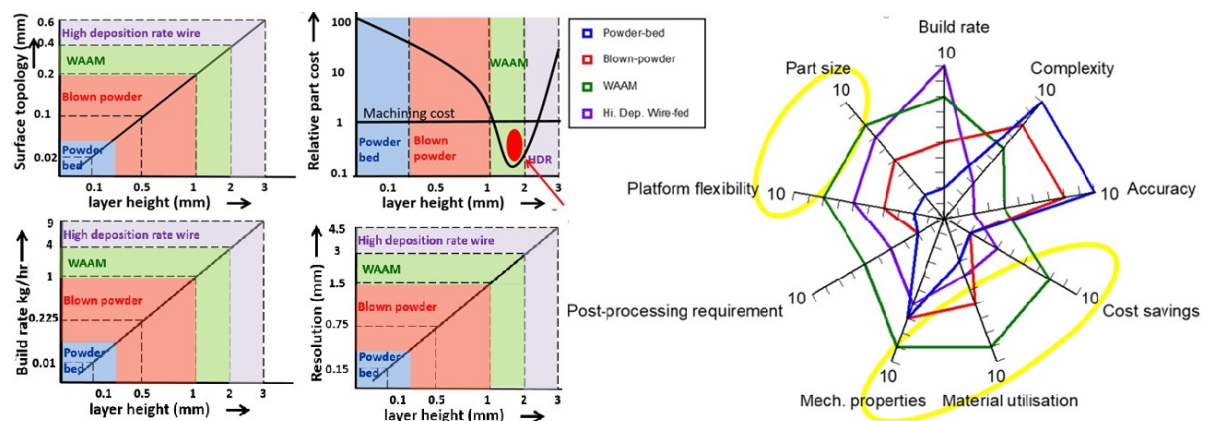


Figure 2.7: Characteristics of WAAM in comparison to other AM-processes

Environmental Impact

Due to its high material efficiency, WAAM is often referred to as a technology which yields potential in reducing environmental impact of end-user metal products. An extensive scientific study to support this claim however has yet not been published. Bekker et al.(2017) [22] performed a comparative study to WAAM and typical competing production processes for free-formed shapes; green sand casting and CNC-milling. Empirical measurements of MX3D's manufacturing process, using a deposition rate of 1 kg/h, were used as input for a cradle-to-gate life cycle assessment (LCA). Green sand casting and CNC-milling were assessed by existing literature and databases. Stainless steel 308L, identical material as the tubular columns that are studied in this research are made of, has been used as comparative material. In figure 2.10 a comparison of the total impact for the three production processes considered is depicted. It can be seen that WAAM and green sand casting have nearly similar environmental impact, with that of WAAM 3.3% lower.

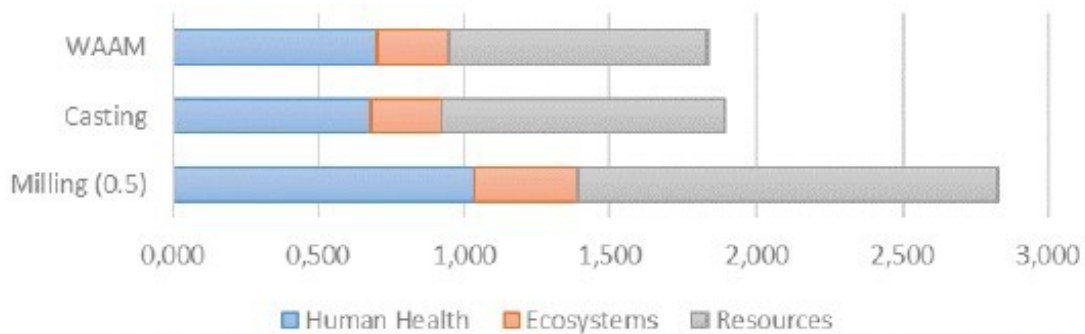


Figure 2.10: Environmental damage of WAAM, green sand casting and CNC-milling to human health, ecosystems and resources [22]

A more thorough analysis reveals the environmental impact of the single processing steps. Figure 2.12 presents a graphical overview from which it can be clearly observed that the clear dominant factor of environmental damage originates from the stainless steel itself. Topology optimisation in combination with WAAM, enables both freedom of shape and a decrease of material usage and waste. Since the environmental impact has a linear dependency to the mass of the end-product, this is exactly where the opportunities of WAAM are. When TO results in a mass reduction of 30% while the product has similar properties, this also yields a results of 30% in environmental impact, waste, material usage and material costs.

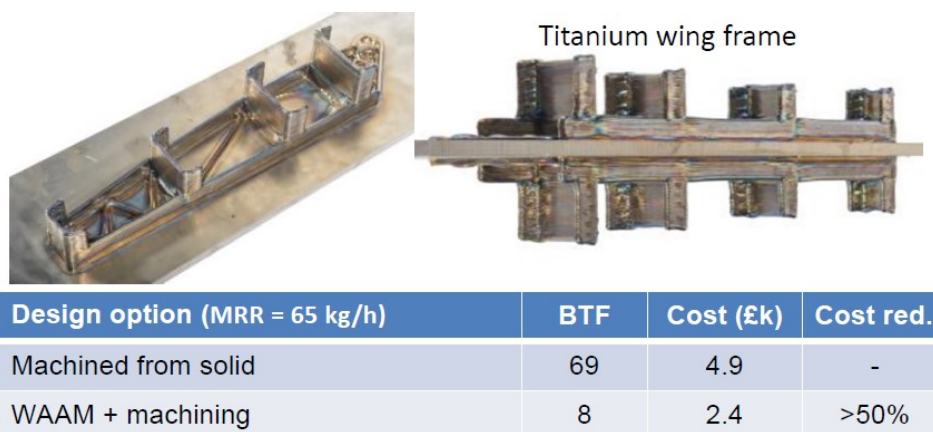


Figure 2.11: Example of reducing BTF and costs by WAAM: Titanium wing frame [23]

Fabrication of metal components contributes significantly to multiple aspects of environmental damage [24]. The impact of the metal industry is especially high in the aircraft sector due to high buy-to-fly ratios that results in high waste volumes. In addition, weight-savings have for example a significant effect on fuel consumption of rockets and aircrafts, which is both from financial and environmental point of view beneficial. This is why aerospace industry is investing a lot in WAAM. Research from Cranfield University [20] proves that a BTF-ratio reduction of factor 8 is achievable for specific aeroplane parts as shown in figure 2.11.

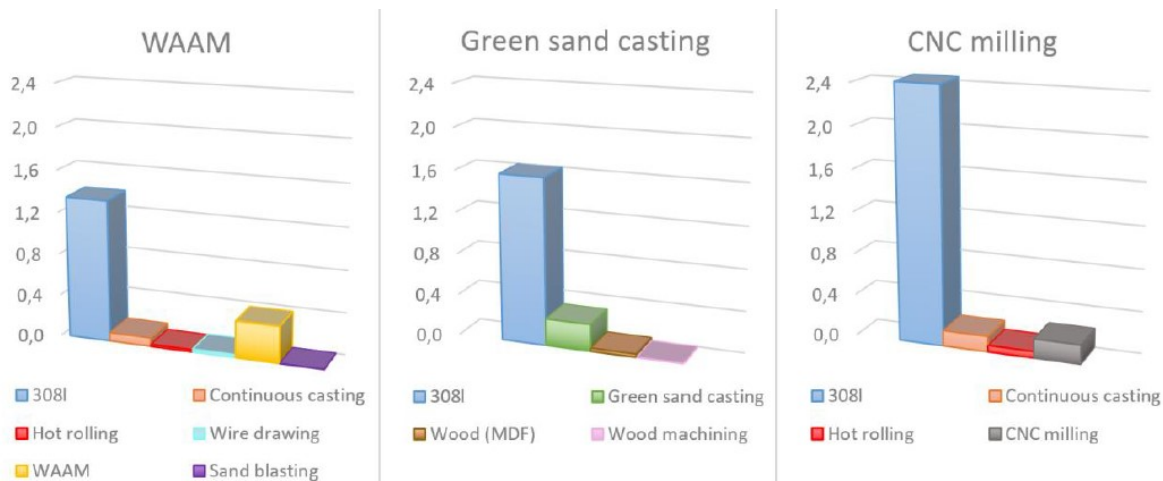


Figure 2.12: Environmental impact of the processing steps of WAAM, green sand casting, and CNC-milling respectively, in ReCiPe endpoints (Pts), per kg of manufactured 308L product [22]

Challenges

Despite recent advancements in the development of WAAM-processes, yet some challenges remain. A selection of major challenges of WAAM is listed below [25],[9]:

- Anisotropic mechanical properties
- Residual stress management
- Distortion
- Accuracy
- Surface finish
- Geometry control and weld pool collapsing
- Defects control due to the repetitive fusion of material
- Lack of interpass fusion
- Lack of available commercial systems
- Lack of qualification and standards

Depending on the demands for a product, parts created by WAAM may require a milling process to acquire a net-shape finish. The repeated passage of deposited layers, creating geometrical imperfections, could be disadvantageous for fatigue loading, friction and corrosive environments. Also the optimisation of deposition strategies to reduce residual stresses, and the recovery of deposition failures remains challenging according to Mehnen et al. [26].

In addition, insufficient data is available of material properties such as material strength, porosity or residual stress development accumulated during the build process of single parts, let alone of the structural rigidity of entire structures made by WAAM. From a large amount of experimental researches there is strong consensus that material properties are strongly related to feedstock characteristics and process parameters. Choren et al. [27] attempted to determine correlations describing Young's moduli and porosities it was concluded that predictive equations yet do not exist. Because of the large quantity of the process parameters involved, and their complex interactions, extensive trial and error research is required to ensure faultless AM-production processes.

Standards

For AM, its strong relation between manufacturing process parameters and material properties requires special attention compared to conventional shaping processes. The influence of a specific AM-process and its production conditions should be considered because they both affect the final properties of a product. All these variables, and in some cases also a lack of scientific knowledge, makes standardisation of AM-processes challenging. It is nonetheless crucial to establish a reliable production process for AM with implemented quality control system, by these means a level of trust is helped being created in the sustained achievability of good structural properties with desirable quality for additively manufactured products. In addition, standards will help support the further acceptance of AM as reliable production process.

Figure 2.13 shows an overview of recent developments in AM-standardisation. It mainly concerns terminology, testing and specifically standardisation of metal powders, because small deviations in powder-properties may have an enormous effect on product properties.

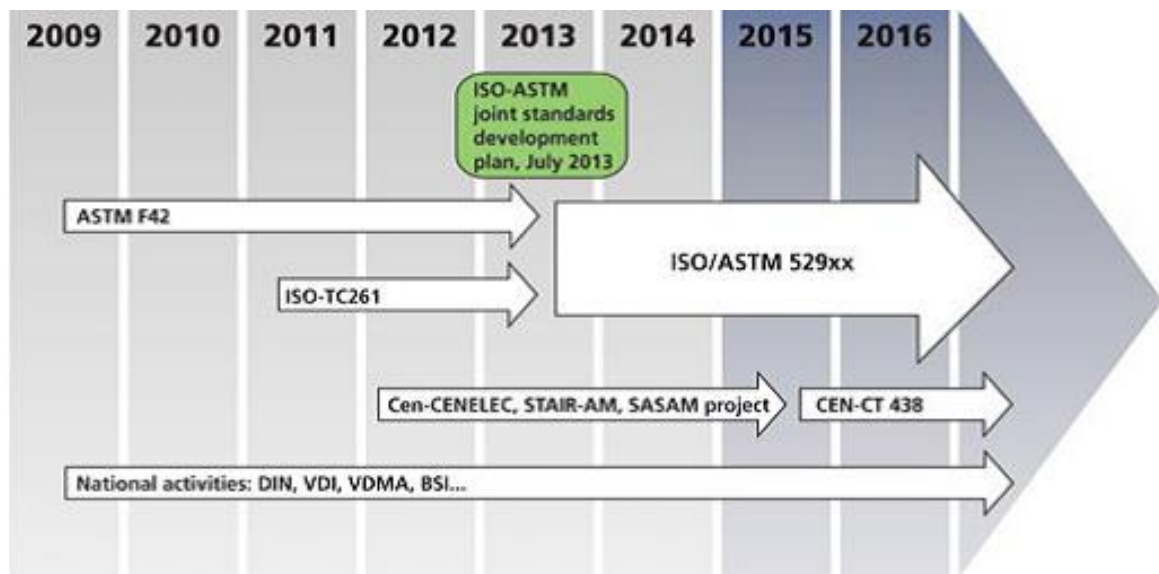


Figure 2.13: Overview of recent developments in AM-standardisation [28]

In the absence of official public regulation, Lloyd's will offer a private form of guarantee to MX3D, thereby enabling the erection of world's first AM metal bridge in Amsterdam. This guarantee will be based on existing WAAM-regulations, a review of completed AM-processes and most importantly on tests of a full-scale printed bridge structure. In addition, Lloyd's is working with the international collaboration of ASTM and ISO⁴ to advance industry standards (from ASTM F42 and ISO Technical Committee 261 towards a joint standards development plan under the designation of ISO/ASTM 529).

⁴American Society for Testing and Materials (ASTM) and International Standards Organization (ISO)

2.2. Base Material: Stainless Steel

In practice there are numerous possibilities to choose of regarding AM materials, or to be more specific, metal alloys. Since this is a relatively unexplored research field, realistically it is not possible to assess buckling behaviour of multiple materials within this thesis. This section presents several criteria which the material should satisfy, in order to be safely used in structures. A justification for the choice to use stainless steel as printing material is given. In the proceeding of this section (2.2.3 and 2.2.4 respectively), these criteria will be elaborated more by means of the microstructural build-up and the mechanical characteristics of stainless steel.

2.2.1. Base Material

The 3D-printing robots of MX3D with their GMAW-head, are capable of printing a wide variety of metals. Previous section already presented a few applications of WAAM with varying alloys which will finally be judged on multiple criteria. When choosing a printing material for structural applications, the following aspects should be considered:

- *Strength*: Yield, tensile, compression, buckling and fatigue strength should be competitive with commonly applied building materials
- *Stiffness*: A decisive material property with regards to load distribution and deformations which can be displayed by a stress-strain curve.
- *Ductility*: The material should exhibit sufficiently ductile behaviour when subject to loading to prevent brittle failure.
- *Durability*: Since the bridge will be located within the crowded city centre of Amsterdam, the need for maintenance, post-treatments and subsequent closing of the bridge should be minimised. Also corrosion resistance should be up to standards while dealing with metals in an urban area.
- *Weldability*: The variety of alloys attain different properties during and after welding. Susceptibility to cracking and other weld defects, especially with respect to the high-detailed geometry, should be reduced to a minimum.
- *Cost*: At the time of writing, the production costs still exceeds the material costs. Partly because of the need for software developers and robot programmers. However, because of developments in AM, production costs are likely to go down at a high rate, while material scarcity might cause rising prices for alloys. As a result, material costs will be increasingly a factor of importance in the course of time.
- *Printing Experience*: Printing a certain material requires customised process parameters. Therefore it is vital to have a well-developed printing strategy and extensive experience with printing of a specific material.

Considering the various criteria listed above, it is evident that printing experience is a decisive factor which reduces the material selection to the specific alloys frequently used by MX3D. MX3D has experience in aluminium, bronze and several steel grades. Especially the latter jumps out in a positive way experience-wise. By far most products printed by MX3D are made in stainless steel. This narrows down the selection of materials to be investigated in this research to stainless steel grades ER 308L and ER 316L.

These low-carbon austenitic stainless grades exhibit good mechanical properties, weldability, and corrosion resistance up to urban environmental level. The lack of necessity for a surface treatment to increase corrosion resistance is a major advantage compared to carbon steel alternatives. The higher alloyed 316L grade exhibits slightly better mechanical properties and improved corrosion resistance [5]. Though, for an urban area where the bridge will be located, 308L attains sufficient durability properties. Pricewise, 308L is the better option because it is up to 40%⁵ cheaper. Additionally the bridge will be printed in stainless steel grade 308L, making it the logical material to investigate in this research. Specifications of the exact welding wire used to print the test specimens are presented in section 3.2.2 and its corresponding datasheet in appendix B.2

⁵Average value for MIG-welding wire prices from multiple key-industry suppliers at the date of writing

However, this material selection should be made for every single product individually. Other structural applications may require different material properties, consequently demanding other materials. Besides by the base material itself, aforementioned material characteristics are also influenced by the printing strategy. In section 2.3 the relation between the most important printing parameters and the resulting specimen properties is elaborated further.

2.2.2. Stainless Steel

Stainless steel is a special type of steel alloy which behaves differently than their carbon steel counterparts. The obvious distinction between carbon and stainless steel is that the latter should by any means be able to resist corrosive attack from normal atmospheric exposure. This property is attained by an invisible and adherent chromium-oxide surface film that, when damaged, has the ability to heal itself in the presence of oxygen [29],[30]. Additionally, stainless steel possesses mechanical properties (as shown in section 2.2.4) and a microstructural composition that differs from carbon steel. When applying stainless steel in a structural design, it is vital to keep these distinctions in mind. Therefore this will be extensively discussed in the following sections.

Despite higher initial costs, stainless steels often outperform carbon steels with respect to durability. This is predominantly due to its increased corrosion resistance which eliminates the necessity for a protective surface finish. Hence reducing the overall life-cycle costs [31]. Nevertheless, special attention should be paid to the application of a material when choosing a stainless steel grade. Certain aggressive environments, for example chloride-rich marine areas, require highly alloyed stainless steels to be able to withstand corrosion.

Also within the stainless steel group, various grades exist which can be subdivided in accordance with their metallurgical structure. Table 2.3 presents an overview of typical properties per steel type.

Table 2.3: Types of stainless steel with their typical properties. Based on [30]

Type	Magnetic	Crystal Struct.	Strength	Ductility	Corrosion Res.	Grades
<i>Ferritic</i>	yes	BCC	Good	Poor	Good	AISI405, 430
<i>Austenitic</i>	no	FCC	Good	Very good	Good	AISI2XX, 3XX
<i>Martensitic</i>	yes	BCT	Very good	Poor	Moderate	AISI403, 410
<i>Duplex</i>	yes	Combination	Very good	Good	Very good	2205
<i>Precip. Hardened</i>	yes	Combination	Excellent	Very good	Very good	17-4PH

The five distinguished types are ferritic, austenitic, martensitic, duplex and precipitated stainless steels of which the austenitic type is most widely applied in structures. Duplex steels have a mixture of austenitic and ferritic grains in their microstructure, which explains the 'duplex' structure. This is achieved by a reduction of nickel content compared to what is required for the production of full austenitic steels [32].

Martensitic and ferritic steels behave less ductile, and just as austenite steels they cannot compete with the superior strength of duplex and precipitation hardened steel grades. Despite their superior strength, both steels are very sensitive during welding as opposed to austenite grades. Besides good strength and ductility, austenitic grades attain the important property of nearly unaffected mechanical characteristics during welding, which makes this grade especially suitable for WAAM. Additionally they have excellent toughness when subjected to very low temperatures and are therefore extensively used in cryogenic environments [29]. Austenite grades can be easily identified by their 200 or 300-series designation with additional letters to identify the composition and certain characteristics of the alloy; e.g. the 308LSi alloy as used in this research (designating low carbon L and extra silicon alloying Si).

2.2.3. Microstructure

The variety of stainless steel alloys can be subdivided by means of their specific crystalline structure and microstructural build-up, both affecting material and mechanical properties. To be able to understand and analyse material properties that are observed in tests, thorough knowledge of the stainless steel microstructure is indispensable. Since the column specimens are printed in an austenitic grade, this section has been written with emphasis on this group of metals. A concise outline is presented using five characteristic subjects. Firstly the crystal structure of the alloy will be discussed, followed by its crystal-based grain structure

which strongly affects engineering properties. Next, the influence of temperature and cooling rate on the microstructure of metals is elaborated under the designation of 'solidification structures'. Finally, distinctive phases for alloys are presented with their typical welding problems.

Crystal Structure

When a liquid solidifies, it attains either an amorphous or crystalline structure. An amorphous structure can be considered as a random structure, lacking any order. Glass and most organic materials are typical amorphous materials. Grains in metals however, form orderly crystalline structures consisting of atoms, or molecules, in a regular three dimensional pattern. The specific arrangement of atoms and molecules in the crystal (also referred to as morphology), determines the type of crystalline structure that is present. Additionally, metals are an allotropic material, meaning that their crystal structure may alter at a certain temperature [33].

All crystal shapes can be subdivided in seven groups, with fourteen possible lattice arrangements. Nonetheless, since the vast majority of metals crystallize in only three basic patterns, these will be shown here. The three basic patterns are face-centered cubic (fcc), body-centered cubic (bcc) and hexagonal close-packed (hcp) respectively. Their typical structures are visualised in figure 2.14.

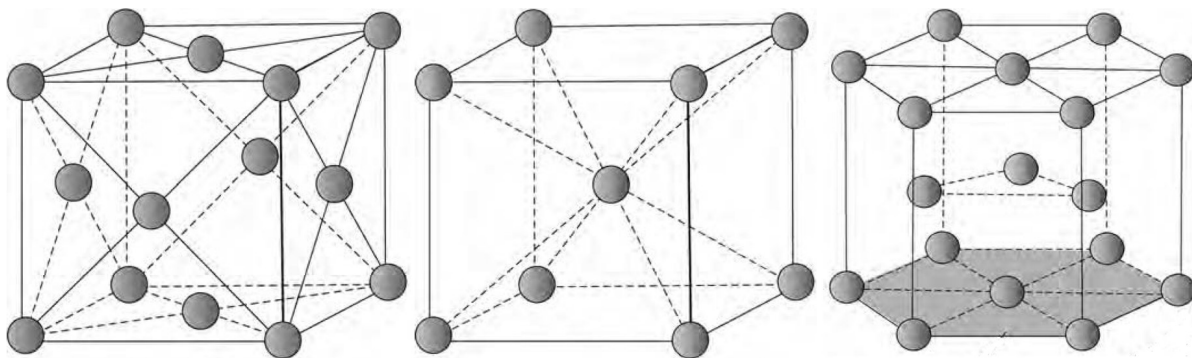


Figure 2.14: From the left to right: fcc-, bcc- and hcp-crystal lattice structure [30]

From those three basic lattice structures, two are of importance for this research; austenite steels attain fcc-lattices (γ -Fe) and ferrite steels bcc-lattices (α -Fe). Duplex steels have a combination of both structures. In case of fcc-crystals, the iron atoms are on the cube corners and at the centres of each cube-face [33]. Ferritic steels may be transformed in steels with an austenite structure by alloying with nickel at room temperature. Phase changes are also induced at certain temperatures. The subject of phase changes will be more thoroughly discussed in the proceeding of this section by means of the iron-carbon phase diagram (see figure 2.23).

Although in aforementioned theory crystal structures are represented as perfectly ordered crystalline lattices, they are rarely perfect in practice. In reality, crystals have irregularities in the arrangement of the atoms that may significantly affect the properties of crystalline solids [34]. These crystal defects can both have a positive and a negative effect on for example mechanical deformation and ductility of steel. Defects can be roughly subdivided in point defects, line defects (or dislocations), planar defects and volume defects. The latter includes porosity and (non-metallic) inclusions, which may substantially reduce strength and fracture resistance. Shrinkage during solidification could lead to micro-porosity, on its turn allowing precipitates voids to occur under certain circumstances, also negatively affecting properties of crystalline solids [34].

Besides negative effects, the presence of dislocations allows movement along the slip planes within the crystalline structure. The accumulated movement along the slip planes on macroscopic level is known as plastic deformation. In case of fcc- (austenite) systems, the iron atoms are structured in a very close packed arrangement; the densest packing that can be obtained in a crystal structure. An fcc-system has four slip planes, each with three possible slip directions as depicted in figures 2.15 and 2.16.

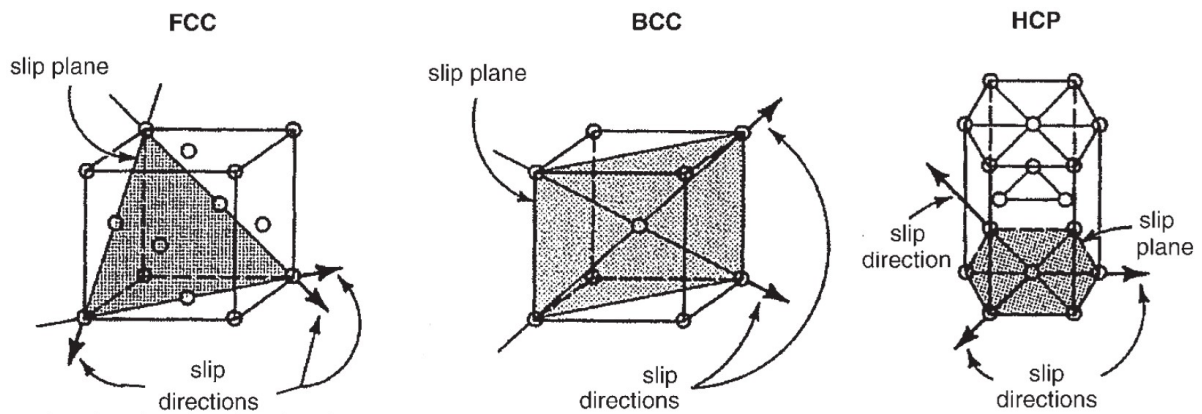


Figure 2.15: Dominant slip systems for the three presented basic lattice patterns [30]

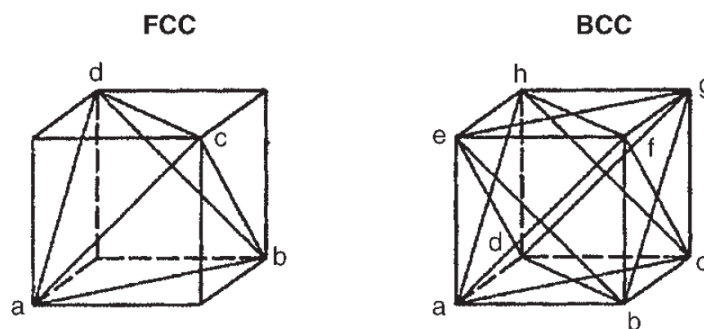


Figure 2.16: The four slip planes in an fcc-lattice and six slip planes in a bcc-lattice

Close-packed planes provide the preferred slip planes for dislocations [34]. This is why austenite metals maintain good toughness and ductility, even at cryogenic temperatures. The non-directionality in the bonding of atoms also allows thermal vibrations to be easily transmitted from one vibrating atom to its neighbours, which explains the high thermal conductivity of austenite stainless steels [33].

In contrast to an fcc-structure, a bcc-lattice structure is not close-packed. In this case slip deformation occurs along nearly close-packed planes. A bcc-structure has more available slip systems, but the operability of these slip planes is more dependent on temperature and chemical composition. When for example lowering the temperature, a ferrite (bcc) metal becomes more brittle. The relation between a metal its atomic structure and its mechanical properties marks the necessity to acquire sufficient knowledge about the exact composition of the stainless steel considered; does one have to deal with a ferrite, austenite or duplex stainless steel?

Microstructure (Grains)

When considering a metal structure on a different scale; one size up from the atomic structure, this is called 'microstructure'. The microstructure of metals is built up from small crystalline grains and their grain boundaries. These grains typically form independently during solidification, together forming a characteristic polycrystalline microstructure as shown in figure 2.17.

Grain boundaries separate the crystal lattices of individual grains, hence serving as barriers to dislocation motion. They are the result of grain disorientation as they are frozen into position during the solidification process. So, grain boundaries are actually regions with many irregularly placed atoms, dislocations and volume defects (voids, pores). As a consequence, these regions are the preferential region for congregation and segregation of impurities. Segregation of alloying elements results in a heterogeneous microstructure: the distribution of austenite and ferrite is uneven. Possible migration of chromium might cause a local reduction in corrosion resistance. Compositional fluctuations of subsequent weld deposits should therefore be considered [35].

Weakening of the microstructure may occur due to phase precipitation or by undesired environmental factors in the grain boundaries [30]. Additionally, weakening may occur due to non-metallic inclusions which commonly mistakenly become entrained within the metal during the manufacturing process. The presence of inclusions does not have an adverse effect on strength, but it does reduce ductility and toughness of the material.

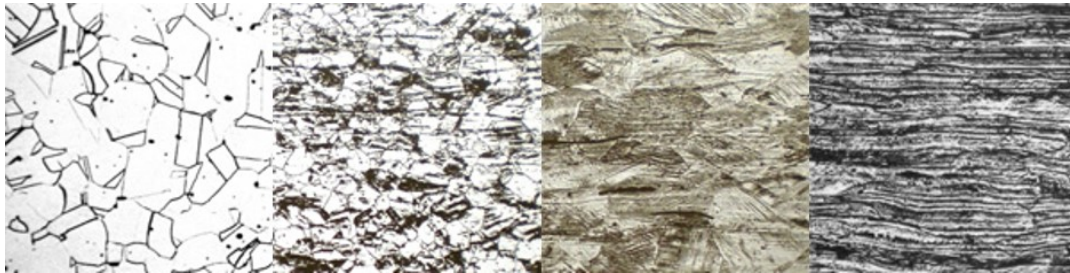


Figure 2.17: Typical austenite microstructure of AISI304 stainless steel. (Magnification 250x, 0% cold working) [36]

Mechanical properties of a metal are intimately related with its grain size, distribution and shape. As yet mentioned, grain boundaries provide a source of strengthening by pinning the movement of dislocations. During cooling of austenite, the new bcc ferrite crystals start to grow from many points. The number of starting points from which new crystals start to grow determines the number of ferrite grains and consequently the grain size. By for example adding alloying elements like aluminium and niobium, the number of starting points from which new crystals grow can be increased, and the grain size decreased [33]. When reducing the grain size, the relative amount of grain boundaries that strengthen the material, increases. A reduction in grain size imposes an increase in brittle fracture resistance. And even more profoundly, a finer grain structure improves the yield strength.

The Hall-Petch equation (2.1) based on independent observations in the early 50's [37],[38] describes the relation between yield stress and grain size mathematically for the three common crystal structures as graphically depicted in figure 2.18. A number of methods have been developed to measure the grain size of a sample. The simplest beholds counting of the grains that are present in a known area of a sample, so that grain size can be expressed in the number of grains per area.

$$\sigma_y = \sigma_0 + \frac{k_y}{\sqrt{d}} \quad (2.1)$$

Where σ_y is the yield stress and d the grain size (or diameter) in millimetres. Both σ_0 and k_y are unique to each material. The first equals the stress at which dislocation movements initiate. And k_y is a strengthening coefficient. Typical values for steel are $\sigma_0 = 70$ and $k_y = 0.74$.

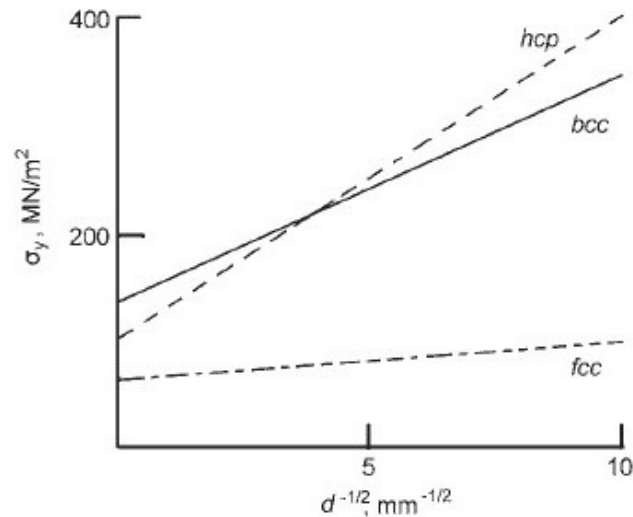


Figure 2.18: The relation between grain size and yield strength for metals with different crystal structures [39]

Grain refinement is therefore an important beneficial mechanism to strengthen structural steels. This refinement can for example be achieved by rolling or cold forming of steel or by temperature treatments (annealing). Since rolling is not an option for additively manufactured products, controlling heat input and corresponding temperature gradient, or cooling rate, is the most predominant way to influence grain orientation. Aforementioned temperature related variables are closely related to the process parameters of the printing process. Section 2.3 describes this relation in more detail.

To be able to study the microstructure of a metal, a specimen of the considered metal should be prepared first. The process of specimen preparation is known as metallography [33]. It usually involves sanding, polishing and chemical etching using an appropriate etchant. After completing this process, the etchant has produced an uneven specimen surface on a microscopical scale. As a consequence, the light reflects in a different way compared to an unetched surface. Hence, under magnification provided by a microscope, the underlying microstructural composition of the material becomes visible (see figure 2.19).

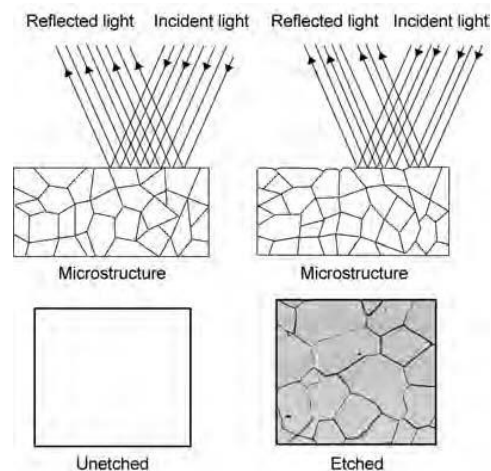


Figure 2.19: Metallography for an etched and unetched specimen [30]

The importance of a clean and correct sample preparation cannot be underestimated because this very process alone can induce microstructural changes to the specimen. Section 3.5 provides the reader with the exact metallographic preparation procedure that is used in this research to prepare the additively manufactured specimens.

Solidification

Molten metal solidifies in a typical crystalline structure by nucleation. During solidification, atoms lose their kinetic energy while forming a crystal lattice. The kinetic energy is released in the form of heat which is called the latent heat of fusion. Three types of crystal growth patterns can be distinguished: planar, cellular and dendritic growth. This growth pattern is determined by the cooling rate and temperature gradient of the system.

When the liquid ahead of the solid-liquid interface (denoted by x_0), attains a positive temperature gradient, heat is removed from the liquid by conduction. The resulting uniform distributed linear temperature gradient perpendicular to the interface induces crystal growth planar to the liquid (figure 2.20(a)). Whereas in case of a temperature decrease ahead of the solid-liquid interface (also referred to as 'undercooling'), either cellular or dendritic growth will occur (figure 2.20(b) and (c)) [30]. This is dependent on the level of undercooling: little undercooling will result in cellular growth, while a large undercooling produces dendritic growth.

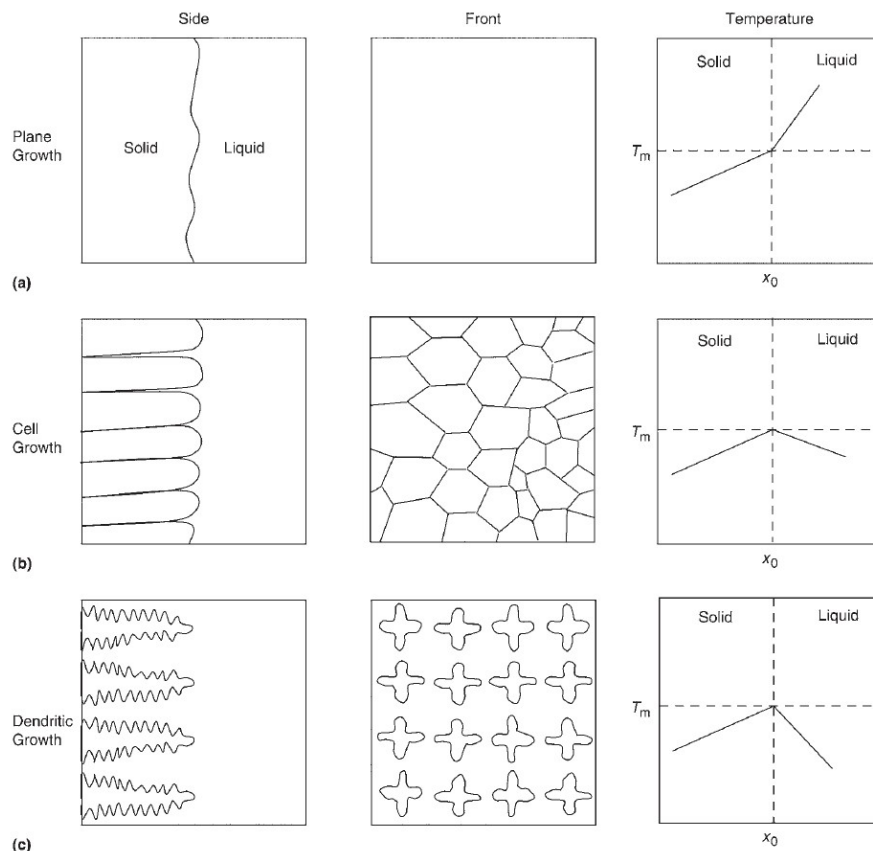


Figure 2.20: Effect of undercooling on solidification structure (a): plane growth; (b): cell growth; (c): dendritic growth [30]

Dendrites can be recognised by their pine trees-shaped crystals. They grow rapidly into the metal because of the high negative temperature gradient. As the primary arm of the dendrite solidifies, it releases its latent heat of fusion which causes a sudden temperature increase adjacent to the primary dendrite arm. As a consequence of this new temperature inversion new (or secondary) dendrites start to grow perpendicular to the primary arms.

Wire-arc additively manufactured structures, can actually be considered as a series of multipass welds. Therefore it is expected that their solidification structures are similar as well. In multipass welds it is observed that dendrites grow in the direction of the temperature gradient as already stated before [40]. When grains form unidirectional due to directional solidification, columnar grain structures can be observed. Since columnar grains results in anisotropic mechanical properties [41], this situation is unfavourable while loading a specimen in multiple directions. Elastic constants correspond to the orientation of the columnar grains. This

anisotropy should therefore be taken into account when applying WAAM-material in structures. Mechanical tests should accordingly be considered in both the print direction and in transverse direction, perpendicular to the thermal gradient.

The solidification structure and its difference across the printed specimen can be studied by analysing micrographs of different cross-sections. Because it might be hard to observe the exact grain orientation in a specimen which has been built up from multiple weld layers, it might be an option to use electron backscatter diffraction. The analysis of the data output can however be very time-consuming.

Vitek et al. [42] showed that cooling rates can have a significant effect on alloys that are not fully austenitic. The microstructural composition of duplex steel welds are altered by high cooling rates. Higher cooling rates typically lead to an increase in ferrite content (with an exception for very high cooling rates) [43]. Typical cooling rate ranges for various solidification processes are given in table 2.4 [44]. The cooling rate of arc welding is relatively low compared to the other solidification processes, but the exact value within this cooling rate range largely depends on the welding process parameters. Section 2.3 discusses the influence of process parameters on mechanical and metallurgical properties in more detail.

Table 2.4: Cooling rates for different fabrication and solidification processes [44]

Fabrication Process	Cooling Rate [K/s]
Directional Solidification	10^{-1} to 10^1
Casting	10^0 to 10^2
Arc Welding	10^1 to 10^3
Electron-Beam Welding	10^2 to 10^4
Laser-Beam Welding	10^2 to 10^6
Single-laser Pulse	10^7 to 10^8

The macroscopic shape of a weld is a decisive factor that influences both the grain size and microstructure of the fusion zone. It is therefore important to understand the basics of weld pool development and its geometry. This will be deduced by means of a simple fusion weld as depicted in figures 2.21 and 2.22. Three major zones of a fusion weld can be distinguished: the fusion zone, its adjacent unmelted heat affected zone (HAZ), and the base metal. In case of an alloy, a fourth zone can be denoted surrounding the weld pool consisting of a liquated (partially melted) zone.

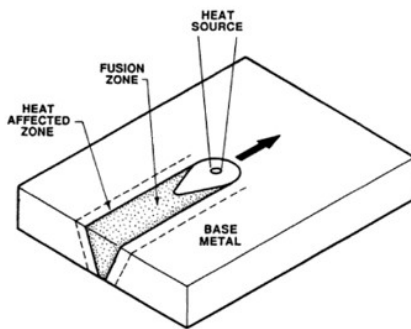


Figure 2.21: Schematic view of three weld zones

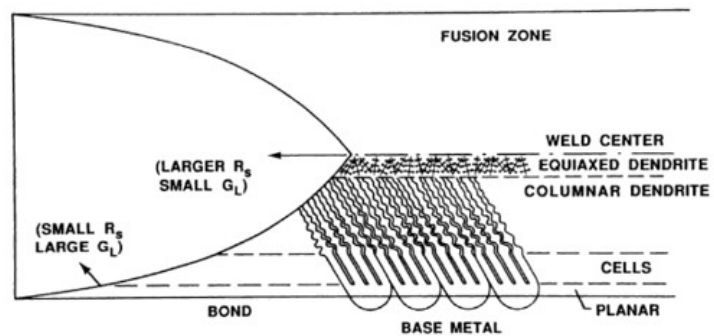


Figure 2.22: Microstructural variations of a weld across its fusion zone

The solidification behaviour in the fusion zone controls the grain size and its orientation. Additionally it determines the extent of segregation of elements and the distribution of inclusions and weld defects. Microstructural changes in the HAZ usually give rise to deterioration of the engineering properties of the weld metal [33]. This means that in case of a multi-layer additively manufactured element, every subsequent layer of welds changes the microstructure of a certain zone around the renewed weld pool. Special attention should be paid to these microstructural changes in the material while performing a microscopic analysis of the WAAM columns.

Phases

With increasing temperature, the crystal structure of steel changes. This is depicted in a typical iron-carbon phase diagram (see figure 2.23). On the vertical axis one can see the temperature, and on the horizontal axis the percentile carbon content. When heating pure iron, so without any added carbon, the bcc-crystals (ferrite) change in fcc-crystals (austenite) at a temperature of 910 degrees Celsius. Below this temperature, the microstructure of pure iron changes [33].

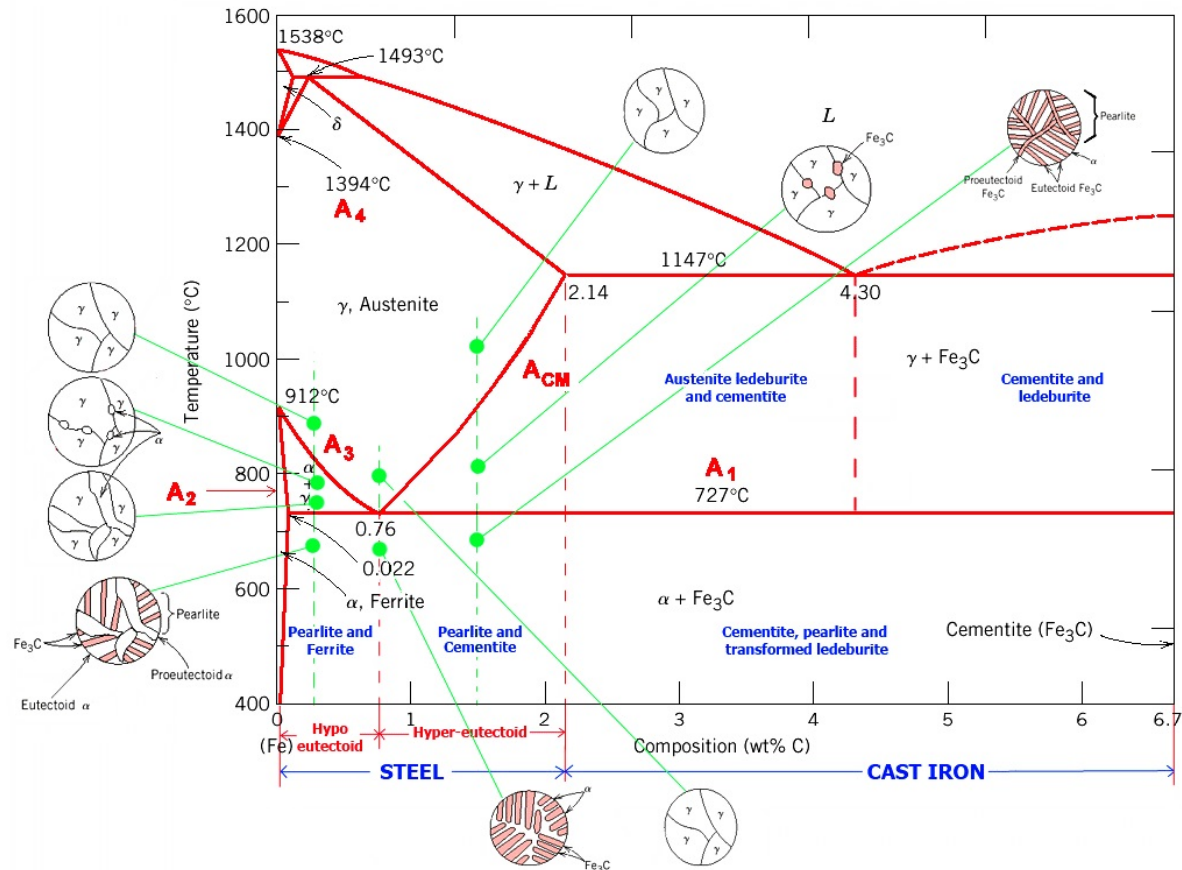


Figure 2.23: Iron-carbon phase diagram⁶

Austenitic stainless steels are either fully austenitic, or austenitic with a small amount of delta (δ)-ferrite. Whereas carbon and low alloy steels undergo phase changes as stated above, austenitic stainless steels experience no phase changes during cooling from its liquid state to room temperature. As a consequence, its mechanical properties are to a great extent unaffected by welding [29].

Properties of stainless steels in general can be significantly enhanced by thermal treatments and cold forming. Since stainless steel alloys may encompass a wide variety of alloy contents, the effect of those treatments differs a lot per steel grade. Higher strength levels can be obtained by for example cold-working, annealing and quenching. However, because the crystal structure of austenitic grades is unaffected by thermal treatment, these grades can only be hardened by cold deformation and full annealing [30]. Cold-worked austenitic stainless steels will contain strain induced martensite, which potentially reduces the corrosion resistance compared to a fully softened austenitic metal. Main hazard is stress corrosion cracking (SCC) induced by tensile stresses [45]. During full annealing of steel, the metal is heated and slowly cooled down afterwards, resulting in an increase of ductility and workability (hardness reduction). Stress-relieving by annealing additionally removes residual tensile stresses, thereby increasing the resistance to SCC.

⁶retrieved from https://www.tf.uni-kiel.de/matwis/amat/iss/kap_6/illustr/s6_1_2.html on 19/09/2017

By alloying, the microstructure of a stainless steel can be altered. Anton Schaeffler published a phase diagram that shows the effects of a certain chemical composition on the microstructure graphically [46]. As can be seen in figure 2.24, alloying elements are assigned to two groups, named chromium and nickel equivalents. These equivalents are determined by multiplication factors to the various elements, reflecting the strength of their effect on the formation of ferrite and austenite. They are denoted on the horizontal and vertical axis respectively. Some alloying elements favour the formation of austenite (nickel, carbon, manganese and nitrogen), where others support the formation of ferrite (chromium, silicon, molybdenum and niobium).

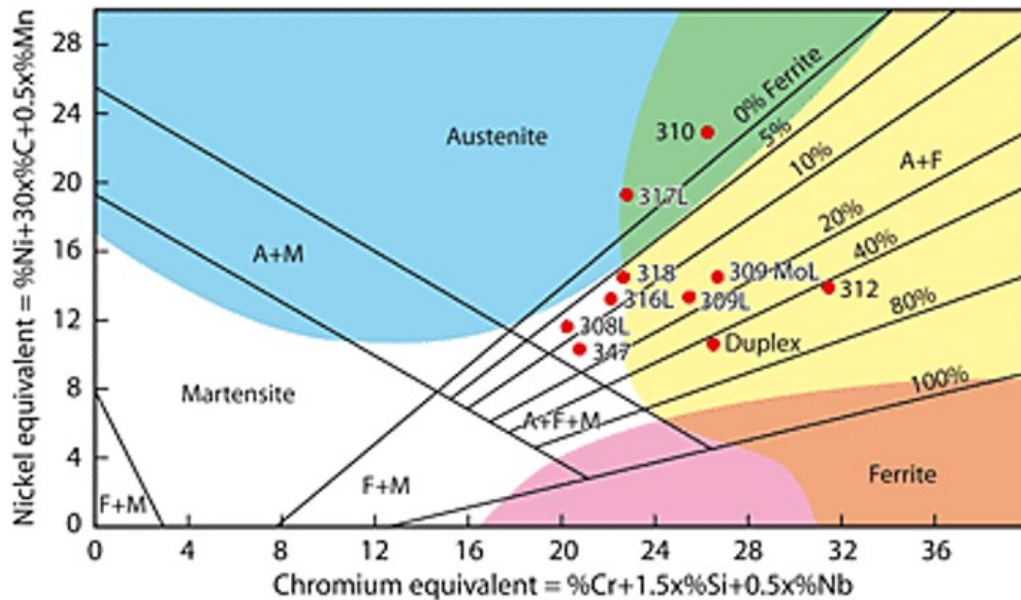


Figure 2.24: Various types of phases present in solidified stainless steel illustrated by a Schaeffler diagram [29]

Weld defects are related to the specific microstructural composition of a metal. The coloured areas in figure 2.24 identify some of the common problems that may be encountered during fabrication of austenitic stainless steels. The blue and green zones corresponds to hot cracking; pink to grain growth and embrittlement; yellow to embrittlement at elevated temperatures or stress relieve; and brown is a combination of problems depicted by the two aforementioned coloured areas.

In addition the diagram shows a selection of the most widely used types of welding wires. Special attention should be paid to the 308L steel grade, since test specimens made from this grade are being investigated in this research. More specifically, the chemical composition of this welding wire is presented in table 2.5 by means of typical alloy-content values. In this grade, silicon is used as extra alloying element to enhance oxidation resistance and the resistance to corrosion by oxidizing acids, hence explaining the suffix -Si in 308LSi.

Table 2.5: Chemical composition of Oerlikon's Inertfil 308LSi welding wire (typical values in %) [47]

Chemical element	C	Mn	Si	P	S	Cr	Ni	Fe
Content (%)	0.02	1.8	0.85	≤ 0.025	≤ 0.020	20	10	5 to 10

This steel grade, together with other commonly applied types as ER 304, 316, and 347, fall exactly within an uncoloured triangular area in the center of the diagram. It denotes that these grades contain a certain amount of δ -ferrite. Ferrite is capable of dissolving an increased amount of sulphur and phosphorus compared to its austenite counterpart, hence avoiding the formation of undesirable liquid films along the grain boundaries. In addition, the presence of ferrite increases the grain boundary area so that liquid films must spread over a greater area. As a consequence, these alloys have a higher resistance to the formation sulphur-containing liquid films [29].

Corrosion & Weld Defects

Despite the fact that stainless steels in general attain a good corrosion resistance, there is a common misconception that stainless steel does not suffer from corrosion at all. In fact, it may in certain environments suffer staining or severe corrosion attacks [31]. This emphasises the necessity to select an appropriate stainless steel grade, taking into account its risk for exposure to corroding environments.

According to Eurocode 3 part 1.4. annex A [48], the correct procedure to verify if a structure meets the environmental requirements firstly involves the calculation of the Corrosion Resistance Factor (CRF). The CRF depends on the severity of the environment and is calculated by the sum of three risk components taking into account exposure to chlorides (from salt water or deicing salts), sulfur dioxide and exposure to washing by rain respectively.

Next, the corrosion resistance class (CRC) can be calculated from the CRF using matching table A2 (see table 2.6). At last, to ease steel grade selection, table A3 (table 2.7) provides a selection of steel grades subdivided according their CRC. Here it can be seen that most austenitic grades are classified in CRC II. Steel grade ER308LSi, used in this research, attains very good intergranular and atmospheric corrosion resistance in urban and rural areas. Therefore this grade is in particular suitable for a WAAM-bridge structure as it will be placed in Amsterdam's city centre. In general holds, the higher the alloy content, the more expensive the steel becomes. Choosing an extra corrosion resistant steel should therefore be avoided to limit unnecessary costs.

Table 2.6: Determination of CRC according to table A2⁷

Corrosion Resistance Factor (CRF)	Corrosion Resistance Class (CRC)
CRF = 1	I
$0 \geq \text{CRF} > -7$	II
$-7 \geq \text{CRF} > -15$	III
$-15 \geq \text{CRF} \geq -20$	IV
CRF < -20	V

Table 2.7: Grade selection in each CRC according to table A3⁷

Corrosion resistance class CRC				
I	II	III	IV	V
1.4003	1.4301	1.4401	1.4439	1.4565
1.4016	1.4307	1.4404	1.4462	1.4529
1.4512	1.4311	1.4435	1.4539	1.4547
	1.4541	1.4571		1.4410
	1.4318	1.4429		1.4501
	1.4306	1.4432		1.4507

The type of surface finish may greatly affect durability. Arrangements which allow dirt entrapment or chemical concentration should be avoided. Wire-arc additively manufactured elements could be extra sensitive when retaining its rough surfaces. This could be reduced by for example sanding the final structure. If in addition visual quality is of importance for a given component, an appropriate finish may be specified in accordance with EN 10088-4 or EN 10088-5.

Whereas a self-repairing adherent chromium-rich oxide film protects stainless steels from reacting with the atmosphere, the level of protection depends on the composition of steel, its surface treatment and the aggressiveness of the environment. The stability of the passive film increases for example with increasing chromium content, and added nickel decreases the corrosion rate. Other alloying elements stabilising the stainless steel are titanium, niobium and molybdenum. To enhance corrosion resistance even further, in particular to intergranular corrosion, some steel grades, including the grade used in this research, have a lowered carbon content (designated by suffix L, f.e. ER308L).

The relevant corrosion mechanisms and weld defects (for austenitic grades) will be concisely explained here:

⁷from NEN-EN1993-1-4:2006/A1:2015 Annex A

Intergranular corrosion

Despite the ability of carbon to stabilise the austenite structure, it is considered as an undesirable impurity in austenitic stainless steels. When austenitic steels are exposed to temperatures between 450 and 900 °C, for example during welding, the carbon in the steel diffuses to the grain boundaries and precipitates chromium carbide ($Cr_{23}C_6$) as shown in figure 2.25. As a result of this process, the chromium content adjacent to the grain boundaries lowers. This phenomenon is known as 'sensitization'. When the chromium level drops below 12%, grain boundaries become susceptible for corrosion. In general this occurs in the heat affected zone of a weld and related corrosion is therefore referred to as 'weld decay'.

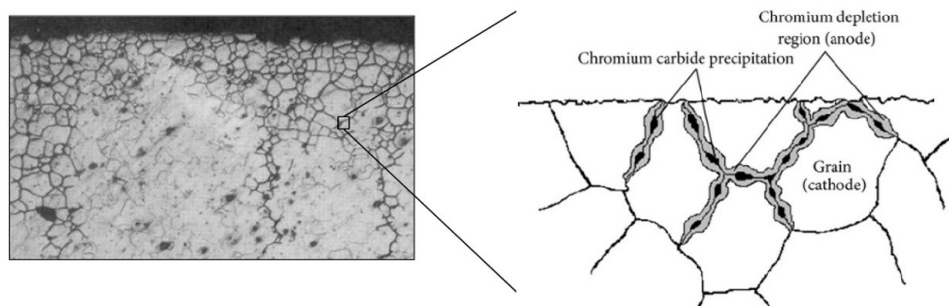


Figure 2.25: Precipitation of chromium carbide in sensitised stainless steel [49]

To avoid intergranular corrosion, or weld decay, the follow measures could be taken:

- Use heat treatment.
- Stabilise the steel with titanium or niobium.
- Use steel with a low carbon content.

Experience has shown that a low carbon content ($\leq 0,03\%^8$) is in most cases sufficiently low to guard against intergranular corrosion after welding [48],[41]. This is particularly applicable to arc processes since this process involves rapid heating and cooling of steel [31]. With a carbon content below 0.02% (see table 2.5), the 308LSi-alloy studied in this research, is sufficiently safeguarded against weld decay. In addition, intermetallic phases can reduce the toughness of duplex steels [50].

Stress corrosion cracking

The simultaneous presence of tensile stresses, increased temperature and aggressive environments might induce stress corrosion cracking (SCC). Special caution should be exercised when high residual stresses are present, for example due to arc welding, and when the member is being used in chloride-rich environments, such as marine areas [51]. With increasing tensile stress and higher temperatures the likelihood of observing SCC also increases [31]. Whereas ferritic and duplex stainless steel are relatively unaffected by SCC, austenite grades could be made more resistant by adding molybdenum. Because molybdenum promotes the formation of ferrite, also nickel should be added to keep the steel structure austenitic.

Solidification cracking

Solidification cracking (also referred to as hot cracking) occurs during solidification of the weld metal when the available supply of liquid weld metal is insufficient to fill the spaces between solidifying weld metal which are opened by shrinkage cracks [52]. Thus these cracks are initiated when the strain on the weld pool is too high due to shrinkage of the weld pool. Solidification cracking is most likely avoided when the steel contains approximately 5% ferrite [51].

⁸According to NEN-EN 1993-1-4: 2006 A.2.6.(4)

Porosity

Porosity may become present by absorption of evolved gases (nitrogen, oxygen and hydrogen) in the molten weld pool which becomes trapped in the metal during solidification [41],[53]. Both nitrogen and oxygen absorption usually originates from poor gas shielding. Increasing area fractions of porosity in a weld section reduces its strength and ductility. In the vast majority of the cases porosity has acceptable levels and is therefore rarely considered as serious defect. However, in case of an experimental fabrication process as robotic WAAM with changing process parameters, the possible presence of porosity should be monitored carefully. Especially while printing on site in an uncontrolled environment, proper gas shielding might be hard to attain.

Inclusions

At certain concentrations (>0.05%), sulphide and phosphide particles can be harmful to the toughness of the steel. To avoid formation of iron sulphide (which is harmful for steels), manganese is added so it can form the relative unharmed manganese sulphide (MnS) [33].

Aforementioned corrosion mechanisms and weld defects will be investigated by microstructural research. How this will be done is explained in section 3.5 whereas the results can be found in section 4.3.

2.2.4. Mechanical Properties

The mechanical behaviour of stainless steels differs from that of carbon steels in a number of respects. Some of the differences are, amongst others, anisotropy due to rolling and a more pronounced response to cold working of the material. Because both rolling and cold working is not applicable to WAAM, these differences will not be discussed any further in this research. How stainless steels behave differently from carbon steels can be explained more profoundly by its stress-strain relation.

Stress-strain relation

Whereas carbon steels typically exhibit linear elastic behaviour up to its yield stress before it reaches a plateau and subsequently encounters strain hardening, stainless steels have a more rounded, non-linear response. Because stainless steels yield gradually and thus lack a clear defined yield plateau, their 'yield' strengths are denoted in terms of a proof strength. Conventionally the proof strength is defined for an offset of 0.2% permanent strain and denoted as $\sigma_{0.2}$ [51]. This is depicted in figure 2.26.⁹

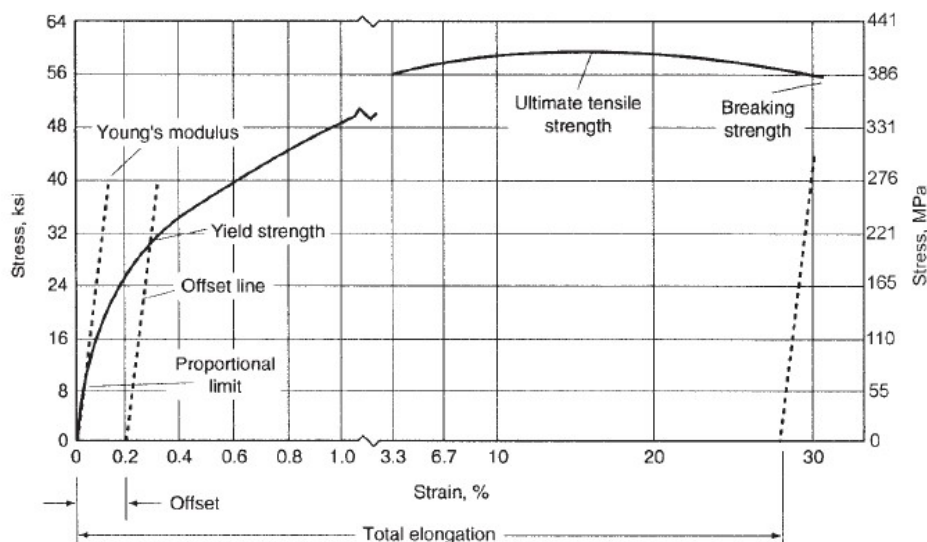


Figure 2.26: Typical stress-strain curve for stainless steel [30]

⁹It should be noted that in annealed conditions, stress strain curves in some cases behave more non-linear in tension than in compression [31] [54].

As stainless steels yield gradually with relatively low proportional limits, designing stainless steel members can be more complex than their carbon steel counterparts [55]. This non-linear behaviour with strain-hardening effects introduces difficulties for plastic global analysis. In addition, high ductility, and foremost, the low yield to ultimate strength ratio implies that serviceability criteria are of greater importance when designing with stainless steel [31]. It is therefore important to realise that, although stainless steels require similar verification checks as those used for carbon steel structures, the design curves and normative formulations differ for each material. Eurocode 3, part 1-4 [48], provides supplementary design rules for stainless steels to the commonly applied Eurocode 3 standard for steel structures [56].

Figure 2.27 shows the stress-strain relations of austenitic steel grades ER304, ER316 and duplex grade 2205. In addition the relation of carbon S355 steel is added in the diagram, which distinguishes itself with a clearly visible yield point. The coloured area marks extreme values from a series of tests on 304 and 316 stainless steel and is therefore represented as a scattered band in the diagram.

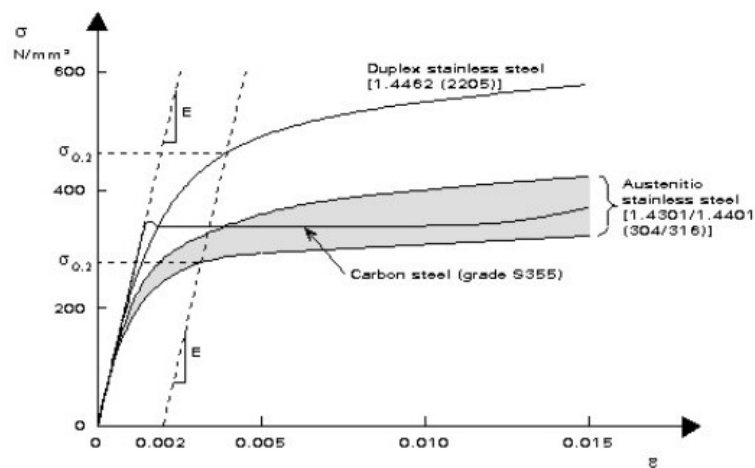


Figure 2.27: Stress-strain curves for stainless steel grades 304, 316, duplex 2205 and S355 carbon steel [45]

The 308L grade used in this research, attains mechanical properties in between grade 304 and 316. For both grades, international standards recommend different design values for their Young’s moduli and ultimate tensile strengths as summarised in table 2.8. More specifically, European standards prescribe design values for low carbon alloys 304L and 316L for various product forms. The considered alloys are marked red in table 2.9. In the proceeding of this research, European standard (EC3) will be used.

Table 2.8: Strength values 304/316 [57]

Grade		Austenitic		
		304 (1/16 Hard in SEI/ASCE)	316 (1/16 Hard in SEI/ASCE)	
UNS		S30400	S31600	
BS		304S31	316S31	
EN		1.4301	1.4401	
Name		X5CrNi18-10		
AS/NZS	E_0	GPa	195	195
	n		4.0–7.5	4.0–7.5
	$\sigma_{0.01}$	MPa	90–140	90–140
	$\sigma_{0.2}$	MPa	195–205	195–205
	σ_u	MPa	520	485
SEI/ASCE	E_0	GPa	193.1	193.1
	n		4.1–8.31	4.1–8.31
	$\sigma_{0.2}$	MPa	248.2–275.8	248.2–275.8
	σ_u	MPa	551.6–620.6	586.1–620.6
	σ_y	MPa	200	200
EC3-1.4	E_0	GPa	200	200
	n		6.0–8.0	7.0–9.0
	$\sigma_{0.2}$	MPa	190–230	200–240
	σ_u	MPa	500–540	500–530

Table 2.9: Nominal strength values for stainless steels to EN10088¹⁰

Type of stainless steel	Grade	Product form							
		Cold rolled strip		Hot rolled strip		Hot rolled plate		Bars, rods and sections	
		Nominal thickness t							
		$t \leq 8$ mm		$t \leq 13,5$ mm		$t \leq 75$ mm		$t \leq 250$ mm	
		f_y	f_u	f_y	f_u	f_y	f_u	f_y	f_u
		N/mm ²	N/mm ²	N/mm ²	N/mm ²	N/mm ²	N/mm ²	N/mm ²	N/mm ²
Ferritic steels	1.4003	280	450	280	450	250 °	450 °	260 °	450 °
	1.4016	260	450	240	450	240 °	430 °	240 °	400 °
	1.4512	210	380	210	380	-	-	-	-
Austenitic steels	1.4306							180	460
	1.4307	220	520	200	520	200	500	175	500
	1.4541							190	500
	1.4301	230	540	210	520	210	520		
	1.4401							200	500
	1.4404	240	530	220	530	220	520	230	530
	1.4539								
1.4571		540		540					

¹⁰According to NEN-EN 1993-1-4:2006/A1:2015 clause 4, modifications to Table 2.1. of NEN-EN 1993-1-1 [56]

Whereas carbon steels are generally modelled using a bi-linear stress strain relation, this cannot be applied to stainless steels. Stainless steel stress-strain curves are often based on the Ramberg-Osgood equations. The Ramberg-Osgood expression [58] aims to approximate the actual stress-strain behaviour deduced from tensile tests. This expression can be used to model stainless steel members up to their 0.2% proof stress only. For higher stress values the equation deviates significantly from tested values, principally because they are extrapolations of curve fits to stresses lower than the 0.2% proof stress. To overcome this problem, Rasmussen modified the Ramberg-Osgood equation in order to describe the full stress-strain relation [59]. Basically, Rasmussen added an equation to the original Ramberg-Osgood expression that is valid in the domain of 0.2% proof stress to ultimate stress. Hence the full stress-strain relation can be written by equation (2.2).

$$\epsilon = \begin{cases} \frac{\sigma}{E_0} + 0.002 \left(\frac{\sigma}{\sigma_{0.2}} \right)^n & \text{for } \sigma \leq \sigma_{0.2} \\ \frac{\sigma - \sigma_{0.2}}{E_{0.2}} + \epsilon_u \left(\frac{\sigma - \sigma_{0.2}}{\sigma_u - \sigma_{0.2}} \right)^m + \epsilon_{0.2} & \text{for } \sigma > \sigma_{0.2} \end{cases} \quad (2.2)$$

Where the first term of (2.2) on the right side describes the elastic part of the strain, while the second term accounts for the plastic part, describing the hardening behaviour. The ultimate strain may be obtained from the approximation $\epsilon_u = 1 - \frac{\sigma_{0.2}}{\sigma_u}$. $E_{0.2}$ represents the tangent modulus of the stress-strain curve at the 0.2% yield strength using (2.3).

$$E_{0.2} = \frac{E_0}{1 + 0.002n \frac{E_0}{\sigma_{0.2}}} \quad (2.3)$$

Non-linearity parameter n is used to attain a good approximation to the measured test values. This parameter is defined as equation (2.4) in which $\sigma_{0.01}$ is the 0.01%-proof stress.

$$n = \frac{\ln(20)}{\ln\left(\frac{\sigma_{0.2}}{\sigma_{0.01}}\right)} \quad (2.4)$$

A low n -value in equation (2.2) gives a round stress-strain curve, whereas high values result in a bi-linear elastic-plastic curve as depicted in figure 2.28. Figure 2.10 shows typical values of n as provided in Annex C of EC3, part 1-4 for strain-hardening materials [48]. The second non-linear parameter m has been derived similarly for the second stage of the stress strain curve and may be determined by $1 + 3.5 \frac{\sigma_{0.2}}{\sigma_u}$.

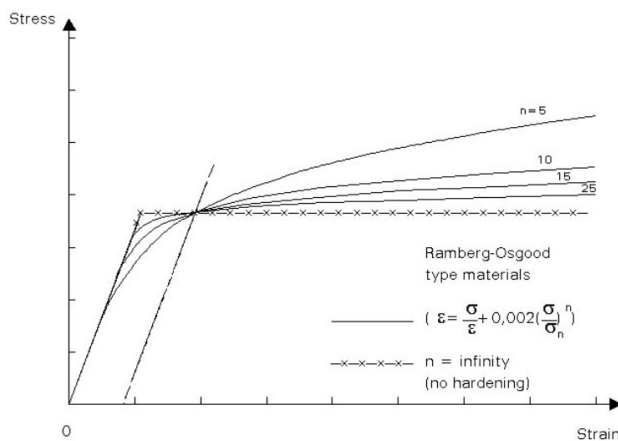


Figure 2.28: Ramberg-Osgood representation of stress-strain curves [31]

Table 2.10: EC3 standard for parameter n [48]¹¹

Steel grade	Coefficient n	
	Longitudinal direction	Transverse direction
1.4003	7	11
1.4016	6	14
1.4512	9	16
1.4301	6	8
1.4306		
1.4307		
1.4318		
1.4541		
1.4401	7	9
1.4404		
1.4432		
1.4435		
1.4539		
1.4571	5	5
1.4462		
1.4362		

Aforementioned non-linearity parameters correspond to experimental data retrieved from tests on ‘ordinary’ stainless steels. Modelling stress-strain behaviour like this could be applied in finite element models of structures. This lies out of the scope of this research. Such a model can however also be implemented by analytical means. The analytical Ramberg-Osgood model including Rasmussen’s modifications can be curve-fitted on stress-strain curves obtained from tensile tests results on WAAM-steel by changing non-linearity coefficients n and m . The ‘ n ’-value for which the most accurate fit was found can be implemented in the analytical (Ayrton Perry) buckling formulas as mathematically derived in section 2.4.3. The outcome is a buckling curve

¹¹According to NEN-EN 1993-1-4:2006/A1:2015 table 4.1

with incorporated material non-linearity in accordance with European (EC3) standards. The attained curve can be used as reference curve for the buckling test results of 3D-printed tubular columns as presented in this research. Besides its stress-strain relation, other mechanical and physical properties are of interest while applying stainless steels in design. They will be concisely discussed here:

Ductility

Ductility is a measure to which extent a material can elongate before yield and eventually fracture under tensile loads. Sufficient ductile behaviour is of major importance in structural design to ensure an adequate redistribution of stresses and to prevent brittle failure in ultimate limit state. As stated in European standard Eurocode 3, part 1-4 [48], the ductility requirements as formulated in Eurocode 3 part 1-1 [56]¹² also apply to stainless steels. These requirements are shown in equation (2.5).

$$\begin{cases} \frac{\sigma_u}{\sigma_y} \geq 1.10 & \text{with } \sigma_y = \sigma_{0.2} \\ \varepsilon_f > 15\% \\ \varepsilon_u \geq 15\varepsilon_y & \text{with } \varepsilon_y = \varepsilon_{0.2} \end{cases} \quad (2.5)$$

Where ε_f equals the elongation at fracture. Austenitic stainless steels are in general being known of having excellent ductility properties. According to the supplier, stainless steel grade 308LSi exhibits its ultimate strain at a value of 35% [47]. Nevertheless, it should be checked from tensile test results if the additively manufactured steel attains similar ductility values and thus whether it complies to the European standards accordingly.

Toughness

The resistance to brittle fracture is commonly referred to as toughness. Toughness is the ability of a material to absorb energy from impact and deform plastically before fracturing. In theory, toughness of a material is proportional to the area under the stress-strain curve from its origin to the elongation level of fracturing. Notches and comparable material defects enhances the susceptibility to brittle fractures [30].

Whereas bcc-latticed metals like pure iron and ferritic stainless steels have the unfortunate characteristic that their resistance to fracture reduces dramatically with decreasing temperatures (because of their relatively high ductile-to-brittle-transition temperature), fcc-metals like austenitic steels does not attain that characteristic. Austenitic grades can absorb considerable impact without fracturing mainly due to their excellent ductility and strain hardening properties [51]. Even with extremely low temperatures, austenitic steels do not fail by cleavage under all loading conditions. Eurocode 3, part 1-4 states that austenitic and austenitic-ferritic stainless steels may be assumed to be adequately tough for service temperatures down to -40 °C[48]. Precipitates may however weaken the grain boundaries, possibly enabling propagation of cleavage cracks along the grain boundaries [33].

To assess the susceptibility of a material to brittle fracture at a certain temperature, a Charpy impact test can be performed. Standardized specimens¹³, typically 10 mm wide and 55 mm long square bars with a machined notch are struck by a pendulum with a controlled weight from a set height. The energy absorbed from the striking pendulum during deformation and fracture of the specimen is used as a measure of impact energy [33]. Tests can be carried out with varying temperatures in order to derive a ductile-to-brittle-transition curve, or to simply provide an indication of notch toughness of the investigated material [60]. The exact test procedure applied in this research to assess toughness of WAAM-stainless steel is provided in section 3.6.3.

Hardness

The hardness of a material is a measure of resistance to deformation during penetration of a loaded indenter in the metal surface. Experiments show the correlation of a material's hardness with its tensile and yield strength. It seems however complex to attain analytical proof for this [61]. Nevertheless, a commonly applied engineering rule of thumb is that the tensile strength in MPa approximately equals three times the Vickers hardness [33].

¹²According NEN-EN 1993-1-1:2005 clause 3.2.2.

¹³Standards for Charpy impact testing are provided in ASTM E23 and ISO148

Over time, multiple hardness tests have been developed: Brinell, Rockwell, Knoop and Vickers tests respectively. The testing methods differ in the type of indenter that is used to penetrate the metal. Whereas Brinell testing applies a hardened steel ball, the Vickers test uses a diamond pyramid (with an included angle of 136°). Because both test methods will be treated in this research, it is important to state that the different hardness measurements correlate closely at not too high values. Conversion tables are available, enabling the comparison of both Brinell and Vickers hardness test results on WAAM-steel.

Fatigue

When structures are subjected to significant levels of repeated stress, the risk of fatigue of metal cannot be neglected. Especially at the location of weld (or print) defects where stress concentrations are observed, the metal is susceptible to fatigue failure. This risk can be limited by reducing the number of discontinuities, sharp edges and stress concentrations in the material [51]. Where the fatigue resistance of a by MX3D printed-stainless steel rod has already been addressed [5], it is concluded that additional research should be conducted to fatigue resistance of specific connections from for example the 3D-printed bridge structure which is expected to be subject to repetitive pedestrian loading. Fatigue behaviour lies however out of the scope of this research.

Physical properties

A few physical properties of stainless steels are relevant to consider in this research. Austenitic stainless steels shows up to 50% greater values of thermal expansion than those of carbon steels. The additional thermal expansion or contraction should be taken into account in design. In addition, stainless steels have a relatively low coefficient of thermal conductivity (15 W/m°C). As a result of this low conductivity, steep thermal gradients can be observed leading to higher residual stresses during welding [45].

2.3. Printing Process Parameters and Properties

Whereas WAAM proves itself as a process that is capable of fabricating well-performing structural parts, its actual performance relies heavily on printing process parameters. Even though optimisation of- and a thorough investigation into process parameters is beyond the scope of this thesis, printing quality (geometric accuracy, surface roughness), microstructural features (grain size, texture), and resultant mechanical (and thus buckling) properties are all strongly process-dependent [17]. This section therefore aims to identify relevant process parameters of MX3D's printing process. Since MX3D makes use of gas metal arc welding (GMAW), at first general GMAW-process parameters will be presented from literature (2.3.1), after which more specifically MX3D's process will be discussed in 2.3.2. Finally, it will be stated in 2.3.3 how these process parameters affect the properties of a printed specimen.

2.3.1. GMAW-Process Parameters

A GMAW-process is characterised by a continuous wire electrode which is drawn from a reel by an automatic wire feeder. The wire is fed through the contact tip in the welding torch. Heat transferred from the welding arc and the internal resistive power causes the wire to melt, like this transferring molten metal to the weld pool [62]. Aside from a certain weld material and shielding gas, the most important GMAW-process parameters are:

- Current
- Voltage
- Wire diameter
- Wire-feed rate
- Welding speed
- Nozzle-to-bead distance
- Preheat temperature
- Gas-flow rate

Despite they are mentioned separately, aforementioned process parameters are all interrelated. Electric current and voltage are related by Ohm's law which states that $V = I \cdot R$, and the electric power relation $P = V \cdot I$ where P designates the electric power in Watts and R the resistance in Ohms.

In addition it is hard to control these parameters separately because in most welding processes (including MX3D's) they are not set directly, but limited to a range of values instead. Most welding processes have a so called 'constant voltage' output characteristic. The arc voltage is established by setting the output voltage on the power supply, which on its turn supplies sufficiently welding current to melt the welding electrode at the rate required to maintain the pre-set voltage (or relative arc length).

Welding current can be controlled by adjusting the wire-feed speed. For example: as the wire feed speed is increased, the arc length will become shorter. As a consequence the arc voltage becomes lower than the pre-set value. If this output is recorded, the power source will supply a higher welding current to correct the pre-set value; the melting rate of the electrode wire increases which corrects the arc voltage and arc length.

Another variable affecting the welding current is the nozzle-to-bead distance. An increased distance results in a larger electrode extension and thus increased electrical resistance of the wire. With increasing resistance, the temperature of the electrode rises. Therefore less welding current is required to melt the electrode at a given feed rate [63].

Aforementioned welding parameters directly influences the cooling rate, as this is an important variable, it will be discussed next.

Cooling Rate

As mentioned earlier in section 2.2.3, the microstructural morphology of a weld and HAZ is determined by the cooling rate. Together with the chemical composition of the alloy, its cooling rate influences the primary mode of solidification and the nucleation and growth behaviour of the ferrite-to-austenite phase transformation during cooling [44]. Heat treated steels are in particular sensitive for changes in cooling rate, as slow cooling rates can for example soften the adjacent weld material, consequently lowering the strength of the weld. Typical cooling rate values for arc welding ranges from 10^1 to 10^3 K/s as depicted in table 2.4.

Like preheat and interpass temperature, heat input is an important variable that influences the cooling rate. Heat input is a relative measure of the energy transferred per unit length of a weld and is calculated as the ratio of the power (voltage times current) to the velocity of the heat source:

$$H = \frac{60EI}{1000S} \quad (2.6)$$

Where H is the heat input in kJ/mm, E the arc voltage in Volts and I the current in Amps. The welding (or travel) speed S is defined as the forward velocity of the arc measured in mm/min [64].

The effect of heat input on the cooling rate is similar to that of the preheating temperature. As either the heat input or preheating temperature increases, the cooling rate decreases as shown in figure 2.29. The relation between preheat temperature, heat input and cooling rate is given by:

$$R \propto \frac{1}{T_0 H} \quad (2.7)$$

Where R designates the cooling rate in $^{\circ}\text{C}/\text{s}$, T_0 the preheat temperature in $^{\circ}\text{C}$, and again H is the heat input in kJ/mm.

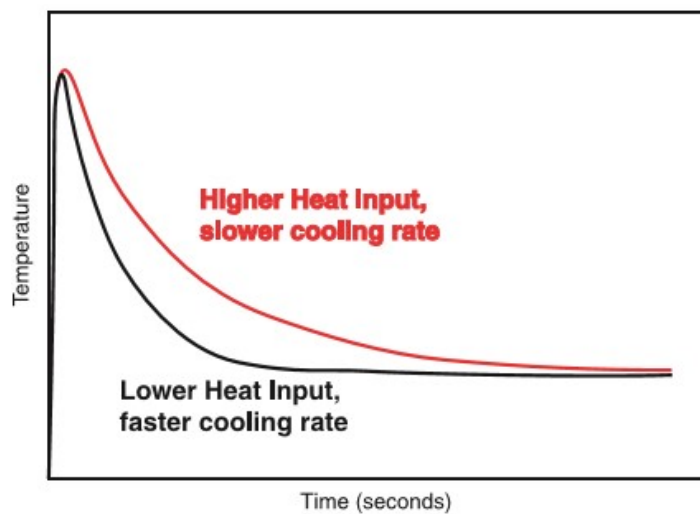


Figure 2.29: Influence of heat input on cooling rate

2.3.2. MX3D's Printing Parameters

In addition to the general GMAW-process parameters mentioned in 2.3.1, MX3D's printing process contains some extra parameters of importance. They will be described in this section. The exact printing parameter values used to print the tubular columns for this research are stated in appendix B.1.



Figure 2.30: MX3D's printing set-up with multi-axis ABB IRB-5-2600 robot and Oerlikon Citowave 3 GMAW-system

The following specific parameters for MX3D's process can be distinguished:

- Welding pulse time
- Layer height
- Nozzle angle
- Workpiece angle
- Interpass temperature

Welding pulse time is the time the machine prints at a certain spot, comparable with the welding speed parameter used in ordinary GMAW-processes. A specimen is built up from a 3D-CAD model, which has been sliced in 2D-profile layers along which the machine deposits its material. The height of such layer is greatly influencing mechanical properties and surface waviness and is therefore of great importance.

MX3D makes use of multi-axis robots (figure 2.30 which are able to print theoretically in every angle. Nozzle angle and workpiece angle can be combined to one angle parameter as this eases the analysis. This is an important variable because gravitational pull changes under an angle, hence possibly changing the properties of the specimen. The influence of printing angle on mechanical properties is investigated by Joosten (2015) [5]. His results are summarized in 2.3.3.

As already stated, cooling rate is an important variable affecting the mechanical properties of a weld. Interpass temperature is the temperature that the metal has to cool between subsequent welding passes so the desired properties can be retained. A minimum value of the interpass temperature is required to control the geometry and surface waviness and a maximum temperature should be adopted to avoid excessive carbide precipitation and thermal-induced stresses. The amount of heat that is being introduced in a specimen is strongly related to the applied printing strategy and the environment in which is being printed.

MX3D makes a distinction between two general printing strategies:

- *Continuous printing*: the metal is deposited in a continuous way along the circumference of the tubular column
- *Dot-printing*: the metal is deposited by successive points (dot by dot) along the circumference of the tubular column

The effect of these different strategies on the metallurgical characteristics of printed tubular columns will be discussed in next the section.

2.3.3. Influence of Printing Process on Properties

Now the different process parameters for GMAW and MX3D's process have been identified, this section will more specifically describe the influence of these parameters on the actual properties of additively manufactured specimens. Because the actual relationship between process parameters and properties requires complex non-linear models and most relations are still subject of research, only a concise overview of conclusions drawn from recent research to multipass welds, WAAM and MX3D's process will be presented.

Ding et al. [17], amongst others (Klingbeil et al. [65]; Mughal et al. [66]; Alimardani et al. [67].), concludes that the control of residual stresses and distortions for large-scale WAAM-processes is a major concern. Besides having an effect on part tolerances, it might also cause premature failure. Local thermally induced stresses are the result of thermally induced strains during non-uniform expansion and contraction of the material. The problem has often limited the use of welding-based technology for manufacturing of some potential, and more critical, applications in the aerospace industry. Post-processing techniques could minimize residual stresses, but yet they are not used by MX3D. Instead, MX3D is optimising its deposition strategy to minimise thermal induced stresses by studying the influence of cooling rates.

Continuous versus dot-by-dot deposition

As the cooling rate has a significant effect on mechanical properties of a metal, and the cooling rate on its turn is directly related to heat input, the printing strategy is a key variable in order to optimise additively manufactured specimens. With regards to designation of 'printing strategy' one should think of; welding parameters, time between subsequent depositions of metal and deposition order. Whereas the specific deposition strategy used for the tubular columns will be more thoroughly explained in section 3.2.2, the distinction between continuous and dot-by-dot deposition has already been made. Both strategies have different effects on the specimen properties as will be discussed here.

Mughal et al. and Sequeira Almeida [66],[9] showed that continuous deposition without interpass cooling causes a larger HAZ, typically leading to tolerance loss, higher residual stresses and a poor surface finish. Mughal et al. have developed a thermo-mechanical model to predict residual stress induced deformations. Some results indicate that continuous deposition may cause local excessive heat input, resulting in high temperature gradients. Remelting of the substrate causes poor dimensional tolerances and surface finish.

Residual stresses seem to be dependent on deposition sequences in continuous deposition: the highest stresses were repetitively found in the last deposition rows. Every time a new row is being deposited, the previous layer is reheated. This causes relaxation of stresses in the former deposits. By assuring sufficient interpass cooling, the residual stress distribution becomes insensitive to the deposition sequence as each deposition sequence does not provide any preheating effects to the next sequence [68].

Dot-by-dot welding shows different characteristics. Whereas research of Ding et al. [17],[69] shows smoother surfaces for continuous deposition, this is in contradiction with observations of MX3D's robot operators, as the patent-pending dot-weld strategy of MX3D shows on average better results. Selective deposition of welds, for example as a series of small 'towers' before joining them together to form one large 'tower', allows for relaxation as they cool down, consequently proving to reduce thermal induced stresses and deformations [32],[70].

However completion of an object using dot-by-dot deposition takes in general more time than while using continuous deposition. This is partly caused by the waiting time between single dot-depositions to enable sufficient cooling of the previous deposition. That is why MX3D is experimenting with various deposition orders to reduce waiting times; during this waiting period the robot does not add any value to the process which is very inefficient.

It should however be noted that both strategies are still very much in development and advancements in print quality are made rapidly. Another proposed welding technique is pulsed-current arc welding, which possibly reduces surface waviness and improves printing quality in general. This is however not being investigated in this thesis. Cooperative research effort of ArcelorMittal and MX3D currently aims to evaluate both strategies by analysing the thermal history of printed specimens using thermal cameras during the entire printing process. The first results seems promising but have however not yet been published.

Printing Angle

In addition to the deposition order, the effect of printing angle on mechanical en geometric properties have been studied by Joosten [5]. Stainless steel (ER308L) rods have been printed under an angle of 0, 30 and 60 degrees. Zero degrees means that the nozzle angle coincides with the longitudinal axis of the (rod) specimen. An example of such a rod specimen is shown in figure 2.31.



Figure 2.31: Tensile test specimen as used by Joosten [5]

Results show a clear difference in geometrical, mechanical and microstructural characteristics for varying print angles. Figure 2.32 schematises the effect of print angle on the geometry of the specimen. Results show that the average rod diameter is affected and an increased diameter variation is observed. Tensile test results show reduced strength values while ductility values have been retained. The results as depicted in figure 2.33 show a clear negative relation between ultimate strength and print angle. Specimens printed at an angle of 60 degrees attain ultimate tensile strength values averaging 10% lower than while being printed at 0 degrees. This effect of print angle on mechanical properties should be taken into account when the designer aims for an economic design.

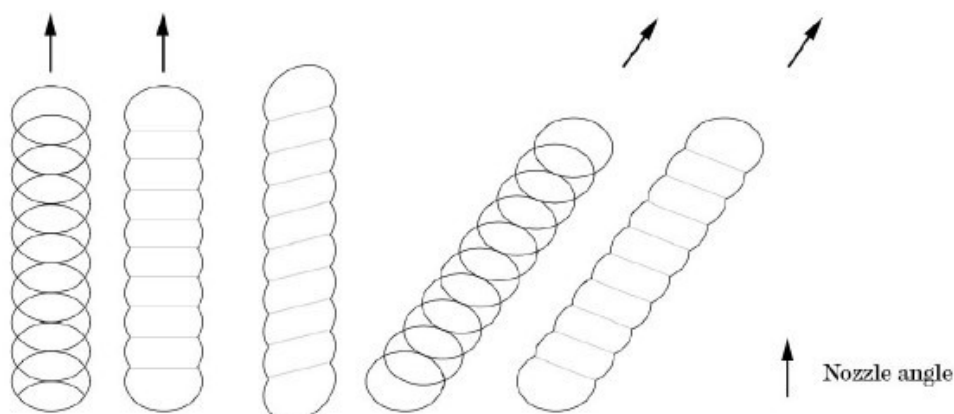


Figure 2.32: Schematization of effect of printing angle on specimen geometry [5]

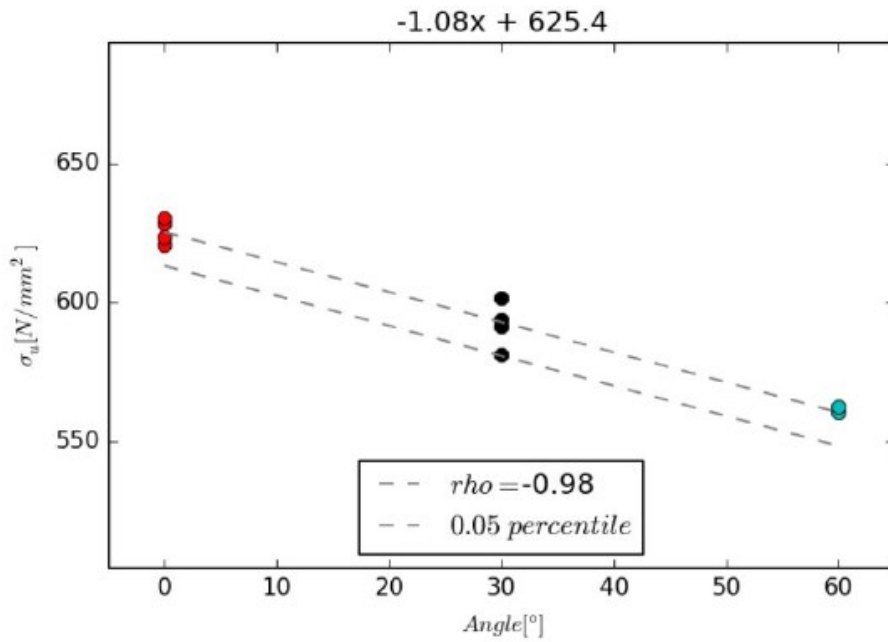


Figure 2.33: Effect of printing angle on ultimate tensile strength [5]

The effect of printing angle has also been studied on microstructural level. In multipass welds, dendrites tend to grow in the direction of the temperature gradient. Since the WAAM process can be considered similar to multipass welds, their solidification structure proves to be comparable as well. Micographs of rod specimens, again printed at an angle of 0, 30 and 60 degrees, show a directional grain growth. Large columnar grain structures can be observed in the direction of the thermal gradient of the weld pool.

While printing at a different angle, the orientation of the weld pool changes due to a change in gravitational pull; so does the direction of the grains with respect to the main orientation of the rod. As depicted in figure 2.34, printing at an angle of 30 degrees results in a grain orientation 6 degrees off from the rod its main orientation, and 18 degrees off at an angle of 60 degrees. The successive deposits with changed orientation can be observed even more clearly in figure 2.35.

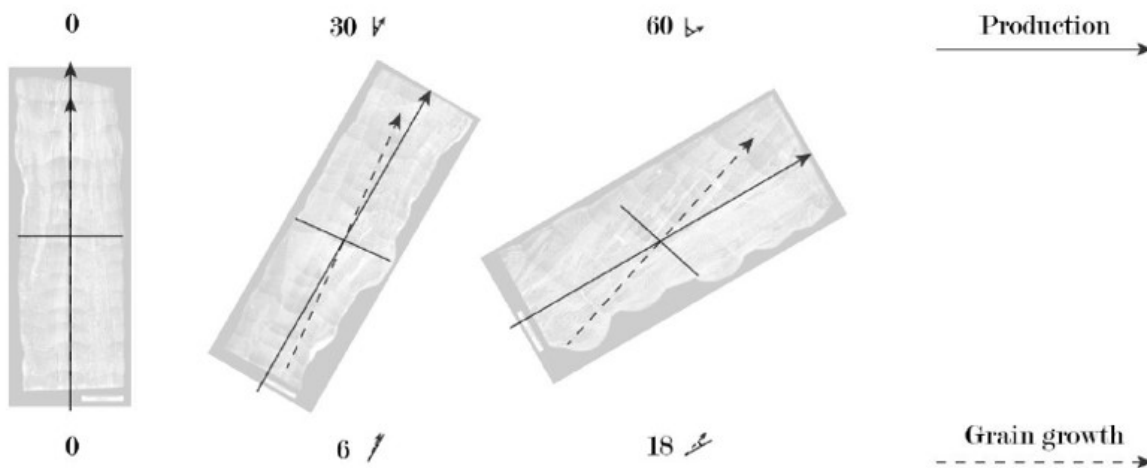


Figure 2.34: Schematization of printing angle and resulting grain orientation with respect to the rod its main orientation [5]

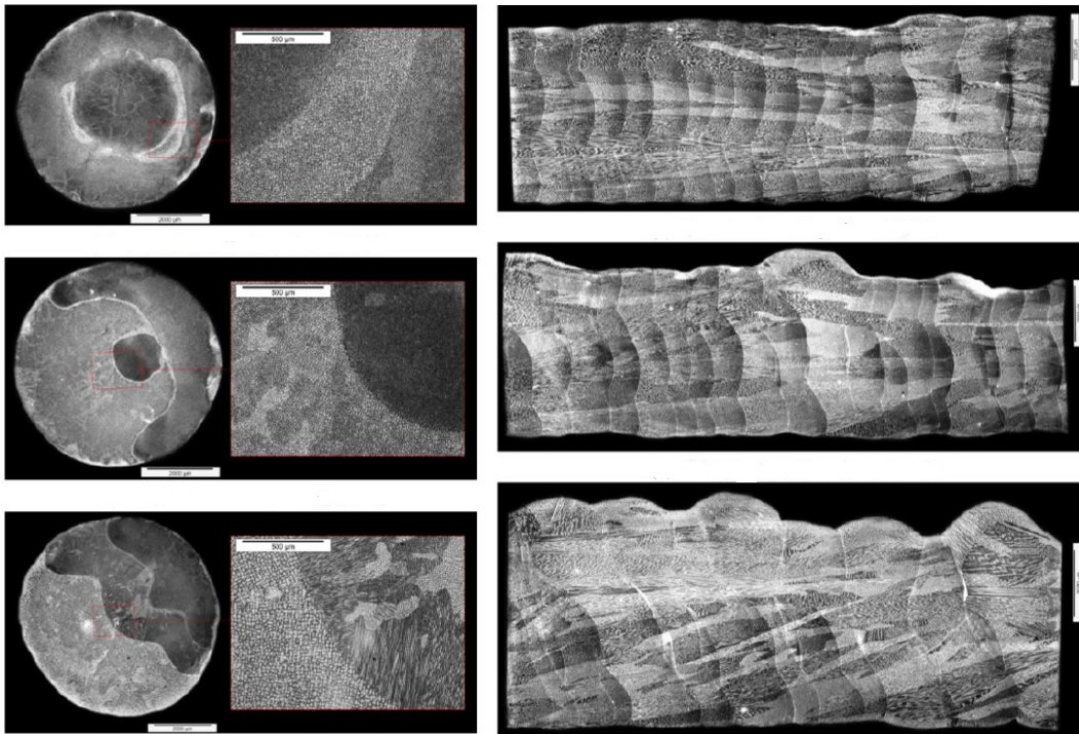


Figure 2.35: Micrographs in longitudinal and transversal direction of a by MX3D-under varying angles-printed stainless steel rod [5]

As grains are formed in a new deposited layer of metal, grains continue to grow without obstruction through each succeeding weld pass in the orientation of the previous grains, together forming large columnar grains. Such interpass epitaxial growth leads to coarse columnar grain structures. They are undesirable because they limit the amount of plastic deformation in the material when loaded in the main orientation of the specimen and leads to extreme anisotropy of mechanical properties. This explains the lowered tensile strength values compared to theoretical values as they were based on the assumption of isotropic material behaviour.

Despite the fact that the tubular columns tested in this thesis are printed at a constant angle of 0 degrees, anisotropic material behaviour is undesired. Therefore tensile tests on milled 3D-printed specimens will be performed and analysed both in print direction and transverse direction to see how much this affects strength values as this is vital for structural application of this material.

There are a few techniques which can be implemented to reduce or mitigate these undesired anisotropic properties, namely: rolling, electromagnetic vibration, thermo-hydrogen welding, interpass peening and as mentioned earlier: pulsed-current welding. These processes are however not worked-out and applied for the specimens used in this research.

Predictive Models

The development of accurate process control models capable of determining weld bead geometry and plate fusion characteristics of the deposited beads from the welding process parameters is one of the crucial software components for WAAM technological and commercial development which would lead to widespread industrial application. Therefore it is vital that the relationship between printing process parameters and the weld bead characteristics of deposited layers is fully understood [9],[71].

In the past decades, mathematical models have been developed to predict and control the final shape of the weld bead for single and multi-pass deposition. Research of Chandel [72] showed that arc current has the greatest influence on bead geometry, and that mathematical models derived from experimental results can indeed be employed to predict bead geometry. Despite the large numbers of attempts to analyse arc welding processes, accurate mathematical models that relate input to output parameters in arc welding process for inclusion in commercial WAAM systems are still lacking [62],[73].

Despite the lack of accurate mathematical models, Murugan and Palmer [71] described trends of welding parameters and their influence on weld bead geometry of stainless steel surfacing. The trends are concisely discussed here. An increased arc voltage resulted in a greater penetration, lower reinforcement, greater bead width and greater dilution. With an increased wire-feed rate the bead width was unaffected while an increased penetration and reinforcement was observed. For an increased welding speed, the opposite effect is observed: a decrease of penetration, reinforcement and bead width. A larger nozzle-to-bead distance on its turn results in a decrease of penetration, bead width and dilution, but an increase of reinforcement. An overview of Murugan and Palmer's findings is shown in table 2.11.

Table 2.11: Overview of direct process effects on respectively geometry, microstructure, strength and ductility [5]

	Geometry		Microstructure			Strength			Ductility
	W	R	P	Di	H	Y	T	F	Du
Voltage	↑	↓	↑	↑	↓	↓	↓	↓	↑
Current	↑	↓	↑	↑	↓	↓	↓	↓	↑
Wire speed	—	↑	↑	↑↓	↓	↓	↓	↓	↑
Welding pulse time	↑	↑	↑	—	↓	↓	↓	↓	↑
Cooling time	↓	↑	↓	↓	↑	↑	↑	↑	↓
Nozzle distance	↓	↑	↓	↓	↑	↑	↑	↑	↓
Layer height	↓	↑	Perhaps similar to nozzle distance						
Rod angle			Possibly anisotropic effects						

Where the characters are respectively designating width (W), reinforcement (R), penetration (P), dilution (Di), hardness (H), yield strength (Y), tensile strength (T), fatigue strength (F) and ductility (Du).

The observations of Murugan and Palmer are in conjunction with the findings of Funderburk on the effect of heat input in SMAW-processes as shown in table 2.12 [64]. For an increased heat input (and thus a lower cooling rate), lower hardness values, a lower yield and tensile strength are observed, and an increased elongation. This makes sense, because as equation (2.7) proves, with a higher heat input the cooling rate decreases, consequently affecting the mechanical properties of the weld metal.

Table 2.12: Effect of increased heat input on material properties for arc welding-processes [64]

Property*	Change
Yield Strength	↓ 30%
Tensile Strength	↓ 10%
Percent Elongation	↑ 10%
Notch Toughness (CVN)	↑ 10%, for $15 < H < 50$ kJ/in ↓ 50%, for $50 < H < 110$ kJ/in
Hardness	↓ 10%

* SMAW with a heat input range of 15 to 110 kJ/in.

2.4. Fundamentals of Buckling

This section presents a comprehensive overview of buckling theory. The goal is to state the important variables affecting stability of stainless steel columns, its mathematical basis and its current prescription in Eurocode 3. In general, members in compression are susceptible to a number of possible buckling modes (torsional, lateral, local, etc.), but since these are irrelevant for thick-walled tubular columns as studied in this research, only flexural buckling due to concentric loading will be considered.

2.4.1. Column Theory

Buckling of a structural member can be defined as the critical state at which the member at particular compression load levels exhibits sudden large (sideways) displacements or even collapse. This phenomenon will be explained by means of the elastic (perfect) and inelastic column theory.

Perfect Column

Columns with very low slenderness are not affected by buckling and can be designed according its yield stress f_y . If local buckling does not affect the member (as assumed for Cross-Section Class (CSC) 1, 2 and 3¹⁴) the compression resistance (also referred to as squash load) equals the plastic resistance of the cross-section which can be obtained by multiplying a column its cross-sectional area A with its yield stress f_y (2.8). Eurocode 3 [56] considers that this is the case when their relative (non-dimensional) slenderness $\bar{\lambda} \leq 0.2$.

$$N_{pl} = Af_y \quad (2.8)$$

More slender columns ($\bar{\lambda} \geq 0.2$) are susceptible to buckling while loaded in compression. Cornerstone of the column theory is the Euler column which can be considered as a mathematically straight, prismatic, pin-ended, centrally loaded element that is slender enough to buckle without the stress at any point in the cross-section exceeding the proportional limit of the material (elastic buckling). Under these assumptions the Euler load, being the critical load at which a slender elastic column can be held in a bent configuration under axial load alone, is given by:

$$N_{cr} = \frac{\pi^2 EI}{L_{cr}} \quad (2.9)$$

Where L_{cr} is the buckling length taking into account the boundary conditions and I is the second moment of area of the considered column section. More of which is described in the course of this section. One can obtain the critical Euler stress σ_{cr} by dividing both sides of (2.9) by A . By subsequently introducing the radius of gyration as $i = \sqrt{\frac{I}{A}}$ and slenderness $\lambda = \frac{L_{cr}}{i}$ the equation becomes:

$$\sigma_{cr} = \frac{\pi^2 E}{\lambda^2} \quad (2.10)$$

This relation with corresponding failure modes has been drawn in figure 2.36 [74].

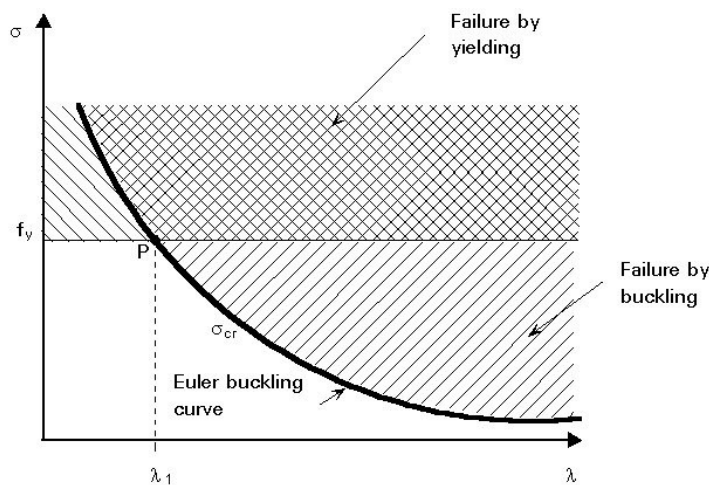


Figure 2.36: Euler buckling curve with corresponding failure modes

¹⁴Cross-Section Classification as specified in NEN-EN 1993 clause 5.5.2 and NEN-EN 1993-1-4 table 5.2 (stainless steel)

After buckling is initiated at the critical load, the column will continue to bend with increasing load until instability is reached at the maximum (collapse) load. The Euler formula for the elastic critical buckling load of a slender column [75] (together with its modification by Engesser for inelastic behaviour [76]) is the earliest engineering design formula that is still in use today.

As already briefly stated, the Euler formula comes with numeral limitations [77]. In unloaded state, the column should be perfectly straight and while carrying the load, it should coincide with the longitudinal centroidal axis of the member. Furthermore it is assumed that residual stresses are present without any variations along the column length. It is also assumed that the stress-strain relationship for both tension and compression are similar and without variation throughout the member. At last, a member is assumed to be pinned; meaning that any friction in the end-constraints is disregarded.

Imperfect Column

In practice however, the real behaviour of steel columns rather differs from the earlier described ‘perfect’ column. Columns generally fail by inelastic buckling before reaching the Euler buckling load and thus one of the key assumptions of the Euler column theory is violated due to a stiffness reduction. This stiffness degradation may be caused by:

- The non-linear (stress-strain relation) material behaviour itself, as is for instance the case for stainless steel. Also local material defects and possible variations of material properties like yield strength might induce inelastic buckling.
- Geometric imperfections and eccentric load introduction.
- Partial yielding due to compressive residual stresses.

Finally the influence of end-restraints and the combined effect of aforementioned factors will be discussed. The post-buckling behaviour is therefore radically different from the elastic perfect column; buckling occurs at the tangent modulus load, where in equation (2.11) the Young’s Modulus E is replaced by a tangent modulus E_t [78].

$$N_{cr} = \frac{\pi^2 E_t I}{L_{cr}} \quad (2.11)$$

It is already noted that stainless steels have no clear yield plateau (see figure 2.26 in section 2.2.4). The equivalent yield stress f_y is defined as 0,2% proof stress $\sigma_{0,2}$. Beyond the proportionality stress σ_p softening of the material occurs and consequently a reduction in buckling strength. A more comprehensive explanation of buckling of stainless steel members is presented in 2.4.3.

Another difference between the elastic buckling theory prediction and the behaviour of a compression member in practice can be attributed to various geometrical imperfections in the ‘real’ element. Initial curvature (or out-of-straightness as visualised in figure 2.37 [74]) will affect instability, as will eccentricity of the (perfectly presumed concentric) applied loads, consequently introducing secondary bending moments at the onset of loading. On its turn it leads to an increase in deflection and a growing amplitude of the lever arm of the compression load; hence resulting in geometrically non-linear behaviour. Compared to a ‘perfect’ column, this may severely weaken the buckling resistance of a structural member.

The magnitude of initial curvature e_0 is usually expressed in terms of a fraction of the length of a member. Despite that these imperfections are commonly in range of standard fabrication tolerances and not visible by the naked eye, they must be taken into account while designing compression members. Especially when considering additive manufacturing, where quality control and guidelines in reliable geometric tolerances are yet not developed on a large scale. As can clearly be observed in figure 2.38, column behaviour of intermediate slenderness ratios deviates most from the Euler curve. The greatest reduction in resistance occurs in the vicinity of λ_1 (relative slenderness $\bar{\lambda} = 1$), where the plastic squash load and elastic buckling load are nearly coincident and therefore interact the most [79]. For very stocky members with a low slenderness which exhibit a failure load close to the squash load, the influence of initial curvature is negligible. At the other extreme, very slender members exhibit a failure load approaching the elastic critical load and the influence of initial imperfections on buckling resistance is therefore limited.

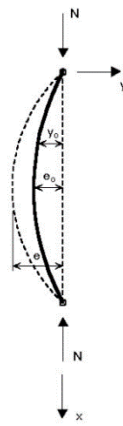


Figure 2.37: Initial curvature of a column

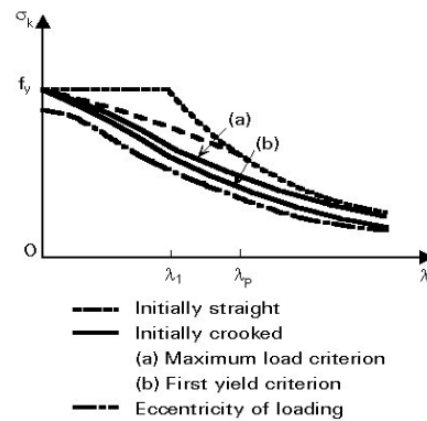


Figure 2.38: Buckling curves for members with geometric imperfections

Besides initial curvature, also eccentricity of loading drastically reduces the buckling resistance. Eccentric load introduction induces first-order bending moments in the column which consequently starts to deflect laterally, similar to initial curved members loaded in compression. Compared to the influence of initial curvature, the reduction of buckling resistance due to eccentricity of loading is less dependent on the column length. Reduction of buckling capacity is more related to the section size of the member. Because the bending moment is constant over the entire column length, stocky members exhibit the largest reduction in buckling. Considering the effect of eccentric loads, special care should be taken of concentric load introduction while performing buckling tests. Column specimens should therefore be cut perfectly straight at both column-ends.

Residual stresses are present in both cold-formed and welded sections. Despite not much is known about residual stress development and distribution in WAAM-sections, it is clear that as a result of local heat input during printing, and uneven cooling, thermally induced residual stresses are present in the printed material. Tensile residual stresses occur in the regions of a section that cooled down slowest. They are counterbalanced by compressive stresses in the remaining part of the section. For thin-walled cold-formed and welded sections usually a constant residual stress distribution over the wall thickness can be assumed.

In general residual stress results in early yielding of local fibres; this occurs before the applied compressive stress attains the material yield stress f_y . The applied stress superimposes on the residual stress that is already present. Yielded fibres have a reduced stiffness compared to the remaining elastic ones because their strains exceed yield strain ϵ_y . Hence the column stiffness is constant until first yielding (point 1 in figure 2.39). The collapse load of a very slender column is therefore not affected by residual stresses.

With increased loading the column stiffness progressively decreases. The effect of residual stresses is again most significant in the range of intermediate slenderness (point 2). In this case premature yielding reduces the bending stiffness and the struts buckle inelastically at a load below both the elastic critical buckling load and the plastic squash load. Stocky (or stub) columns, are practically unaffected by residual stresses. Their failure load is usually higher than the yield load (point 3) due to strain hardening effects.

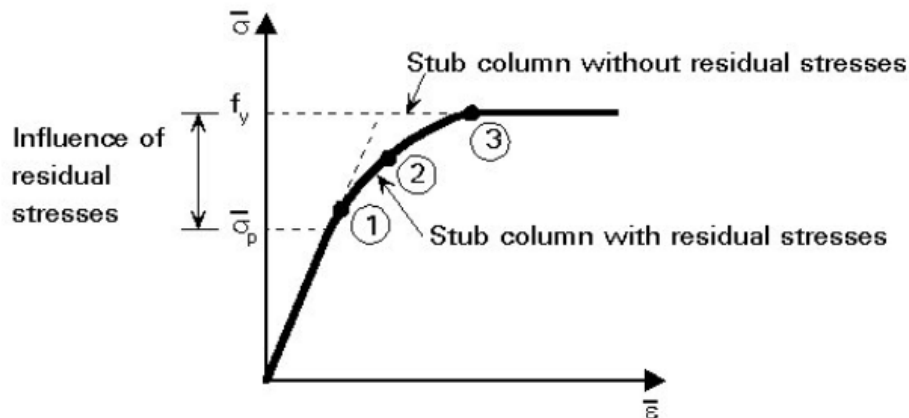


Figure 2.39: Influence of residual stresses on the stress-strain relation of carbon steel [79]

In practice all effects mentioned above occur simultaneously. To emphasise the complexity of these effects combined, research shows initial curvature and residual stress variations are related. Tests and numerical studies to hot-rolled steel sections of Batterman and Johnston (1967) [80] and Bjorhovde (1972) [81] prove that the separate effects of residual stress and initial out-of-straightness cannot simply be added to give a good approximation of the combined effect on the maximum column strength. For intermediate slenderness ratios and low residual stresses the combined effect is less than the sum of the parts while for other cases it can be more.

Furthermore these studies prove that variations in column resistance can be explained by differences in the shape of the residual stress patterns. This affects initially curved columns more than columns that are initially straight.

However, it should be clearly marked that all (combined) effects of residual stresses and geometrical deviations as described above are determined from tests on welded, cold-formed and hot-rolled steel sections. Until now no tests are performed to verify the effects of residual stresses in printed stainless steel columns.

Finally it should be noted that the test set-up plays a vital role while evaluating buckling test results since end-restraints may significantly affect the resistance to buckling. In a perfect world the end-restraints (in this research pinned-pinned as explained in section 3.4.2) behave frictionless. In practice however, this is not completely the case. Methods have been developed to account for end-restraints with rotation stiffness making use of effective length factors, but the question of how to use this in design is still unresolved [78]. For example, should restraint factors for different kinds of end restraints be tabulated so it can be adopted using effective length method, or should the effect of end-restraints be included in buckling design curves like the AISC¹⁵ approach [82].

Because constructing a buckling curve is the aim of this thesis, the effective length concept is used in this research. The effective buckling length, denoted by L_{cr} , of a supposedly hinged-hinged member is equal to the distance between both rotation points of the hinges. This can be formulated as $L_{cr} = K \cdot L$, where L is the member length, K the effective length factor and L_{cr} is defined as the distance between the two points of contraflexure (points of zero moment) along the column length.

¹⁵American Institute of Steel Construction

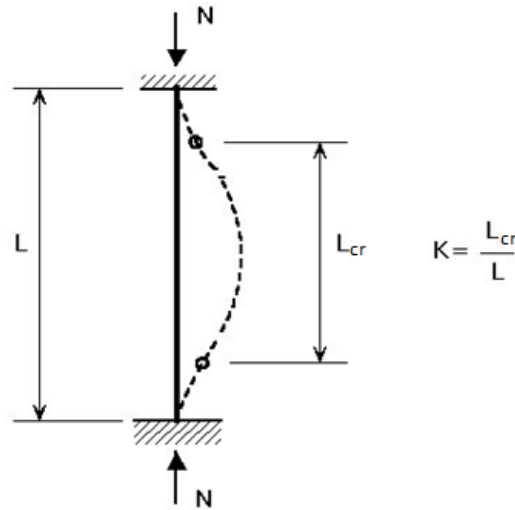


Figure 2.40: Effective buckling length for a laterally restrained column [74]

For the specific test set-up used in this research to test columns on buckling stability, the friction of the end-restraints will be accounted for using an experimental derived effective length factor. The adopted strategy is explained further in section 5.3.1.

2.4.2. European Buckling Curves (ECCS)

From 1960 onwards, an international experimental programme was initiated by the ECCS¹⁶ to study column behaviour of standard hot-rolled, cold-formed and welded columns. Over a thousand buckling tests on numerous types of sections were investigated [83]. Among those types were I, H, T, U, circular and square hollow sections with varying slenderness, ranging from 55 to 160. Using these column tests, associated with theoretical analysis, buckling curves as presented in the course of this section, are derived as function of a relative slenderness $\bar{\lambda}$.

The effects of residual stresses are accounted for in these curves relative to each considered type of cross-sectional shape. A yield strength of 240 MPa was used as reference value for all calculations. Additionally, a half sine-wave-shaped geometric imperfection with a maximum amplitude of a thousandth of the member length ($e_0 = \frac{L}{1000}$) was taken into account. This value was primarily chosen because it equals the upper limit of acceptable tolerances of fabricated steel members, consequently considered as a conservative assumption.

A variety of initial curvature shapes have been measured of hot-rolled and welded sections as shown in figure 2.41. Besides their different double curved shapes, some columns exhibit its maximum eccentricity at a quarter of their height instead of halfway. This shape can be approximated by Fourier series. For an eccentricity of $\frac{L}{650}$ at a quarter of the column height and the substituted half a sine wave with maximum amplitude of $\frac{L}{1000}$ mid-column, both calculated column curves appeared to be in good agreement.

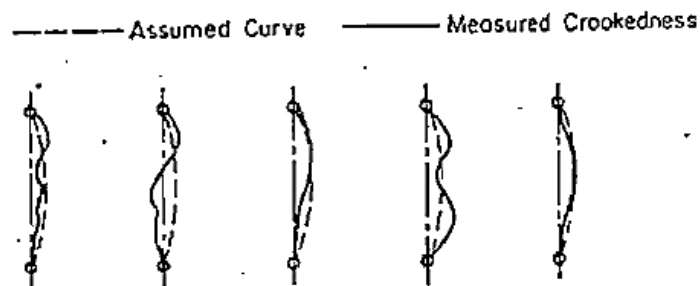


Figure 2.41: Measured and assumed shapes of column out-of-straightness [83]

¹⁶European Convention for Constructional Steelwork

Derivation European buckling curves

Aforementioned experimental program analysing column imperfections led to the formulation of the existing European buckling curves. These curves can be mathematically described using the Ayrton-Perry formula as explained by ESDEP¹⁷ [74]. This derivation is elaborated here.

Considering a column with a half sine-wave imperfection with amplitude e_0 as denoted in figure 2.37, the initial deformed shape can be written algebraically as:

$$y_0 = e_0 \sin\left(\frac{\pi x}{L}\right) \quad (2.12)$$

The differential equation for the deformation of a pinned-pinned restraint column loaded by axial force N is:

$$\frac{d^2 y}{dx^2} + \frac{N(y + y_0)}{EI} = 0 \quad (2.13)$$

Solving after substitution of equation (2.12) in (2.13) and taking into account the boundary conditions gives:

$$y = \frac{e_0}{\left(\frac{N_{cr}}{N} - 1\right)} \sin\left(\frac{\pi x}{L}\right) \quad (2.14)$$

Where N is the maximum axial load limited by buckling. After introducing $n = \frac{N_{cr}}{N}$, the expression for the maximum total deflection mid-column e simplifies to:

$$y\left(x = \frac{L}{2}\right) = e = e_0 + \frac{e_0}{n-1} = e_0 \frac{n}{n-1} \quad (2.15)$$

The latter term is known as the amplification factor. One may define the normal stress as $\sigma_b = \frac{N}{A}$. Considering the maximum bending moment, stress equilibrium of the column during buckling requires that:

$$\frac{N}{A} + \frac{Ne}{W} = \sigma_b + \sigma_b \frac{eA}{W} = f_y \quad (2.16)$$

After introducing the Euler critical stress ($\sigma_{cr} = \frac{\pi^2 E}{\lambda^2}$) and substitution of (2.15), equation (2.16) can be formulated as:

$$\sigma_b + \sigma_b \frac{e_0}{\left(1 - \frac{\sigma_b}{\sigma_{cr}}\right)} \frac{A}{W} = f_y \quad (2.17)$$

Which can be written as the classic form of the Ayrton Perry formula [84]:

$$(\sigma_{cr} - \sigma_b)(f_y - \sigma_b) = \eta \sigma_{cr} \sigma_b \quad (2.18)$$

Where $\eta = \frac{e_0 A}{W}$ is called the generalised imperfection factor accounting for various defects like geometric imperfections, residual stresses and eccentric loading. Knowing that $W = \frac{I}{v}$ and $i^2 = \frac{I}{A}$, the imperfection factor can be rewritten using the definition of slenderness $\lambda = \frac{L}{i}$, which gives:

$$\eta = \frac{e_0 \lambda}{L\left(\frac{i}{v}\right)} \quad (2.19)$$

Where denominator term $\frac{i}{v}$ is the relative diameter of the inertia ellipse on the axis where buckling is considered. Introducing the slenderness plateau we may write (2.19) as:

$$\eta = \frac{e_0 \pi \sqrt{\frac{E}{f_y}}}{L\left(\frac{i}{v}\right)} (\bar{\lambda} - \bar{\lambda}_0) = \frac{\lambda_1}{\gamma\left(\frac{i}{v}\right)} (\bar{\lambda} - \bar{\lambda}_0), \quad \text{where } \gamma = \frac{L}{e_0} \quad \text{and} \quad \lambda_1 = \pi \sqrt{\frac{E}{f_y}} \quad (2.20)$$

Assuming that $\sigma_{cr} = \frac{f_y}{\lambda^2}$ and $\chi = \frac{\sigma_b}{f_y}$ one can express the basic form of the buckling curve as a quadratic equation:

$$\chi^2 \bar{\lambda}^2 - \chi(1 + \eta + \bar{\lambda}^2) + 1 = 0 \quad (2.21)$$

¹⁷European Steel Design Education Program

Solving (2.21) leads to the smallest root:

$$\chi = (1 + \eta + \bar{\lambda}^2) - \sqrt{\frac{(1 + \eta + \bar{\lambda}^2)^2 - 4\bar{\lambda}^2}{2\bar{\lambda}^2}} \quad (2.22)$$

After multiplying by its conjugate, one arrives at the European formulation of the buckling reduction factor [56].

$$\chi = \frac{1}{\phi + \sqrt{\phi^2 - \bar{\lambda}^2}} \leq 1, \quad \text{where } \phi = 0.5(1 + \eta + \bar{\lambda}^2) \quad \text{and} \quad \eta = \alpha(\bar{\lambda} - \bar{\lambda}_0) \quad (2.23)$$

Coefficient η is an imperfection factor dependent on section geometry, buckling direction and fabrication or forming process (i.e. welded, cold-formed or hot-finished). The original Ayrton Perry formula did not include a limiting slenderness $\bar{\lambda}_0$, but was solely based on the onset of yielding at any point of the cross-section. The introduction of an imperfection factor alpha and limiting slenderness (which defines the limit under which buckling failure is insignificant), both derived from tests, allows for actual column failure instead of 'first yield' [51].

Key challenge was to account for the large variability in cross-section geometries with all forthcoming sorts of column imperfections, and still be able to draw a representative reliable column curve. An option was to draw one curve with a certain band of strength variation. Eurocode 3 however, made a subdivision of a few groups of sections with a mean or similar curve for each group. This is known as the 'multiple column curve concept'.

Using the stated assumptions of material characteristics $E = 210$ GPa, $f_y = 255$ MPa, and the maximum initial curvature $e_0 = \frac{L}{1000}$, the imperfection parameters can be calculated for different cross-sections as defined in table 6.1 of Eurocode 3 part 1-1 [56]. The higher the value for alpha, the larger the imperfection that is taken into account. For carbon-steel buckling curves the limiting slenderness is equal to $\bar{\lambda}_0 = 0.2$, whereas for some stainless steel sections this value is increased to $\bar{\lambda}_0 = 0.4$ (see section 2.4.3). The resulting column curves (a_0 , a , b , c and d) are shown in figure 2.42. They give the value for the reduction factor χ of the column resistance as a function of relative slenderness $\bar{\lambda}$ for various cross-sections. Hence the Eurocode 3 resistance to flexural buckling for CSC 1 to 3 is given by:

$$N_{b,Rd} = \frac{\chi A f_y}{\gamma_{M1}} \quad (2.24)$$

Where γ_{M1} is the partial safety factor equal to 1.1 for members checked on instability. In design the following requirement should be met: $\frac{N_{Ed}}{N_{b,Rd}} < 1$.

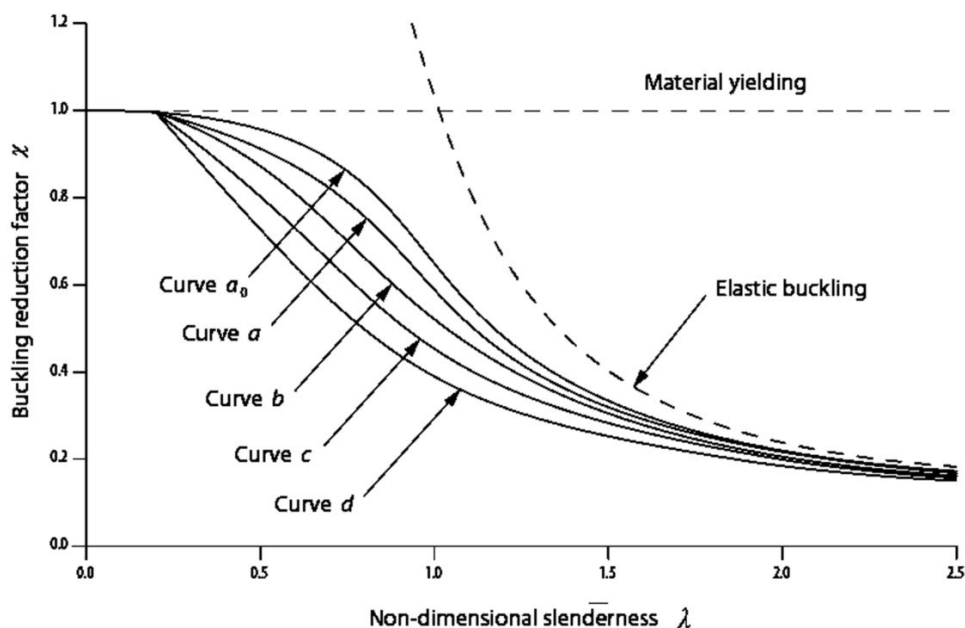


Figure 2.42: European (ECCS) column curves [51]

Each curve represents a certain cross-sectional shape and associated column imperfection. Table 6.2 of Eurocode 3 part 1-1 formulates which designation (a_0 , a , b , c and d) is suitable for the considered column [56]. This is summarised in table 2.13.

Table 2.13: European column curve designation and its corresponding imperfection parameters

Buckling Curve	Type of member	α	$\bar{\lambda}_0$
a_0	Quasi perfect shapes; hot-rolled I-sections with thin flanges (S460)	0.13	0.20
a	Quasi perfect shapes; hot-rolled I-sections with thin flanges	0.21	0.20
b	Medium imperfections; welded hollow sections	0.34	0.20
c	Large imperfections; welded open sections (major axis)	0.49	0.20
d	Max. imperfections; welded open sections (minor axis)	0.76	0.20

Because all the deviations from the ideal strut and material are subject to statistical variations, it is impossible to accurately predict the real resistance of a specified standard strut shape. For design purposes, lower bound resistance curves are used which ensure, to a specified probability, that the calculated buckling loads do not overestimate the actual ultimate resistance. The question raises; how was this conservativeness achieved for the ECCS buckling curves as yet presented in figure 2.42?

From the ECCS column tests, the nominal collapse stress was determined for each slenderness ratio using the mean value of the test results minus twice the standard deviation ($\mu - 2\sigma$). Consequently an experimental column curve valid for the specific type of section which had been tested could be drawn (figure 2.43). This methodology ensured a value of collapse stress with uniform probability along the entire curve for all slenderness ratios [83].

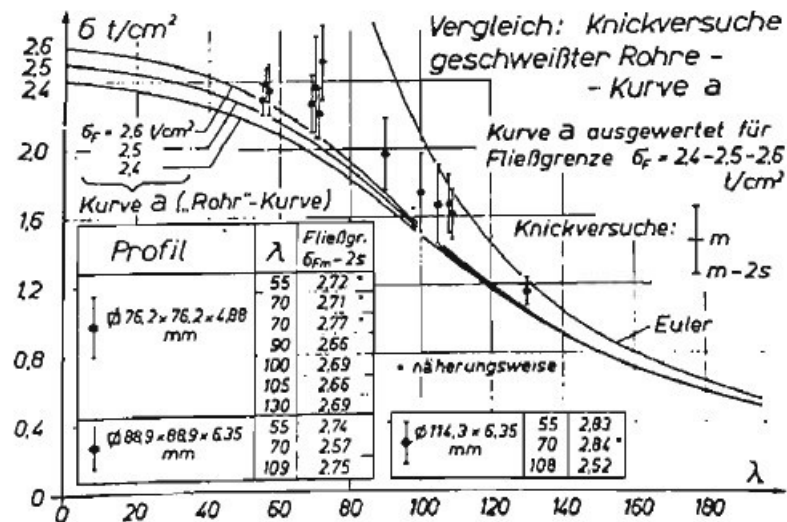


Figure 2.43: Tested values for nominal collapse stress and representing column curve 'a' [83]

Using these experimental column curves, a comprehensive computer analysis was carried out by Beer and Schulz [85] which had led to the presently proposed ECCS multiple column curves. Next section provides further insight in column curves used for stainless steels.

2.4.3. Buckling of Stainless Steel Columns

Previous section described the derivation of column curves and design formulas as presently used. They are however based on the assumption of an ideal bi-linear stress-strain relationship with accompanying well-defined yield plateau. It has already been explained (in 2.2.4 and 2.4.1) that this assumption cannot be justified for stainless steels since it exhibits clear non-linear material behaviour. Besides stainless steels, other materials behaving in a similar matter, such as aluminium alloys, become more and more apparent in structures. This explains the increasing effort to incorporate material non-linearity in engineering standards.

Material non-linearity plays an important role in the buckling behaviour, especially in the first stage of the material model. Accurate approximations of column buckling resistance using models which include material non-linearity often involve complicated iterative solution procedures [86]. Simplified buckling resistance formulas are usually provided to ease the design practice. These formulas can be subdivided in four categories [78]:

- Empirical formulas based on column experiments
- Formulas based on the yield-limit state
- Formulas based on tangent-moduli
- Formulas based on maximum strength

Of which the latter two are embodied in the most widely used standards. They will be discussed briefly.

Tangent modulus approach

A possible methodology to determine buckling resistance in stainless steel members is the tangent modulus approach. Instead of the constant Young's modulus E as used in carbon steel standards, this variable in the Euler formula is replaced by the tangent modulus E_t related to the corresponding buckling stress. Since E_t depends on the stress level, and buckling stress is also a function of E_t , this methodology requires an iterative procedure to find the buckling resistance. Research by Johnson and Winter [87] supports using this approach to account for gradual yielding of stainless steel columns. This formulation is used in the ASCE¹⁸ standard for cold-formed sections and is referred to in the Design Manual for Structural Stainless Steel [51].

¹⁸American Society of Civil Engineers

Rewriting equation (2.10) by replacing the constant modulus of elasticity by the stress-dependent tangent modulus E_t gives:

$$\sigma_{cr} = \frac{\pi^2 E_t}{\lambda^2} \quad (2.25)$$

The buckling reduction factor is given by

$$\chi = \frac{1}{\bar{\lambda}_c^2} = \left(\frac{1}{\lambda^2} \right) \left(\frac{E_t}{E} \right) \quad (2.26)$$

Where the subscript c used for the relative slenderness refers to carbon slenderness. A mathematical description of the tangent modulus is given by the Ramberg-Osgood law [58] as stated in section 2.2.4:

$$E_t = \frac{d\sigma}{d\varepsilon} = \frac{E f_y}{f_y + 0.002 n E \left(\frac{\sigma}{f_y} \right)^{n-1}} \quad (2.27)$$

Where n is Ramberg Osgood's material non-linearity parameter and σ the attained stress level during loading. It may be assumed that at buckling for the buckling reduction factor holds $\frac{\sigma}{f_y} = \chi$. Inserting respectively former assumption and (2.27) in (2.26), this results in the recursive model of Euler's formula:

$$\chi = \frac{1}{\bar{\lambda}^2} \left(1 + 0.002 \frac{nE}{f_y} \chi^{n-1} \right)^{-1} \quad (2.28)$$

It is important to note that since this is a rewritten version of Euler's 'perfect column' formula, this method only incorporates material non-linearity effects; it does not take into account any initial imperfections. Figure 2.44 shows the material non-linearity sensitivity for this tangent modulus approach. It can clearly be seen that intermediate slender columns are most sensitive for non-linear material behaviour. This can be explained by the fact that stainless steels are softer than bi-linear modelled carbon steels when the column stress lies between the limit of proportionality and the 0.2% proof stress. Since in this research short and intermediate columns are tested, this emphasises the need to include material non-linearity when modelling buckling of AM columns.

When n approaches infinity, this model equals the Euler curve with a constant Young's modulus. Appropriate n -values for stainless steels are stated in section 2.2.4. For the purpose of deriving a buckling curve of the specific material tested in this research, an n -value will be derived by curve-fitting the Ramberg Osgood-Rasmussen formulation [59] to the experimental based stress-strain curves.

At intermediate slendernesses, i.e. when the average stress in the column lies between the limit of proportionality and the 0.2% proof stress, stainless steel is "softer" than carbon steel. This leads to reduced strengths of stainless steel members compared to similar carbon steel members.

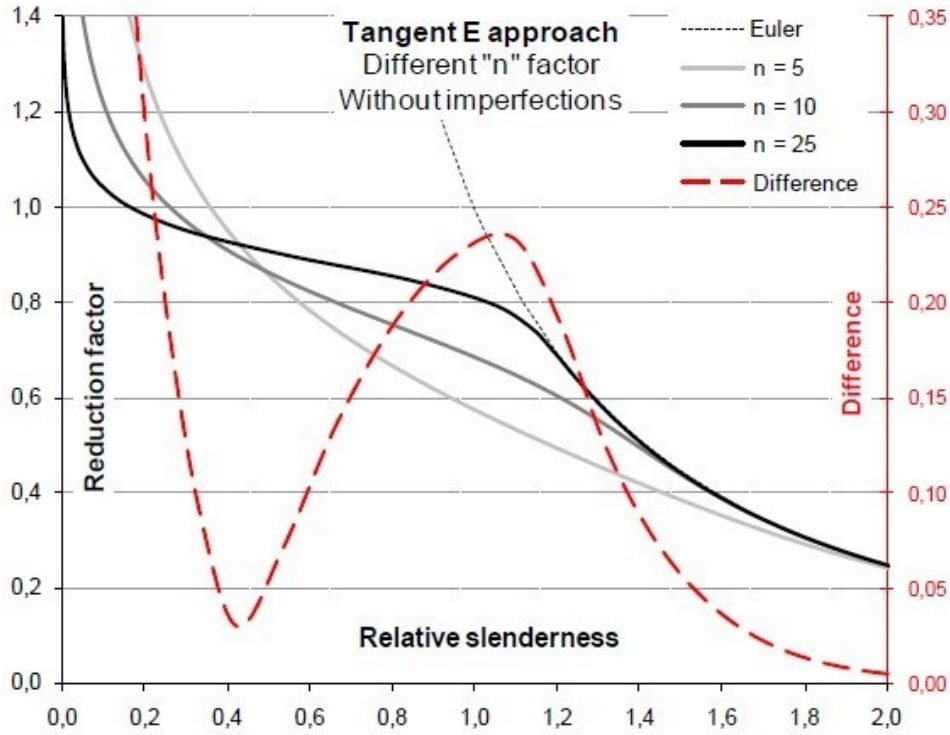


Figure 2.44: Non-linearity parameter sensitivity for tangent modulus model *without* initial imperfections ($f_y = 300\text{MPa}$) [57]

Maximum strength approach

Another approach has been adopted for the European column buckling curves. Similar to the carbon-steel standards, their column design formulas are based on studies to maximum strength of geometrically imperfect columns containing residual stresses. This is a significant difference with the tangent modulus approach which comprehences an adaptation of Euler's perfect-column formula. The curves are derived from experimental column tests and incorporate numerical analyses to compare both results. A reliability analysis, as presently used in the design standards, has been performed leading to the resistance factors. Part 1.4 of Eurocode 3 [48] provides supplementary rules for stainless steel structural members. Unlike its American and Australian counterparts, these are applicable to both cold-formed and fabricated sections.

Rasmussen [86] used the earlier introduced Ayrton Perry formula to incorporate material non-linearity. This was done by adopting non-linearity factor n and introducing the non-dimensional proof stress $e = \frac{\sigma_{0.2}}{E_0}$ in the Ramberg-Osgood model. Subsequently, a validation has been performed by calibrating (2.28) with curve-fits.

Imperfection factor η in (2.23) has been rewritten to:

$$\eta = \alpha \left[(\bar{\lambda} - \bar{\lambda}_1)^\beta - \bar{\lambda}_0 \right] \geq 0, \quad \text{where:} \quad (2.29)$$

$$\alpha = \frac{1.5}{(e^{0.6} + 0.03) \left(n \left(\frac{0.0048}{e^{0.55}} \right)^{1.4} + 13 \right)} + \frac{0.002}{e^{0.6}} \quad (2.30)$$

$$\beta = \frac{0.36 \exp(-n)}{e^{0.45} + 0.007} + \tanh \left(\frac{n}{180} + \frac{6 \cdot 10^{-6}}{e^{1.4}} + 0.04 \right) \quad (2.31)$$

$$\bar{\lambda}_0 = 0.82 \left(\frac{e}{e + 0.0004} - 0.01n \right) \geq 0.2 \quad (2.32)$$

$$\bar{\lambda}_1 = 0.8 \frac{e}{e + 0.0018} \left[1 - \left(\frac{n - 5.5}{n + \frac{6e - 0.0054}{e + 0.0015}} \right)^{1.2} \right] \quad (2.33)$$

The expression for imperfection parameter η was chosen because it is in conjunction with the standard linear expression used for carbon steels. Furthermore it proved sufficiently flexible to produce strength curves of adequate accuracy [57],[86]. This method assumes that e and n are determined from a stress-strain curve obtained from stub column tests. The proposed curves are defined in such a way that for $n \rightarrow \infty$ this model provides the same strength curves as specified in Eurocode 3 for carbon steel columns [56]. However, another formulation is capable of describing the same effect more clearly without the need of regression analysis to fit the experimental data [57]:

$$\bar{\lambda}^* = \bar{\lambda} \sqrt{1 + 0.002 \frac{nE}{f_y} \chi^{n-1}}, \quad \text{where} \tag{2.34}$$

$$\chi = \frac{1}{\phi + \sqrt{\phi^2 - \bar{\lambda}^2}} \leq 1, \quad \text{where } \phi = 0.5(1 + \eta + \bar{\lambda}^2) \quad \text{and} \quad \eta = \alpha(\bar{\lambda}^* - \bar{\lambda}_0^*) \tag{2.35}$$

With the following limitation: $\bar{\lambda}_0^* < 1.0$, hence $\bar{\lambda}_0^* < \frac{1}{\sqrt{1 + 0.002n\frac{E}{f_y}}}$

The obtained recursive equation (2.34) can be solved by iteration. Figure 2.45 illustrates the influence of the non-linearity parameter for this model under the assumption of $\alpha = 0.49$, $\bar{\lambda} = 0.2$ and $E = 200$ GPa (which resembles European buckling curve c of figure 2.42).

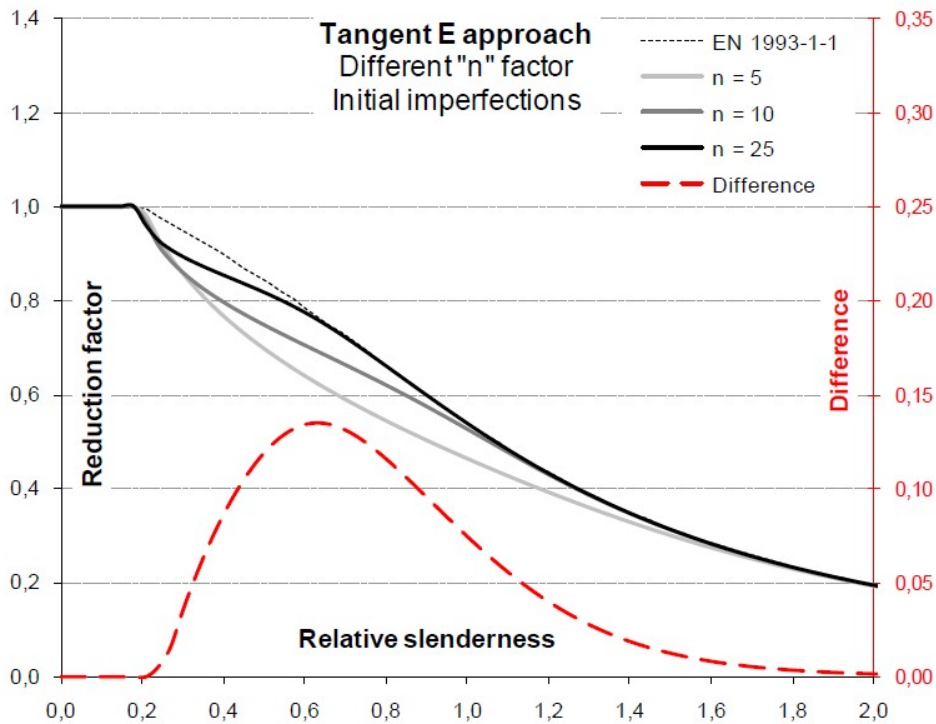


Figure 2.45: Non-linearity parameter sensitivity for the tangent modulus model *with* initial imperfection (for $f_y = 300$ MPa)

Two specific stainless steel buckling curves are specified in Eurocode 3 part 1.4 [48]: one for cold-formed sections, and one for fabricated (welded) sections (figure 2.46). The column curve for welded sections is based on European tests on AISI 304, AISI 316, and S31803 alloys at ambient and elevated temperatures [88]. Accompanying imperfection parameters as given in table 5.3 of [48] are shown in table 2.14.

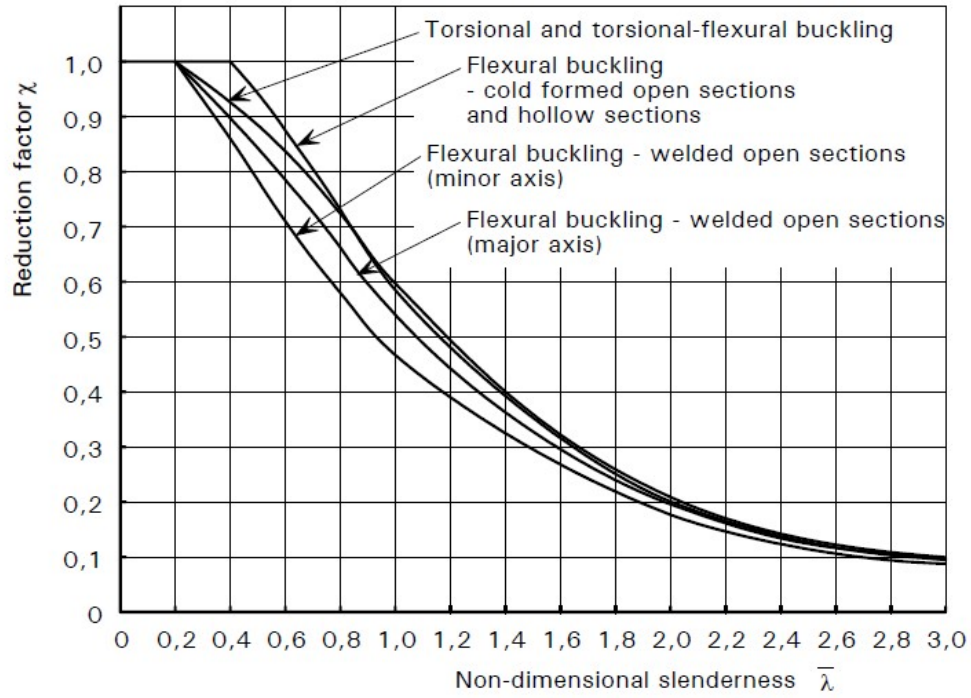


Figure 2.46: European buckling curves for stainless steel as presented in EC3 [48]

Table 2.14: European stainless steel column curve designation and its corresponding imperfection parameters

Buckling Mode	Type of member	α	$\bar{\lambda}_0$
<i>Flexural</i>	Cold formed open sections	0.49	0.40
	Hollow sections (welded and seamless)	0.49	0.40
	Welded open sections (major axis)	0.49	0.20
	Welded open sections (minor axis)	0.76	0.20
<i>Torsional and torsional-flexural</i>	All members	0.34	0.20

2.4.4. Buckling of Additive Manufactured Elements

The European buckling curves as yet presented in this report are derived solely from tests and numerical analyses on ‘conventional’ hot-rolled, cold-formed and welded sections. However, how these results relate to additively manufactured steel columns is yet unknown. If existing buckling curves do not adequately describe the buckling behaviour of the tested specimens, it may be required to derive a new buckling curve. All possible column imperfections as described in section 2.4.1 should be accounted for in an imperfection factor α and safety factor γ_{M1} , which ensure a lower bound approximation and safe design graphs. The derivation of a safety factor requires extensive statistical analysis which lies out of the scope of this thesis. Assumptions should be made regarding the safety factor.

Buckling tests on MX3D-printed WAAM stainless steel rods have been performed by Joosten [5]. A concise outline of methodology and results is presented here. Buckling tests have been executed in two rounds using first a clamped set-up, and in the second round a hinged set-up. Rod specimens with varying diameter (averaging 6.5 mm) and lengths (ranging from 109 to 237 mm) have been tested, resulting in a relative slenderness range equal to $0.7 \leq \bar{\lambda} \leq 3.5$. An example of a specimen is shown in figure 2.47. For the second round, both rod-ends were manually grinded into a pointy tip which fits into a small cavity of the bearings to serve as hinge. This allows for free rotation in all directions. The force was exerted by a hydraulic cylinder with a displacement of 0.005 mm/s and the test was stopped when the buckling load was reached. As can be seen in figure 2.48, the cylinder displacement was measured using a Linear Variable Differential Transformer (LVDT).



Figure 2.47: Rod specimen

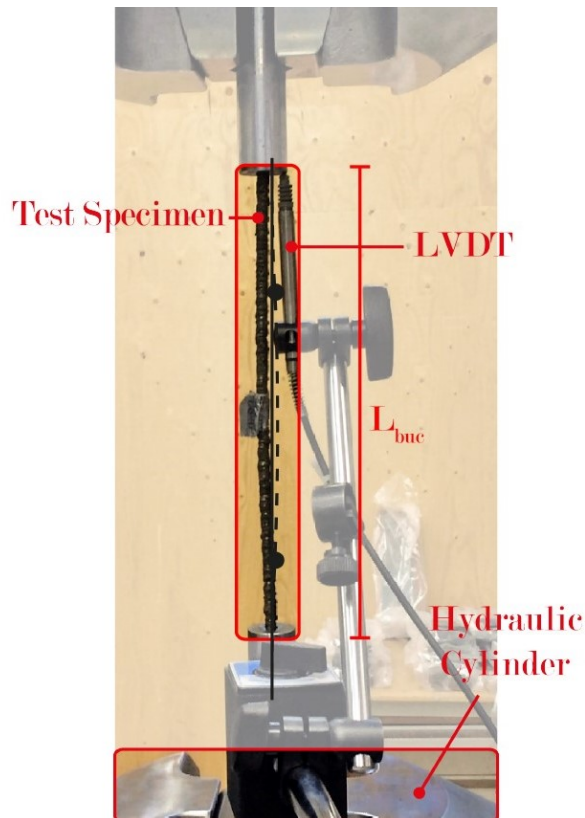


Figure 2.48: Buckling test set-up [5]

Figure 2.49 displays the results of both clamped and hinged tests. This graph has been derived assuming a Young's modulus of $E = 190000 \text{ N/mm}^2$ and an average yield strength of 280 N/mm^2 . The average rod diameter was used to determine calculate $N_{pl} = Af_y$ and a partial factor of $\gamma_{M1} = 1.1$. Since the existing buckling curves do not represent the test results, a new curve has been proposed with $\bar{\lambda}_0 = 0.1$ to account for local deviations in geometry. Additionally, buckling imperfection factor α has been set to 3 to be able to draw a conservative design curve.

It should be noted that some of the results of the tests, especially of the most slender rods, can be criticized since they attain values exceeding the Euler curve. The argument put forward in [5] that these exceeding values can be explained by strain hardening seems unlikely because the exceedance is also observed for a relative slenderness of $\bar{\lambda} = 3.5$. For such a slender member will the attained stress still be (very close to or) in the linear elastic phase, so that strain hardening does not have any effect on buckling stability.

These distinctive values are more likely caused by friction at the bearings. This reduces the effective buckling length. When one still assumes a frictionless bearing, the effective buckling length assumed as the specimen length is overestimated, consequently leading to an overestimated buckling capacity. On the other hand, since pure concentric load introduction in such thin rods is extremely hard to achieve, eccentric loading might have caused a reduction of buckling strength. Despite aforementioned remarks, these results will, together with existing curves, be considered as reference for the tests on columns, since this is the only known buckling curve for MX3D's printed stainless steel.

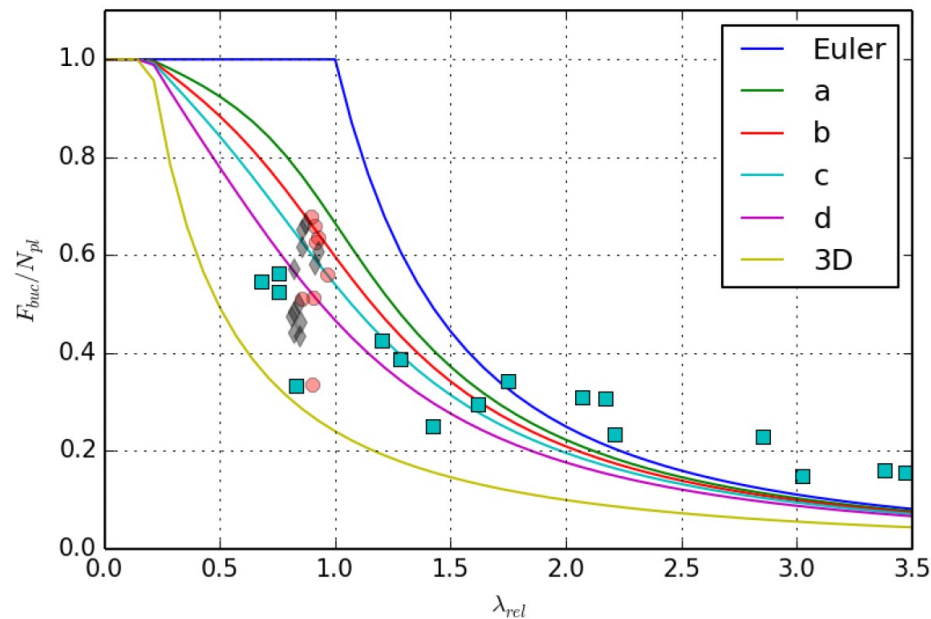


Figure 2.49: Buckling test results for WAAM stainless steel rods [5] compared with EC3 curves [56]

Where Joosten (2015) provides us with buckling test results of by MX3D printed stainless steel rods, literature research does not provide us with any buckling test results on wire and arc additively manufactured steel columns in general. Additionally, the specific print-strategy used by MX3D with associated printing parameters (see appendix B), has unknown effects on the columns their material and mechanical behaviour. It marks the necessity for material and mechanical tests on WAAM-columns, in this case printed using MX3D's strategy as explained in chapter 3. A few important aspects, yet not covered in literature, which will be investigated in this research will be highlighted:

To start with, geometrical imperfections should be carefully analysed. One of the unknowns is the accuracy of reproduction of the digital 3D-model used as input for the printer. Which tolerances should be accounted for regarding the column its macro-geometry, knowing that initial curvature and other possible macro-geometrical defects like lack of roundness may significantly affect buckling stability? May a maximum amplitude of initial curvature equal to $e_0 = \frac{L}{1000}$ as presently used in EC3 buckling calculations be considered as a proportional value for the wire and arc additively manufactured columns in this research? And does the assumption of half-sine wave initial imperfection hold for these columns?

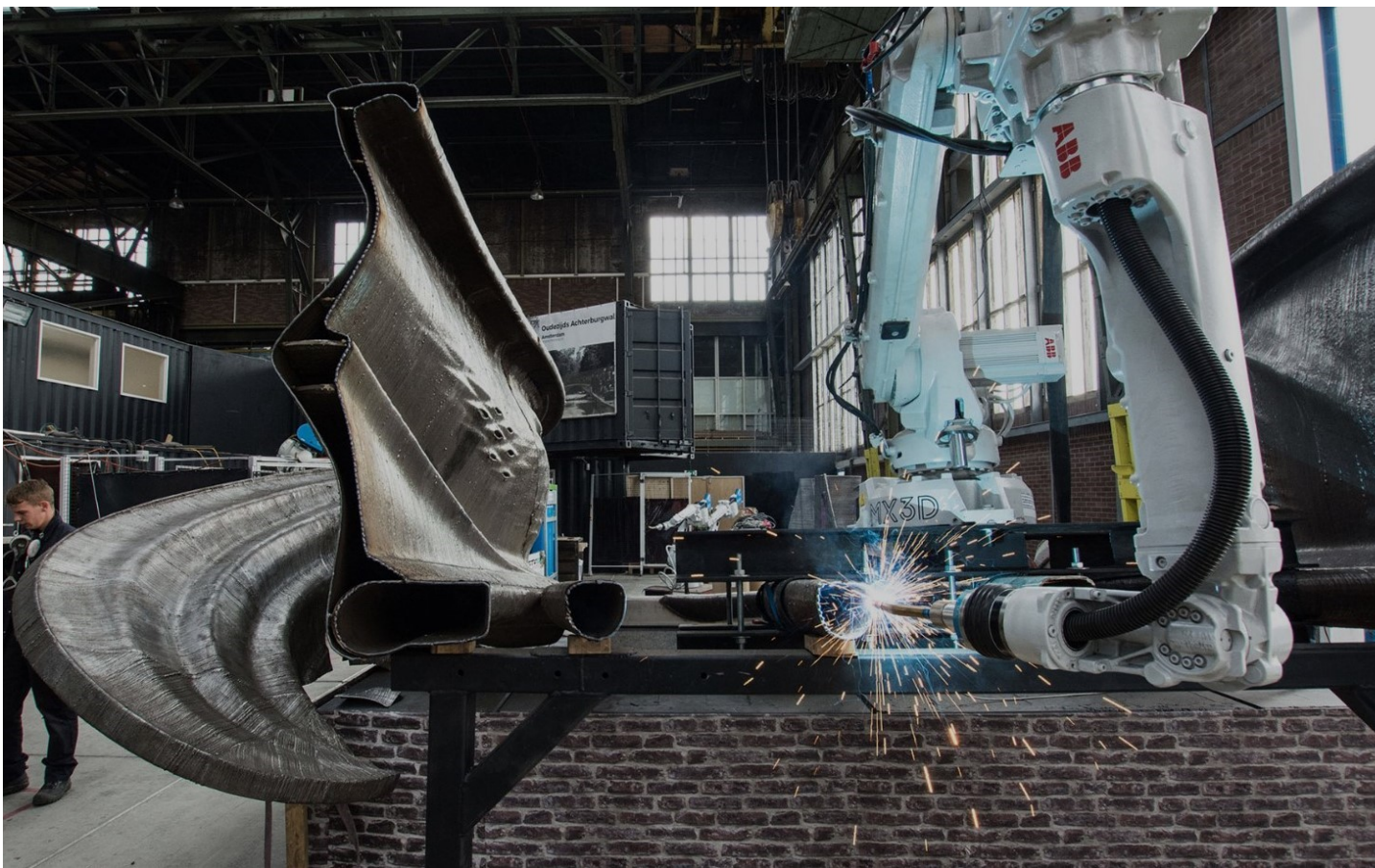
Another geometry-related unknown is the cross-sectional area A . Because of deviations in wall thickness over both the column its perimeter and length, a safe design value should be derived taking into account the (statistical) presence of minimum wall thicknesses. An effective cross-section area A_μ may be derived which can be used in buckling calculations.

Subsequently, the material and mechanical characteristics of these WAAM columns are not known. Young's moduli E and yield strengths f_y can be derived from tensile tests. Since stainless steels lacks a clear yield plateau, this behaviour should be incorporated appropriately using non-linear stress-strain models. Furthermore, material defects like porosity and non-metallic inclusions might be present, possibly inducing local variations in mechanical behaviour. This research will provide a workflow to cover all aforementioned aspects, hence enabling to perform stability analyses. Until now the distribution and influence of residual stresses related to the printing process is not well known. Much research has been conducted to welded built-up sections (as stated in sections 2.3.3 and 2.4.1), but not to WAAM printed tubular columns. It could be beneficial to analyse the effects of changing printing parameters and order of 'weld' deposition in order to reduce thermally induced residual stresses, but stress modelling lies outside the scope of this research.

Next chapter will present an extensive outline of test and measurement methodology as adopted in this thesis, which finally led to a buckling curve derivation of wire and arc additively manufactured stainless steel tubular columns.

3

Test & Measurement Methodology



This chapter describes the applied methodology for mechanical tests, metallographical tests and measurements to the geometry of printed tubular columns. Section 3.1 presents a schematic overview of tests and how they relate to the research questions. Secondly, section 3.2 presents how the specimens are printed and which parts are used for every single test.

Extensive measurements have been performed to the geometrical properties of the printed specimens. Section 3.3 presents the different measurement techniques that are used to quantify initial curvature; cross-sectional variations and surface roughness. Lastly, test equipment and corresponding procedures for the executed mechanical and material tests are stated in sections 3.4 to 3.6.

3.1. Test Methodology

Before the actual test and measurement procedures are explained, an overview of all tests and their relation to the research question is given. Figure 3.1 presents this overview schematically. At this preliminary stage assumptions are made to be able to designate test set-ups and their corresponding equipment. Bearings for example, should be sufficiently strong to withstand local forces applied by the specimens. Furthermore the machines should be capable of exerting a certain load onto the tubular columns.

After the assumptions were stated (see section 3.2), measurements on specimen geometry are done. To start with, their weight and length have been determined. Using fluid measurements (Archimedes' principle) an average cross-section was deducted which has been used later on to derive bending and buckling capacity given the stated assumptions. Next important variable is initial curvature or out-of-straightness e_0 of the printed columns. This has been evaluated by means of 3D-scans and hand drawing. Thereafter calculations were made to design test set-ups. Different tests require varying column lengths, explained in section 3.2.3. After cutting all columns to the right size, aforementioned procedure for geometry measurements has been repeated.

Having completed all geometry measurements, multiple mechanical tests have been executed so that the assumptions made for mechanical properties of the printed specimens could be verified and buckling behaviour be studied subsequently. Firstly, calibration tests are performed to validate the test results following from the applied test methodology and test set-up. This has been done for both four-point bending and buckling tests using columns with well-known material and geometrical properties. From last-mentioned an effective buckling length can be derived, necessary to study the buckling capacity. The effective bending stiffness EI has been analysed by means of four-point bending tests.

Furthermore, tensile test results from OCAS research centre¹⁹ on 3D-printed plate material have been studied to examine their stress-strain relation. Hence its modulus of elasticity E_0 and yield strength $f_{0.2}$ has been derived. Finally, all aforementioned data considered together, a buckling curve is presented which can be used to answer this research's core question; 'how can the buckling behaviour of 3D-printed stainless steel tubular columns be described?'

¹⁹Part of Finocas Group; a joint venture between ArcelorMittal Belgium and the Flemish Region

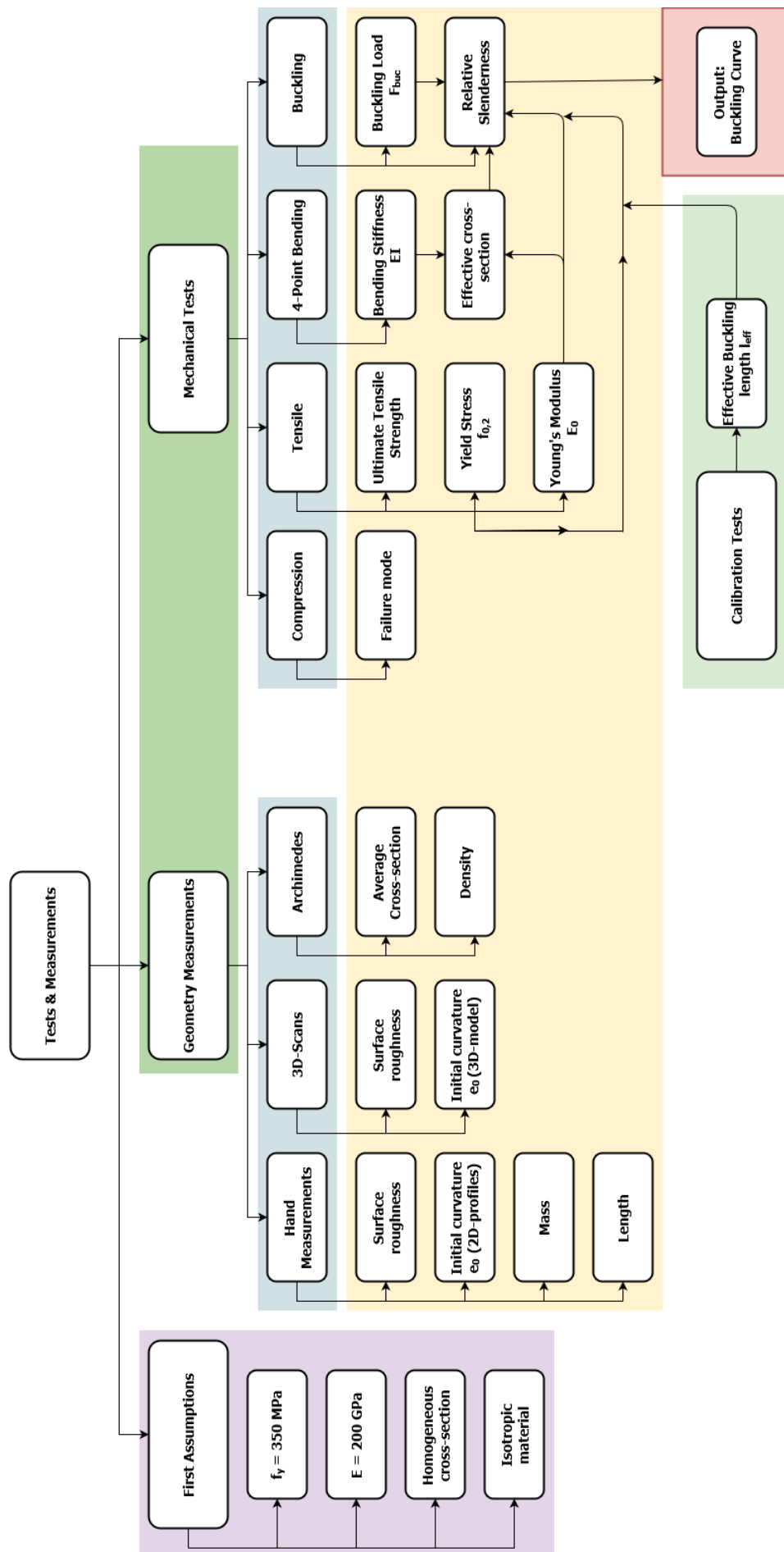


Figure 3.1: Tests and measurements overview (with exception of hardness, toughness and metallography)

3.2. Column Specimens

3.2.1. Specimen Choice

As main structural element to be used for world's first printed steel bridge, it is chosen to study tubular columns in this research. Since this is a widely used shape in structures under compressive loading, it is a good starting point for further optimisation of such a shape and a logical follow-up for the already investigated wire, or rod [5]. Of course this way of manufacturing enables the production of practically every shape imaginable, beyond 'standard' shapes. However, since even the basic properties material and geometrical characteristics of this specific way of manufacturing are not known, at first a standard tubular shape is investigated to enable research to - and a greater understanding of - more complex shapes later on.



Figure 3.2: Tubular columns with a length of 1.30 metre as produced by MX3D's 3D-printing robot

Since one of the main objectives of this research is to construct a buckling curve, columns with varying slenderness ratios should be tested. Obviously, slenderness is amongst other variables depending on both cross-sectional area and column length. The larger a cross-section, the longer a column should be to obtain the same slenderness. For the sake of this thesis with a limited amount of time and budget, tube lengths and thus printing time should be kept to a minimum. Hence a small cross-section is chosen to also enable testing of specimens with intermediate slenderness (at least up to a relative slenderness of $\lambda_{rel} = 1.5$).

An outer diameter of 33.7 mm coincides with a standard nominal pipe size of 1 inch according to ISO standards.²⁰ Using a standard size eases the comparison of printed columns with conventionally produced columns in future research. Therefore a mean diameter of 30.1 mm has been chosen with an average wall thickness of 3.6 mm. Yet the assumption of a homogeneous cross-section should be rejected. Because the print nozzle is aligned to a mean diameter and the wall thickness varies a lot, the proposed in- and outside diameter cannot be exactly produced (see figure 3.3).

In addition, it seemed from previous trial tube samples that the proposed wall thickness of approximately 3.6 mm is the absolute minimum to sustain a certain print quality. A thinner wall results in an even more irregular surface and more important, a lack of consistency between the point welds²¹. Consequently, the low diameter over thickness ratio ($D/t < 10$; CSC 1) will most likely rule out local buckling. It should be noted that this is an average value. Local variations in geometry might influence (local) buckling behaviour.

²⁰ISO1127:1992 or ISO4200

²¹This holds only for dot-printing strategy; not for continuous strategy. Further explained in section 3.2.2



Figure 3.3: Column sections as cut from the welding plate with irregular cross-sections

3.2.2. Specimen Printing

MX3D is currently able to print pieces in stainless steel grades Thermanit MTS3 (EN1.4903), 308L (EN1.4316), 316L (EN1.4404) and bronze, aluminium, copper. Even more grades are being tested with varying parameters to optimise the printing process. The bridge however will be printed in austenitic stainless steel 308L (EN1.4316) simply because MX3D has extensive experience with this specific steel grade. Therefore 308L is used to print the columns for this research.

The exact welding wire used by MX3D is called 'Inertfil 308LSi' with a thickness of 1 mm. A low carbon content (designated with 'L') improves the resistance against intergranular and atmospheric corrosion which is a prerequisite for a bridge structure to be placed in Amsterdam. In addition to the 308L grade it contains extra silicon to improve wetting behaviour. According to the datasheets of supplier Oerlikon, provided in appendix B.2.1 [47], the material possesses a yield strength of 350 MPa, a tensile strength of 520 MPa and an ultimate strain of 35%. Furthermore, Eurocode steel provides us with a Young's modulus of $E = 200$ GPa for austenitic stainless steels²² assuming isotropic material behaviour.



Figure 3.4: Oerlikon Inertfil 308LSi welding wire

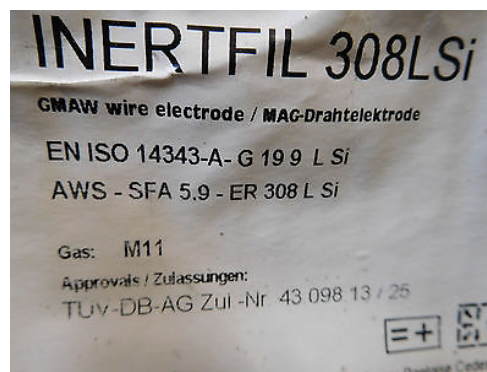


Figure 3.5: Welding wire label

In total twelve tubular columns are printed with an approximated length of 1.30 meter using point weld (or 'dot-by-dot') printing strategy. This strategy is being discussed here. The columns printed for this research were at the time²³ the longest ever produced by MX3D what came up with several challenges. One of which is the printing duration. Even though the applied WAAM-printing technique is known for significantly reducing production time compared to its powder-based manufacturing rivals; printing of large samples still takes a lot of time. Therefore reducing the production time had priority. Since for buckling tests a certain column length is required, this in practice meant reducing the cross-section.

²²EN 1993-1-4: 2006 (E) section 2.1.3.(1)

²³mid-April 2016

Another limitation is the thickness: using the 1 mm welding wire, a wall thickness range of approximately 3 to 8 millimetres can be achieved. As mentioned before, this is just an approximate value, because the current state of geometry control during the printing process does yet not allow for the thickness output to exactly match the desired digital input.

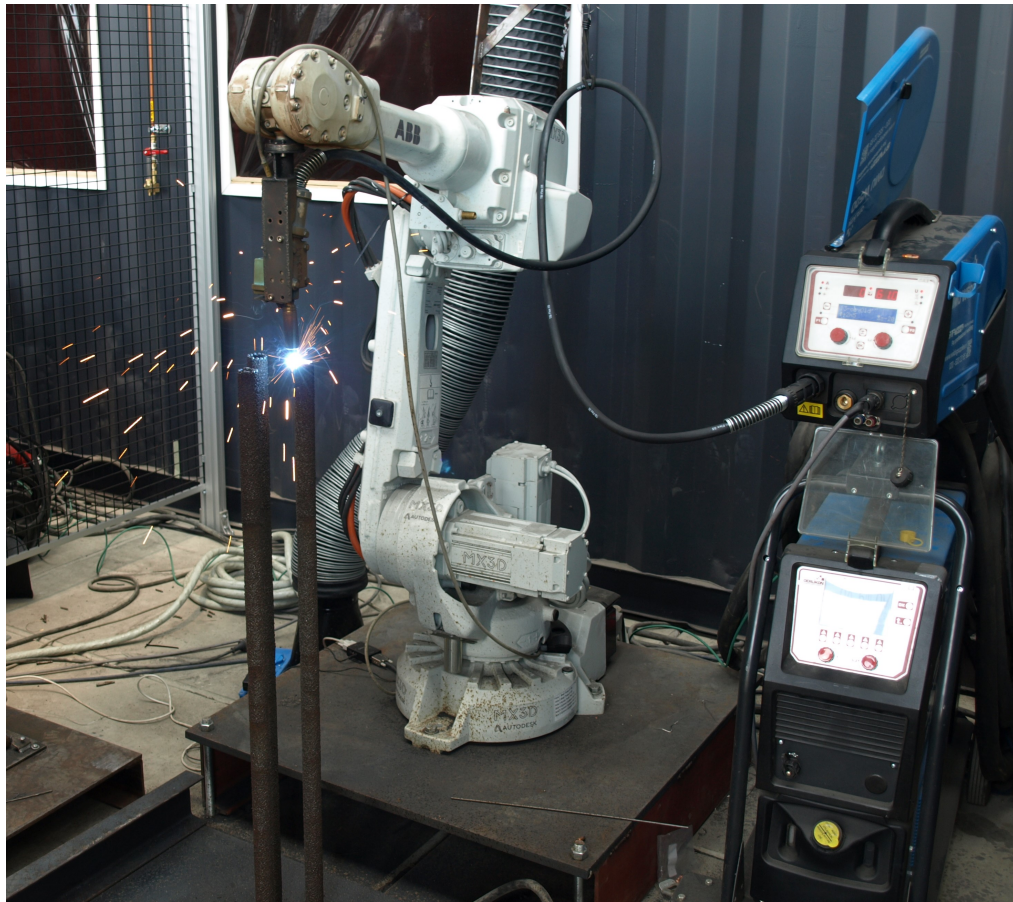


Figure 3.6: MX3D Column printing using an ABB robot with welding head

Using a multi-axis ABB-robot (IRB-5-2600 robot) with a gas metal arc welding head (Oerlikon Citowave 3) as shown in figure 3.6, the columns are printed vertically, three at a time as modelled in Rhinoceros (see figures 3.7 and 3.8). A steel platform, with sufficient rigidity to withstand robot accelerations has been used to elevate the robot 20 centimetre above ground level. This extra height was needed to gain sufficient vertical range to print specimens of 1.3 metres long. Hence the welding head is positioned vertically and not under an angle during each metal deposition. Monitoring printing time has not been done carefully. Due to the large amount of stops and restarts of the robot, and a lack of memory capacity of the robot computer which monitors the exact operating time, only an estimation of printing time can be given.

Printing three columns of 1.3 metre length with a wall thickness of 3.6 mm and mean diameter of 30.1 mm took 15 to 19 hours, averaging a material deposition rate of 0.65 kg/hour. Consequently, one batch of three columns is not produced within one working day. Therefore cold restarts during the printing process are unavoidable. The effects of cold restarts on the structural properties of printed elements, and more specifically their buckling strength is not known. These layers are included in the tensile specimen batch so that any possible negative effect of overnight cooling is incorporated in the results.

Printing each column separately does not increase the production speed because the material needs to sufficiently cool down before a new metal layer can be deposited. The robot will have to pause its printing program rather than it is able to print, which will drop the deposition rate. To establish a more efficient production process, the printer switches from one column to an other after each deposited layer.

The necessity for such a strategy arises from the choice for a small cross-section in this research. A new layer deposit spread over a larger cross-section is more likely to be cooled down completely before the next layer-deposit is scheduled. Up to now there is insufficient knowledge about this cooling behaviour. No specific guideline for print and cooling time has been used in this printing process. Just rules of thumb guided by (increasing) experience. ArcelorMittal, with cooperation of MX3D, is currently investigating cooling ratios and heat input for various printing strategies with advanced thermal imaging.

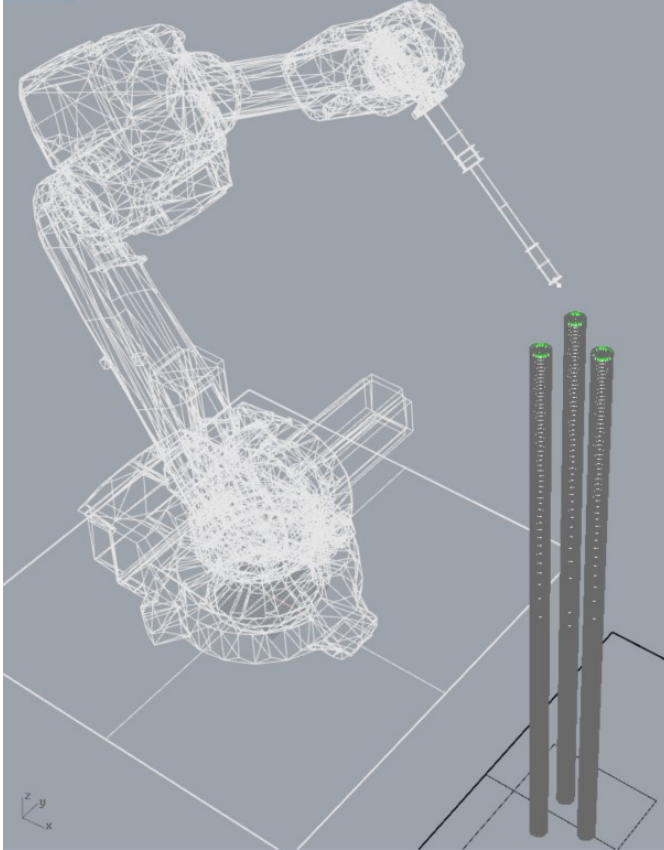


Figure 3.7: 3D-view of specimen printing model

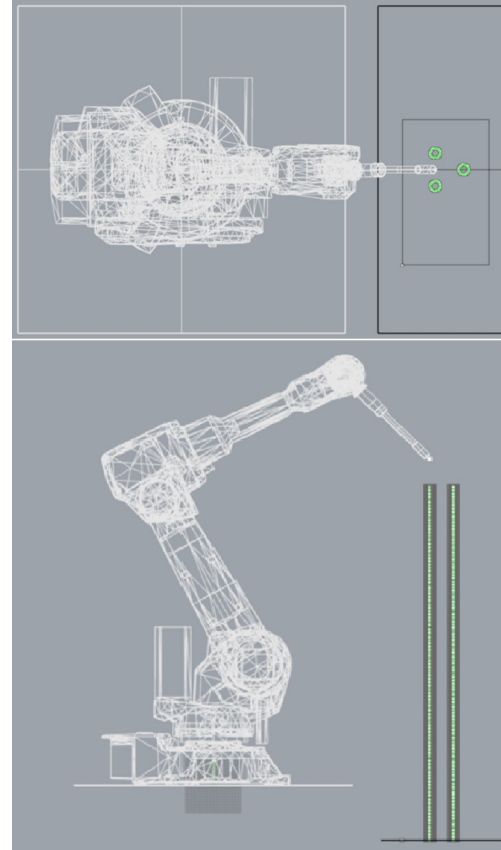


Figure 3.8: Top- and side-view of printing model

MX3D is experimenting with several printing strategies to optimise production speed and quality. A major distinction can be drawn between the so-called continuous strategy (lines) and point (or 'dot') strategy. Considering the latter strategy, endless options of 'point-weld' deposition order are possible. As an advantage over continuously printing strategy, 'dot-by-dot' printing enables the robot operator to 'play' with order of metal deposition and subsequently manage the cooling rate of the material globally or locally. Furthermore, the dot-by-dot strategy allows a quicker response to printing errors.

Continuous strategy is sensitive for printing errors which is mainly caused by the progressive effect of an error while using lines; one wrong deposition causes a 'shift' in the entire layer. However, the relevance of aforementioned argument will likely be of decreasing value where the number of printing errors is expected to drop drastically over time. What effect a certain printing strategy has, for instance on the development of residual stresses is not known. How both strategies affect the microstructure of steel will be studied in section 3.5.



Figure 3.9: Printing according the 'Merlon strategy' with clearly visible its distinctive point welds

The specific point (or 'dot') strategy program adopted to print the columns is called 'Merlon' and is modelled point by point in Rhinoceros software. As visualised in figure 3.10, the column is built up spiralwise where each layer is shifted according to the golden ratio (also called divine proportion). Additionally, the order of point-deposition of each layer around the circumference is programmed like this: 1-6-11-16-..., after which the gaps are filled: 2-7-12-17-... Each time four intermediate points are skipped before in the next round those are filled up in a similar manner. These distinctively deposited point welds during printing can be seen in figure 3.9. This through experience guided strategy resulted in a visually satisfactory column specimen.

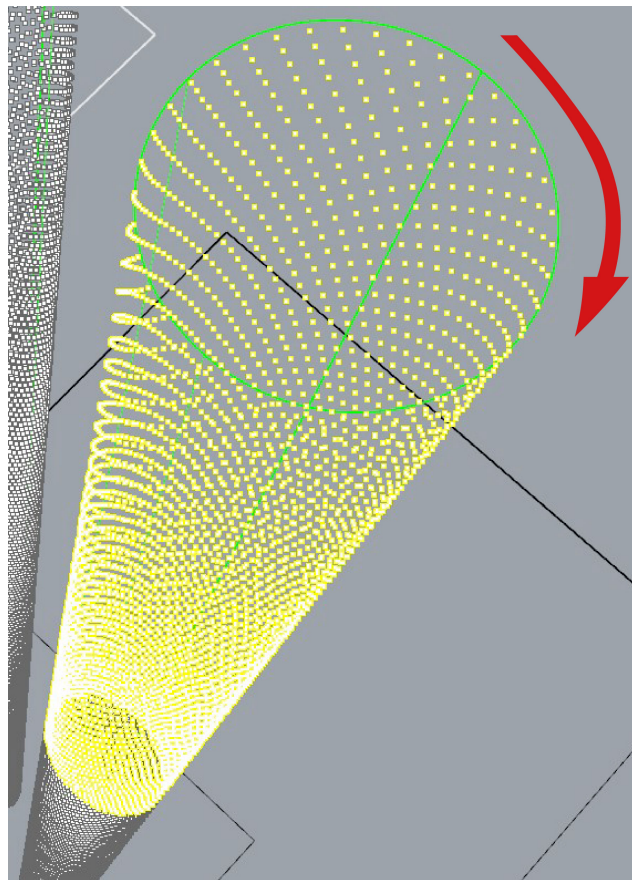


Figure 3.10: Spiralwise built-up tubular column as modelled in Rhinoceros (print direction marked with red arrow)

To rule out any possible effects of printing parameters like voltage, wire-feed speed, nozzle height, etcetera; all specimens are printed with the same settings so aforementioned parameters are kept constant. However, during the research process, three columns with a different print strategy were added. These continuously printed columns are included in this research to investigate and compare their cross-sections, capacity and microstructure with dot-printed specimens. The continuously printed columns are produced²⁴ with a wire-feed speed of 3 metres per minute and a layer height of 1.2 millimetres. Similar to the dot-printed specimens they are produced three at a time to minimise inactivity of the robot. Detailed information of the chosen parameters for both printing strategies is attached in appendix B.1.

When all the printing was finished and the samples had cooled down, the columns were cut from the base plate using a grinder. Despite that this was the most practical way to remove the samples from their base plate, the result was an undesirable non-straight cut. For buckling and compression tests it is crucial to have a perfect perpendicular plane onto which the samples can be loaded in compression. A straight cut at the column-ends has been achieved using a water-cooled beltsaw available in Stevin II-laboratory (figure 3.11).



Figure 3.11: Columns are cut perpendicular by a belt-sawing machine

Post-fabrication treatments like surface treatment and cleaning is intentionally not performed, since removing surface irregularities of the columns has unknown effects on the properties of the specimens. Additionally, when cleaned, the stainless steel surface reflects too much light for a 3D-scanner which will be used later for measurements on geometry. Residual stress developments in these column specimens are yet not investigated, hence the effects of stress-relieving by annealing are also unknown. It would be interesting to analyse residual stress developments and the influence of various post-fabrication treatments, but this lies outside the scope of this research.

3.2.3. Specimen Overview

This section provides an overview of all column specimens used in this research. They were not directly printed at the desired length. The raw un-sawn columns, in total twelve dot-printed with a length of 1.3 metres and three continuously printed specimens with a length of 1 metre are sawn to the desired length later on. Table 3.1 provides an overview of chosen sample lengths in tabular form. The specimens are marked with three-character labels (\$-LL-X\$ or \$-X-\alpha\$) which can be interpreted like follows: the first character marks the test wherefore this specimen is used - 'A' stands for buckling, 'B' for bending and 'C' for compression test. Buckling specimens receive an additional numerical mark 'LL' representing the column length in centimetres. Additionally, character 'X' designates a specimen number (f.e. 1 or 2) because multiple tests have been executed on the same type of columns. The remaining character ' α ' designates the applied print strategy: 'A' is dot-printed; 'B' continuously printed.

²⁴Continuously printed columns are produced in November 2016

Table 3.1: Overview test specimens (*columns of bending tests are reused for buckling tests)

Test	Label	Amount	Length L [mm]	Diameter D_{mean} [mm]	Thickness t_{avg} [mm]
<i>Bending</i>	B-X-A	3	650	30.1	3.7
	B-X-B	3	650	30.1	3.2
<i>Buckling</i>	A-48-X	3	480	30.1	3.7
	A-85-X	3	850	30.1	3.7
	A-125-X	3	1250	30.1	3.7
	B-X-A*	3	650	30.1	3.7
	B-X-B*	3	650	30.1	3.2
<i>Compression</i>	C-X-A	8	100	30.1	3.7
	C-X-B	9	100	30.1	3.2

Additional remarks should be made regarding the quality control of the production process. From visual inspection several printing errors were observed as exemplified in figure 3.12. The result of the considered error can be described as a misfit of one or more successive deposition layers causing a misalignment or 'shift' from the longitudinal column axis.

It is however assumed that these errors are solely the result of a lack of experience in the very early stage of the development in printing such long specimens. Hence the assumption that in the near future the printing process rapidly improves and that these errors will not be present is valid. Actually this can already be confirmed by analysing the most recent tubular column samples, where aforementioned errors are not observed. It is therefore chosen to saw the specimens in such a way that major misalignment errors are avoided if possible.

Figures 3.13 and 3.14 show colourwise which sections of the columns are used per specific test. Images of the test specimens are collected in appendix C.1.

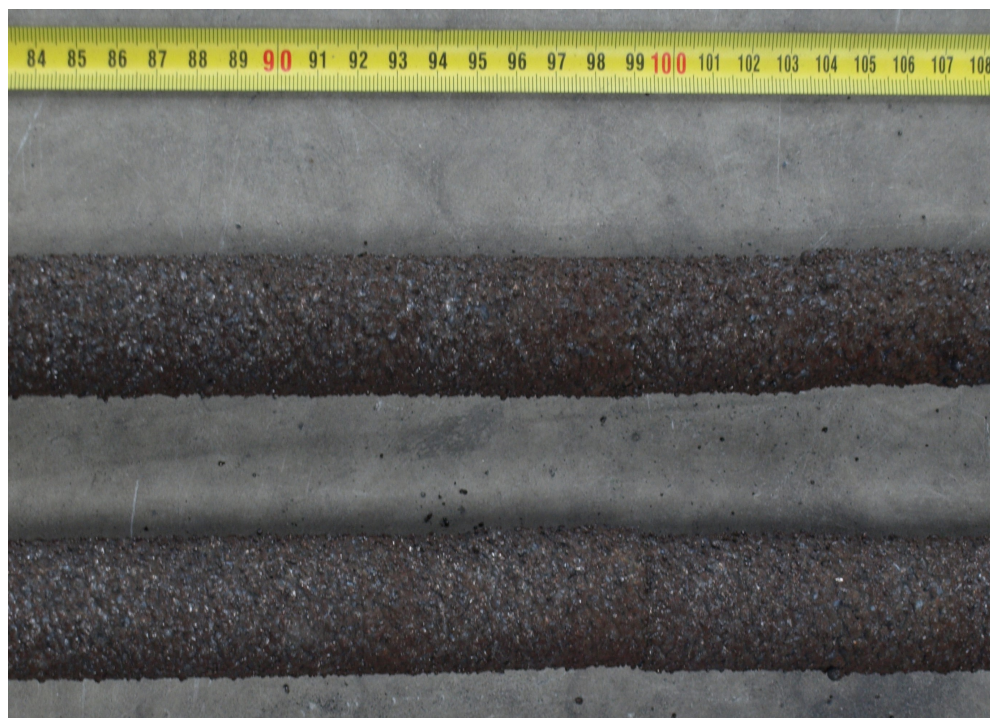


Figure 3.12: Printing error causing a misalignment of successive layers from the longitudinal axis

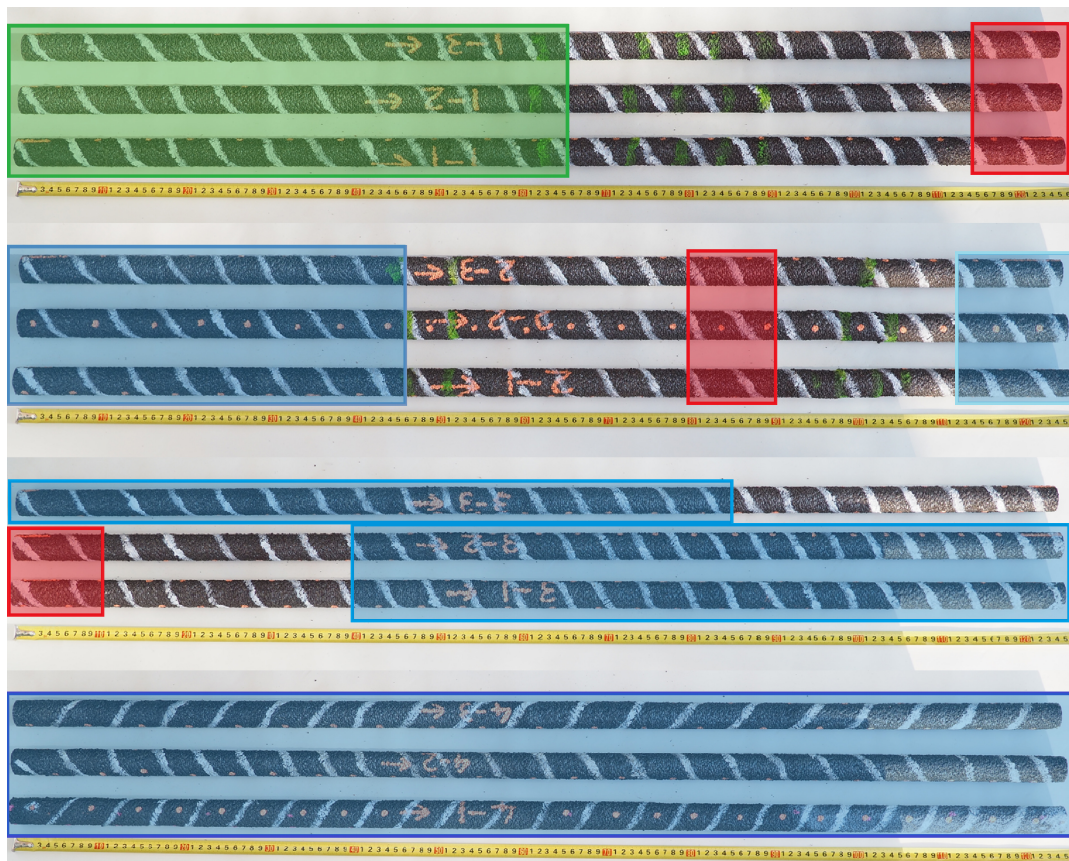


Figure 3.13: Overview of dot-by-dot printed column sections and their use per test: Blue = buckling; Green = bending & buckling; Red = metallography & compression

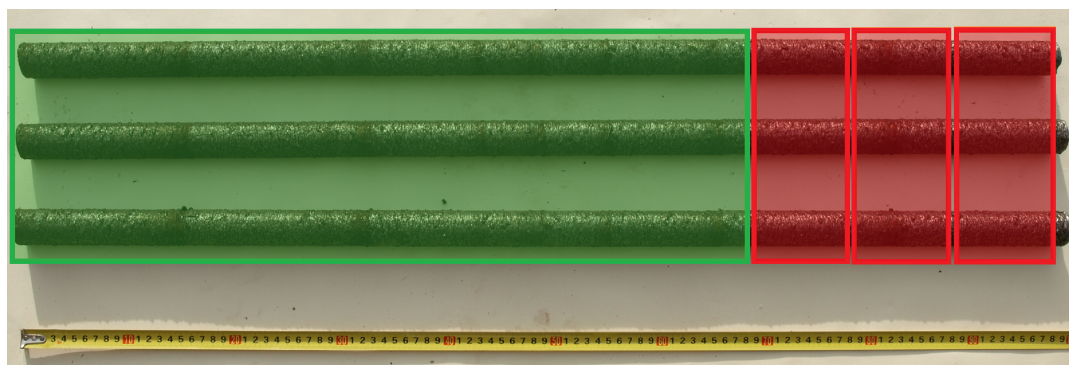


Figure 3.14: Overview of continuously printed column sections and their use per test: Green = bending & buckling; Red = metallography & compression

3.3. Geometry Measurements

Solely visual inspection of tubular column geometry is not sufficient and accurate enough to quantify macrogeometrical imperfections and local thickness variations. Before any buckling test can be initiated, the initial curvature should be determined. Usually the maximum deflection at midspan is used (half a sine wave-shape), but in this case the maximum deviation from the longitudinal axis due to misalignments of certain column sections (printing errors) might be governing. To analyse geometrical characteristics of the test specimens, several measuring methods have been adopted. The column length can be determined relatively easy. In order to quantify the initial curvature of the specimens, two ways of measurements are applied. Firstly, hand measurements by drawing lines and secondly a more refined method using advanced 3D-scanners, explained in sections 3.3.1 and 3.3.2 respectively.

An average value of the cross-sectional area can be deduced from volume measurements using Archimedes' principle. This is explained in section 3.3.3. However, this method does not take into account any cross-sectional variations in both longitudinal and transversal sections. Additional measurements to multiple column sections could be useful to gain insight in statistical presence of wall thickness minima. Another option is to derive an 'effective' cross-section from the combined result of bending and tensile tests (see section 5.1). This data could be very useful for safe design and calculation models of 3D-printed elements. A schematic overview of this section is presented in figure 3.15.

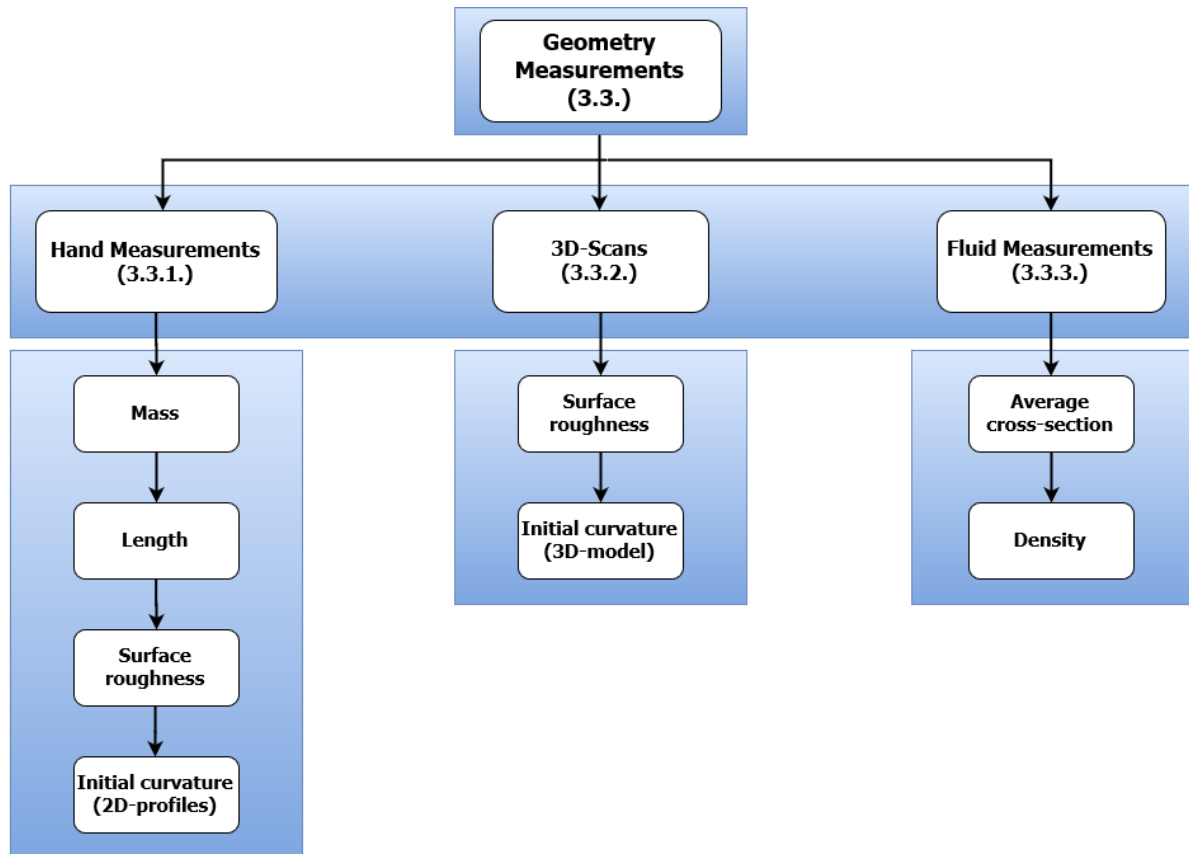


Figure 3.15: Outline section 3.3.: Geometry Measurements

3.3.1. Hand Measurements

Firstly, length and weight of the specimens have been determined by using a simple tape measure and weighing machine (accuracy to 5 grams). The column its outer diameter has been measured at several points along the perimeter and along its length with a(n) (electronic) Vernier's Caliper. Although a Vernier's Caliper measurement itself is accurate (0.05 to 0.01 mm for a digital Caliper), it is limited to one dimension only. While in reality specimen geometry is variable in three dimensions. By performing multiple measurements across the length and perimeter a general idea of diameter variation can be obtained. Without sawing the specimens, the wall thickness can only be measured non-destructively along the perimeter of both column-ends. Thickness variations of column sections in the longitudinal plane can only be studied by cutting them in parts. Clearly this is only possible after finishing the mechanical tests.

Secondly, hand measurements are done by drawing lines. By simply using a large piece of paper, a carpenter's square and a pencil, lines parallel to the column in longitudinal direction can be drawn. This is depicted in figures 3.16 and 3.17. A sawing machine guider is used to support the carpenter's square. The latter can move freely perpendicular to the guider, consequently able to follow the column its length profile. To draw lines on paper, a pencil has been mounted to the carpenter's square. The column itself is stabilised to prevent it from moving while drawing lines.

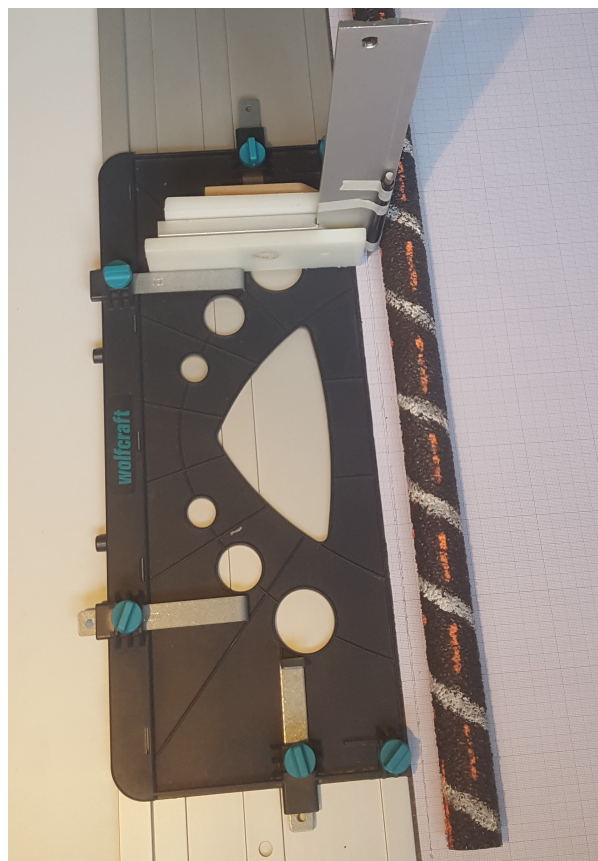
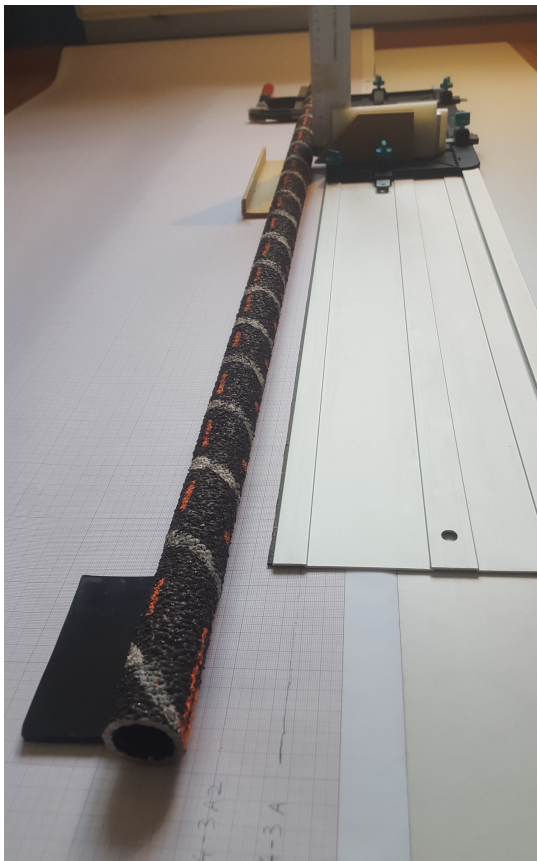


Figure 3.16: Set-up used to draw lines parallel to column surface Figure 3.17: Saw machine guider with mounted carpenter's square

Starting point for each parallel line is marked around the perimeter of the columns. Two points are equally divided around the perimeter and chosen such that they coincide with the axis on which maximum eccentricities have been observed. This can be obtained from 3D-scan data. Besides surface irregularities, curvature and other deviations from the longitudinal axis can be measured as well. The result is four longitudinal profiles per column, whereas the two facing lines can be compared to obtain a more accurate curvature profile. The intention is to quantify the out-of-straightness e_0 of the columns which may be expressed relatively to their length (f.e. $L/1000$). Final results are presented in section 4.1.1. Using this technique a general idea of surface roughness can be obtained as well. Major drawback however is that all profiles are in one dimension only, whereas the geometry varies in three dimensions. A more sophisticated approach using 3D-scanners is used to create a 3D-model of the column geometry explained in section 3.3.2. Consequently this model can be compared with the hand-measured one-dimensional profiles to verify the measurements.

3.3.2. 3D-Scans (Macro-Geometry)

As a more sophisticated and quicker alternative for photogrammetry (which was used by Joosten [5] to create a digital model of a 3D-printed rod geometry), 3D-scanning has been used in this research. Additive manufacturing aids to the increasing popularity of this technique. It enables exact reproduction of any shape by first scanning and subsequently 3D-print the object using the obtained scan data. Commercial companies provide 3D-scan services, but as it turned out, that was too expensive for this research. Fortunately, it was possible to use 3D-scanners from the Faculty of Industrial Design of Delft University of Technology and to make use of the scan experience available there.

The complexity of scanning these specific printed objects lies in the significant length of the object (1.3 meter), little margins in which the specimen's initial curvature should be sought for and the refined surface geometry which requires very sophisticated and accurate scanners. During the first test scan, the Artec Eva scanner was used, but because its working distance is 0.4 to 1 metre, it had a hard time to identify such a slender object like the printed specimen. Also the scanner showed difficulties in recognising the column's surface because it was not distinctive enough.

Subsequently the most accurate scanner was installed. This specific high resolution Artec Spider handheld scanner, as shown in figure 3.18, uses blue LED flash bulbs to identify the geometry and its texture. Simply said, the scanner captures lots of images (up to 7.5 frames per second) and fits all images together to one 3D-point cloud. A 3D-point accuracy up to 0.05 mm can be reached, which is sufficient accurate for this research's purpose. By these means it is possible to capture initial curvature, local deviations and surface roughness of the printed specimens in one go. The disadvantage of only being able to model the outside of the column however remains. Another downside becomes apparent during the scanning process and post-processing of its data. Since the Artec Spider has a limited working distance (0.17 to 0.35 m), capturing the entire column surface requires a lot of frames. To convert the resulting scan files with such accuracy in a complete 3D-image requires a lot of calculation time. This demanded a different computer with additional random-access memory (32 GB) and an improved graphics card.



Figure 3.18: The two 3D-scanners used: at the left Artec Eva and right the more accurate Artec Spider

Several set-ups were built in order to scan as accurate and efficient as possible. To aid a practical execution of the scans, at first a simple support structure was made so that the columns remain stable in vertical position while they were scanned. This was achieved with a rigid standard to which a small diameter aluminium tube was mounted. Aforementioned tube fits perfectly in the printed specimen, in this way stabilising it in vertical position. Placing the entire set-up on an automatic rotating platform enabled capturing the complete circumference of the specimen while scanning from one position. However, because of its weight, the top of the specimen swayed during rotating. This little movement prevented a consistent scanning process.

By placing the specimen in horizontal position clamped between two blocks, still allowing the aluminium tube to rotate freely, a more stable set-up was obtained. Small timber pieces mount the specimen in an easy way even further to the aluminium tube. In this way rotating the aluminium tube let the specimen rotate as well. A custom-made frame with slider on top of which the scanner was mounted, facilitated scanning with constant speed while the scanner stayed within its working distance of 17-35 cm. Figure 3.19 visualises the set-up.

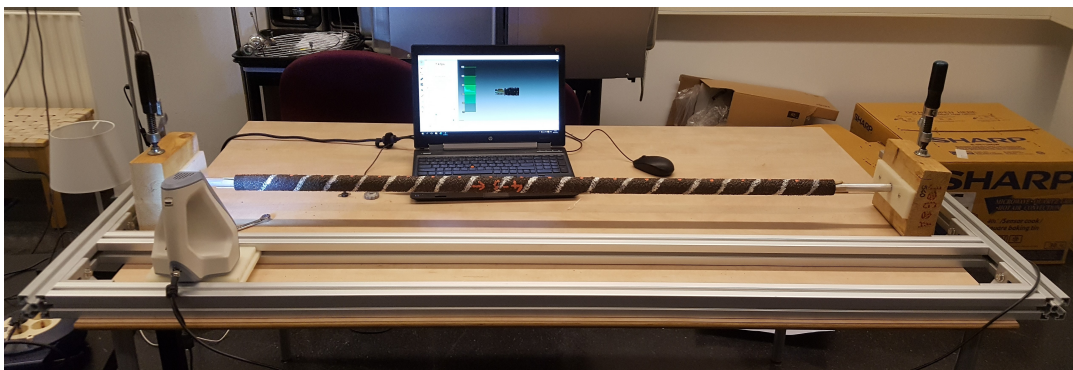


Figure 3.19: 3D-scan set-up with sliding frame to enable consistent scanning

Before scanning can be initialised, additional measures were taken to obtain optimal results. First the 3D-scanner itself was calibrated using its own calibration procedure. This includes a calibration rig with a pattern which should be scanned from multiple locations and distances; its included software corrects the scanner accordingly. Secondly, it is crucial to prevent any reflections of the light source from the stainless steel. Therefore, the printed columns are not cleaned and polished to the shiny surface which is its common appearance. The aluminium inner tube which is used to support the printed specimen is too reflective as well. Anti-reflective spray paint and tape is used to eliminate this.

After several test scans, the scanner still had difficulties to align all scanned frames and it was not always able to compose a consistent 3D-model out of the point cloud. This problem is related to the indistinctive character of the specimen's geometry and their monotone surface texture. Painting white spirals and coloured dots on the columns helped with recognising and identifying the multiple frames. It also eased the analysis after tests, since the relation between the obtained geometrical imperfections from the 3D-model and the location of buckling failure could more easily be drawn.

With aforementioned methodology, multiple scans are made from the same specimen. By aligning the 3D-models and by creating a surface-distance heat map, the reproducibility of making a 3D-model like this has been evaluated. To enhance the measurement and alignment of multiple scan results of the same specimen even further, drops of glue were put on the specimen. These drops marked the alignment points for the column models. At last, when a satisfying accuracy was obtained, it gave green light to initiate the final scans using this methodology. From here on the process from scanning to final model can be distinguished in 3 phases.

Scanning

Scanning has been done in the Multi-Sense lab of the Faculty of Industrial Design to reduce light pollution from outside. Because of the complex geometry and texture it is chosen to scan both at the same time. After a 30-minute warm-up, the scanner's light-bulb is on its optimal temperature (52°C). First the correct start-position of the scanner should be checked. A small piece of the test set-up should be scanned to capture the column-edges completely. Furthermore the optimal working distance and temperature should be monitored during the entire process.

The scanner is slowly moved sideways along the sliding frame with constant speed. By rotating the specimen at the same time, the entire column surface can be captured. It is crucial that there is sufficient overlap of scanned frames to enable the post-processing algorithm to align the separate frames so a 3D-model could be created. In case some frames were missing from the model, only that specific part was scanned again. However, where sufficient overlap should be guaranteed, reducing the number of scanned frames had priority since post-processing the data is very time consuming. This entire scanning process itself takes approximately two minutes.

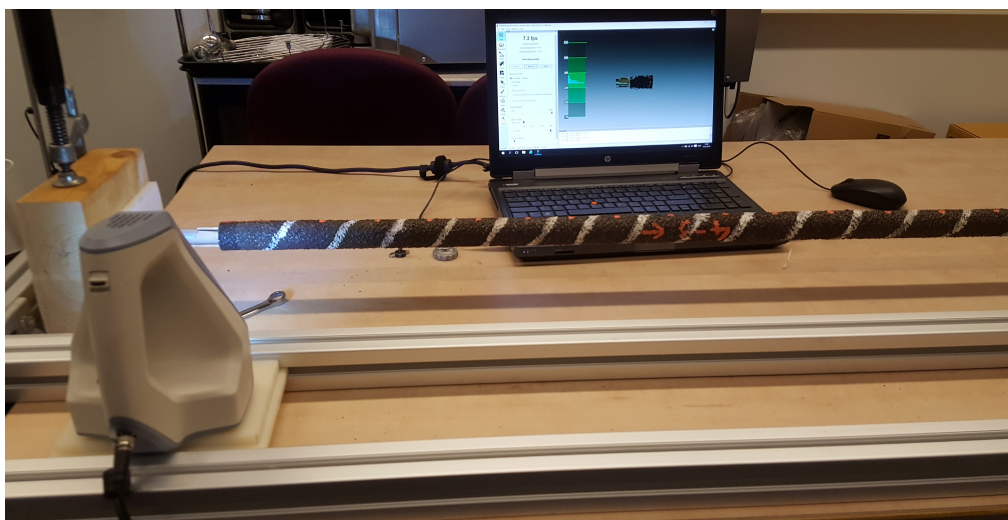


Figure 3.20: Scanning procedure

Post-Processing 3D-data

A post-processing algorithm from the scanning package Artec Studio 11 Professional was used to obtain a 3D-model from scan data. Several iteration steps were necessary to complete the model. Firstly a rough, than a fine and global registration should be performed to align frames. This is the most time-consuming step, subsequently a high-end computer processor is a prerequisite. When the software indicates a 0.1 to 0.3 error this is acceptable. In case this value is exceeded, specific frames causing that error should be deleted. Secondly the remaining frames are fused together to one model. After this, texture images are added to the scanned geometry. To finalise the 3D-model, the tube frame which is partly scanned together with the specimen and the drops of glue, should be removed. In Geomagic Studio this is can be done easily. At last the mesh-doctor option is used to remove spikes, double layers and other mesh inconsistencies. Emphasising the amount of data used for this model; an average column model consists of 4 to 5 million triangles.

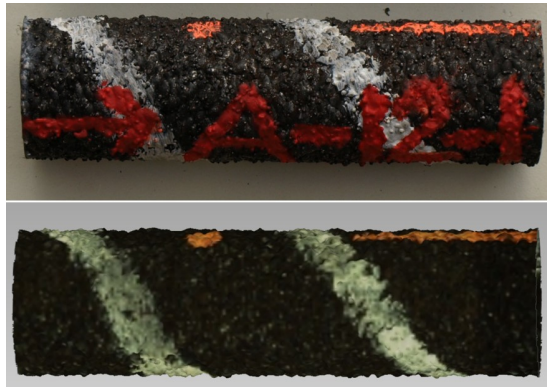


Figure 3.21: Object (top) versus 3D-model (bottom)

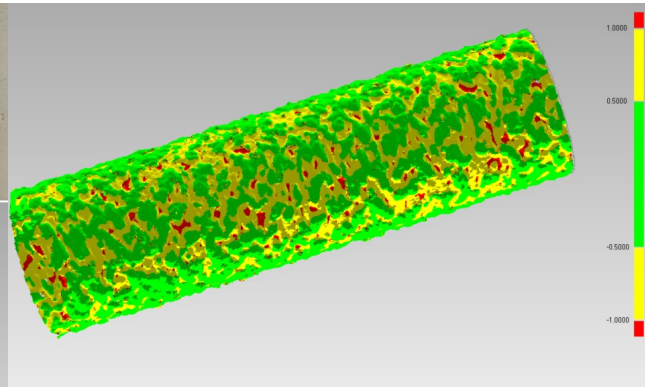


Figure 3.22: Surface-distance heatmap of printed column section

Analysis of imperfections

In order to quantify initial imperfections of the specimens, the scans are compared with a 3D-model of a 'perfectly' straight column. This column is modelled in Rhinoceros using the average outer diameter obtained from volume measurements. First a manual pre-alignment is done in GOM-Inspect freeware to place the 'perfect' column on top of the scan-model. Finally a more refined alignment in Geomagic Studio was performed. Using the same program, a surface-distance heatmap was produced which makes the differences between a perfect column and the printed specimen clearly visible (figure 3.21-3.23).

Next the maximum difference and its location was studied. Its location around the perimeter was marked and a line was drawn on which the maximum eccentricity was observed; buckling is expected to occur in that direction. The same line was also used for hand-drawing measurements to be able to compare results. Above stated procedure has been used for the maximum columns lengths (as they were printed) and repeated for every specific test specimen after they were sawn in the desired length. In this way imperfections can be analysed of entire columns and of columns as they were used for testing. An overview of obtained results is given in section 4.1.1.

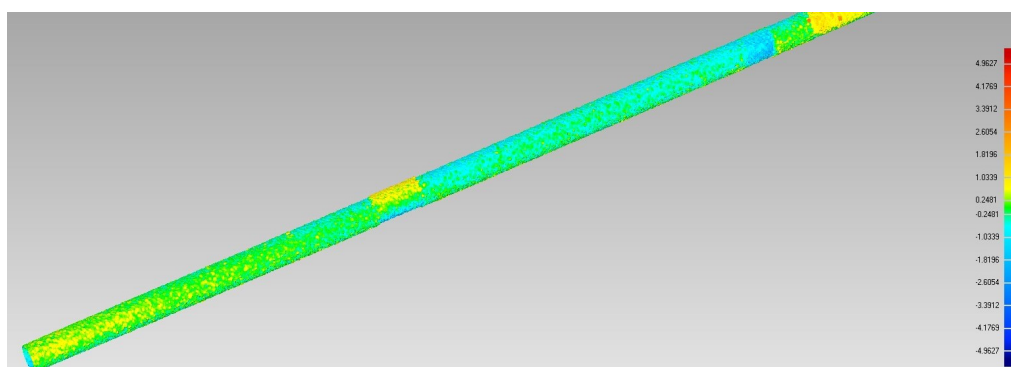


Figure 3.23: Example of a surface-distance heatmap of a 1300 mm column section in Geomagic Studio

3.3.3. Volume Measurements

It is hardly possible to quantify cross-sectional variation accurately without cutting the specimens in parts. Therefore an other method has been adopted to determine an average cross-sectional area. This value is used to predict failure loads and to determine the required material for the preparation of test set-ups.

The volume of the printed column specimens can be determined by using Archimedes' principle. By submerging a specimen into fluid, its volume can be deduced by measuring the displaced fluid volume. In this case a transparent PVC-tube with an inner diameter of 57 mm was used. A plastic pipe-end able to resist high water pressure takes care of a water-tight sealing. First the plastic tube was filled with water. Figure 3.24 shows the entire set-up. After ensuring a perfect straight water column, the water level was measured and marked. A bit of soap was used to eliminate adhesion of water to the plastic tube wall. Secondly, the printed column was carefully inserted in the plastic PVC-tube with the water column. After renewed levelling of the tube, the water level was marked and the difference in water level was measured. This procedure has been repeated twice for every specimen and repeated again after sawing all specimens to the right size for the mechanical tests.

Knowing the inner diameter of the PVC measuring tube, the displaced water volume (or specimen volume), can easily be calculated. Furthermore the length of the printed columns are known. By dividing the measured specimen's volume by its length an average cross-section A_{μ} is obtained. Now that the specimen's mass and volume is accurately known, the actual density can be found as well by dividing its mass by its volume. Stainless steel welding wire supplier Sadev provides an average density value of 7.90 g/cm^3 for, amongst others, alloy 308LSi [89]. This value can be compared with the outcome of measurements.



Figure 3.24: Set-up used to perform Archimedes' volume measurements

3.4. Mechanical Tests

As the geometry characterisation procedure has already been described in previous section, this section continues with the mechanical test procedures. The results of measurements to the specimen's geometry are used to make preliminary calculations so failure loads can be predicted. This is necessary to be able to choose appropriate measurement equipment. The test set-up will be designed according these values in order to successfully perform tests.

Figure 3.25 provides an overview of executed mechanical tests for which the adopted test methodology is described in this section. The methodology for four-point bending, buckling, compression and tensile tests will be stated in sections 3.4.1, 3.4.2, 3.4.3 and 3.4.4 respectively. At last it will be explained how the hardness values are obtained in section 3.4.5.

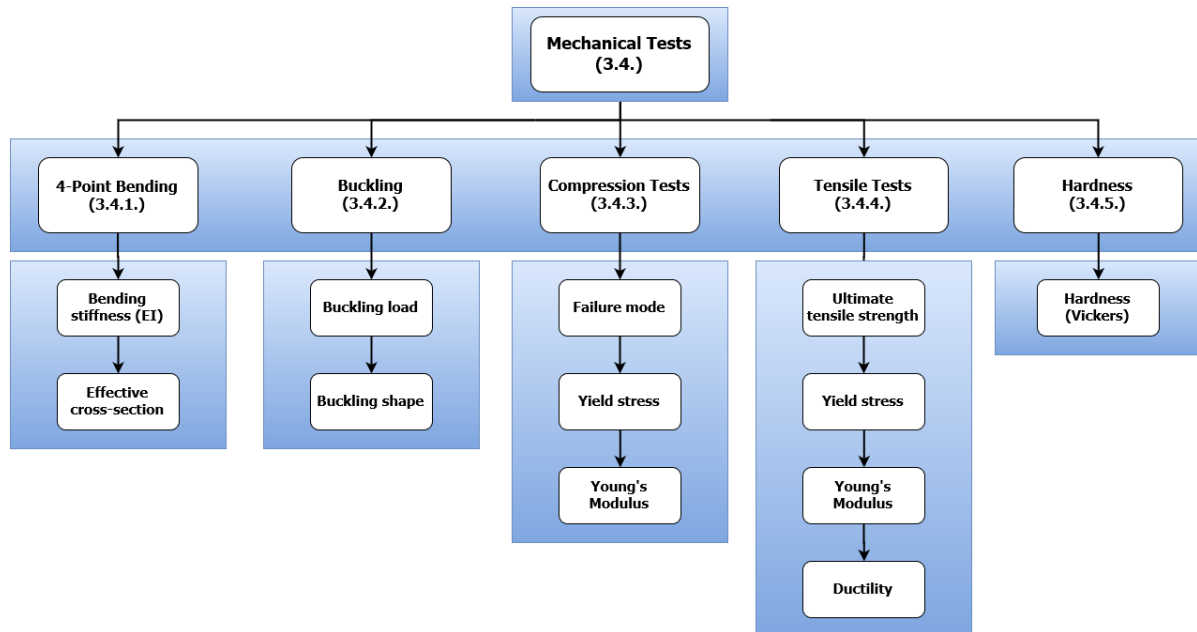


Figure 3.25: Outline section 3.4: Mechanical Tests

3.4.1. Bending Tests

To determine the columns their bending stiffness EI , four-point flexural tests were performed on unmachined column specimens. Distinctively from a three-point bending test, this test is characterised by the much larger part of the specimen in which the maximum stress is present. For both printing strategies (continuous and dotted), three columns have been tested. First, the specimens were sawn to a length of approximately 650 mm so they exactly fit in the test set-up. Since they were cut from the same columns which were also used to perform buckling tests on, they have approximately similar cross-sections. An overview of test specimens with corresponding dimensions is shown in table 3.2.

Table 3.2: Overview four-point bending test specimens

Test	Label	Amount	Length L [mm]	Diameter D_{mean} [mm]	Thickness t_{avg} [mm]
Bending	B-X-A	3	650	30.1	3.7
	B-X-B	3	650	30.1	3.2

Printing specimens is costly and time consuming. Consequently only a limited amount of specimens are available and multiple tests need to be performed on the same column specimens. This test aims to analyse the elastic bending stiffness. To be able to reuse bending specimens for buckling tests, it needs to be assured of that the applied loads are sufficiently low and do not introduce (local) yielding.

Before testing, a calculation is made using (3.1) to predict the elastic bending moment capacity $M_{el,Rd}$. Where $W_{el,min}$ is the minimum elastic section modulus which depends on the column its cross-sectional properties. Because of the geometrical variations, an average value for cross-sectional area A_μ has been introduced in this calculation. How this value is determined is described in section 3.3. For yield strength f_y a value of 350 N/mm² is assumed, as provided in the datasheet of the welding wire supplier [47]. Both assumed values require verification by additional tests and measurements. From the bending capacity it is derived that the maximum applied load P should not exceed 9.8 and 8.6 kN for dot and continuously printed specimens respectively. The latter (lower) value for continuously printed specimens is explained by their slightly smaller cross-section. As a conservative measure, the maximum test load has been set to 4 kN for dot-printed specimens and 3 kN for continuously printed specimens.

$$M_{el,Rd} = W_{el,min} f_y \quad (3.1)$$

Similar to the buckling tests, all bending tests are performed at the Stevin II-laboratory. A Schenck hydraulic driven machine has been used with a maximum load capacity of 250 kN. Its hydraulic driven ramp pushes the frame with the specimen upwards against the fixed upper frame, resulting in a force exerted to the specimen. The specimen itself rests on a steel frame with a span l of 602 mm. Figure 3.26 shows its simplified mechanical scheme.

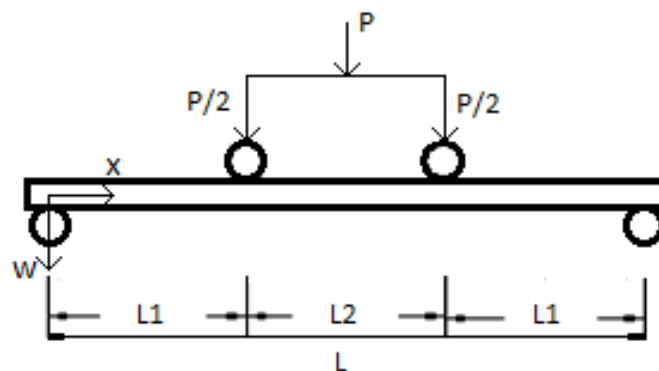


Figure 3.26: Mechanical scheme four-point bending test with $L_1 = 168.5$ mm; $L_2 = 265$ mm; $L = 602$ mm

The test is displacement driven, using a prescribed ramp speed of 0.02 mm/s both at loading, and unloading. During the test, the applied load has been recorded and the midspan deflection has been measured by laser. The rough surface of the specimen results in an unclear measurement of the laser. Therefore a timber cube with a hole of the size of the specimen its outer diameter has been mounted on the printed specimen at the location of the laser measurement. As shown in figure 3.27, the cube is covered by cardboard to ensure a smooth measurement surface.

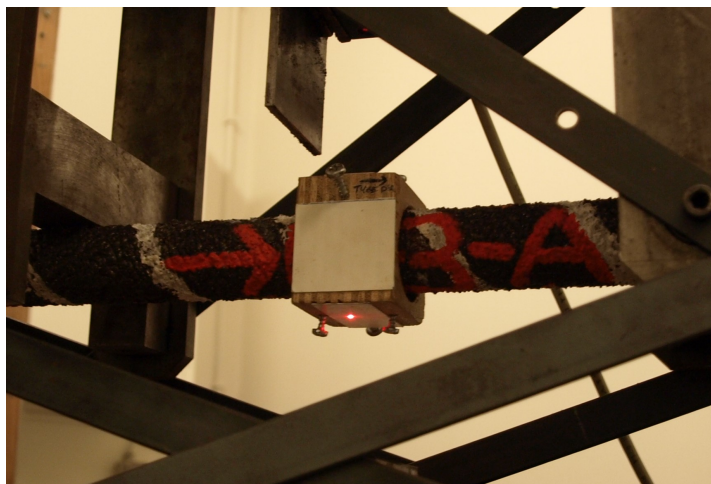


Figure 3.27: Timber cube with cardboard cover to create a smooth measurement surface

The output of the test should be a linear load-displacement curve, where the displacement is given by the deflection of the column at midspan. The bending stiffness is obtained from the tangent to the descending branch (unloading stage) of the load-displacement curve. Adopting a mathematical derivation of the deflection at midspan using the mechanical scheme from figure 3.26, the deflection at midspan $w(\frac{L}{2})$ is given by (3.2).

$$w\left(\frac{L}{2}\right) = \frac{PL^2L_1\left(3 - 4\frac{L_1^2}{L^2}\right)}{48EI} \quad (3.2)$$

Where P is the applied load. Hence the bending stiffness can be obtained by inserting the tangent value from the test and by solving for EI with simple algebra (3.3).

$$\frac{P}{w\left(\frac{L}{2}\right)} = \frac{48EI}{L^2L_1\left(3 - 4\frac{L_1^2}{L^2}\right)} \rightarrow EI = \frac{P}{w\left(\frac{L}{2}\right)} \frac{L^2L_1\left(3 - 4\frac{L_1^2}{L^2}\right)}{48} \quad (3.3)$$

Before the actual tests have been initiated, calibration tests on 'common' round steel (diameter $D = 20$ mm; $E = 210$ GPa) and cold-drawn steel oil pipes (identical pipes as the ones used for buckling calibration tests) were performed. Unlike additively manufactured specimens, their cross-sectional variations are very much limited (allowing to consider it as homogeneous), and their material properties as yield strength and Young's moduli are known. Consequently, their bending stiffness can be predicted by analytical means and the outcome can be compared with the test results.

Significant difference between both values might indicate flaws in the test set-up; implicating that adjustments are necessary. As can be seen in figure 3.28 a small steel plate has been welded to the specimen to create a larger area to point the laser at. It is thereby assured of that only the deflection is measured and not the rounding of the specimen. Hence a more accurate deflection measurement is achieved.



Figure 3.28: Round steel (20 mm) calibration specimen with welded plate to enable deflection measurement

During the calibration tests also the bearings were adjusted. At first handmade Azobé D70 timber parts with half a cylinder shaped holes were used to prevent lateral movement of the column during loading at the location of the supports. The column fits perfectly as shown in figure 3.29. Initial tests showed however that these supports cause a substantial increase in vertical displacements. Apparently these hardwood bearings are not sufficiently stiff to resist the resultant vertical forces exerted by the specimens.

The timber bearings have therefore been removed for the final test runs, so that the specimens are directly supported by the steel frame of the test set-up. Simple timber pieces are used on both sides of the column to prevent lateral movement by clamping the specimens in the U-shaped hinged steel bearings. In this way, the vertically exerted forces are carried directly by the steel frame as depicted in figure 3.30.

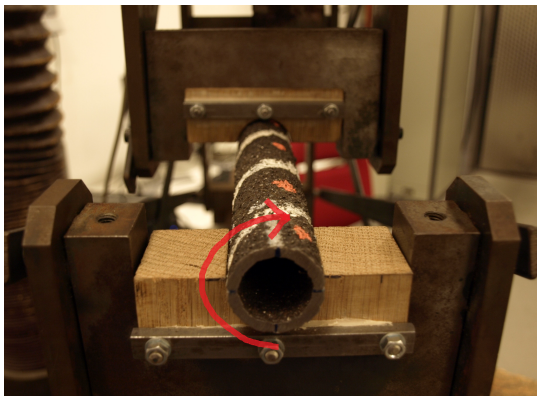


Figure 3.29: Timber bearings for lateral support of specimen

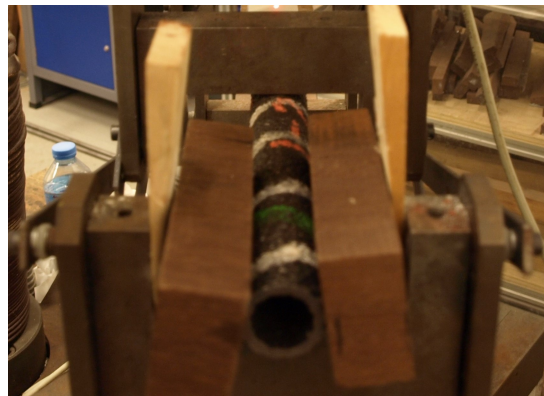


Figure 3.30: Specimen directly on steel frame with lateral support

All six specimens have been tested at least four times. After every test, the column is rotated 90 degrees around its longitudinal axis (as indicated by the red arrow) and tested once again. This has been done to monitor possible bending resistance variations due to cross-sectional variations around the perimeter of the column. An overview of bending test results is given in 4.2.1 and all test data is collected in appendix C.2.1.

3.4.2. Buckling Tests

One of the main objectives of this research is to construct a buckling curve. Therefore columns with varying (relative) slenderness ratios λ_{rel} are tested. Geometrical deviations are neglected while calculating the section properties I and A . Considering a homogeneous cross-section as derived from fluid measurements (section 3.3.3), theoretical buckling lengths are calculated using the Eurocode 3 equations stated in section 2.4. Only theoretical values of material properties are known. Making assumptions for the yield strength f_y (here designated as proof stress $\sigma_{0.2}$) and Young's modulus $E_{0.2}$ is therefore inevitable. According to Oerlikon's product sheet of stainless steel grade inertfil 308LSi (EN1.4316), the yield strength equals 350 N/mm². In addition, Eurocode 3²⁵ prescribes a Young's modulus value for austenitic and austenitic-ferritic steels of 200000 N/mm² [48].

Table 3.3 presents an overview of the chosen buckling test specimen lengths (ranging from an average of 480 to 1250 mm) and its corresponding approximated slenderness ratios. Aforementioned assumptions of material properties require verification since they are directly related to the slenderness ratio. This is done by performing bending and tensile tests on printed specimens as explained in section 3.4.1 and 3.4.4.

Table 3.3: Overview buckling test specimens

Label	Amount	Length L [mm]	Diameter D [mm]	Thickness t_{avg} [mm]	Rel.slend. λ_{rel} [-]
A-48-X	3	480	30.1	3.7	0.65
B-X-A ²⁶	3	650	30.1	3.7	0.81
B-X-B ²⁶	3	650	30.1	3.2	0.81
A-85-X	3	850	30.1	3.7	1.1
A-125-X	3	1250	30.1	3.7	1.6



Figure 3.31: Buckling specimens with a length of 1250 mm including orange marks to depict the expected buckling direction

²⁵NEN-EN 1993-1-4:2006 table 2.1.3.

²⁶Dot-and continuously-printed specimens used for four-point bending tests are reused for buckling tests

The longest column specimens are depicted in figure 3.31. From measurements on geometry the out-of-straightness is determined and where these maximum eccentricities are located. From that analysis, the expected buckling direction is derived and marked on the specimen so that it can be correctly placed in the test set-up; meaning that the expected buckling direction coincides with the tensile wires that measure the lateral deflection. Despite the thorough analysis of geometrical imperfections, it can not be fully ensured that the specimens actually buckle in the expected direction. The cross-section is assumed to be symmetrical. This implies the need for bearings that allow rotation in every direction.

Test Set-Up

Special measures have been taken to allow free rotation in every direction by using spherical plain bearings at both column-ends. Whereas a clamped (fixed) boundary condition might reduce the complexity of the test set-up, this also implies that the specimen's effective buckling length halves. In order to draw a buckling curve over a certain slenderness range, sufficient slender (and thus long) columns are required. Because printing (multiple) long specimens is time-consuming and less practical to transport, it was desirable to reduce the column lengths as much as possible. Bearings that allow free rotation are thus a prerequisite for this buckling test set-up.

Several options of rotational bearings were considered. Figure 3.32 depicts the spherical plain bearing (GE30AW) that was proposed and tested first. This bearing allows rotation in every direction and is placed on top of the pressure box that measures the force exerted on the specimen. On top of the bearing a custom-made cylinder is placed (and fixed with glue) so that the tubular columns fits in, preventing undesired lateral movement during loading as shown in figure 3.33. After accurate centric positioning of the specimen, screws are tightened to prevent lateral movement of the column even more. This allows transfer of forces from the specimen to the spherical plain bearing.



Figure 3.32: First test: spherical plain bearing



Figure 3.33: Cylinder on top of bearing

When assuming a frictionless rotational bearing, the effective buckling length L_{cr} is equal to the system length: that is the distance between the rotation points of both spherical plain bearings which corresponds approximately with the actual specimen length L ($K = 1$). It should however be taken into account that friction unquestionably will prevent free rotation of the bearings.

Hence the actual effective buckling length should be derived from additional tests. Using specimens with known cross-section, imperfections and mechanical properties, in this case cold-drawn thick-walled steel tubes with an outer diameter of 30 mm and wall thickness $t = 4.0$ mm, buckling tests have been performed parallel to the tests on printed columns as shown in figure 3.41. This test procedure is repeated after every change in the test-set up. With known properties of the cold-drawn tubes it is possible to predict the buckling failure load according to existing buckling curves of Eurocode 3 [56].

Despite all aforementioned measures (such as greasing spherical plain bearings) to reduce friction of bearings under loading, multiple buckling tests on cold-drawn tubes resulted in buckling loads well-exceeding the expected values for a test set-up with freely rotating bearings. Considering the known mechanical properties of the tube, these high buckling loads are a clear prove that this test set-up does not allow for free rotation of the column-ends. This can be caused by friction in the spherical bearings itself, or by the specimen not being capable of transferring the axial loads to the spherical plain bearings properly.

Since this is undesired, different bearings are adopted for the remaining tests. As depicted in figure 3.34, ball bearings are used that fit in the earlier tested cylinders. Because locally large forces are expected to be present while transferring the load from the ball to the cylinder, the cylinder bottom is reinforced with thick steel plates to prevent the ball from pushing in.

Before testing, both column-ends are carefully sawn perpendicular to the column its longitudinal axis and the edges of the inner diameter are smoothed to ensure concentric load introduction. The difference is clearly visible in figure 3.35. In addition, special measures have been taken to prevent the ball bearing from pushing in the column. This risk is especially present for the short columns where high buckling loads are expected. Therefore large bolts with an inner diameter similar to the outer diameter of the column are used as reinforcement of both column-ends as depicted in figure 3.37.



Figure 3.34: Ball bearings as they are used for buckling tests



Figure 3.35: Column-ends sawn and smoothed

All buckling tests are performed in the Stevin II-laboratory at the Civil Engineering faculty of Delft University of Technology using a test rig with its own manually operating hydraulic jack. However, its maximum capacity of 5000 kN is well-exceeding the expected buckling load of 30 kN for the most slender columns. Above all it is hard to apply this force slowly and in a controllable way using this high-capacity manual-operated jack. Therefore it is chosen to use a hand-operated pump and to use the test rig only as frame to build the test set-up. Figure 3.41 and 3.42 shows the entire test set-up.

The force is being applied by a 'Lukas 8L' manually operated hand pump (figure 3.36) capable of slowly exerting sufficient force on the specimen to let it buckle according to predictive calculations. As can be seen in figure 3.38, the force is recorded by a pressure box with a capacity of 100 kN. Vertical displacements are measured by a linear variable differential transformer (LVDT).

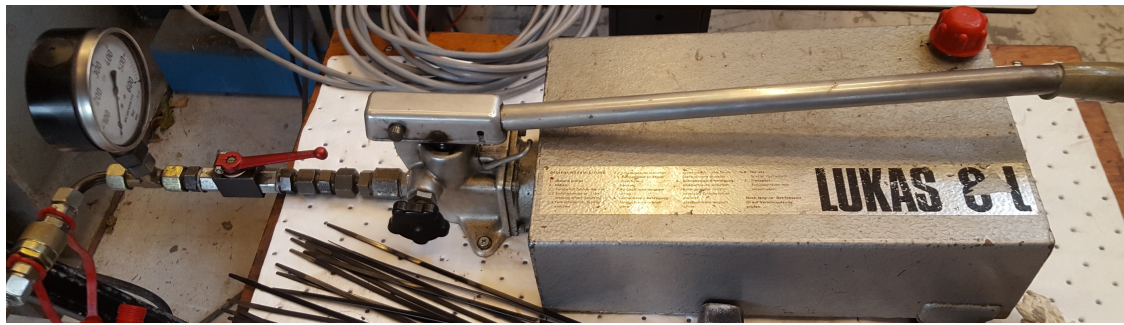


Figure 3.36: Manually operated hand pump applied to exert force on the columns



Figure 3.37: Column-end reinforcement with a bolt



Figure 3.38: Pump, pressure box and displ. measurement

For the measurement of lateral displacements, multiple options have been explored. One of the options was a laser. A laser is in this case however not capable of performing accurate measurements because of the surface roughness of the printed columns. In addition it would measure the roundness of the column, instead of 'real' displacements. The difficulty lies in the fact that the specimens are tubular and therefore have no preferential buckling direction.

Despite the analysis of initial curvature from which an expected buckling direction is determined, it cannot be guaranteed that the specimen will indeed buckle in that direction. For that reason it is chosen to measure lateral deflections with linear displacement sensors in two principle directions as depicted in figure 3.40. The sensors with a measuring range of 50 mm are mounted on a timber frame and connected with little hooks and a circular metal strip to the specimen. A total of 6 sensors are used, at three different heights: at a quarter, a half, and at three quarters of the specimen height, see figure 3.39. Because at every height two sensors measure perpendicularly to each other, they are capable of measuring every movement regardless the direction. Besides monitoring of the buckling behaviour of printed columns, this also allows for an analysis of the buckling shape.



Figure 3.39: Location of linear displacement sensors

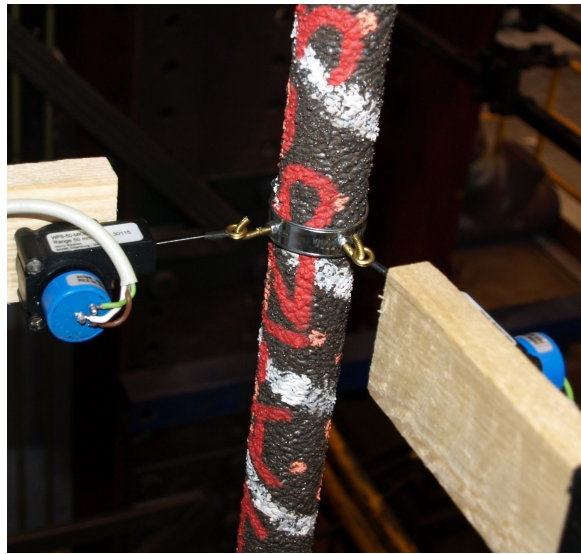


Figure 3.40: Displacement measurement in two directions



Figure 3.41: Buckling test on a cold-drawn tube



Figure 3.42: Buckling test on a printed column

Before the test begins, accurate centric placement of the specimen is ensured by using a laser from bottom to the top bearing. After placement in the test set-up, the specimen's vertical position is checked with a (spirit) level. During the test special care was taken to apply the load slowly with consistent pace, while at the same time the lateral deflections are carefully monitored. Since buckling is characterised by a sudden sideways deflection and the maximum deflection is expected halfway the column's height, the sensors mounted at this point are critical. The displacement sensors only have a measuring range of 50 mm, meaning 25 mm extension and 25 mm contraction. It is therefore crucial to stop the test way before the lateral deflections exceed this value, in this way preventing breaking the sensors.

The test results are presented in section 4.2.2 and further analysis is provided in section 5.3. In this section is also explained how the effective buckling length of the test set-up has been derived.

3.4.3. Compression Tests

Because of the cross-sectional variations of the printed specimens, it is not possible to derive the Young's moduli from bending tests only. Without additional analysis of the inside of the columns, the distinction of Young's modulus E and second moment of area I from the tested bending stiffness EI is simply not possible to make. Therefore additional tensile or compression tests on milled specimens has been proposed to derive yield strengths and Young's moduli. At first the feasibility of compression testing of such samples have been checked. This is done by studying the failure mode that will occur during loading. Since the specimens are relatively thin-walled, the risk of local buckling is present, consequently disturbing an accurate stiffness and yield-strength measurement.

Prerequisite for the specimens that are used in this test is a well-defined cross-sectional area on which the force is being exerted. This is a complex task since both the in- and outside of the column specimen's surface is irregular. Using a metalworking lathe, a column sample of 50 mm length from both dot-by-dot and continuously printed steel has been milled to an average outer diameter of 32.9 mm and a wall thickness of 2.7 and 2.0 mm respectively. They are shown in figure 3.43 and 3.44. The geometry of the specimens is measured making use of an electronic Vernier's caliper at multiple locations across the perimeter, inner diameter and height.



Figure 3.43: Milled dot-printed compression specimen



Figure 3.44: Milled continuously printed compression specimen

Steel plate bearings transfer the compression force applied by the Schenck 600 kN dynamic test machine onto the specimen as shown in figure 3.45. For this feasibility test no strain gauges are used, only the (cylinder) displacement of the machine has been measured. The test is displacement-controlled. Three different cylinder speeds are used during testing: 0.01 mm/s (elastic stage and plastification); 0.02 mm/s (continuing strengthening); 0.05 mm/s (declining phase). An overview of compression test results is given in section 4.2.3.



Figure 3.45: Compression test set-up

3.4.4. Tensile Tests

OCAS performed tensile tests on by MX3D printed Ugitech 308LM stainless steel specimens. Despite some minor differences in chemical composition, Ugitech's datasheet [90] proves that its welding wire complies with the same standards as Oerlikon's 308LSi stainless steel: AWS-SFA 5.9: ER 308LSi, EN ISO 14343-A: 19.9LSi and corresponding material number (EN)1.4316.

Stress-strain behaviour is affected by strain-rate. Stainless steels tend to be more sensitive to a change in testing rate than carbon steels. Generally an increase in strain rate leads to higher ultimate strengths and lower ductility [31]. Therefore the usual precautions and requirements for tensile test procedures and results evaluation are taken conform ISO 6892-1:2016.

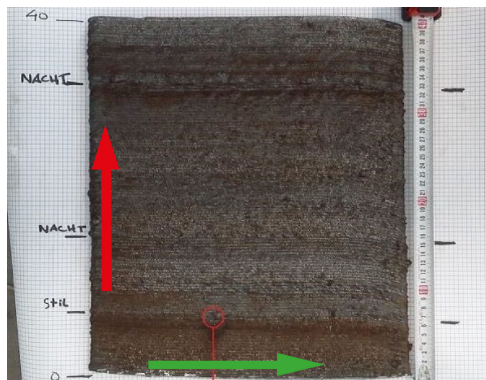


Figure 3.46: Dot-printed plate from which the tensile specimens are milled

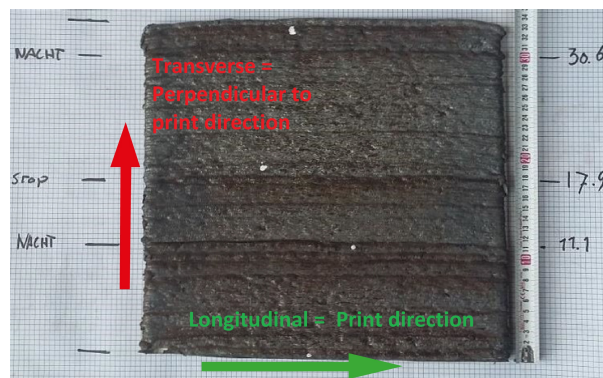


Figure 3.47: Continuous-printed plate from which the tensile specimens are milled

Figure 3.46 and 3.47 depict both the dot- and continuously printed plate elements (produced in september 2016) from which the tensile specimens are sawn and milled with A50 specimen geometry (see figure 3.48). Samples in both longitudinal (printing direction as marked with a green arrow) and transversal direction (perpendicular to printing direction as marked with a red arrow) are tested. Clearly visible are the dark horizontal lines representing overnight cooled print-layers. These layers are intentionally left in the specimen to check possible reduction in tensile strength due to overnight cooling. Furthermore a defect (marked in red) in the dot-printed specimen due to burn-in was observed. Unfortunately the specimen was already milled before observing this defect what makes it impossible to trace back these positions on the test samples.



Figure 3.48: Milled tensile test specimens with A50-geometry



Figure 3.49: Zwick/Roell Z250 tensile test machine

Tensile tests are performed with a Zwick Z250 tensile test machine as shown figure 3.49) according to standard NEN-EN ISO 6892-1 method A1-(closed-loop strain control). Up to the yield point, the test speed was $0.00025 \frac{1}{s}$, where for higher strains the speed was increased to $0.0067 \frac{1}{s}$. During the test the applied force was measured and the strains were measured using extensometers accordingly. From the resulting stress-strain relation the 0.2%-proof stress and Young's moduli can be derived and differences between longitudinally and transversally tested specimens analysed accordingly. The results are presented in section 4.2.4.

3.4.5. Hardness

The hardness of a material is a measure of its resistance to plastic deformation. During a hardness test a loaded indenter is forced to penetrate the surface of the metal. Different hardness tests are developed such as Knoop, Rockwell, Brinell and Vickers tests. Common static testing methods of indentation hardness differ in the shape of the indenter which is forced into the metal. Whereas the Brinell test uses a hardened steel ball, the Vickers test uses a square-based diamond pyramid with an included angle of 136° . The Vickers test is the most advanced method described in European standards. In addition, the department of Materials Science and Engineering at Delft University of Technology is well-equipped with (micro)hardness test equipment as shown in figure 3.50 and 3.51.

Hardness of a metal depends on ductility, elastic stiffness, plasticity, strain strength, toughness and viscoelasticity and is in general roughly proportional to the strength of a material. The correlation of hardness values with other measures of resistance to deformation such as yield or tensile strength exists but this relationship is complex and can only be obtained experimentally. A common engineering rule of thumb is that the tensile strength in N/mm^2 is approximately equal to three times the Vickers hardness.

During hardness testing, a minimum spacing distance should be taken into account between the indentations. Also the distance from the indentation to the edge of the specimen must be taken into account to avoid interaction between the work-hardened regions and to avoid edge effects. Where as depicted in table 3.4 the minimum distances slightly differ in ISO 6507-1 and ASTM E384 standards, the ISO-standards have been followed in this hardness analysis.



Figure 3.50: Struers Durascan G5 Hardness tester

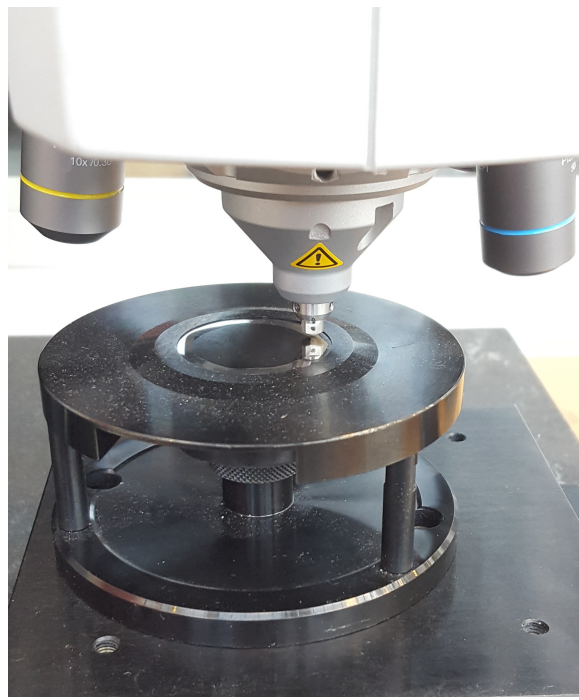


Figure 3.51: Hardness indentation of a column section

Table 3.4: Standards for minimum spacing distance between indentations

Standard	Distance between indentations	Distance from the center of the indentation to the edge of the specimen
ISO 6507-1	> 3·d for steel and copper alloys and > 6·d for light metals	2.5·d for steel and copper alloys and > 3·d for light metals
ASTM E384	2.5·d	2.5·d

The hardness tests are performed on the specimens that were already prepared for metallographic analysis. These include both continuously and dot-by-dot printed specimens and longitudinal and transversal column sections so that hardness differences between samples of different printing strategy and different areas of the cross-section can be studied. Special attention will be paid to hardness variations between the in- and outside of the column walls due to different cooling conditions. Moreover they will be compared with the hardness values obtained by OCAS as explained in section 3.6.2.

For the tests a Struers Durascan G5 automatic microhardness test machine has been used, whereas the indentations are chosen in a line from the in- to the outside of the column wall taking into account the minimum spacing. A load of 3 kgf is applied corresponding with the HV3 hardness scale. After a successful indentation the machine automatically measures the diagonals and converts this to the Vickers hardness scale. The results are presented in section 4.2.5 and appendix C.2.4.

3.5. Metallography: Tubular Columns

In addition to the mechanical characteristics, the microstructural composition of printed column specimens is investigated by metallography. At first the grain formation and orientation will be examined by means of digital microscopy. Special attention will be paid to the subsequent weld deposits and signs of column grain formation which could indicate anisotropic behaviour. Both longitudinal as transversal sections will be analysed of dot-by-dot and continuous printed specimens so they can be compared.

Secondly a study to pores, inclusions and other impurities has been performed using electron microscopy. By these means it can be investigated whether they are harmful to the mechanical or corrosion resistance. Finally x-ray diffraction has been used to identify phases and possible harmful precipitations at the grain boundaries.

The metallographic specimens were both prepared and examined in the Material Science & Engineering-laboratory of Delft University of Technology. Metallographic samples are prepared conform to specification ASTM E3-01:2007. First of all, areas of interest have been identified and sawn from the tubular column specimens. Longitudinal (figure 3.52) and transversal sections (figure 3.53) for both dot-by-dot and continuously printed columns have been selected and prepared. Longitudinal sections can reveal the successive layers and the grain structure in the direction of the thermal gradient, while from transversal sections the quality of fusion between the depositions in the other direction can be studied. Furthermore microstructural differences between dot-by-dot and continuously printed specimens can be analysed.

Several processing steps are required to prepare the specimen for microscopic observations. Regarding sectioning one should be aware that due to faulty sawing conditions severe surface damage and acute thermal damage could arise, consequently causing changes in microstructural. As a result metallographic characterisation could be compromised. This is prevented by using an abrasive silicon carbide cut-off wheel, a low cutting speed, low load and a liquid coolant to avoid overheating.

The sections were subsequently mounted in cold-setting epoxy resin using a mounting press with an applied force of 25 kN. Next step involves manually grinding of the specimen with rotating discs using abrasive silicon carbide paper. In steps the coarseness of the abrasive is decreased from 200 to 20 micron. The specimen is even more smoothed by polishing with a loose abrasive in two steps from 3 to 1 microns. Lastly the specimen is cleaned using ethanol and an ultrasonic bath and ethanol.

If the surface of the metallographic specimen is proven to be sufficiently smooth, it is ready to be chemically etched. By the chemical reaction of the etchant with the metal, the material reveals its microstructural characteristics even further. The suitability of an etchant is largely depending on the chemical composition of the specimen and the type of microstructural analysis.

At first a common etchant for austenitic stainless steels, Kalling no.2 is used. This solution contains cupric chloride (12 grams), hydrochloric acid (20 ml) and alcohol (225 ml). However, experience of Joosten [5] showed that a specifically produced etchant led to the best results on his printed 308L stainless steel specimens. By applying both etchants on printed column specimens this is confirmed, hence this etchant was utilized. The etchant is made by mixing water (10 ml), hydrochloric acid (27%) and hydrogen peroxide (30%). Immersion for approximately five seconds in the etchant fluid proved to give the best results.



Figure 3.52: Longitudinal section prepared for micrography



Figure 3.53: Transversal section prepared for micrography

Micrography

After completion of the etching process, the sections were studied through an optical microscope as depicted in figure 3.54. Several magnifications were used to locate the areas of interest, such as impurities, and pores. These areas are subsequently photographed and saved for further analysis by electron microscopy.



Figure 3.54: Optical microscope during analysis of a specimen

Additionally composite images are made by stitching overlapping photographs using the microscope depicted in figure 3.55. From the obtained high resolution images a good overview of the overall grain structure of multiple deposition layers is obtained.



Figure 3.55: Microscope used to acquire composite images of the microstructure

Scanning Electron Microscopy (SEM)

Now areas of interest on the metallographic specimens have been selected, they can be further analysed by using an electron microscope. A scanning electron microscope (SEM) uses a focused beam of high-energy electrons as visualized in figure 3.56 and 3.57. The signals derived from electron-metal interactions reveals information about the specimen; external morphology, chemical composition and crystalline structure [91]. Besides making images with a magnification up to 30000x, a SEM is also capable of performing an analysis to specific locations pinpointed on the sample. Using energy-dispersive x-ray spectroscopy (EDS) a quantitative chemical composition can be made of the chemical composition of the selected points of interest. In this way impurities and possible undesired oxide inclusions can be detected and analysed.

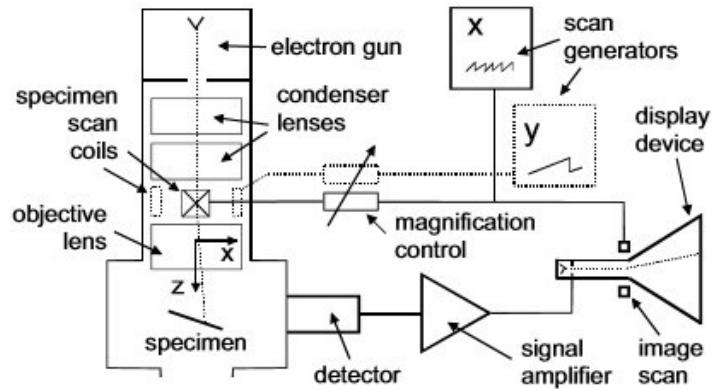


Figure 3.56: Working mechanism of an scanning electron microscope [91]

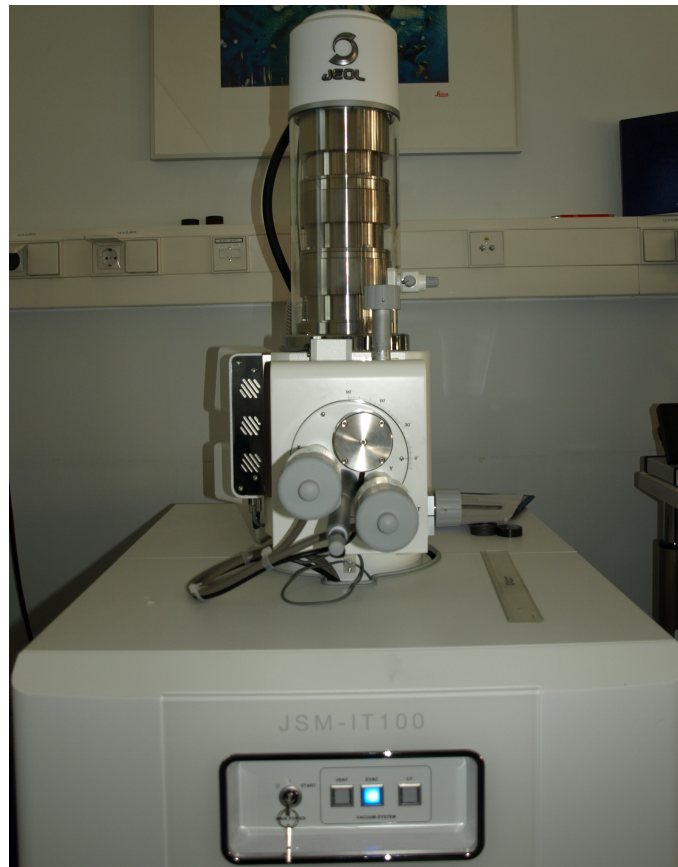


Figure 3.57: Scanning electron microscope as utilised for the metallographic analysis

X-Ray Diffraction (XRD)

An x-ray diffractometer can be used to detect precipitates, such as undesired chromium carbide, and for phase identification. The various phases present in a specimen can be distinguished if they have different crystal lattice structures. In this way it can be investigated whether the sample attains a fully austenitic or duplex, i.e. austenitic-ferritic structure.

At the x-ray facility in the faculty of Material Science & Engineering a metallographic specimen has been analysed. This sample was intentionally made larger in order to have sufficient surface area to detect precipitates. The Bruker D8 Advanced diffractometer utilised is shown in figure 3.58.

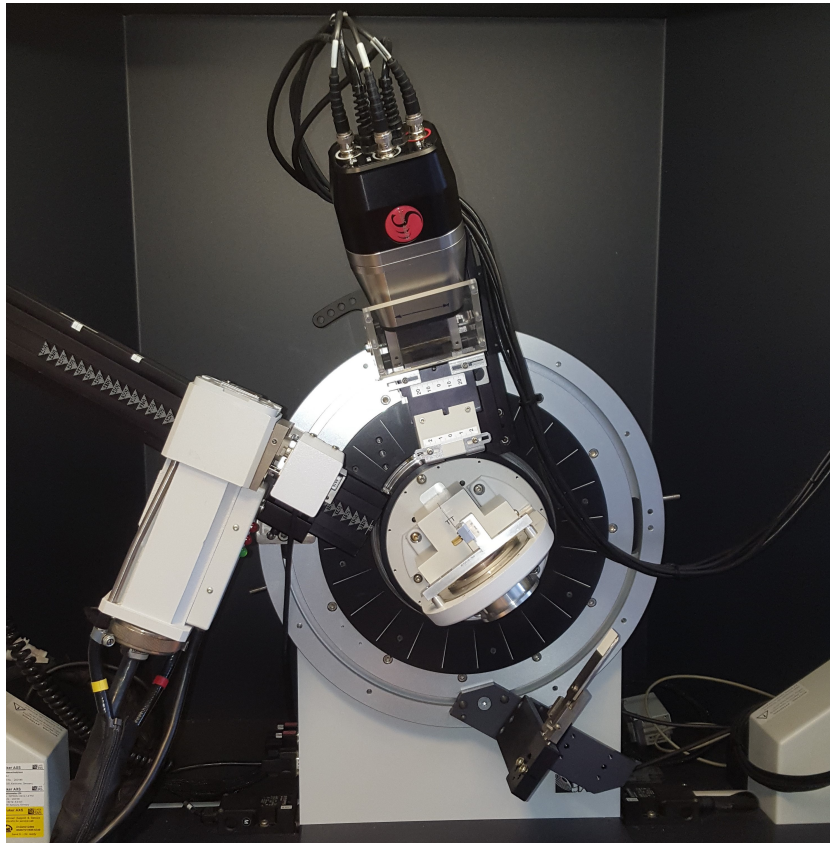


Figure 3.58: Bruker D8 Advance diffractometer used for XRD-measurements

A selection of the relevant obtained results from the analysis of metallographic specimens is presented in section 4.4.1.

3.6. Metallographic & Mechanical Tests: Plate Material (OCAS)

The following tests are performed by OCAS on plate material. The specimens are acquired from plate material that is also used to extract tensile test specimens from. These plates are shown in figure 3.47 and 3.46. Additional tests on column samples are required to verify the validity of the results for columns, but as the printing technique and material is (nearly) identical, test results are a good reference and might provide good insight of material characteristics.

3.6.1. Metallography

This section describes shortly what has been analysed by OCAS. Micrographic observations are performed to analyse solidification, microstructure and grain size. The transition between two layers of deposited metal is observed after nitro hydrochloric acid etching. Furthermore the internal cleanliness is checked using optical microscopy in accordance with standard ASTM E45-D. More specifically, a chemical characterization has been made of inclusions and cracks by Energy-Dispersive X-ray Spectroscopy (EDS) and using SEM.

3.6.2. Hardness

To quantify hardness of the specimens, Brinell hardness measurements are executed on the Charpy-samples conform standard EN ISO 6506-1. This test characterises hardness by the scale of penetration of an indenter. Just as Vickers hardness measurements, but in this case a tungsten carbide ball with a diameter of 2.5 mm is used.

The Brinell Hardness Number (*BHN*) is commonly expressed as *HBW*. Where *H* stands for Hardness, *B* for Brinell and *W* represents the material of the indenter (tungsten wolfram carbide). The *HBW*, expressed in N/mm^2 , is calculated by equation (3.4).

$$HBW = 0.102 \frac{2F}{\pi D(D - \sqrt{D^2 - d^2})} \quad (3.4)$$

Where *F* equals the applied force; *D* the diameter of the indenter and *d* the diameter of indentation both in mm. During this test the applied force was equal to 1839 N (= 187.5 kg) with an indentation time of 12 seconds. Since Brinell hardness measurements correlate quite closely with Vickers hardness measurements as performed on the column sections, the values can be compared. The results are presented in section 4.2.5.

3.6.3. Toughness

Toughness is can be defined as the ability of a material to absorb energy and deform plastically before fracturing. Toughness is in general proportional to the area under the stress-strain curve from the origin to its breaking point. Austenitic steels do not fail by cleavage. Precipitates might however weaken grain boundaries, allowing cleavage cracks propagate along these boundaries.

To quantify the resistance to brittle failure, Charpy pendulum impact tests (ISO 148-1) are performed on standard notched samples of 10 mm as depicted in figure 3.59. The samples are extracted from printed 308LSi plate material identical to the material that is used for tensile tests. Samples in both transverse and longitudinal direction, as well for both printing strategies (dot and continuous) have been tested. They are milled and shaped by Electric Discharge Machining (EDM). Tests are performed at three temperatures, namely -40; -20 and +20 °C. The results are presented in section 4.4.3.

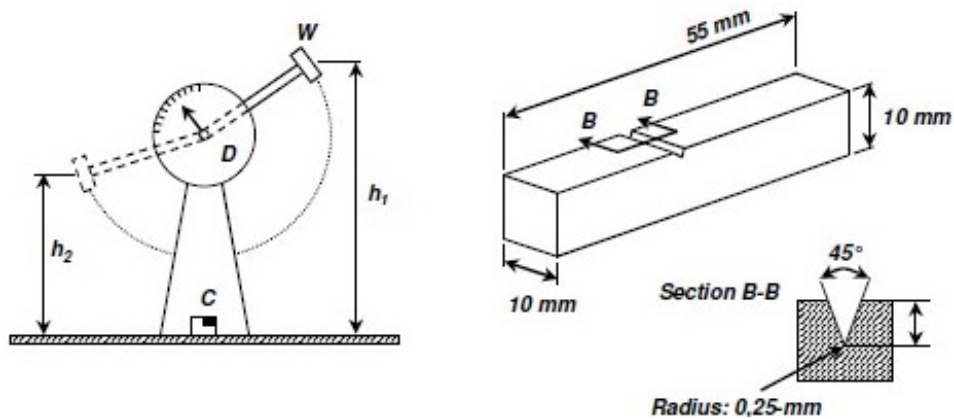
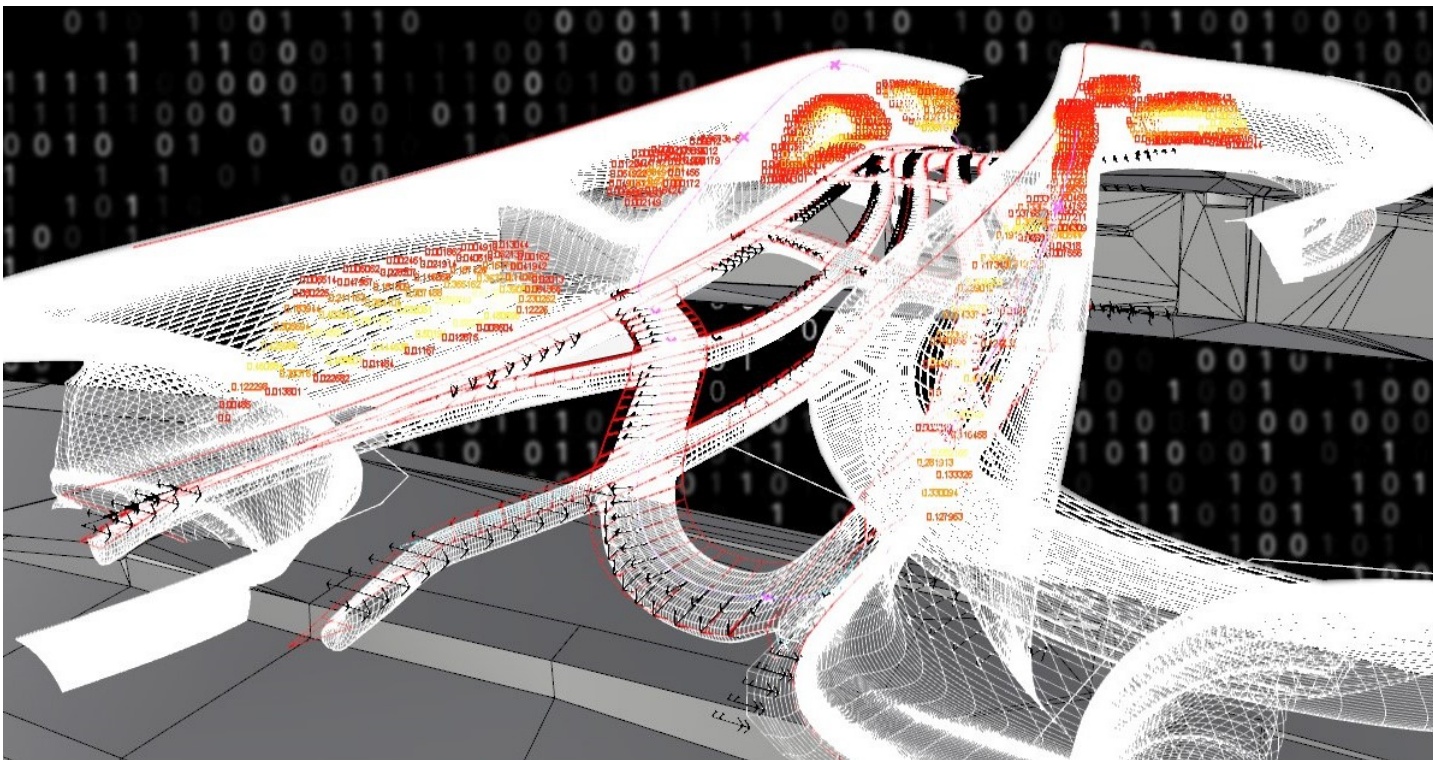


Figure 3.59: ISO 148-1 Charpy pendulum impact test set-up and specimen

4

Results



As a logical follow-up to chapter 3 where the test and measurement methodology has been described, this chapter presents the obtained test results. At first the results of measurements to the specimen's geometry will be discussed in section 4.1. Section 4.2 subsequently provides an overview of bending, buckling, compression, tensile and hardness test results. Next, the results of metallography of printed columns is given (section 4.3), followed by the results of metallography, hardness and toughness tests on printed plate specimens (section 4.4), as provided by research institute OCAS.

4.1. Geometry Measurement Results

Before the results of mechanical tests will be discussed, first the characterisation of the printed tubular column geometry will be presented. The results of the measurements to imperfections acquired by hand measurements and 3D-scan analyses are provided in section 4.1.1. Finally an average cross-sectional area is deducted as summarised in section 4.1.2

4.1.1. 3D-Scans & Hand Measurements (Initial Imperfections)

By means of hand measurements and 3D-scans the initial curvature of the buckling specimens has been determined. An overview of the results is given in table 4.1. For specimens of 480 mm and shorter, the global initial curvature was negligible compared to the observed local surface irregularities. Therefore only the longest columns have been added to the results.

Table 4.1: Initial curvature obtained from hand measurements and 3D-scan analysis

Specimen	Hand Measurements		3D-Scans	
	e_0	St.dev. σ (%)	e_0	St.dev. σ (%)
A-125-X	L/593	L/25	L/588	L/12
A-85-X	L/604	L/97	L/623	L/19
B-X-A	L/707	L/43	L/688	L/7
B-X-B	L/791	L/32	-	-
<i>Average</i>	L/674	L/49	L633	L/13

The initial curvature is expressed in ratio eccentricity over the length of the considered member. The shorter the column, the smaller the observed initial curvature. This is probably down to the length effect; the smaller the specimen length, the less likely a print error is present which might result in a geometrical imperfection. The total average value obtained from hand measurements is $e_0 = L/674$ with a standard deviation of L/49. Whereas 3D-scans were more reproducible, they gave more consistent results with an average value of $e_0 = L/633$ and a fairly low standard deviation of L/13. From both analyses it can be concluded that the initial curvature of printed specimens is larger than those of the buckling columns tested in EC3, where a conservative imperfection of $e_0 = L/1000$ is assumed for buckling calculations.

From the 3D-scan analysis it can be concluded that the eccentricities are partly explained by local imperfections 'shifts' (1 - 1.5 mm), rather than by a parabolic-shaped global curvature (see figure 4.1). Such shifting of successive layers is caused by welding errors. These damage parts are in some cases manually grinded off the specimen, often not with a perfectly straight cut. Grinding is done manually and often not perfect perpendicular. It very much complicates print restarts and causes shifts (misalignments) in the column, because the metal is deposited as programmed; namely as the underlying surface is perfectly straight. Another issue specifically relating to printing of longer columns is vibration of the specimens. The firm horizontal acceleration of the industrial robot while shifting from one point to another, might cause the columns and the robot foundation to vibrate. As a consequence the next deposits possibly deviate from their intended position.

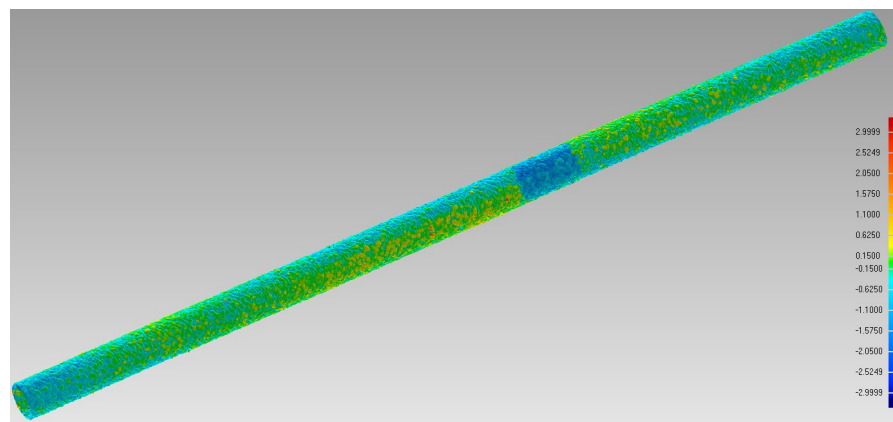


Figure 4.1: 3D-scan result: local shift from longitudinal axis of successively deposited print layers

4.1.2. Volume Measurements

By submerging the column specimens into fluid, in this case water, the volume of the specimens is determined using Archimedes' principle. In addition, length and weight have been measured. All measurements have been performed twice and have been averaged. From the volume, length and weight, an average cross-section area and density has been deducted. Table 4.2 and 4.3 summarises the obtained results for dot-by-dot and continuously printed specimens respectively.

Table 4.2: Volume measurement results of bending specimens printed dot-by-dot

Specimen	Volume [cm ³]	Length L [mm]	Weight [g]	Avg. C-S. A_{μ} [mm ²]	Density [g/cm ³]
B-1-A	234.6	671	1855	350	7.91
B-2-A	232.8	668	1835	348	7.88
B-3-A	234.6	671	1860	350	7.93
<i>Average</i>	234.0	670	1850	349	7.91
<i>St. deviation σ</i>	0.9	1	11	1	0.02

Table 4.3: Volume measurement results of bending specimens printed continuously

Specimen	Volume [cm ³]	Length L [mm]	Weight [g]	Avg. C-S. A_{μ} [mm ²]	Density [g/cm ³]
B-1-B	198.9	661	1580	301	7.94
B-2-B	200.1	665	1590	301	7.95
B-3-B	200.7	665	1590	301	7.92
<i>Average</i>	199.9	664	1587	301	7.94
<i>St. deviation σ</i>	0.8	2	5	0	0.01

The obtained average cross-sectional area A_{μ} of dot-by-dot printed columns equals 349 mm². This approximately coincides with a tubular column section, assumed homogeneous, with an outer diameter of 33.8 mm and a wall thickness of 3.7 mm ($A = 349.88$ mm²). Where the outer diameter has been adopted from averaged Vernier's caliper measurements.

Because the continuously printed column samples have a thinner wall, lower A_{μ} values are obtained averaging 301 mm². This corresponds with a column section, assumed homogeneous, with an outer diameter of 33.3 mm and wall thickness of 3.2 mm. For all tubular columns a nominal diameter of 30.1 mm is assumed. This nominal diameter is the laser-guided path followed by the welding robot. A_{μ} values for both dot-by-dot and continuous samples show a low standard deviation, which proves consistency in print quality. From here on, these A_{μ} values are used to predict resistances of mechanical tests as explained in section 4.2.

For both strategies quite similar density values have been obtained: 7.91 and 7.94 g/cm³. According to material supplier Sadev [89], this is in conjunction with the standard density value of 7.90 g/cm³ provided for 308LSi stainless steel. This little difference could be explained by the additional alloying constituents. Large-scale porosity is consequently ruled-out as this would have lowered the density values.

4.2. Mechanical Test Results

Test results of all the executed mechanical tests will be presented in this section. First the results of four-point bending tests are stated in section 4.2.1. Section 4.2.2 will subsequently provide results of buckling tests, whereas compression and tensile test results will be presented in section 4.2.3 and 4.2.4. Finally the obtained hardness results are shown in 4.2.5.

4.2.1. Bending Tests

Four-point bending tests are performed on both dot-by-dot and continuously printed specimens. The bending stiffness EI (expressed in Nmm^2) has been deduced using the tangent line to the load-deflection curve during unloading of the specimen as shown in figure 4.2. The unloading stage is chosen to exclude inaccuracies of the initial loading phase.

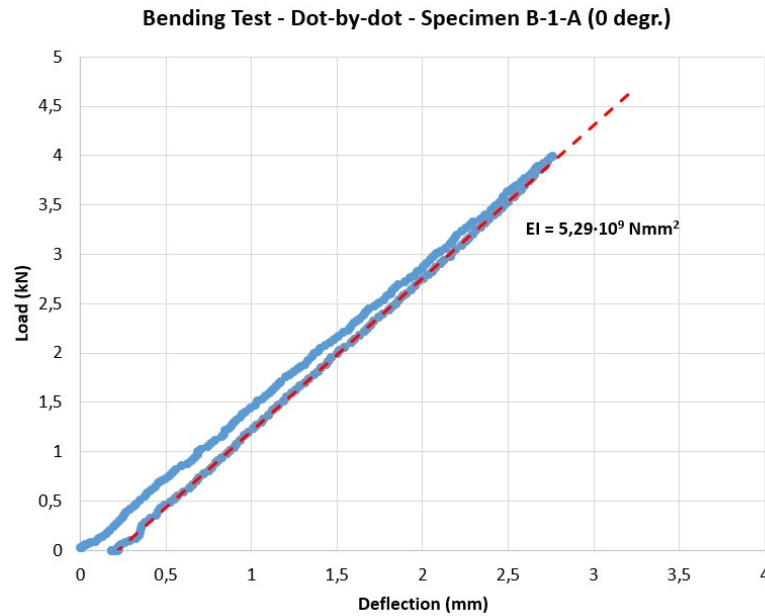


Figure 4.2: Load-deflection curve of four-point bending test on specimen B-1-A

In order to investigate stiffness variations in the cross-section, four bending tests have been performed on the same specimen, where after each test the column is rotated 90 degrees around its longitudinal axis. This is designated by 'side 1' (0 degrees rotation), side 2 (90 degrees rotation), etcetera. The obtained results for dot-by-dot printed columns are shown in table 4.4. It can be observed that the obtained stiffness values are very consistent, both around the perimeter of a single specimen and between the different specimens.

Table 4.4: Results of four-point bending tests on dot-by-dot printed column sections

Specimen/Side	Bending Stiffness EI [Nmm^2]				Mean	St.dev. σ (%)
	Side 1	Side 2	Side 3	Side 4		
B-1-A	$5.29 \cdot 10^9$	$5.14 \cdot 10^9$	$5.24 \cdot 10^9$	$5.10 \cdot 10^9$	$5.19 \cdot 10^9$	1.47
B-2-A	$5.02 \cdot 10^9$	$5.08 \cdot 10^9$	$5.14 \cdot 10^9$	$5.12 \cdot 10^9$	$5.09 \cdot 10^9$	0.90
B-3-A	$5.07 \cdot 10^9$	$5.08 \cdot 10^9$	$5.18 \cdot 10^9$	$5.05 \cdot 10^9$	$5.10 \cdot 10^9$	0.95
Mean					$5.13 \cdot 10^9$	
St.deviation σ (%)					0.91	

In figure 4.3 the results are graphically presented. By analytical means a prediction for the bending stiffness has been made as a reference for the obtained test results. With an assumed Young's modulus of 200 GPa, as provided by Eurocode 3 [48] for (isotropic) austenitic steels and an assumed nominal column diameter of 30.1 mm, the wall thickness t can be varied to fit the obtained test results. From the figure it can be clearly seen that with a value of $t = 3.7$ mm as adopted from the volume measurements and the earlier mentioned Young's modulus value, a stiffness overestimation of 35% is obtained. Further reducing of the wall thickness results in a value of 2.4 mm in order to match the result obtained from bending tests.

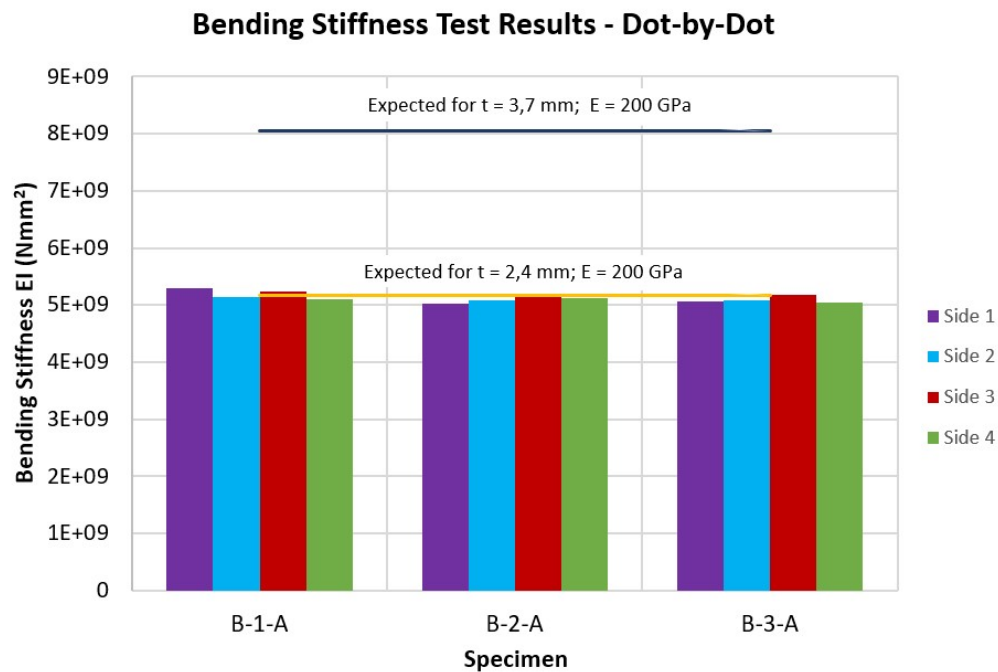


Figure 4.3: Graphical presentation of four-point bending test results on dot-by-dot printed column sections

Besides dot-by-dot printed specimens, also continuously printed columns have been tested. Since the cross-section of these columns is a bit smaller than that of the dot-by-dot printed columns, one should not compare them directly. The mutual variations of the continuously printed columns can be compared as presented in table 4.5. Similar to the dot-by-dot printed columns it is observed that the obtained stiffness values are very consistent, both around the perimeter of a single specimen and between the different specimens. Standard deviation in per cents range from 0.93 to 2.73%. Figure 4.4 shows that a wall thickness reduction from 3.2 to 1.8 mm is required to match the obtained test results. This corresponds to a reduction of approximately 43%.

Since bending stiffness EI is a multiplication of Young's modulus E and second moment of area I , the question raises whether the observed low bending stiffness is caused by reduced stiffness values or a reduction in cross-section, consequently lowering the second moment of area of the column specimens. Further analysis to the effective cross-sectional area is performed in section 5.1. The load-deflection curves are attached in appendix C.2.1.

Table 4.5: Results of four-point bending tests on continuous printed column sections

Specimen/Side	Bending Stiffness EI [Nmm ²]				Mean	St.dev. σ (%)
	Side 1	Side 2	Side 3	Side 4		
B-1-B	$3.98 \cdot 10^9$	$3.94 \cdot 10^9$	$3.89 \cdot 10^9$	$4.00 \cdot 10^9$	$3.95 \cdot 10^9$	1.08
B-2-B	$4.00 \cdot 10^9$	$3.95 \cdot 10^9$	$4.03 \cdot 10^9$	$3.94 \cdot 10^9$	$3.98 \cdot 10^9$	0.93
B-3-B	$4.01 \cdot 10^9$	$3.87 \cdot 10^9$	$4.08 \cdot 10^9$	$3.82 \cdot 10^9$	$3.94 \cdot 10^9$	2.73
Mean					$3.96 \cdot 10^9$	
St.deviation σ (%)					0.39	

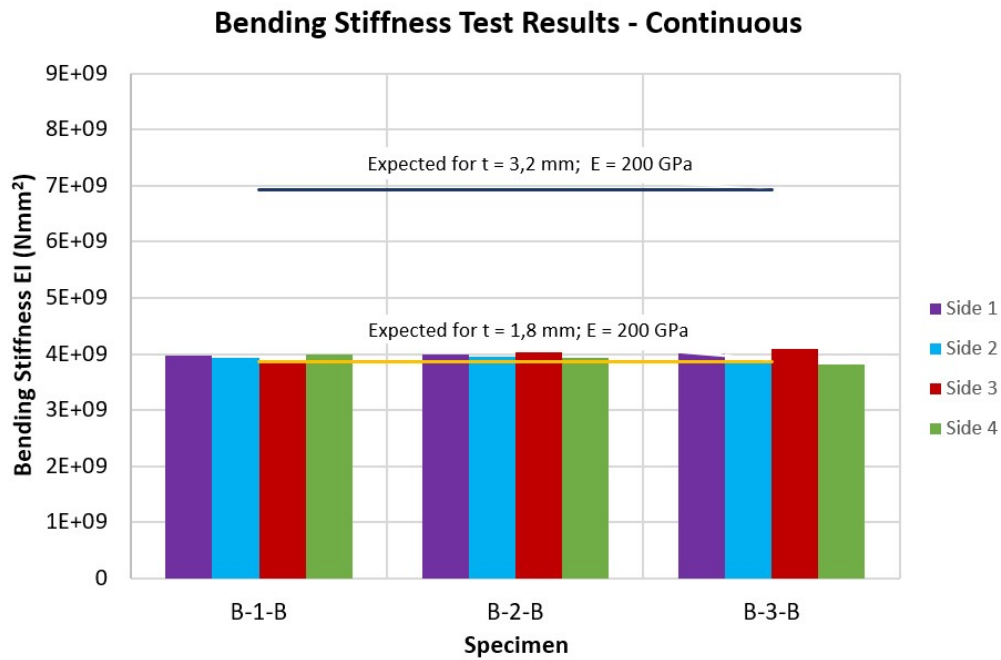


Figure 4.4: Graphical presentation of four-point bending test results of continuously printed column sections

4.2.2. Buckling Tests

In this section the tested buckling strength of printed tubular columns for a varying range of column lengths is presented. Details of the specimens their geometry are given in table 3.3. The obtained results for dot-by-dot printed specimens are shown in table 4.6 and in table 4.7 for continuously printed specimens. From the results a buckling curve is drawn, which is provided in figure 4.5. Within their slenderness category, the columns show little spread in buckling resistance. This also holds for continuously printed columns, of which only one slenderness have been tested. The obtained buckling resistance lies perfectly on the buckling curve for dot-by-dot printed specimens.

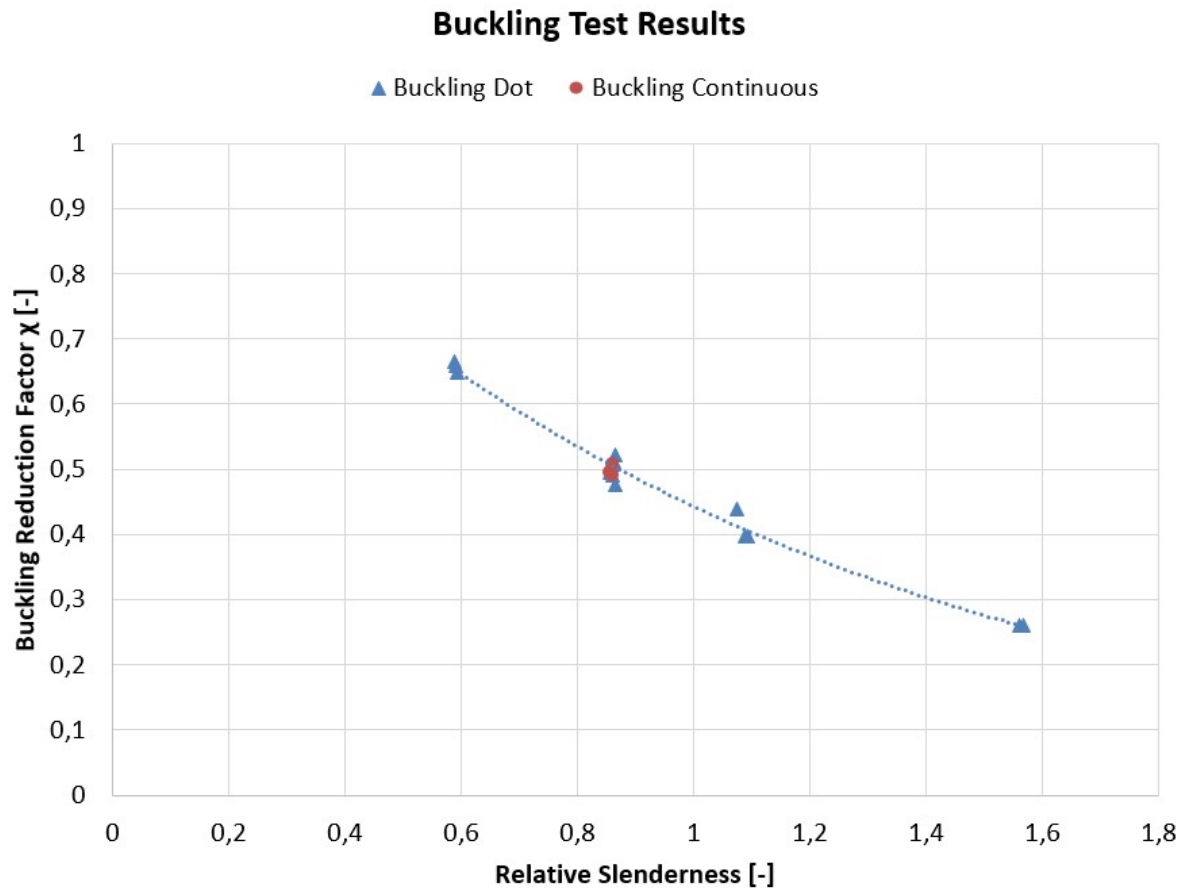
An exception is specimen A-125-3. The buckling load obtained for this column is higher than the Euler load, hence way higher than expected. This is the only specimen tested with spherical plain bearings. With progressive insight they have been replaced by ball bearings to attain fully hinging bearings. This value has therefore been discarded from the curve in figure 4.5.

Table 4.6: Buckling test results for dot-by-dot printed columns - assuming $E = 200 \text{ GPa}$ and $\sigma_{0,2} = 350 \text{ N/mm}^2$

Specimen	Buckling Length L_{eff} [mm]	Rel. Slend. λ_{rel} [-]	Buckling load F_{buc} [kN]	Euler Load N_{cr} [kN]
A-125-1	1256	1.560	31.96	32.06
A-125-2	1261	1.566	31.84	31.81
A-125-3	1284	1.595	55.88	30.68
A-85-1	865	1.074	53.80	67.68
A-85-2	880	1.092	48.79	65.39
A-85-3	875	1.087	48.76	66.07
B-1-A	697	0.866	58.45	104.12
B-2-A	694	0.862	62.68	105.02
B-3-A	697	0.865	63.99	104.12
A-48-1	477	0.592	79.34	
A-48-2	475	0.590	80.71	
A-48-3	474	0.588	81.57	

Table 4.7: Buckling test results for continuously printed columns - assuming $E = 200$ GPa and $\sigma_{0,2} = 350$ N/mm²

Specimen	Buckling Length L_{eff} [mm]	Rel. Slend. λ_{rel} [-]	Buckling load F_{buc} [kN]	Euler Load N_{cr} [kN]
B-1-B	687	0.855	52.38	82.77
B-2-B	691	0.860	51.97	81.81
B-3-B	691	0.860	53.87	81.81

Figure 4.5: Buckling test results; assumed $E = 200$ GPa and $\sigma_{0,2} = 350$ N/mm²

Assumptions have been made while deriving these buckling test results. The relative slenderness λ_{rel} is dependent on both Young's modulus E_0 and proof stress $\sigma_{0,2}$. For E_0 a value of 200 GPa is assumed in conjunction with Eurocode 3 [48] and a yield stress value of 350 N/mm² is assumed in conjunction with the material data sheet of the supplier [47]. The Euler load is calculated using the average bending stiffness value obtained from the four-point flexural test results (section 4.2.1). Aforementioned assumptions require verification, which will be achieved by tensile tests. The tensile test results are given in section 4.2.4.

Tests on the shortest columns ($L = 120$ mm, $\lambda_{\text{rel}} = 0.2$) have been discarded because the test set-up, and more specifically the applied bearings did not allow such thick-walled stocky columns to buckle. In addition it is assumed in this calculation that the effective buckling length is equal to the measured system length (hinge-to-hinge distance). However, hinged bearings are always subject to friction during rotation. Additional tests have been performed to derive the real effective buckling length to account for the friction effects. This is explained in section 5.3.1.

If the effective buckling length is known and the values for E and $\sigma_{0,2}$, the buckling curve has been redrawn. This new curve is presented in section 5.3. A complete overview of load-deflection curves from buckling tests is provided in appendix C.2.2.

4.2.3. Compression Tests

Compression tests on milled column specimens were executed to check if it was feasible to extract basic properties as yield strength and Young's moduli. From the acquired stress-strain relation shown in figure 4.8 it can be seen that both the dot-by-dot and continuously printed specimens attains a 0.2% proof stress of 303 N/mm^2 . The compression resistances correspondingly equal 75 and 57 kN respectively. It can also be observed that the dot-by-dot printed specimen has a slightly higher elastic stiffness compared to the continuous specimen.

Furthermore the failure mode has been studied. Figures 4.6 and 4.7 show the specimens after testing. Visual observation of the specimens during loading showed local thickening of the cross-section which after continuing loading resulted in buckled specimens shown in the earlier mentioned figures. This result is of importance because early local buckling disturbs an accurate stiffness and yield-strength measurement.



Figure 4.6: Specimen C8A after compression test



Figure 4.7: Specimen C9B after compression test

Concluding from the stress-strain curves, the measured deformations from both specimens seem too high. On its turn this is not completely unexpected since strains are not measured on the specimens itself, but they are deducted from the cylinder displacement only. Also it was observed that the local stresses were so high that the specimens left a clear mark on both steel bearing plates. They were pressed into the plates, which resulted in an overestimation of specimen deformation, especially at higher loads. After the elastic phase the specimen showed a very long, almost linear strengthening phase in plastic stage. This is down to the buckled shape that regains strength in the plastic stage.

Obviously, aforementioned problems could be overcome by improving the test procedure. First of all, a shorter column specimen could be used to assure prevention of early buckling behaviour. This also eases concentric load introduction. Strain gauges can be added so that strains can be measured directly. Given in by practical arguments, it is nonetheless decided not to continue with compression tests. Machining of printed column up to the point where a smooth homogeneous section is obtained is extremely time consuming, costly and labour intensive. Especially for the dot-printed samples it proved to be hard to attain a complete smooth surface because surface irregularities were significant.

The absence of a homogeneous cross-section and a lack of time and budget limited the options to perform tests on identical printed column sections. For this reason it is decided to deduct stiffness and yield strength values from tensile tests that are performed by OCAS on similar printed and machined stainless steel sections. The acquired results of these tests are presented in the next section.

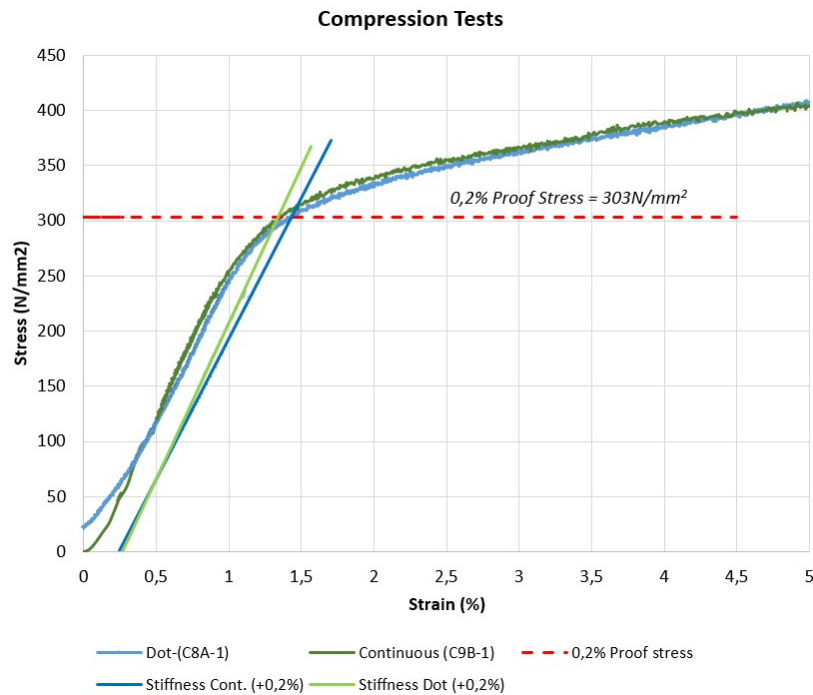


Figure 4.8: Stress-strain relation from compression tests: dot versus continuous

4.2.4. Tensile Tests

The results of tensile tests performed by OCAS on by MX3D-printed milled plate material will be presented in this section. From the obtained stress-strain curves the 0.2% proof stress, ultimate tensile strength, stiffness and ultimate strain have been deducted. It should be noted that for the deduction of Young's moduli, the initial stiffness E_0 has been used. Mechanical properties (as weld deposit) as provided by material supplier Oerlikon and Ugiweld have been used as reference values.

Table 4.8 and figure 4.9 depict the obtained results for dot-by-dot printed specimens in both longitudinal (print direction) and perpendicular to print (or transversal) direction. A total of twelve specimens have been tested; three for both strategies and for both print directions. Whereas the average ultimate tensile strength for dot-by-dot printed specimen in longitudinal direction (614 N/mm^2) exceeds both reference values ($520\text{--}600 \text{ N/mm}^2$), the tensile strength observed in transverse direction, although with a large spread, is significantly lower (511 N/mm^2). A similar trend is observed for the 0.2% proof stresses, which are lower in transversal direction (342 versus 319 N/mm^2).

This anisotropic behaviour is also clearly visible in the lower stiffness values obtained in transverse direction (155 GPa) compared to the stiffness in longitudinal direction (181 GPa). Both values are significant lower than the assumed 200 GPa which is prescribed by Eurocode 3 for cold-formed austenitic stainless steels [48]. Furthermore it can be observed that specimens tested in longitudinal print direction behave more ductile than their transversely tested counterparts, from which one specimen did not pass the ductility requirements from Eurocode 3 (see equation (2.5)) due to early fracture ($\epsilon_f < 15\%$).

Table 4.8: Tensile test results of dot-by-dot printed specimens

	0.2% Proof Stress $\sigma_{0.2} [\text{N/mm}^2]$	Ult. Tensile Strength $\sigma_u [\text{N/mm}^2]$	Young's Modulus $E_0 [\text{GPa}]$	Ultimate Strain $\epsilon_u [\%]$	Fracture Strain $\epsilon_f [\%]$
<i>Oerlikon - as welded 20°C</i>	>350	>520	-	>35	
<i>Ugiweld - as welded 20°C</i>	360	600	-	>35	
Longitudinal (print dir.)	342	614	181	29.7	38.9
<i>St. deviation σ</i>	3	0	5	0.9	1.0
Transversal	319	511	155	18.6	19.3
<i>St. deviation σ</i>	7	33	6	5.6	6.1

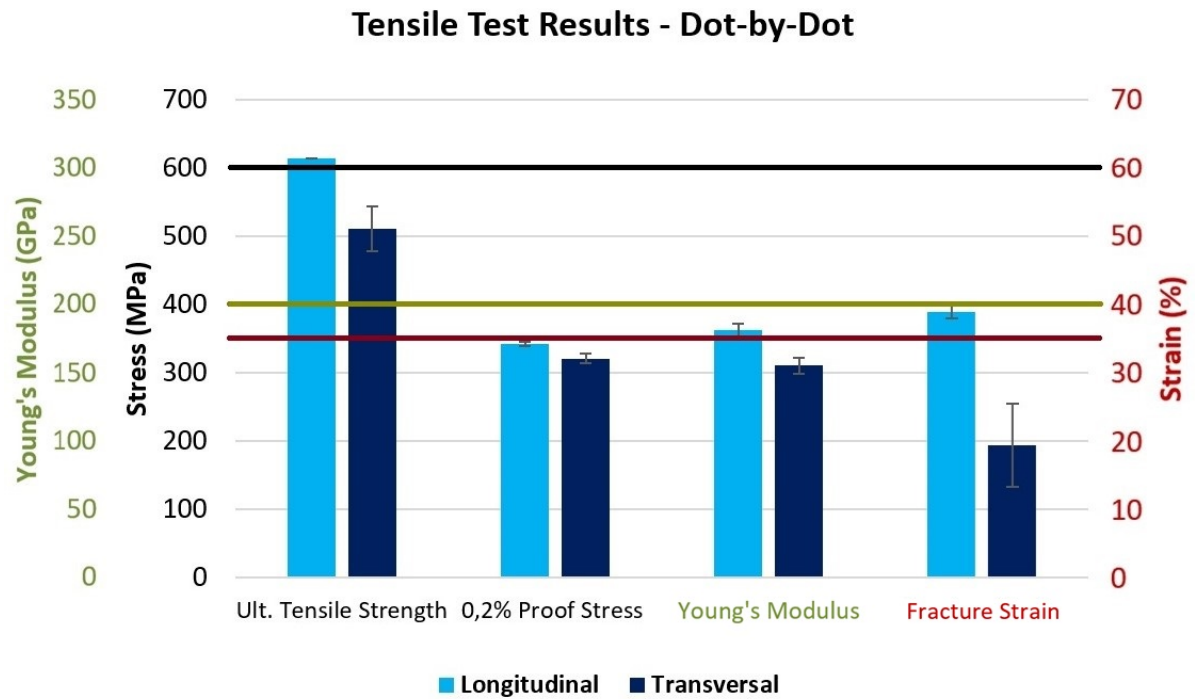


Figure 4.9: Graphical representation of tensile test results for dot-by-dot printed specimens

Table 4.9 and more graphically, figure 4.10 depict the obtained results for continuously printed specimens. Overall the obtained strength values of continuously printed specimens are lower than for dot-by-dot printed specimens. Both the 0.2% proof stresses and ultimate tensile strengths are significantly lower. Especially the stiffness values (137 GPa and 121 GPa) are low compared to the reference value of 200 GPa.

Despite these lowered values, continuous specimens prove to exhibit slight less anisotropic mechanical behaviour looking at the differences between longitudinally and transversally tested specimens. Differently from the dot-by-dot printed specimens, the strength values for continuously printed specimens are slightly higher in transverse direction. Specimens tested in transversal direction behave more ductile compared to longitudinally tested specimens. All stress-strain curves from the analysed tensile tests are provided in appendix C.2.3.

Table 4.9: Tensile test results of continuously printed specimens

	0.2% Proof Stress $\sigma_{0.2}$ [N/mm ²]	Ult. Tensile Strength σ_u [N/mm ²]	Young's Modulus E_0 [GPa]	Ultimate Strain ϵ_u [%]	Fracture Strain ϵ_f [%]
<i>Oerlikon - as welded 20°C</i>	>350	>520	-	>35	
<i>Ugiweld - as welded 20°C</i>	360	600	-	>35	
Longitudinal (print dir.)	307	544	137	21.2	22.0
<i>St. deviation σ</i>	5	28	6	3.5	3.8
Transversal	321	568	121	30.9	34.9
<i>St. deviation σ</i>	6	11	6	0.9	4.7

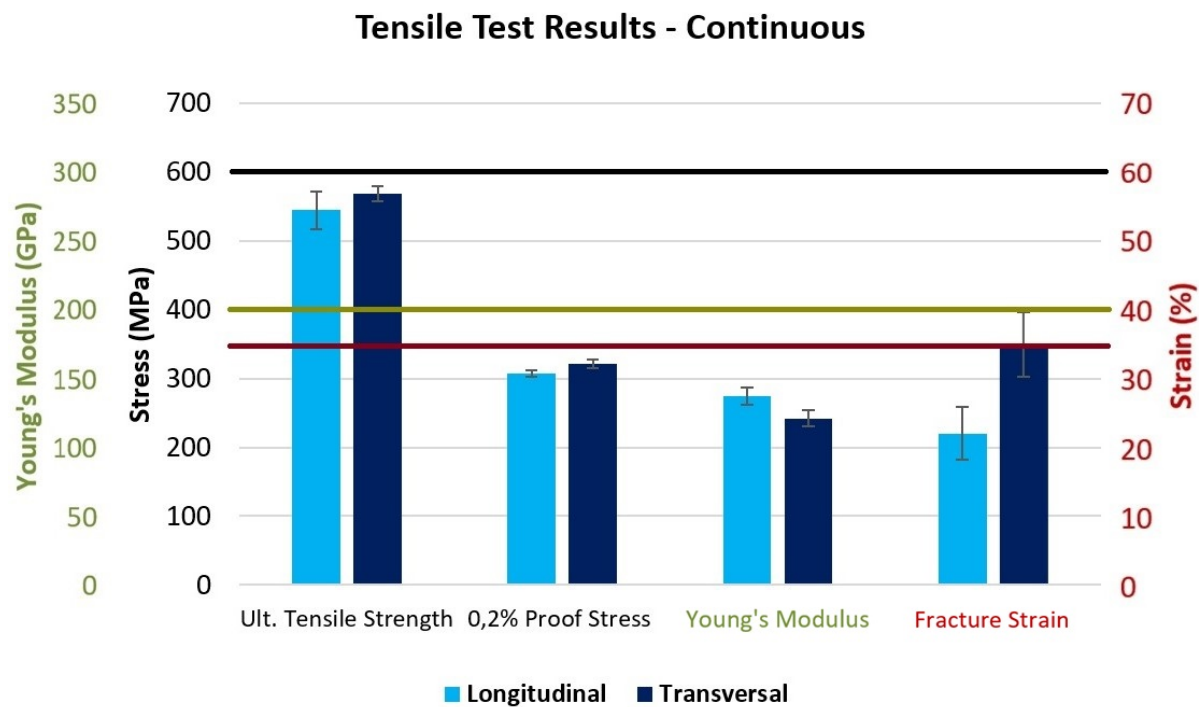


Figure 4.10: Graphical representation of tensile test results for continuously printed specimens

The obtained tensile test results of milled specimens from plate material will be adopted in the analysis of tubular columns. Some remarks should however be made regarding this adoption. Since the tubular columns are printed spiralwise, the deducted mechanical characteristics in transverse direction are most important because during buckling and bending the column is loaded in that direction. More importantly, it is not known what influence the difference in geometry between a plate and a tubular column has on the tensile properties of the specimen. Even when the specimens are milled, the difference in printing strategy and corresponding difference in heat input and cooling rate may affect their mechanical properties.

It is not known why lowered stiffness values are observed for the tested specimens. A few explanations could be given for this observation. Accurate measurements of stiffness during tensile testing is hard since the outcome is strongly related to the accuracy of the strain measurement. Special attention should be paid to the test methodology and an accurate definition of the cross-sectional area of the specimens. While milling the tensile specimens, it should be assured of that a smooth and homogeneous cross-section over the height is achieved.

Furthermore it is known that stainless steel exhibits non-linear stress-strain behaviour. The stiffness is therefore expressed in terms of initial stiffness E_0 . It should be taken care of that this tangent line is adopted from the elastic phase in the stress-strain diagram and that strain hardening was not initiated yet. Another possible cause for lowered stiffness values is the presence of residual stresses which is related to the printing process parameters and printing strategy of this specific specimen. Additional research is required to investigate the presence and the influence of residual stresses on mechanical properties of printed stainless steel.

In addition a remark should be made with regards to the tested material. Despite the fact that an identical printing robot and a similar stainless steel grade (308LSi) have been used, the tensile tested material is provided by Ugieweld (308LM), whereas the tubular columns are printed with Oerlikon's Inertfill 308LSi. Regardless both grades are designated as grade 308LSi, both welding wires show minor chemical differences as can be seen in appendix B.2.

Since there is little known about the exact heat input during printing these specimens it is not possible to determine the influence of the chemical differences on the mechanical properties of both welding wires. It is also not known how the chemical composition of the base material (welding wire) changes in the printing

process. Analysis of a printed specimen using Energy Dispersive X-Ray Fluorescence (EDXRF) shows a slight deviation (reduction) in Si- and (an increase) in N-levels, compared to typical Ugieweld 308LM welding wire composition values. This deviation is observed at both printing strategies. The question raises whether this change is caused by a compositional change during the printing process or whether the composition of the input wire deviates from the corresponding datasheet of the supplier. Additional chemical analysis of the input wire is required to answer this question.

The non-linearity of the stress-strain relation will be further studied and quantified in section 5.2. This enables incorporation of the stress-strain relation in finite element models in future research.

4.2.5. Hardness

As explained in section 3.4.5, Vickers hardness line-measurements (HV3) have been performed on longitudinal and transversal sections of both dot-by-dot and continuously printed specimens. Figures 4.11 and 4.12 present the results for dot-by-dot printed specimens and figures 4.13 and 4.14 for continuously printed specimens graphically. Measurements of a section along a specified line are performed from the outside (indicated on the horizontal axis by 'measurement 1') to the inside of a column wall ('measurement 5').

Slightly higher hardness values are observed for dot-by-dot printed specimens, averaging 195 Vickers compared to 190 Vickers for continuously printed specimens. For both printing strategies it is observed that the outside of the column wall (averaging 194 Vickers) is slightly harder than the inside (averaging 191 Vickers). In addition it is observed that longitudinal sections for both strategies attain significantly higher hardness values (203 Vickers) than transversal sections (187 Vickers).

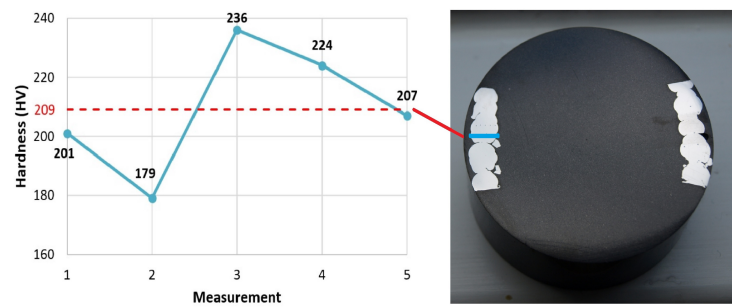


Figure 4.11: Vickers hardness measurement (HV3) to a dot-by-dot printed longitudinal section

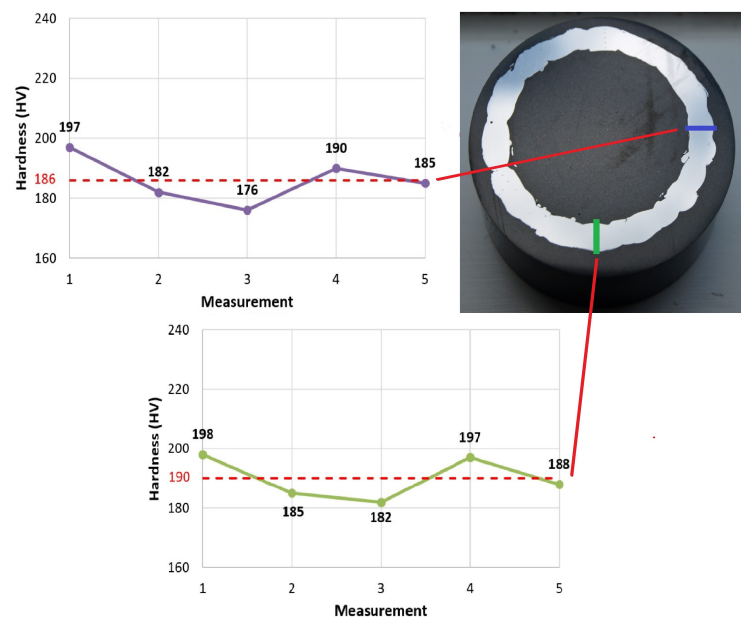


Figure 4.12: Vickers hardness measurement (HV3) to a dot-by-dot printed transversal section

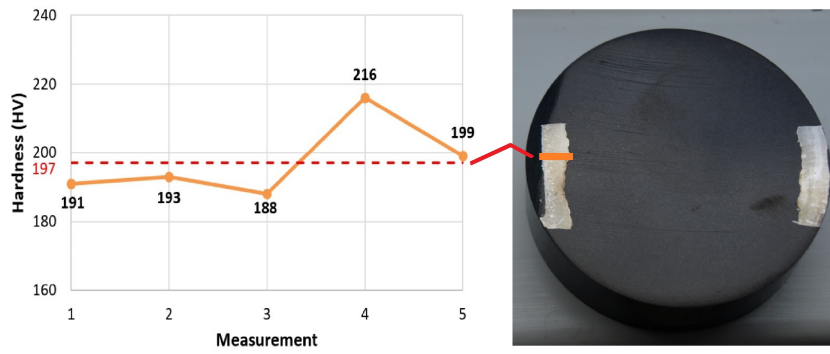


Figure 4.13: Vickers hardness measurement (HV3) to a continuously printed longitudinal section

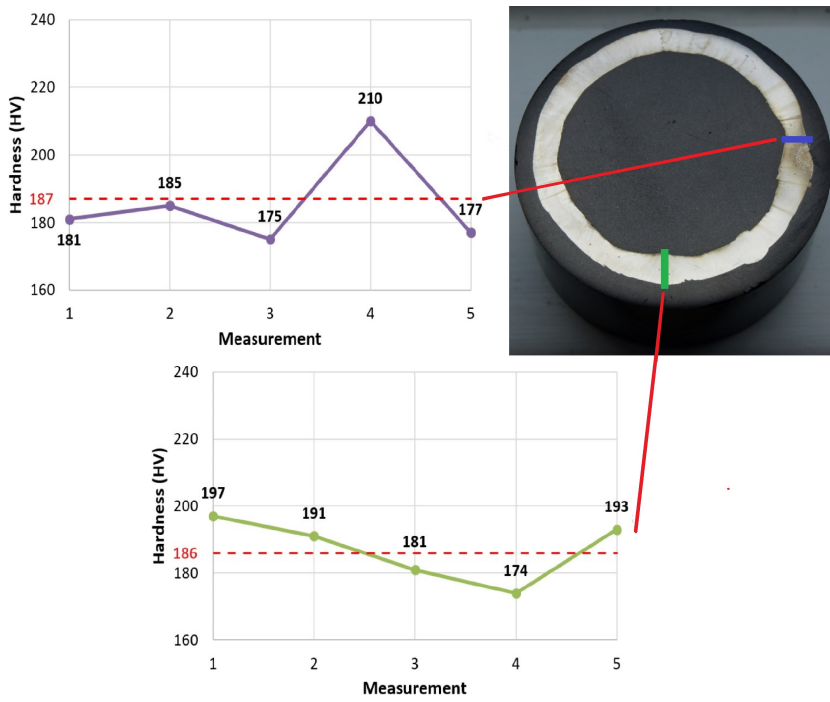


Figure 4.14: Vickers hardness measurement (HV3) to a continuously printed transversal section

4.3. Metallography Results: Tubular Columns

In this section the results of metallography of specimens extracted from the printed tubular columns will be presented. At first the results of (electron) microscopy will be stated. Finally the outcome of x-ray analysis is given.

Microscopy

Using optical microscopy, images have been made of both dot and continuously printed specimens. The images reveal a directional grain growth, most clearly visible on the longitudinal sections as can be seen in figures 4.15 and 4.16. Large columnar grains are formed following the thermal gradient of the weld pool. Also the successive weld layer deposits are visible from which new grains are formed that fuse together and take the orientation of previous grains. It can indeed be seen that large columnar grains grow across multiple weld passes, which explains the anisotropic mechanical properties.



Figure 4.15: Longitudinal section dot-by-dot strategy

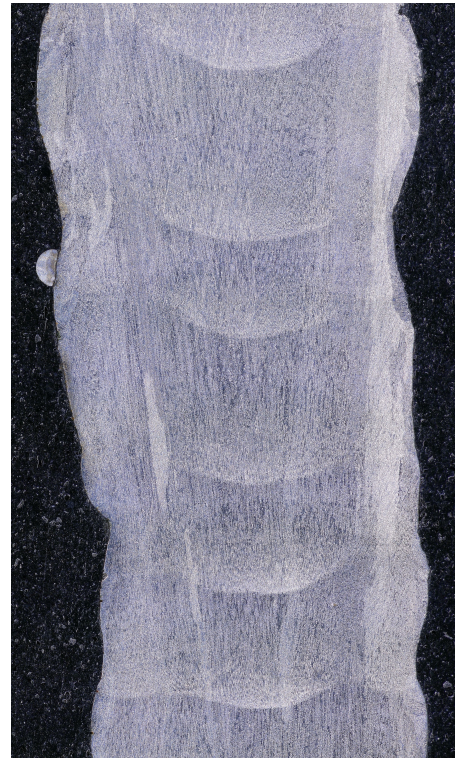


Figure 4.16: Longitudinal section continuous strategy

Images of transversal metallographic specimen sections are displayed in figure 4.17 and 4.18. Whereas the different point welds can be distinguished for dot-printed specimen, the continuously printed specimen show a more homogeneous image with less geometrical imperfections.



Figure 4.17: Transverse section dot-by-dot strategy

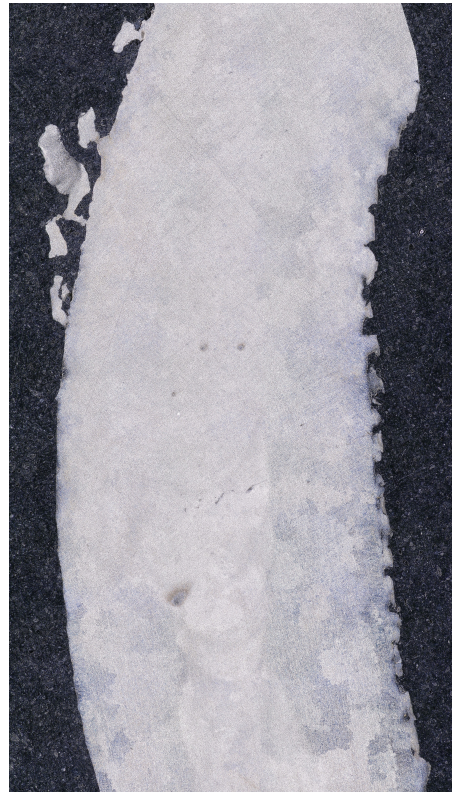


Figure 4.18: Transverse section continuous strategy

Scanning Electron Microscopy (SEM)

Using Electron microscopy, areas of interest have selected and further analysed. As depicted in figure 4.19, the dot-by-dot specimen showed some large pores of which the largest was approximately $200\ \mu\text{m}$ diameter across. Such large pores may negatively affect ductility and strength values. Furthermore Oxide-layer formation is observed as shown in figure 4.20.

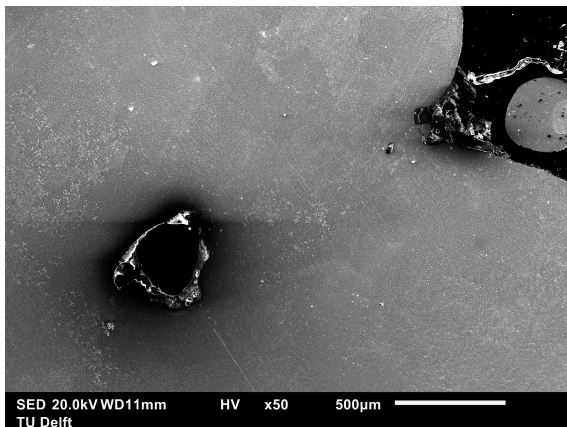


Figure 4.19: Pore in dot-by-dot specimen

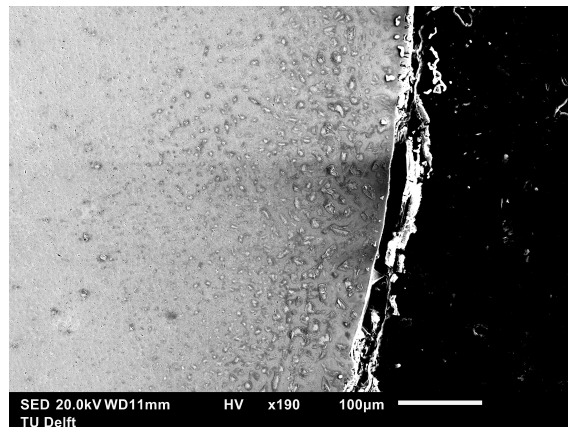


Figure 4.20: Oxide layer formation in dot-by-dot specimen

The chemical composition at the selected points of interest has been investigated to analyse impurities in the specimen. Several oxide inclusions have been found which are included as a result of the printing process. Reports of the chemical analysis performed with the SEM are attached in appendix C.3.1.

X-Ray Diffraction (XRD)

With an x-ray diffractometer, the area within the red square of figure 4.21 is measured.

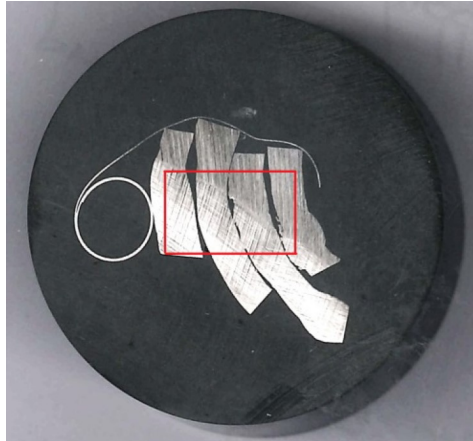


Figure 4.21: Measured area of (M20) mounted XRD-sample

Figure 4.22 shows the measured pattern of the sample in blue and of the black embedding material in gray. The coloured peaks show the positions and corresponding intensities of the identified phases. Austenite phases have been detected mostly, but also ferrite phases are present (green peaks). So the microstructure should be considered as mostly austenitic with a small amount of ferrite, as predicted by the the Schaeffler diagram. From the analysis no precipitates could be identified.

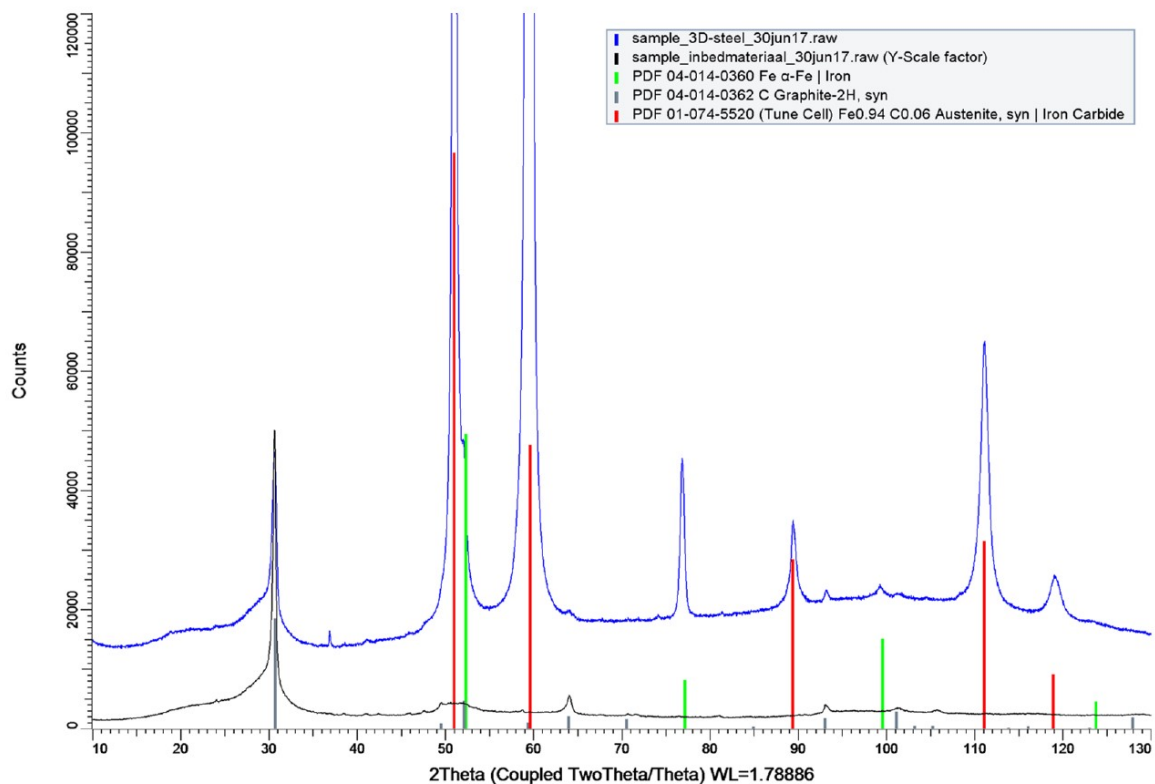


Figure 4.22: Results of x-ray diffraction measurements

4.4. Metallography & Mechanical Test Results: Plate Material (OCAS)

In addition to the earlier presented tensile tests on milled plate material of by MX3D printed 308L stainless steel, OCAS performed a chemical and metallographical analysis of the same printed plates. The results of this analysis are stated in section 4.4.1. Furthermore additional mechanical tests have been performed. The results of Brinell hardness measurements and Charpy impact tests are given in section 4.4.2 and 4.4.3 respectively.

4.4.1. Microstructure

The microstructure of the printed specimens has been analysed by firstly performing a chemical analysis and secondly by optical microscopy. The results are shown below.

Chemical Composition

An elemental analysis has been performed on printed specimens in order to be able to compare results with typical values as provided by welding wire supplier Ugieweld. By using Energy Dispersive X-Ray Fluorescence (EDXRF), the chemical composition of both dot-by-dot and continuously printed specimens has been identified quantitatively as depicted in table 4.10.

Table 4.10: Chemical composition of dot-by-dot and continuously printed specimens compared with typical values

	C*	Si	Mn°	Ni°	Cr°	Mo	Cu	N*	S*	P	O*
Typical (datasheet 308LM)	0.025	0.7-1.0	1.5-2.0	9.5-11.0	19.5-20.5	0.3	0.2	0.06	0.015	0.020	
Dotted	0.031	0.57	1.79	9.97	19.45	0.16	0.15	0.153	0.010	0.020	0.0354
Continuous	0.030	0.56	1.78	9.96	19.44	0.16	0.15	0.181	0.010	0.020	0.0429

From the analysis of the printed specimen a slight deviation (reduction) in Si-levels and an increase in N-levels from typical Ugieweld 308LM welding wire composition values can be observed. This observation holds for both printing strategies. The change in composition can be explained by inclusions added during the printing process. Inspection of internal cleanliness using optical microscopy and Energy Dispersive X-ray (EDX) analysis indeed shows that inclusions are present in all specimens. This is depicted in figure 4.23.

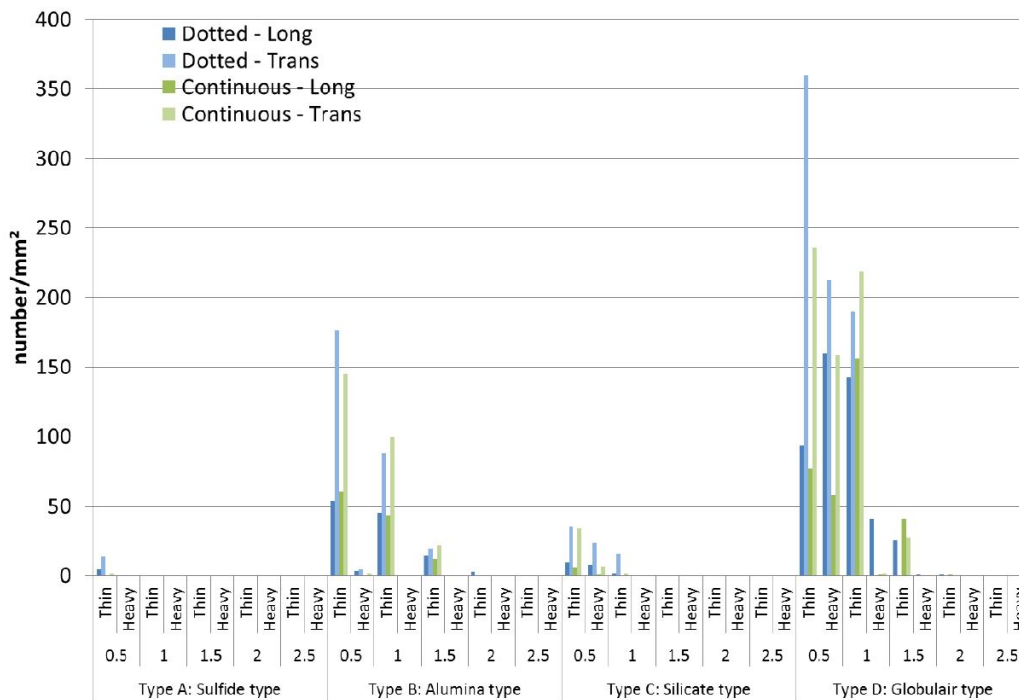


Figure 4.23: Internal cleanliness analysis of dot-by-dot and continuously printed specimens

In both specimens the inclusions, mainly globular oxides rich in silicon, manganese and sulphur, are heterogeneously distributed. However, specimens printed dot-by-dot show more inclusions compared to their continuously printed counterparts.

Whereas inclusions are indeed detected, the question raises if the difference between the chemical composition of the specimens is solely caused by a compositional change during the printing process, or if the composition of the input wire deviates from the corresponding datasheet of the supplier. An increase of Nitrogen (N) in the structure can for example also be explained by a poor shielding condition. Subsequently causing an increase of yield strength and a loss of ductility compared to the properties of the original welding wire material. A chemical analysis of the input wire is required to be able to analyse what causes this difference.

Metallography

From optical microscopy typical solidification structures can be observed, where the different 'dots' in the dot-by-dot printed specimens are clearly visible in figure 4.24 and 4.25. In the analysed longitudinal section (figure 4.24) some accidental microstructural errors can be seen. Similar to the dot-by-dot printed specimens, the analysed continuously printed specimens (figure 4.26 and 4.27 show heterogeneous and anisotropic solidification structures, consequently affecting their mechanical properties.

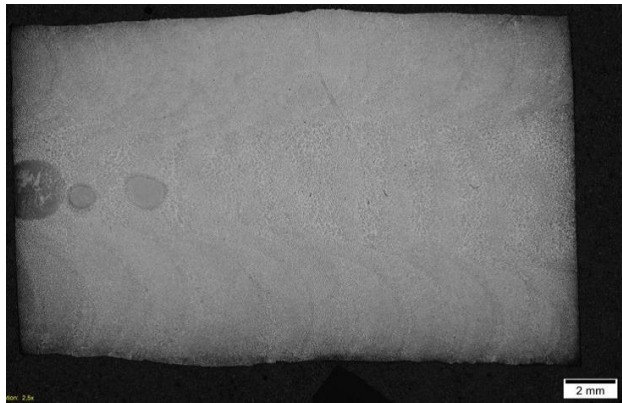


Figure 4.24: Dot-by-dot solidification structure (longitudinal)

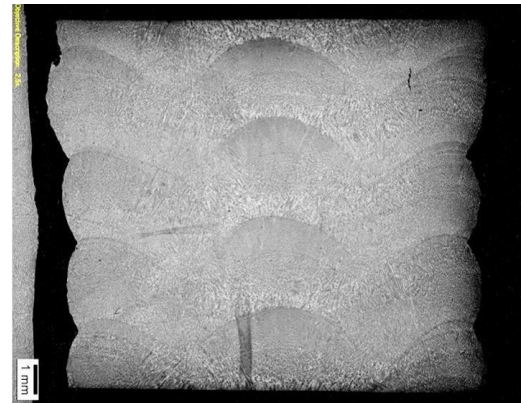


Figure 4.25: Dot-by-dot solidification structure (transversal)

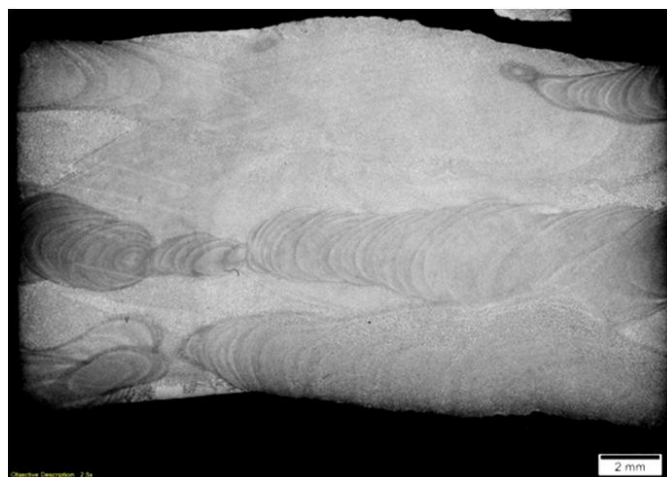


Figure 4.26: Continuous solidification structure (longitudinal)

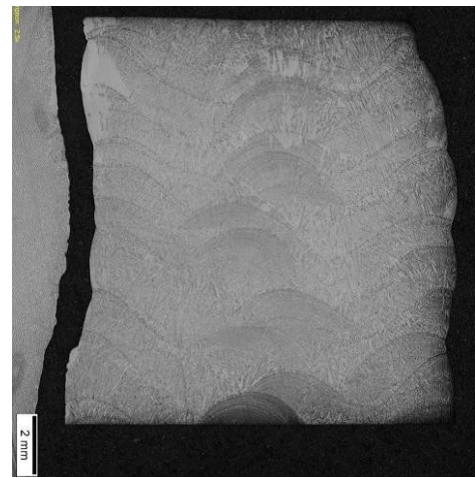


Figure 4.27: Continuous solidification structure (trans.)

The microstructure has been investigated into more detail using a microscope with higher magnifications. For both dot-by-dot (figure 4.28 and 4.29) and continuously printed metallographic specimens (figure 4.30 and 4.31), a heterogeneous microstructure and an anisotropic grain size is observed. Dendritic structures can be seen with (at higher magnifications) second phase distribution delta-ferrite at the grain boundaries. For both printing strategies it is clear that the microstructural composition differs in each point due to differences in thermal history.

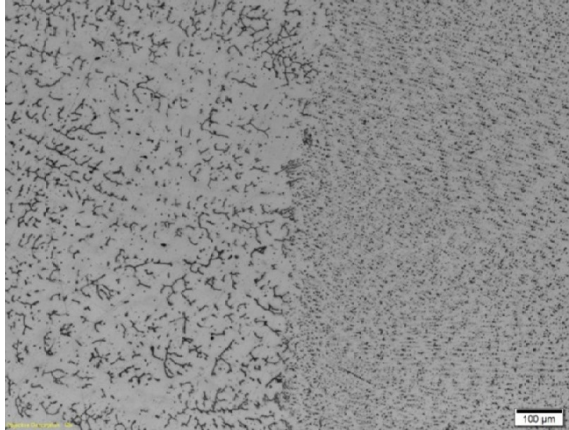


Figure 4.28: Dot-by-dot microstructure (100 μm scale)

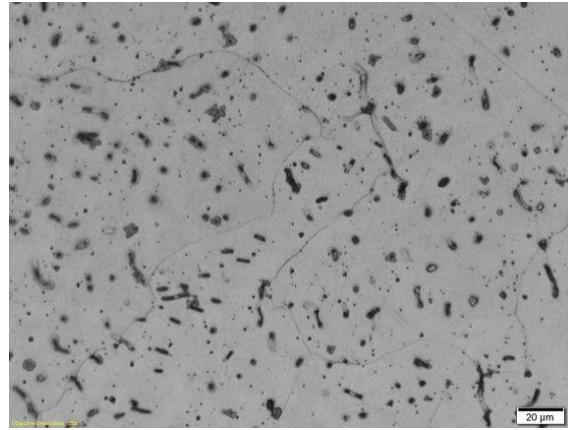


Figure 4.29: Dot-by-dot microstructure (20 μm scale)

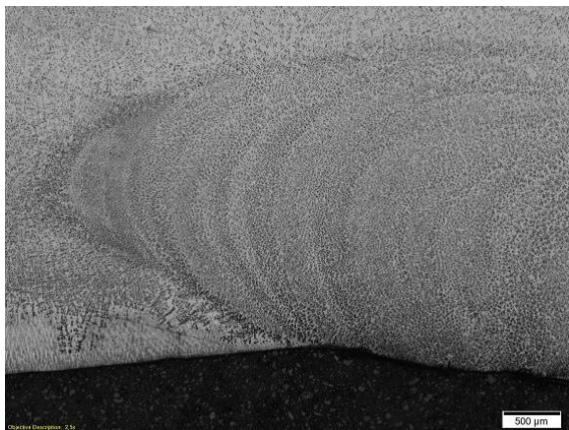


Figure 4.30: Continuous microstructure (500 μm scale)

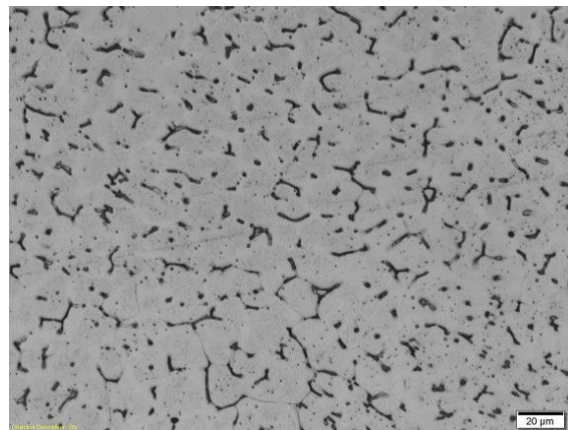


Figure 4.31: Continuous microstructure (20 μm scale)

4.4.2. Hardness

Brinell hardness measurements have been performed on both dot-by-dot and continuously printed plate specimens. For the values in this range, Brinell and Vickers values nearly correspond to each other and can therefore be compared. In contrast to the (Vickers) hardness measurements performed on column specimens, the continuously printed specimens are observed to be harder than the dot-printed specimens.

The exact reason for this difference is not known, but the large spread in test results and the minor difference between both averages makes it difficult to draw conclusions. It is known that the number of heat cycles experienced by the metal during printing correlates inversely with the hardness [92]. This means that because the final layer deposits of a WAAM-specimen experiences fewer thermal cycles, the hardness at these location might improve. More hardness tests should be performed on various sections to investigate whether the observed variations of hardness can be explained by this theory.

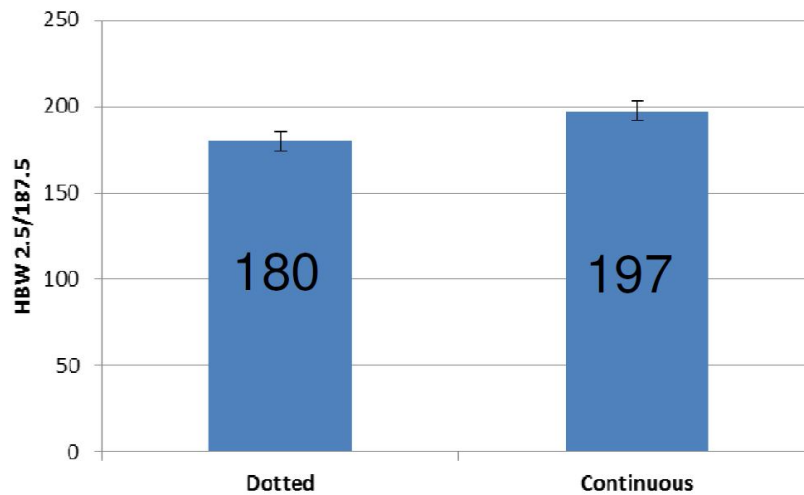


Figure 4.32: Brinell hardness measurement results

4.4.3. Toughness

The results of Charpy pendulum impact tests are shown in figure 4.33 and 4.34. Typical values for 'as weld deposit' material as provided by the material supplier are added as reference. Considering a temperature of 20°, this value equals 160 and 120 J/cm² For TIG- and MIG-processes respectively.

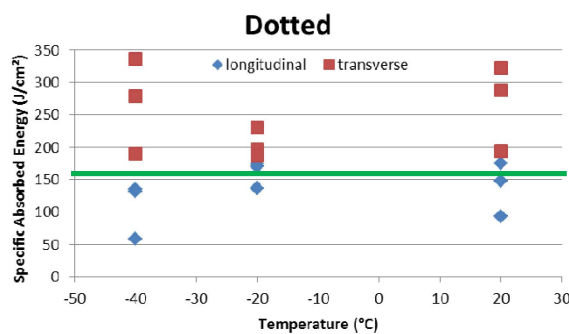


Figure 4.33: Charpy impact toughness results - dot-by-dot

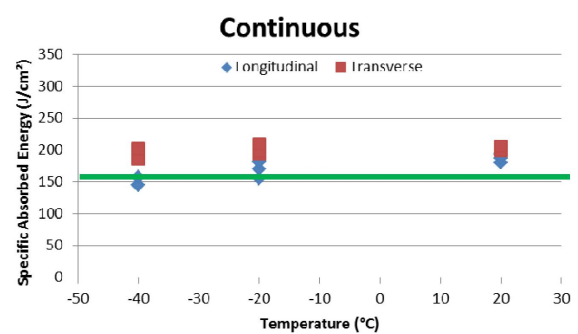
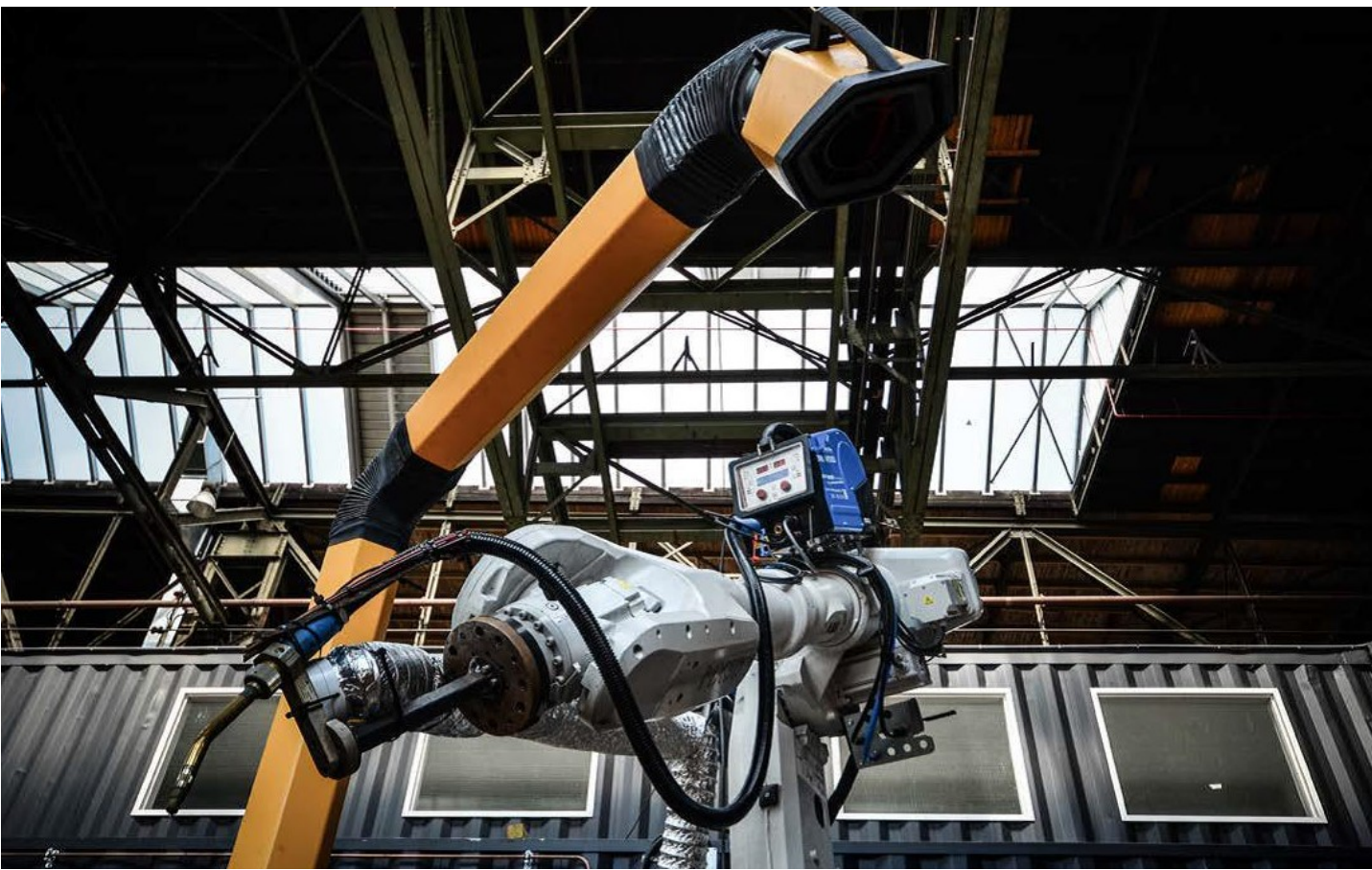


Figure 4.34: Charpy impact toughness results - continuous

It is observed that dot-by-dot printed specimens attain high absolute toughness values, but show a very high spread. Whereas the toughness values of transversal sections all exceed the reference value, the longitudinal sections show significantly lower toughness values. For the continuous printing process also consistently good toughness values are observed comparable with the reference value for TIG- or MIG-processes (160 J/cm²) - and with a low spread.

5

Analysis



This chapter provides a further analysis of the test and measurement results (chapter 4). Because the tested variables that influence stability are interrelated, they will here be considered simultaneously and combined to be able to construct a buckling curve for 3D-printed tubular columns.

First an effective cross-section is derived from combined bending and tensile test results in section 5.1. In section 5.2 the stress-strain relations acquired from tensile tests are approximated with Ramberg-Osgood-Rasmussen equations to quantify the level of non-linearity. At last the buckling behaviour of 3D-printed tubular columns is studied and a design buckling curve is proposed in section 4.2.2.

5.1. Cross-Sectional Variations

In section 4.2.1 the bending stiffness of printed tubular column specimens is determined from multiple four-point bending tests. Low stiffness values for both dot-by-dot and continuously printed specimens are observed. Since bending stiffness EI of a section is a multiplication of the Young's modulus E with the second moment of area I , the reduced stiffness values are caused by one of, or both, aforementioned variables.

The second moment of area I to start with, is dependent on the location of the material that is present around the centroidal axis of an object. Since the object of study is a tubular section, it may usually be assumed that I is constant. In this case however this assumption cannot be made because variations in wall thickness are clearly present in both longitudinal sections as can be seen in figures 5.1 and 5.2 and transversal sections (figure 5.3 and 5.4). The pictures on the left show the dot-by-dot printed sections and on the right the continuously printed ones.

A thorough statistical analysis of wall thickness variations in multiple cross-sections is required to quantify the presence of wall thickness minima over the length of a section; the longer a section, the more likely such a minimum wall thickness is encountered. Since the wall thickness varies at every point of the section, it is not possible to measure the exact thickness using a Vernier's caliper. Only a continuous measurement is capable of acquiring thickness variations accurately. Because it is complex and extremely time-consuming to derive a design graph in this way, an other, more convenient approach has been used.

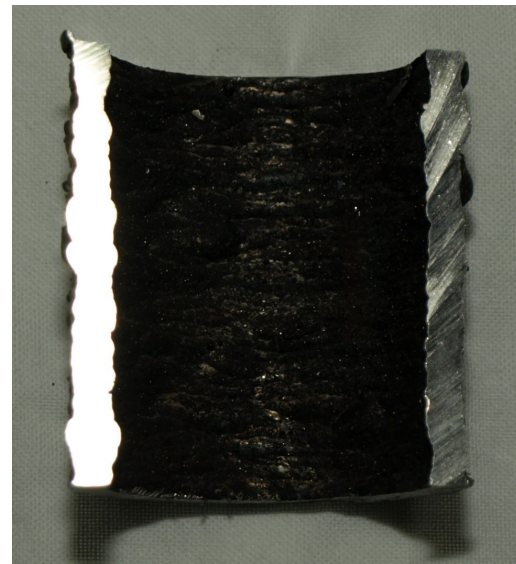


Figure 5.1: Longitudinal section dot-by-dot printed column Figure 5.2: Longitudinal section continuously printed column



Figure 5.3: Transversal section dot-by-dot printed column Figure 5.4: Transversal section continuously printed column

With this alternative approach, four-point bending test results are combined with tensile test results to deduce a so-called effective 'homogeneous' cross-section. Bending test results showed only very minor variations in stiffness along the perimeter of the columns. These variations are therefore discarded in the following analysis. Hence, the average bending stiffness EI for both dot-by-dot and continuously printed specimens has been used. Furthermore the elastic stiffness E_0 is known in transverse direction for dot-by-dot (155 GPa) and continuously (121 GPa) printed material. After dividing the bending stiffness EI with the initial stiffness E_0 of the corresponding specimens, the outcome is equal to the second moment of area I .

Assuming a constant nominal column diameter of 30.1 mm, along which the laser-guided robot deposits its material, a linear relation between wall thickness and second moment of area is obtained. As depicted in figure 5.5 the intersection lies at 3.01 and 3.06 mm for continuously and dot-by-dot printed specimens respectively. This is the effective wall thickness of a homogeneous section, which designers could use in strength calculations for the in this research considered column sections. By expressing the reduction of wall thickness in absolute values (0.64 mm for dot and 0.19 mm for continuously printed sections), these values could be used for other section sizes as well, hence enabling designers to calculate with a homogeneous or 'working' cross-section, significantly easing calculations.

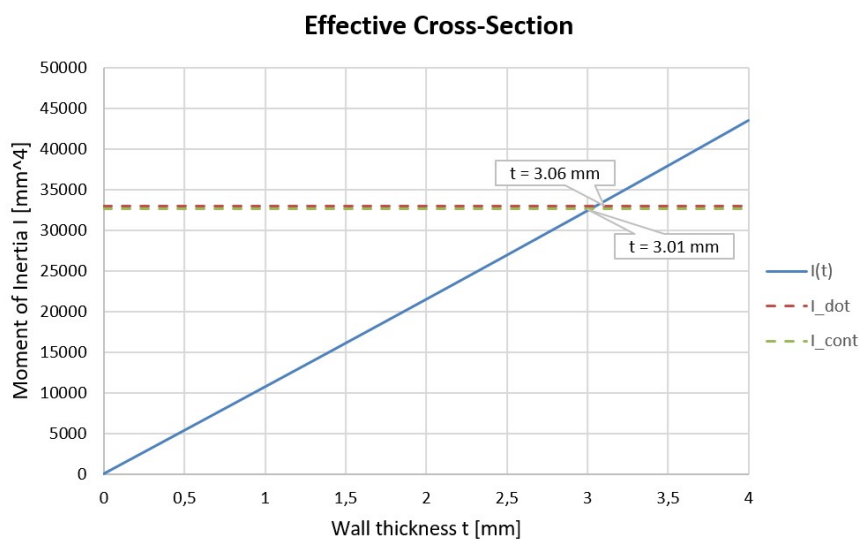


Figure 5.5: Effective cross-section for dot-by-dot and continuously printed column specimens

Thus the effective wall thickness is lower than the measured average wall thickness as earlier adopted. For dot-by-dot specimens wall thickness $t = 3.7$ mm reduces to an effective thickness of $t_0 = 3.06$ mm, which is a reduction of nearly 17.3%. Whereas a continuously printed specimen's thickness reduces from $t = 3.2$ mm to an effective thickness of $t_0 = 3.01$ mm, which is a reduction of only 5.9%. This is in conjunction with visual inspection of column sections. As shown in figure 5.6, dot-by-dot sections indeed clearly show more geometrical irregularities.

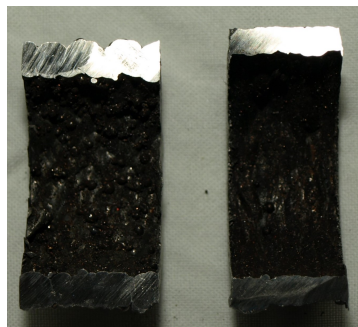


Figure 5.6: Dot-by-dot versus continuously printed longitudinal sections

5.2. Modelling of Non-Linear Stress-Strain Relation

Whereas carbon steels are commonly modelled with a bi-linear stress-strain relation, stainless steels undergo strain hardening effects. To model this non-linear behaviour, stress-strain curves can be approximated by the Ramberg-Osgood expression, modified by Rasmussen as explained in section 2.2.4.

The Ramberg-Osgood expression modified by Rasmussen (equation (2.2)) consists of two domains: the first is capable to approximate the stress-strain relation up to the 0.2% proof stress and the second domain from the 0.2% proof stress $\sigma_{0.2}$ up to the ultimate stress σ_u . The level of non-linearity is incorporated in the expression by means of material non-linearity parameters n and m for the first and second domain respectively.

By varying aforementioned non-linearity parameters, the Ramberg-Osgood relation has been curve-fitted to the stress-strain curves obtained from tensile tests on 3D-printed steel (see also appendix C.2.3). The goodness of fit has been evaluated by using the sum of squares due to error (SSE). An example of such a fit for both domains of a dot-by-dot printed specimen tested in longitudinal direction is depicted separately in figure 5.7 for values up to the 0.2% proof stress and in figure 5.8 for values exceeding the 0.2% proof stress with corresponding non-linearity parameters.

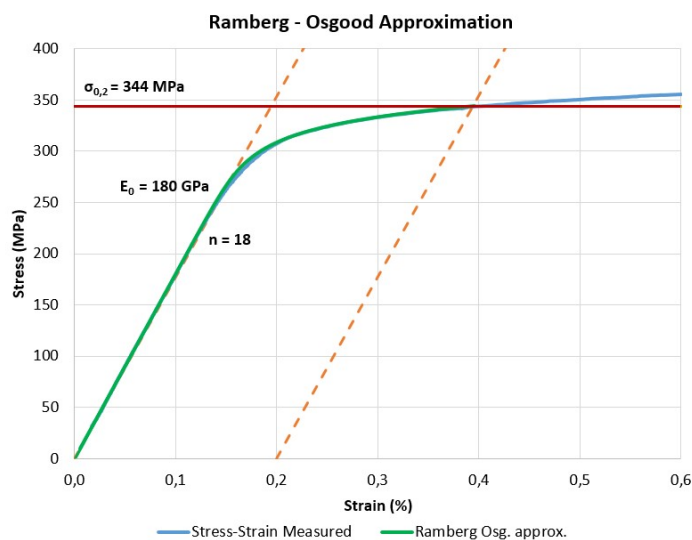


Figure 5.7: Ramberg-Osgood approximation of stress-strain relation up to 0.2% proof stress

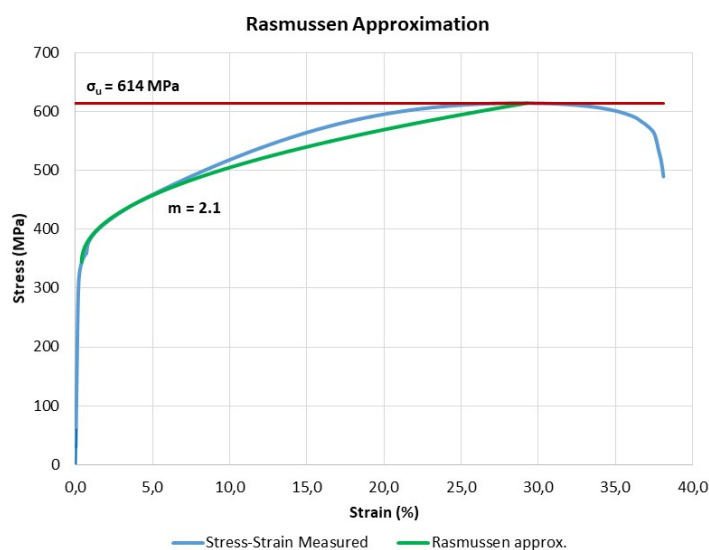


Figure 5.8: Rasmussen approximation of stress-strain relation for stresses exceeding the 0.2% proof stress

The obtained results of all the curve-fits are summarized in table 5.1 for dot-by-dot printed specimens and in table 5.2 for continuously printed specimens. For dot-by-dot specimens non-linearity parameter values of $n = 16$ and $m = 2.2$ are proposed when loaded in the print (longitudinal) direction and $n = 12$ and $m = 2.0$ for specimens loaded perpendicular to the print (transversal) direction. For continuous specimens the proposed values slightly differ: $n = 16$, $m = 1.7$ and $n = 14$, $m = 1.6$ for longitudinally and transversally loaded specimens respectively.

Table 5.1: Deduced non-linearity parameters for dot-by-dot printed specimen

	Non-Linearity Parameter	Specimen (1)	Specimen (2)	Specimen (3)	Mean	St. dev. σ
Longitudinal	Ramberg Osgood n [-]	18	18	13	16.3	2.4
	Rasmussen m [-]	2.13	2.18	2.30	2.20	0.07
Transversal	Ramberg Osgood n [-]	15	11	10	12.0	2.0
	Rasmussen m [-]	1.90	2.15	1.90	1.98	0.12

Table 5.2: Deduced non-linearity parameters for continuously printed specimen

	Non-linearity Parameter	Specimen (1)	Specimen (2)	Specimen (3)	Mean	St. dev. σ
Longitudinal	Ramberg Osgood n [-]	14	16	18	16.0	1.6
	Rasmussen m [-]	1.81	1.60	1.69	1.70	0.09
Transversal	Ramberg Osgood n [-]	12	14	16	14.0	1.6
	Rasmussen m [-]	1.79	1.60	1.41	1.60	0.16

From this analysis can be concluded that the stress-strain relation of both dot-by-dot and continuously printed specimens is more non-linear in transverse direction. In addition it can be concluded that the proposed values are significantly higher than the values stated in table 4.1 of EC3 part 1-4 (see also table 2.10). These values, obtained from tests on 'common' 304L and 316L stainless steels, range from $n = 6-8$ (longitudinal - transverse direction, 304L) and $n = 7-9$ (longitudinal - transverse direction, 316L). Although stainless steel grade 308L is not included in EC3, n -values for this grade are expected to lie in between the values for grade 304L and 316L. Since higher n -values correspond to less non-linear behaviour, the obtained results are especially beneficial with regards to deflection requirements in the serviceability limit state.

The proposed non-linearity parameters are in particular useful for application in finite element models of structures built up from WAAM stainless steel. In addition to tubular columns, finite element modelling allows to study the structural behaviour of a wide variety of shapes. This lies however out of the scope of this research.

The proposed n -values can also be implemented in the analytical (Ayrton Perry) buckling formulas as algebraically derived in section 2.4.3. The outcome is a buckling curve with incorporated material non-linearity in accordance with European (EC3) standards. The obtained curve can be used as additional reference curve, possibly providing a better fit to the buckling test results on 3D-printed tubular columns as presented in section 5.3.2. This analysis has however not been performed in this thesis and is therefore subject for additional research.

5.3. Buckling Analysis

In this section all test results are combined to analyse the buckling behaviour of additively manufactured tubular columns. First the effective buckling length of the test set-up will be derived in section 5.3.1. To conclude, a buckling curve is proposed with the validated test results in section 5.3.2.

5.3.1. Effective Buckling Length

While drawing the buckling curve of figure 4.5, it was assumed that the rotational bearings behave frictionless. The effective buckling length was thus assumed as the length between the rotation points of the bearings. It is obvious that the applied ball-bearings do not rotate frictionless, which leaves aforementioned assumption invalid. In this section the real effective buckling length of the test set-up is derived, incorporating friction.

Parallel to the buckling tests on additively manufactured tubular columns, buckling tests on cold-drawn carbon steel tubular columns with similar cross-sectional dimensions have been performed. In contrast to the printed specimens, these cold-drawn steel columns have a well-known homogeneous cross-section and known mechanical properties. However, the yield strength values as provided by supplier are conservative. Therefore additional tensile tests have been performed in Material Science & Engineering-laboratory of Delft University of Technology on these specimens to derive their real yield strength. Figure 5.9 shows the tensile specimens with a welded-in plug to reinforce the column-ends, like this enhancing gripping of the test set-up (figure 5.10).



Figure 5.9: Cold-drawn carbon steel specimens



Figure 5.10: Tensile test set-up

It can be seen in figure 5.11 that the ultimate tensile strength F_u equals 91 kN assuming a bi-linear stress-strain relation. Dividing by its cross-sectional area corresponding to a homogeneous circular column section with $D_{\text{out}} = 30$ mm and $t = 4.0$ mm, this results in a yield stress of 278 N/mm^2 . This is significantly higher than 225 N/mm^2 which was provided by the supplier. From the tangent line of the force-strain curve a Young's modulus of 226 GPa is deducted. This is a common value for carbon steels. The obtained test result will be used in the proceeding of this analysis.

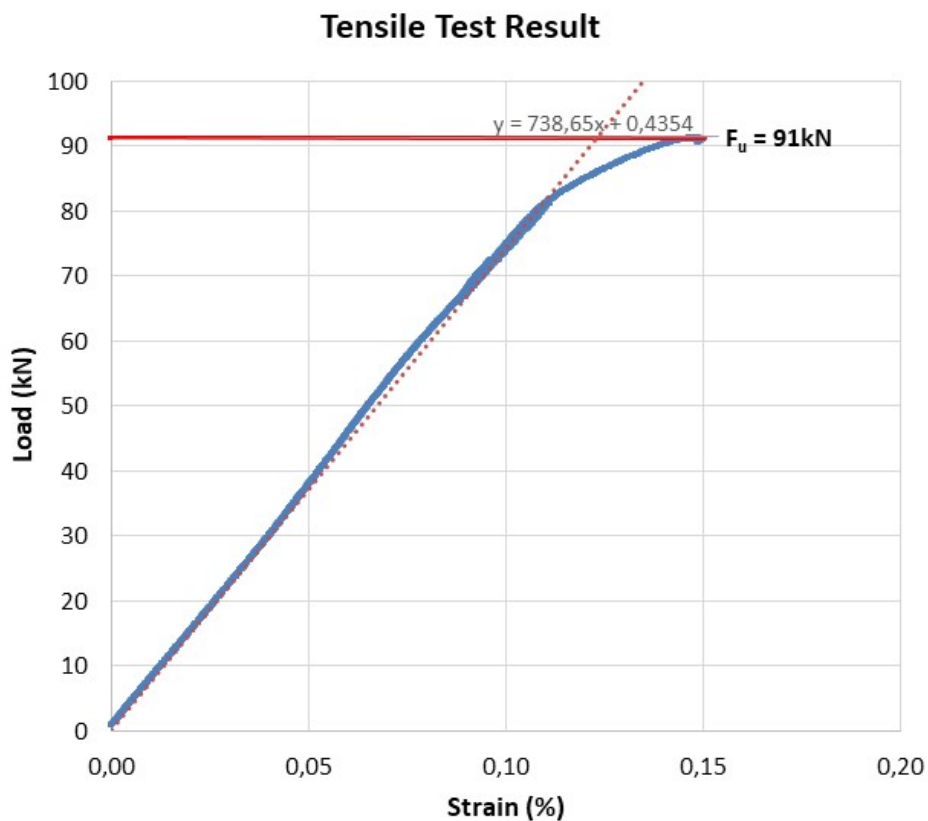


Figure 5.11: Tensile test result of cold-drawn carbon steel specimen

The following results have been obtained from the buckling tests on cold-drawn steel specimens (from now on called 'Dummy'). In table 5.3 it can be seen that all four set-up lengths are tested. From the attained buckling loads and the earlier deduced plastic capacity of 91 kN, the buckling reduction factor χ can be calculated.

Table 5.3: Buckling test results for cold-drawn steel columns

Specimen	Buckling Length L_{syst} [mm]	Buckling Load F_{buc} [kN]	Plastic Cap. N_{pl} [kN]	Red.Fact. χ [-]
Dummy-125-1	1288	56.47	91.00	0.621
Dummy-125-2	1288	36.47	91.00	0.401
Dummy-125-3	1274	38.18	91.00	0.420
Dummy-85-1	874	47.00	91.00	0.517
Dummy-85-2	884	78.00	91.00	0.857
Dummy-65-1	684	81.72	91.00	0.898
Dummy-48-1	514	82.96	91.00	0.912

Using column curve 'c' of Eurocode 3 [56] as shown in figure 2.42, the relative slenderness λ_{rel} can be calculated using the from tests obtained buckling reduction factors χ . It should however be noted that this is a conservative approach because this buckling curve is a design curve. The European buckling curve is fitted on buckling test results minus twice the standard deviation. As a consequence, the derived effective buckling length and resulting buckling strength is lower than the actual tested value. This should be taken into account when proposing a buckling curve for wire and arc additively manufactured specimens.

Using the Eurocode 3 definition²⁷ [56] of relative slenderness λ_{rel} for flexural buckling, the effective buckling length L_{eff} have been calculated. Hence, the effective buckling length factor K is obtained by dividing the

²⁷NEN-EN 1993-1-1+C2 clause 6.3.1.3

effective buckling length L_{eff} by the measured system length L_{sys} . Where the latter is the distance between rotation points of both ball bearings. The result is shown in table 5.4.

Table 5.4: Effective buckling length factor calculation

Specimen	Rel Slend. λ_{rel} [-]	L_{eff} [mm]	L_{sys} [mm]	Effective Buckling length factor K [-]
Dummy 125	1.28	1063	1288	0.825
Dummy 48	0.38	316	514	0.614

For the most slender column an effective buckling length factor of $K = 0.825$ is obtained, whereas for the most stocky column a value of $K = 0.614$ is obtained. This is a logical result because the stocky columns are subject to higher forces which results in increased friction at the rotational bearings. In the proceeding of the analysis these length factors will be used to calculate the effective buckling lengths. K -factors for columns in between the most and least slender will be interpolated. Section 5.3.2 presents the obtained buckling test results with newly incorporated effective buckling lengths.

5.3.2. Proposed Buckling Curve

After having adopted and analysed a wide variety of mechanical tests, this section combines all the obtained results in one buckling curve. Whereas the buckling curve as proposed in section 4.2.2 is bounded to the assumptions made regarding the 0.2% proof stress, Young's modulus, effective cross-section and effective buckling length; the buckling curve proposed in this section is based on validated tests. Both the 0.2% proof stress and the Young's moduli are derived by analysing the tensile test results as provided in section 4.2.4. The effective buckling length has been derived in section 5.3.1 by performing buckling tests on steel columns with known mechanical and geometrical characteristics. Furthermore, the effective cross-sectional area is derived using both tensile and four-point bending test results as described in section 5.1.

Due to changing variables L_{eff} and λ_{rel} , the buckling curve as earlier presented in figure 4.5 has shifted. See table 5.5 and 5.6 for the final results.

Table 5.5: Final buckling test results for dot-by-dot printed specimens

Specimen	Eff. Buckling length L_{eff} [mm]	Rel. Slend. λ_{rel} [-]	Buckling load F_{buc} [kN]
A-125-1	1040	1.416	31.96
A-125-2	1040	1.417	31.84
A-125-3	1059	1.443	55.88
A-85-1	623	0.849	53.80
A-85-2	634	0.864	48.79
A-85-3	631	0.859	48.76
B-1-A	470	0.640	58.45
B-2-A	468	0.637	62.68
B-3-A	470	0.640	63.99
A-48-1	293	0.399	79.34
A-48-2	292	0.397	80.71
A-48-3	291	0.396	81.57

Table 5.6: Final buckling test results for continuously printed specimens - assuming $E = 200$ GPa and $\sigma_{0.2} = 350$ N/mm²

Specimen	Eff. Buckling length L_{eff} [mm]	Rel. Slend. λ_{rel} [-]	Buckling load F_{buc} [kN]
B-1-B	495	0.757	52.38
B-2-B	498	0.762	51.97
B-3-B	498	0.762	53.87

Figure 5.12 shows the final obtained buckling test results graphically. As a reference, the European buckling curves [48] for stainless steel hollow sections and welded open sections are added to the diagram. The results clearly show reduced buckling strength values for all members within the tested slenderness range compared to the reference curves. This can be explained by the geometrical imperfections in the printed columns both globally and locally. Wall thickness variations are present across the considered buckling planes, whereas only an average cross-sectional area is used for the calculation of the relative slenderness.

Additionally, global imperfections, despite being induced by local printing errors, are larger than accounted for in EC3. An initial curvature averaging $e_0 = L/633$ has been obtained for printed columns, whereas for the European buckling calculation a conservative imperfection of $e_0 = L/1000$ is assumed. A larger initial curvature of a column implies more eccentric loading and a reduced buckling capacity.

The Young's moduli and yield strength values are incorporated in the calculation of the buckling curves by means of buckling imperfection parameter α . Obviously, the lowered stiffness and 0.2% proof strength values in transversal (perpendicular to print) direction compared to standard values for 308L-grade stainless steel causes a further reduction of buckling capacity in comparison with the Eurocode values.

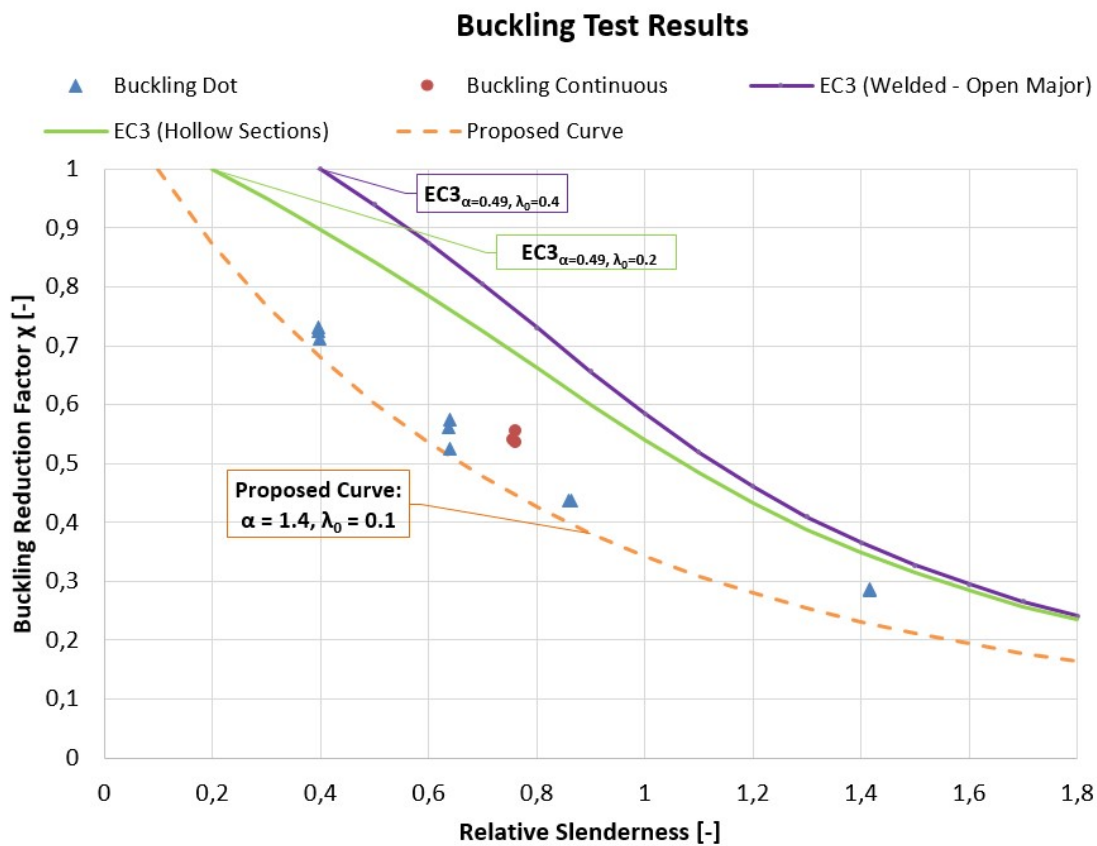


Figure 5.12: Final buckling test results and proposed buckling curve

Without adopting the effective cross-section, a buckling curve with imperfection factor of $\alpha = 1.4$ and limiting slenderness of $\lambda_0 = 0.1$ gives a good fit for the buckling test results. The proposed buckling curve has been fitted to the average buckling strength values (for a given tested column length), minus twice the standard deviation. This is in conjunction with the buckling curves in EC3. The obtained result is a large improvement compared to the deducted buckling curve for printed stainless steel rods proposed by Joosten [5] where an imperfection factor of $\alpha = 3.0$ has been applied to fit the test results.

In section 5.1 it is already proven that because of wall thickness variations, the effective cross-sectional area is smaller than the deduced average cross-section. Especially for dot-by-dot printed columns this reduction is significant (17.3 %). This explains why for continuously printed columns, despite only one column length

has been tested, higher buckling reduction factors are observed which results in a relatively higher buckling resistance. To show the effect of wall thickness variations, the buckling curve has been redrawn in figure 5.13, now using the effective cross-sectional area as derived in section 5.1. Indeed, a higher buckling resistance can be observed with values closer to the reference curves. In this case a curve with an imperfection factor of $\alpha = 1.0$ and limiting slenderness of $\bar{\lambda}_0 = 0.2$ gives a good fit to the buckling test results. Again the proposed buckling curve has been fitted to the average buckling strength (for a given tested column length) as tested minus twice the standard deviation.

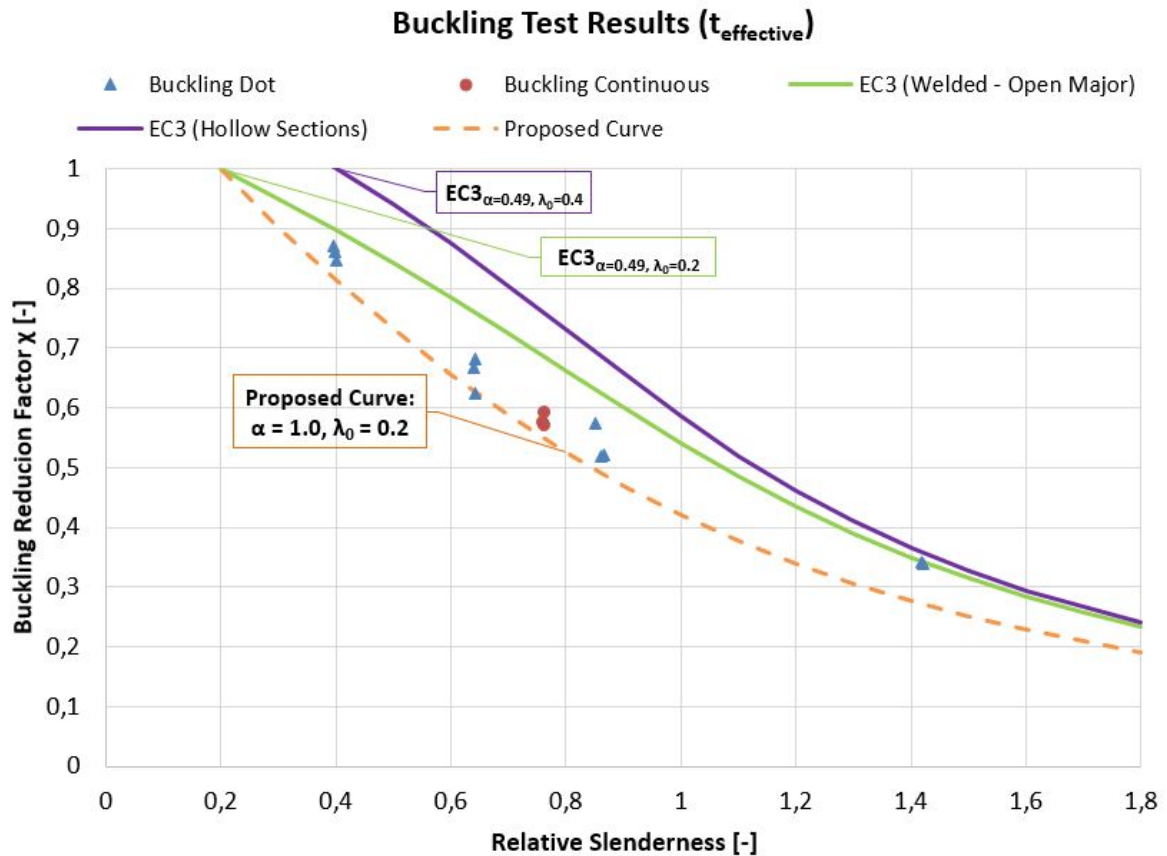


Figure 5.13: Final buckling test results and proposed buckling curve using effective cross-sections

Referring to the expression for the design buckling load $N_{b,Rd}$ (equation (2.24)), EC3 prescribes a partial safety factor of γ_{M1} equal to 1.1 for members checked on instability. Because in this research relatively few tests have been performed compared to EC3, a higher value may have to be used to achieve a level of safety similar to conventionally produced steels. This analysis however requires extensive statistical research that is not part of the scope of this thesis. Therefore the safety factor as prescribed by the Eurocode, $\gamma_{M1} = 1.1$, has nevertheless been assumed in this research. Future research should confirm whether the assumed safety factor provides the desired level of safety.

6

Conclusions & Recommendations



Chapter 6 discusses all the results acquired from literature study and the conducted tests. In section 6.1 first the final conclusion is drawn which answers the research question, after which the conclusions are further elaborated arranged by subject. Recommendations are stated in section 6.2 providing guidance for future research topics.

6.1. Conclusions

In this chapter conclusions will be stated Arranged by the main subjects that are covered in this research. First a general conclusion is given which presents an answer to the formulated research question.

Answer to Research Question

Anticipating to the application of wire-arc additive manufacturing for the production of large-scale structural elements and the lack of understanding of the stability of such elements, the following research question has been formulated:

What are relevant geometrical and material properties of 3D-printed steel to assess the stability of wire and arc additively manufactured stainless steel tubular columns?

Based on the literature study and experiments on additively manufactured stainless steel tubular columns the research question can be answered:

It can be concluded that local wall thickness variations and relatively high out-of-straightness values, that induce eccentric loading, reduce the buckling capacity and should therefore be considered while assessing stability of printed columns.

Furthermore it is concluded from tests that material properties of 3D-printed steel differ from conventional steel. The printing process with accompanying printing parameters is greatly affecting the material characteristics. Following the thermal gradient of the weld pool, large columnar grain structures are observed giving rise to anisotropy. A heterogeneous grain structure is observed with varying grain size. The coarseness of the grain structure negatively affects mechanical properties and thus affects stability.

Indeed, anisotropic material behaviour is observed in test results and this should be taken into account in calculations. Stiffness, strength and ductility values prove to be dependent on the print direction. The obtained stiffness values are significantly lower than is commonly assumed for structural steels. In particular the lowered stiffness and yield strength of the material are negatively affecting the buckling capacity of printed members and should therefore be accounted for in a stability assessment.

With the identified material and geometrical properties of 3D-printed steel, a buckling curve is proposed. Similarly to the existing buckling equations in the European standard for stability of (stainless) steel members [48], it is based on the Ayrton-Perry equations. The proposed curve is fitted to the obtained buckling test results by adjusting imperfection factor α and limiting slenderness $\bar{\lambda}_0$ in the Ayrton-Perry equations. In this way the specific geometrical and material properties of 3D-printed steel are incorporated in the assessment. It can be concluded that by using the existing European buckling standards of steel members (EC3), considering the obtained values for the 0.2% proof strength $\sigma_{0.2} = 319$ MPa and the Young's modulus equal to $E_0 = 155$ GPa, the proposed curve is capable of describing the buckling behaviour of 3D-printed steel tubular columns with an imperfection factor of $\alpha = 1.4$ and a limiting slenderness of $\bar{\lambda}_0 = 0.1$.

In accordance with EC3 the design buckling load $N_{b,Rd}$ is obtained by deviding the characteristic value by a prescribed partial safety factor γ_{M1} equal to 1.1 for members checked on instability [56]. Because in this research relatively few tests have been performed to derive a safety factor, a higher value may have to be used to guarantee the desired level of safety is at the current level of conventionally produced steels. This analysis requires however extensive statistical research that is not part of the scope of this thesis. Therefore the safety factor γ_{M1} , prescribed by the Eurocode, has been adopted in this research.

The proposed buckling curve, based on own experiments, will be a next step towards a safe stability model suitable for structural applications of additively manufactured tubular steel members.

More specifically the following is concluded sorted per subject:

Geometrical Properties

Cross-Sectional Analysis

Visual inspection shows a highly irregular surface with accompanying wall thickness variations, in particular for dot-by-dot printed specimens. This is observed in both longitudinal and transversal column sections. For thin-walled dot-printed specimens there is an increased risk that the heterogeneous structure locally results in a reduced wall thickness between each spot weld. The heterogeneity of the structure can be partly explained by changing cooling conditions caused by the travel of the robot and the number of print starts/stops. In some sections microcracks were observed at locations that coincide with the location of two merging spot welds. Such a microcrack may reduce the fatigue-life drastically. This analysis is however not part of this thesis. Therefore the continuous printing strategy is currently preferable for industrial grade structural elements that are exposed to cyclic loads.

From length measurements and by submerging the specimens in fluid (Archimedes' principle), an average cross-sectional area of printed tubular column sections has been deduced. Due to wall thickness variations the effective cross-section, meaning the cross-sectional area that effectively contributes to the resistance to loads, proves to be smaller than the (homogeneous assumed) average cross-section as deduced from volume measurements.

By combining results of four-point bending and tensile tests, assuming a nominal diameter of 30.1 mm around which the wall thickness varies, the effective cross-section is derived for both continuously and dot-by-dot printed columns. For dot-by-dot printed sections, the wall thickness of dot-by-dot printed sections reduced from 3.7 to 3.06 mm, yielding a reduction of cross-sectional area of 17.3% compared to the homogeneous assumed average cross-sectional area. Continuously printed sections show significantly less reduction: from 3.2 mm to 3.01 mm, yielding a reduction of 5.9%. This effective wall thickness of a homogeneous assumed section can be used by structural engineers in strength calculations.

It should be remarked that the percentage reduction only holds for the specimens that are specifically tested in this research. By expressing the reduction of wall thickness in absolute values (0.64 mm for dot and 0.19 mm for continuous printed sections), it enables structural engineers to calculate with a homogeneous 'working' cross-section that can be applied to printed sections with different dimensions and shapes as well. This methodology additionally allows designers to apply 3D-printed elements directly, without any post-surface treatment to overcome geometrical irregularities. With regards to these irregularities it can be concluded that continuous printing is the more efficient strategy.

Yet it should be acknowledged that this conclusion is drawn for specimens that are printed over a year ago²⁸. With current rapid advancements in improving the printing process, the occurrence of geometrical imperfections and corresponding cracks in the sections is soon expected to reduce drastically. Dot-printed elements are consequently over time likely to be more competitive with their continuously printed counterparts regarding consistency in geometry.

Global Imperfections

Global imperfections, despite being induced by local printing errors, are larger than assumed in Eurocode 3 for steel buckling members. From both hand measurements and 3D-scan analyses, it can be concluded that the out-of-straightness of printed columns, expressed in ratio eccentricity over the column length, average $e_0 = L/674$ with a standard deviation of $L/49$. Whereas 3D-scans were more reproducible, they gave more consistent results with an out-of-straightness of $e_0 = L/633$ and a fairly low standard deviation of $L/13$. From both analyses it can be concluded that the initial curvature of printed specimens is larger than of the steel buckling members tested in Eurocode 3, for which a conservative imperfection of $e_0 = L/1000$ is accounted for in buckling resistance calculations. A larger initial curvature of a column implies more eccentric loading and a reduced buckling capacity of the considered member.

²⁸mid-April 2016

From 3D-scan analyses and visual observations it can be concluded that these values can be largely explained by local printing errors. More specifically an entire print layer might be shifted from the longitudinal axis of the column. This error is a common phenomenon for AM. Since the columns are printed vertically, successively deposited print layers might deviate from their intended position due to vibration of the column specimen or misalignments of the welding head, consequently causing additional out-of-straightness. It can however be concluded that due to rapid advancements of the printing process, these errors have largely been overcome for specimens being produced at the date of writing. It is expected that specimens without these printing errors have a higher resistance to buckling.

Mechanical Properties

Bending Stiffness

From four-point bending tests on both dot and continuously printed columns, their bending stiffness is obtained from the tangent to the descending branch (unloading stage) of the load-displacement curve. The columns are rotated 90 degrees around their longitudinal axis and tested once again (repetitively four times) to analyse flexural stiffness variations. The tests showed a very high consistency in results with a standard deviation of 1 to 2%. It can be concluded that, despite the presence of wall thickness variations, bending stiffness variations across the section are negligible. Yet, the reduced effective cross-section, together with reduced elastic stiffness values E_0 (further addressed in 'Tensile Properties'), the tested bending stiffness is lower than predicted. This holds for both continuously as dot-by-dot specimens.

Tensile Properties

Research institute OCAS performed tensile tests on milled specimens extracted from a by MX3D printed plate-geometry. The results have been analysed in this thesis. Specimens loaded both in their print direction and perpendicular to their print direction have been tested for both print strategies. From the obtained stress-strain curves, their corresponding 0.2% proof stress, ultimate tensile strength, stiffness and ultimate strain is deducted.

Whereas the ultimate tensile strength for dot-by-dot printed specimens in longitudinal (print) direction, with an average value of 614 N/mm^2 exceeds both reference values of 'as welded' material provided by the material supplier ($520\text{-}600 \text{ N/mm}^2$), the tensile strength observed in transversal (perpendicular to print) direction, although with a large spread, is significantly lower (511 N/mm^2). A similar trend is observed for the 0.2% proof stresses, for which lower values are observed in transversal (perpendicular to the print) direction (averaging 319 versus 342 N/mm^2 in longitudinal direction).

This anisotropic behaviour is also clearly visible in the lower (initial) stiffness values E_0 obtained in transversal direction (averaging 155 GPa), compared to the stiffness in longitudinal direction (averaging 181 GPa). This reduction is even more imminent in the stiffness values of continuously printed specimens, where average values of 137 and 121 GPa are observed in respectively longitudinal and transversal direction. Both values are significant lower than 200 GPa , which is prescribed by Eurocode 3 for cold-formed austenitic stainless steels.

Furthermore it is observed that specimens tested in longitudinal direction behave more ductile than their transversely-tested counterparts. One specimen tested perpendicular to its print direction did not pass the ductility requirements of Eurocode 3 due to early fracture: ($\epsilon_f < 15\%$). Since all other results prove that the material is sufficiently ductile, this specific early fracture was probably caused by a print error. However, to guarantee sufficient deformation capacity, early detection of defects by means of a quality inspection of printed elements is crucial.

The non-linearity of the stress-strain relation has been approximated by curve-fits using the analytical model of Ramberg-Osgood-Rasmussen. For dot-by-dot printed specimens non-linearity parameter values of $n = 16$ and $m = 2.2$ are proposed in longitudinal direction and $n = 12$ and $m = 2.0$ for specimens loaded in transversal (perpendicular to print) direction.

For continuous specimens the proposed values slightly differ: $n = 16$, $m = 1.7$ and $n = 14$, $m = 1.6$ for longitudinally and transversally loaded specimens respectively. From this analysis it can be concluded that both dot-by-dot and continuously printed specimens behave more non-linear in transversal direction.

In addition it can be concluded that the proposed non-linearity parameters are significantly higher than the values prescribed in table 4.1 of EC3 part 1-4. These values are obtained from tests on 'common' 304L and 316L stainless steels and range from $n = 6 - 8$ (longitudinal – transversal direction, 304L) and $n = 7 - 9$ (longitudinal - transversal direction, 316L). It is concluded that the advised EC3 values are very conservative for this 3D-printed material.

The proposed non-linearity parameters are particularly useful to incorporate this specific stress-strain relation in finite element models. Besides modelling tubular columns, finite element modelling allows the study of the structural behaviour of a wide variety of shapes, hence the full potential of WAAM can be exploited.

Hardness & Toughness

Vickers hardness line-measurements (HV3) have been performed on longitudinal and transversal sections of both dot-by-dot and continuously printed column specimens. Slightly higher hardness values are observed for dot-by-dot printed specimen, averaging 195 Vickers compared to 190 Vickers for continuously printed specimens. For both printing strategies it is observed that the outside of the column wall (averaging 194 Vickers) is slightly harder than the inside (averaging 191 Vickers). In addition it is observed that the longitudinal tested specimen sections for both strategies attain significantly higher hardness values (203 Vickers) compared to transversal sections (187 Vickers).

Additional Brinell hardness measurements have been performed by OCAS on dot-by-dot and continuously printed specimens. In contrast to the (Vickers) hardness measurements performed on column specimens, the continuously printed specimens are observed to be harder than the dot-printed specimens. The exact reason for this difference is not known, but the large spread in test results and the minor difference between both averages makes it difficult to draw conclusions. It is known that the number of heat cycles experienced by the metal during printing correlates inversely with their hardness [92]. This means that because the final layer deposits of a WAAM-specimen experiences fewer thermal cycles, the hardness at that location might increase. More hardness tests should be performed on various sections to investigate whether the observed variations in hardness can be explained by this theory.

OCAS performed Charpy pendulum impact test on both dot-by-dot and continuously printed specimens at a temperature of -40, -20 and 20 °C. The results are studied in this research. It is observed that dot-by-dot printed specimens attain high absolute toughness values, but also show a very large spread in results. This is possibly caused by inclusions, which increases the susceptibility to brittle fracture. Tensile test results show indeed relatively low fracture strains for dot-by-dot printed specimens loaded perpendicular to their direction. Whereas the toughness values of transversal sections all exceed the reference value, the longitudinal sections show significantly lower toughness values. The continuous printing process also shows good toughness values comparable with the reference value for TIG or MIG processes (160 J/cm²) and with a low spread.

Metallography

Grain Formation, Solidification Structure & Phase Identification

Large columnar grain structures are observed in both continuously and dot-by-dot printed specimens. The grain structures follow the direction of the thermal gradient of the weld pool. These formations are undesirable since they limit plastic deformation, which consequently results in anisotropy of mechanical properties. This directional grain structure also explains the lowered ultimate strain values for certain specimens as observed during tensile testing.

The microstructural composition differs in each point due to changes in thermal history. Interpass epitaxial growth results in coarser grain structures, consequently negatively influencing mechanical properties.

From the x-ray diffraction analysis no precipitates have been detected. This is a positive result since precipitates could promote intergranular corrosion. From the same analysis it is found that both austenitic and ferrite phases are present in the printed sample.

Material Defects

Several oxide inclusions have been detected by scanning electron microscopy. These non-metallic inclusions might affect the material properties negatively. In addition, pores with a maximum diameter of 200 micrometer across have been detected. Such large pores possibly lowers ductility and strength values.

From volume and weight measurements an average density has been determined. For columns printed by continuous and dot-by-dot strategy similar results are obtained with a density of 7.94 and 7.91 g/cm³ respectively. This is in conjunction with the standard density value of 7.90 g/cm³ provided for 308LSi stainless steel. Consequently there is no indication of large-scale porosity as this would have lowered the density values.

Using Energy Dispersive X-Ray Fluorescence (EDXRF), the chemical composition of both dot-by-dot and continuously printed specimens has been identified quantitatively. From the analysis of the specimens a slight deviation (reduction) in Si- and (increase in) N-levels from typical Ugiweld 308LM welding wire composition values can be observed. This observation holds for both printing strategies. The change in composition can be explained due to inclusions added during the printing process.

Inspection of internal cleanliness using optical microscopy and Energy Dispersive X-ray (EDX) analysis indeed shows that inclusions are present in all analysed specimens. The inclusions, mainly globular oxides rich in silicon, manganese and sulphur, are unevenly distributed. In dot-by-dot printed specimens more inclusions are observed than in their continuously printed counterparts. The increase of Nitrogen in the structure can be explained by a poor gas shielding condition, possibly causing an increase of yield strength and a loss of ductility compared to the properties of the original welding wire material.

Dot-by-Dot versus Continuous Printing

From this research it can be concluded that material and geometrical properties of dot-by-dot printed material significantly differ from that of continuously printed material.

Despite dot-by-dot printed specimens attain more surface irregularities compared to continuously printed ones, which might give rise to a lowering of fatigue resistance, dot-by-dot printing has an advantage over continuous printing: it allows for production of a wider range of shapes. More importantly, this technique allows to 'play' with the order of material deposition, so that subsequently the cooling rate of the material can be managed globally or locally. In general a higher cooling rate results in a stronger (but less ductile) material [71]. Dot-by-dot printing allows for quicker cooling in between material deposits. Tensile test results indeed confirm this theory, since for dot-by-dot printed specimens higher strength values (in print direction) and a more brittle behaviour (perpendicular to print direction) is observed. By these means printing strategy is an important tool to achieve the material properties that are desired for a specific wire and arc additively manufactured product.

Despite dot-printing provides more freedom in material deposition, continuously printing is undoubtedly a more stable process. It gives more control over the process in practice so that the interpass temperatures can be managed accurately. This is not the case for dot-printing as predictive thermomechanical models for large-scale dot-by-dot printed geometries are lacking, which makes it difficult to optimise the dot-by-dot printing process.

Additionally it is important to state that for continuous printing a higher deposition rate can be achieved than for dot-by-dot printing. Where this is very much depending on the geometry, values range from 2-3 kg/h for continuous printing versus an average of 0.75 kg/h for dot-by-dot printing. It can be concluded that dot-by-dot printing proves to be a good alternative for the much wider applied continuous printing strategy with regards to mechanical properties, but is advised for complex, relatively small shapes only (for instance connections). Or for use in combination with continuously printed parts. Additional research to fatigue resistance of both continuously and dot-printed specimens is however required, especially when WAAM is used to produce structural connections or entire structures that are subject to repetitive loads.

6.2. Recommendations

In this section a few subjects are mentioned that should be addressed in future research to assess the stability of wire and arc additively manufactured steel members further.

It would be recommended to:

- Develop a finite element model capable of predicting the stability of WAAM members using the material and geometrical properties as deducted from tests in this research. Material non-linearity should be incorporated adequately. Besides tubular columns, this additionally enables the modelling of complex shapes, so the full potential of 3D-print technology can be exploited.
- Conduct tensile tests on milled specimens extracted from column sections (instead from a plate geometry).
- Extend the slenderness range of tested tubular columns and test more slender columns ($\lambda_{rel} > 1.5$).
- Validate the partial safety factor as prescribed by Eurocode 3, $\gamma_{M1} = 1.1$, for members checked on instability by performing additional tests and a corresponding statistical analysis of the results.
- Determine the grain size of WAAM-specimens quantitatively and analyse its heterogeneous distribution.
- Develop predictive thermomechanical models for both continuous as dot-printing to predict the residual stress development and cooling behaviour in WAAM-columns. Print parameters can subsequently be optimised.

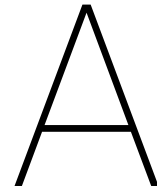
To improve the stability of WAAM tubular columns, the following actions can be undertaken:

- Live monitoring of the printing process, for example by thermal imaging and 3D-scan equipment, to reduce printing errors and defects and assure a consistent quality of the product. This could prevent misalignments of print layers, consequently greatly reduce the out-of-straightness of a printed column so that the resistance to buckling will increase.
- Apply active cooling, to control the cooling behaviour during manufacturing, like this enhancing strength values and reducing the down-time of the printing robot between weld deposits. This results in a more efficient process and a product with higher quality.

In order to enhance the structural application of WAAM in general it would be recommended to:

- Study the overall behaviour of structures that are - or consist of parts that are - wire and arc additively manufactured, such as for example complex connections, internally reinforced columns, shell or bridge structures.
- Start an extensive continuing test program to monitor improvements of material properties over time, at the same time assuring a consistent quality of the printed product is achieved.
- Study the fatigue resistance of structures that are additively manufactured or consists of additively manufactured parts.
- Apply active grain refinement and releasing of residual stresses using high-pressure rolling (only for standard shapes).
- Train and certify robot/print-operators to welding experts.
- Develop test and material standards. Standardization of tests and adopting quality records of tests is required to attain full confidence of construction industry for a large-scale structural application of additively manufactured structures or parts.

Appendices



General Information

A.1. Graduation Committee

em. Prof. ir. F.S.K. Bijlaard

Chairman

Position: Professor Steel Structures
University: Delft University of Technology
Faculty: Civil Engineering and Geosciences
Department: Structural Engineering
Office: Stevin II - 2.54
Address: Stevinweg 1,
2628 CN Delft
The Netherlands
Telephone: (+31) (0)15 27 84581
E-mail: F.S.K.Bijlaard@tudelft.nl

Prof. dr. I.M. Richardson

Representative Materials Science and Engineering (MSE) department

Position: Professor of Joining Technology
University: Delft University of Technology
Faculty: Mechanical, Maritime and Materials Engineering
Department: Materials Science and Engineering
Office: H-1-260
Address: Mekelweg 2,
2628 CD Delft
The Netherlands
Telephone: (+31) (0)15 27 85086
E-mail: I.M.Richardson@tudelft.nl

Ir. P.A. de Vries*University Supervisor*

Position: Researcher Steel and Timber Structures
University: Delft University of Technology
Faculty: Civil Engineering and Geosciences
Department: Structural Engineering
Office: Stevin II - 2.56
Address: Stevinweg 1,
2628 CN Delft
The Netherlands
Telephone: (+31) (0)15 27 84034
E-mail: P.A.deVries@tudelft.nl

A.2. Candidate**G.S. van Bolderen***Student Structural Engineering, Steel and Timber Structures*

Given names: Geoffrey Sebastian
University: Delft University of Technology
Faculty: Civil Engineering and Geosciences
Department: Structural Engineering
E-mail: gvan@bolderen.nl

A.3. Others Involved**MX3D:**

Tim Geurtjens

CTO & Co-Founder MX3D

Gijs van der Velden

COO & Co-Founder MX3D

Filippo Gilardi

*MX3D Expert, Developer and Robot Operator***TU Delft:**

Dr.ir. Marcel Hermans

Ass. Prof. Material Science and Engineering department, TU Delft: Metallography

John Hermsen

Lab Technician Stevin II-Laboratory, TU Delft: Mechanical tests and test set-ups

Bertus Naagen

Technician Faculty of Industrial Design, TU Delft: 3D-scans

B

Printing Parameters & Base Material

B.1. Printing Parameters

B.1.1. Dot-Print Strategy

The printing parameters in table B.1 have been used to manufacture the tubular columns with a dot-by-dot printing strategy.

By request of MX3D, the printing process parameters in table B.1 have been excluded from the public version of this thesis. Please contact MX3D: for contact information see appendix A.

B.1.2. Continuous-Print Strategy

The printing parameters applicable to the continuous printing strategy differ from the parameters that are used for the dot-printing strategy. Despite the use of the same base material, continuous printing does for example not involve any 'point distance' since the material is non-stop being applied.

By request of MX3D, the printing process parameters in table B.2. have been excluded from the public version of this thesis. Please contact MX3D: for contact information see appendix A.

B.2. Base Material

This section provides datasheets with chemical and mechanical characteristics of the welding wires that are used to 3D-print the specimens.

B.2.1. Datasheet Oerlikon Welding Wire

Oerlikon's Inertfil 308LSi welding wire has been used to print all specimens except for the plate material tested by OCAS (see section B.2.2).

INERTFIL 308LSi



**Drahtelektroden für das Schutzgasschweißen
korrosions- und hitzebeständige Stähle**

Massivdrahtelektrode für das MAG-Schweißen artähnlicher austenitischer Cr-Ni-Stähle/-Stahlgussorten. Unter Beachtung der Anforderungen auch einsetzbar für ferritische nichtrostende Cr-Stähle. Unter nasskorrosiven Bedingungen für Betriebstemperaturen bis 350 °C, zunderbeständig bis 800 °C. Höherer Siliziumgehalt für besseres Anfließen und Nahtaussehen. Spritzerarmer Werkstoffübergang im Kurz-, Sprüh- und Impulslichtbogen.

Normbezeichnungen		Zulassungen		Grad	
EN ISO	14343-A: G 19 9 L Si	DB			●
AWS	A5.9: ER 308L Si	TÜV			●

Chemische Zusammensetzung (typische Werte in %)

C	Mn	Si	P	S	Cr	Ni	Ferrit
0.020	1.8	0.85	≤ 0.025	≤ 0.020	20	10	5-10

Mechanische Eigenschaften des reinen Schweißgutes

Wärmebehandlung	Streckgrenze (MPa)	Zugfestigkeit (MPa)	Dehnung A5 (%)	Kerbschlagarbeit ISO-V (J)	
				20 °C	-120 °C
Unbehandelt	≥ 350	≥ 520	≥ 35	≥ 80	≥ 32

Schutzgas 98% Ar+2% O₂

Schutzgase - EN ISO 14175 : M12, M13

Werkstoffe

AISI 304 - 304L - 302
1.4541 (X6CrNiTi18-10); 1.4301 (X4CrNi18-10); 1.4311 (X2CrNiN18-10)

Lagerung/Rücktrocknung	Stromart/Polung/Schweißposition
Trocken lagern	DC+
	

Figure B.1: Datasheet Oerlikon Inertfil 308LSi welding wire (in German) [47]

B.2.2. Datasheet Ugiweld Welding Wire

For the tests performed by OCAS, a welding wire from Ugiweld with minor differences in chemical composition has been used to print the plate-shaped specimens. Figure B.2 and B.3 presents its specifications.

UGIWELD™ 308LM

Filler metal chemical composition	C	Si	Mn	Ni	Cr	Mo	Cu	N	S	P
	0.025	0.7 - 1.0	1.5 - 2.0	9.5 - 11.0	19.5 - 20.5	0.3	0.2	0.060	0.015	0.020

21-06-2013 – REV03

Category Stainless steel welding wires

Standards W Nr.: 1.4316
AWS - SFA 5.9: ER 308LSi
EN ISO 14343 – A: 19.9LSi

Approvals

	MIG	TIG	Subarc
TÜV (Germany)	X	X	X
DB	X	X	X
CE	X	X	X

Corrosion resistance

- Good general corrosion resistance. This grade is particularly recommended where there is a risk of intergranular corrosion.
- Very good atmospheric corrosion resistance in urban and rural medias.
- 308LM suits most food products and lot of chemical products such as cold alkaline solutions when diluted, cold organic acids when diluted, neutral and alkaline salt without holidays,....

Applications UGIWELD™ 308LM is a filler metal well suited for welding of austenitic stainless steels type 304 and 304L, and also stabilised austenitic stainless steel type 321.

- Equipment for chemical industry.
- Equipment for food processing industry.
- Pipes and tubes.
- Boiler engineering.

UGIWELD™ 308LM may be used for welding of some ferritic steels such as 409: automotive exhaust systems.

Figure B.2: Datasheet Ugiweld 308LSi welding wire (1/2) [90]

UGIWELD™ 308LM

Filler metal chemical composition	C	Si	Mn	Ni	Cr	Mo	Cu	N	S	P
	0.025	0.7 - 1.0	1.5 - 2.0	9.5 - 11.0	19.5 - 20.5	0.3	0.2	0.060	0.015	0.020

21-06-2013 – REV03

Recommended welding conditions

TIG welding

Shielding gas: Argon and/or Helium. Active gases are not recommended.

- **Welding parameters:** Look at the recommendations of the torch producer:

- Current: 50 - 250 A
- Voltage: 10 - 20 V

Interpass must be controlled to less than 150°C.

MIG welding

Shielding gas: Recommended shielding gases are:

- Argon + Oxygène (1 à 3 %)
- Argon + CO₂ (1 à 2..5 %)

- **Welding parameters:**

Ø Filler metal (mm)	0.8	1.0	1.2	1.6
Short-Arc				
Current (A)	60/80	80/120	100/150	
Voltage (V)	15/17	15/17	17/19	
Spray-Arc				
Current (A)	140/210	180/250	200/290	250/350
Voltage (V)	25/28	26/29	26/29	27/30
Flow of gas (L/min)	15	20	20	20

Water-cooled torch is recommended for high current above 250 A.

Interpass must be controlled to less than 150°C.

UGIWELD™ 308LM is suited for pulsed arc welding.

Mechanical properties on as weld deposit (typical values)

Using the recommended above welding parameters, the mechanical properties will be as follows

Temperature	TIG			MIG		
	-196° C	20° C	400°C	-196°C	20°C	400°C
Tensile (Mpa)		600	460		600	440
Yield (Mpa)		400	320		360	270
Elongation (5 dia.) (%)		40	30		35	25
Striction (%)		60			55	
Impact ISO V (J/cm ²)	110	160		70	120	

Figure B.3: Datasheet Ugiweld 308LSi welding wire (2/2)

C

Test & Measurement Results

C.1. Overview Specimens

In this section all specimens that are tested on their buckling and bending capacity are presented.



Figure C.1: Buckling test specimens - 125 cm



Figure C.2: Buckling test specimens - 85 cm



Figure C.3: Buckling test specimens - 48 cm



Figure C.4: Buckling and bending test specimens - 67 cm



Figure C.5: Buckling and bending test specimens - 67 cm; continuous-strategy

C.2. Mechanical Tests

C.2.1. Bending Tests

In this appendix the load-deflection curves obtained from four-point bending tests are presented. Tests have been performed on both dot-by-dot and continuously printed specimens. For both printing strategies three tubular columns have been tested four times. After every bending test the same column is rotated 90 degrees around its longitudinal axis as explained in section 3.4.1. The results are shown below.

Dot-by-dot - Specimen B-1-A

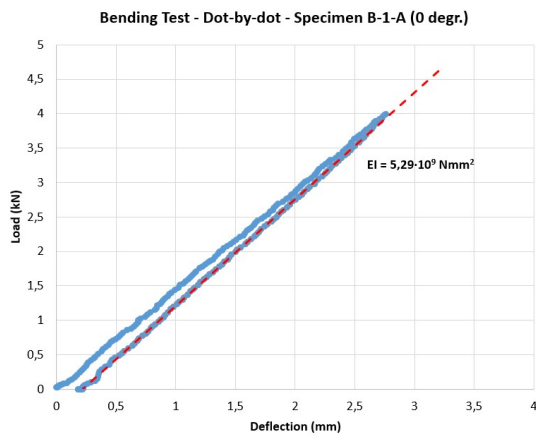


Figure C.6: Load-deflection: dot-by-dot - B-1-A (1)

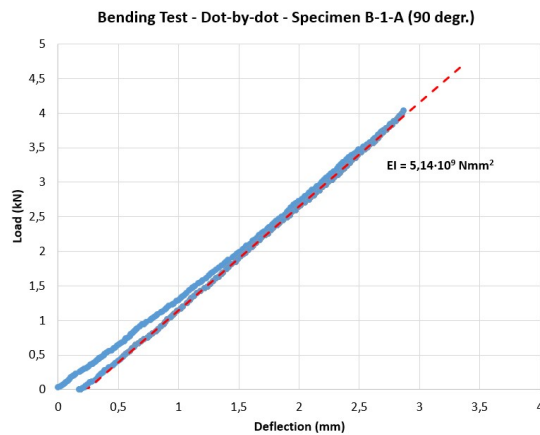


Figure C.7: Load-deflection: dot-by-dot - B-1-A (2)

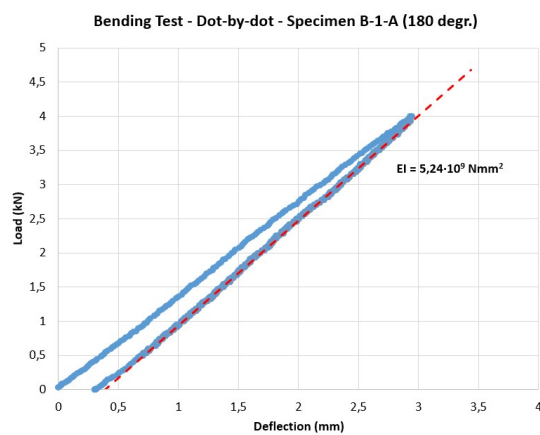


Figure C.8: Load-deflection: dot-by-dot - B-1-A (3)

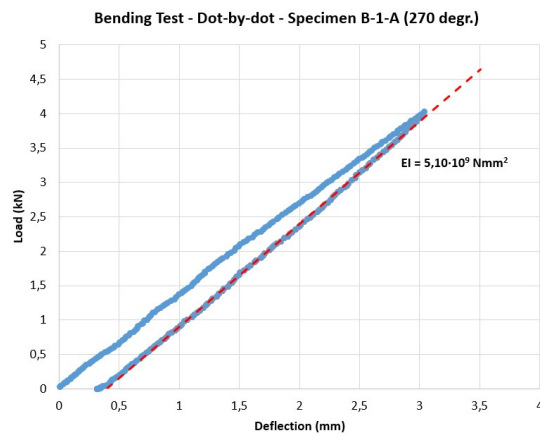


Figure C.9: Load-deflection: dot-by-dot - B-1-A (4)

Dot-by-dot - Specimen B-2-A

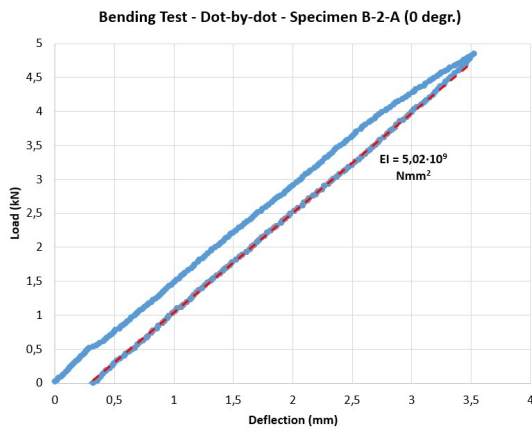


Figure C.10: Load-deflection: dot-by-dot - B-2-A (1)

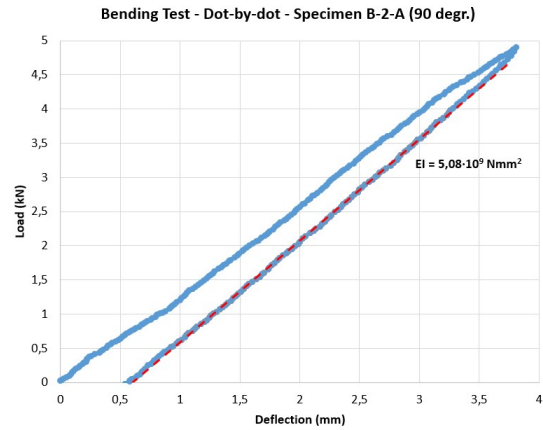


Figure C.11: Load-deflection: dot-by-dot - B-2-A (2)

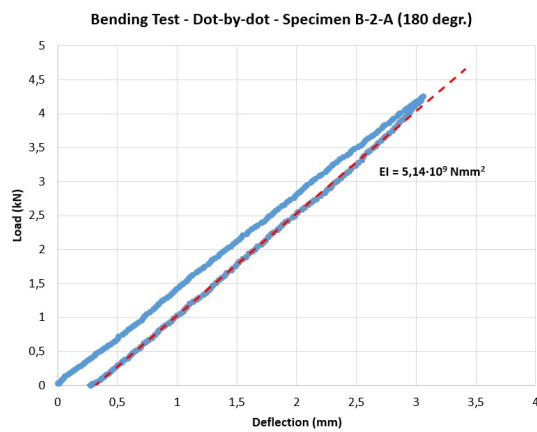


Figure C.12: Load-deflection: dot-by-dot - B-2-A (3)

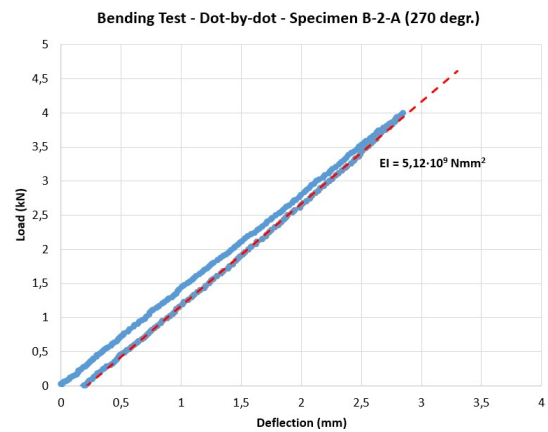


Figure C.13: Load-deflection: dot-by-dot - B-2-A (4)

Dot-by-dot - Specimen B-3-A

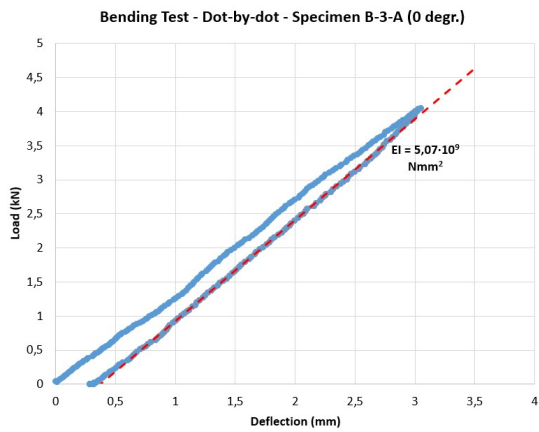


Figure C.14: Load-deflection: dot-by-dot - B-3-A (1)

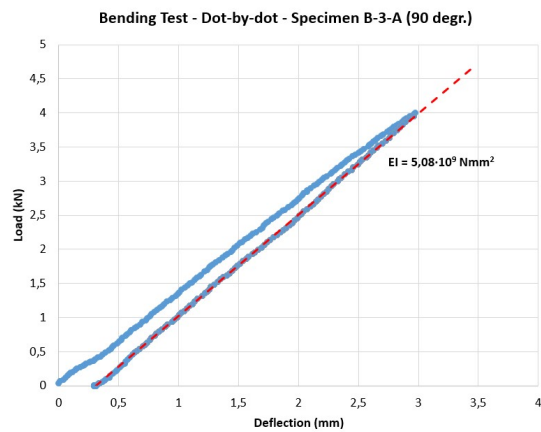


Figure C.15: Load-deflection: dot-by-dot - B-3-A (2)

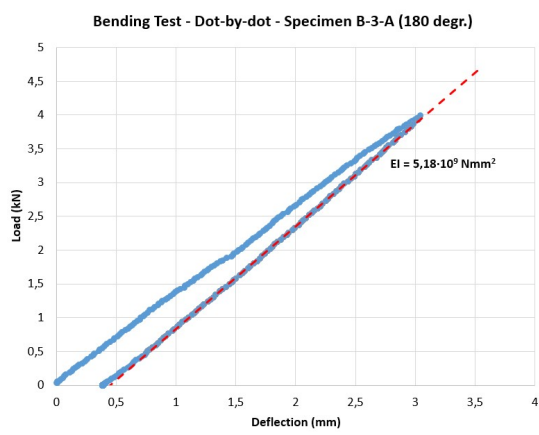


Figure C.16: Load-deflection: dot-by-dot - B-3-A (3)

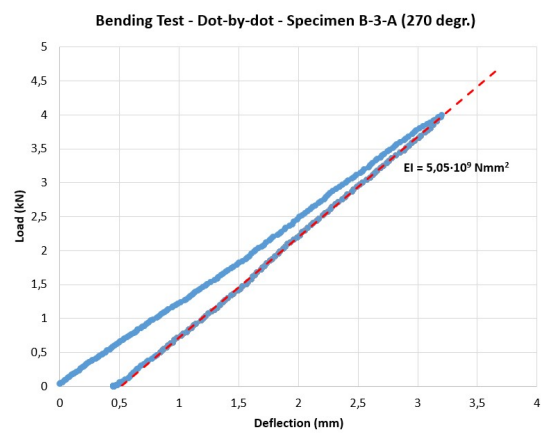


Figure C.17: Load-deflection: dot-by-dot - B-3-A (4)

Continuous - Specimen B-1-B

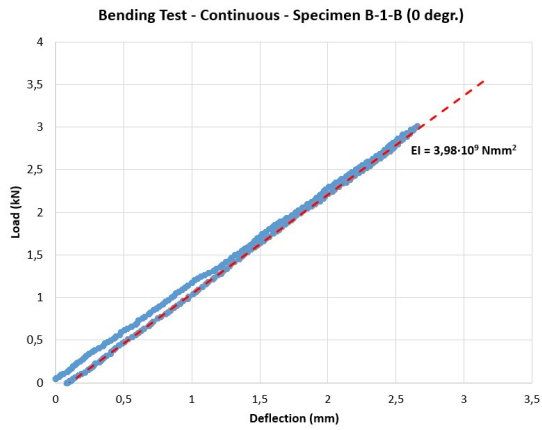


Figure C.18: Load-deflection: continuous - B-1-B (1)

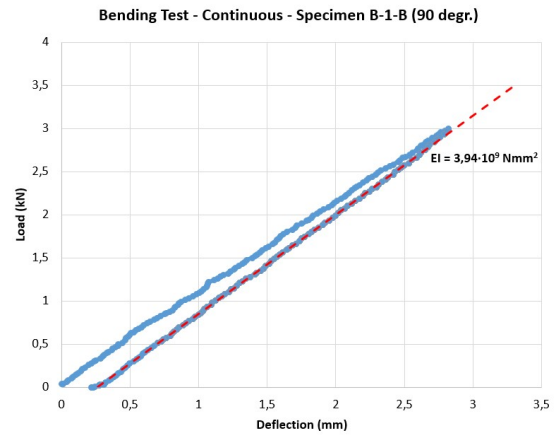


Figure C.19: Load-deflection: continuous - B-1-B (2)

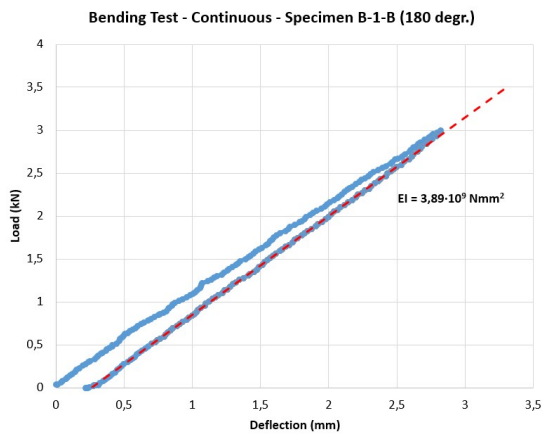


Figure C.20: Load-deflection: continuous - B-1-B (3)

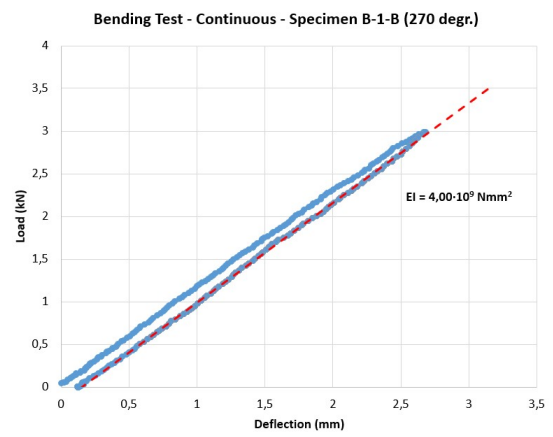


Figure C.21: Load-deflection: continuous - B-1-B (4)

Continuous - Specimen B-2-B

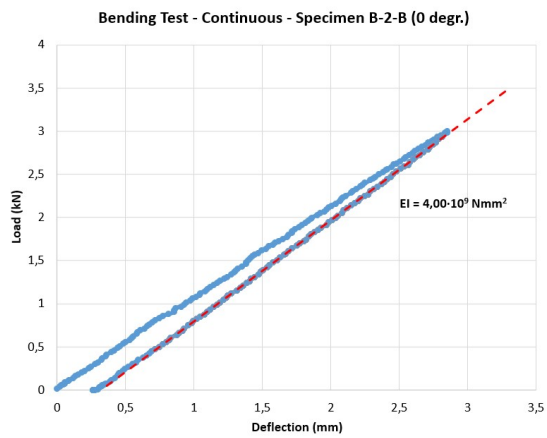


Figure C.22: Load-deflection: continuous - B-2-B (1)

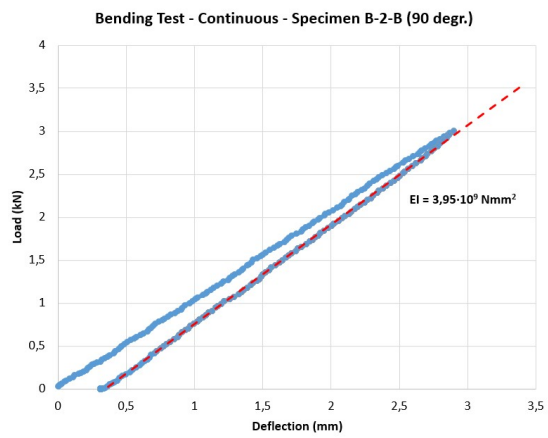


Figure C.23: Load-deflection: continuous - B-2-B (2)

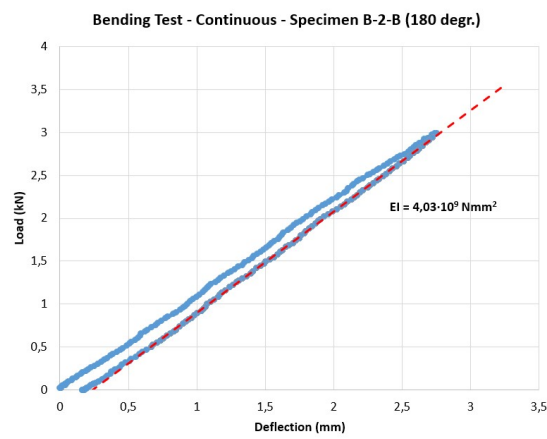


Figure C.24: Load-deflection: continuous - B-2-B (3)

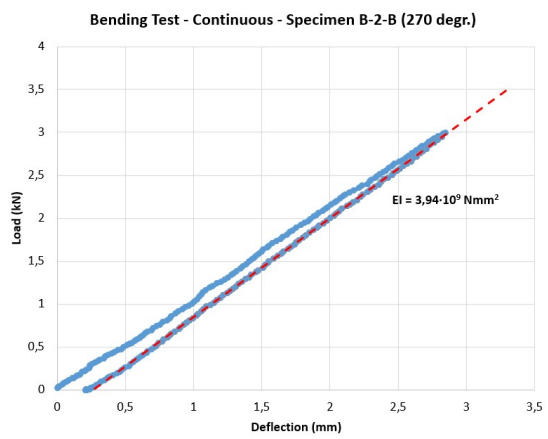


Figure C.25: Load-deflection: continuous - B-2-B (4)

Continuous - Specimen B-3-B

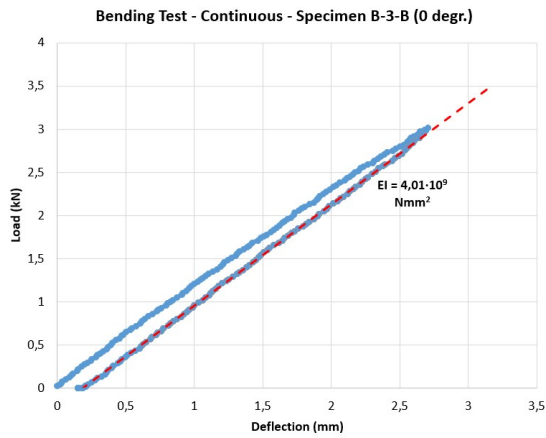


Figure C.26: Load-deflection: continuous - B-3-B (1)

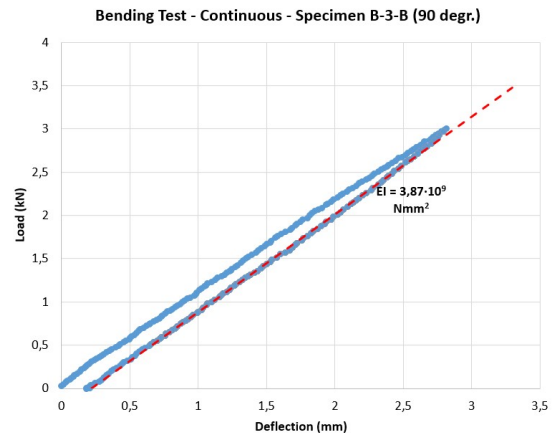


Figure C.27: Load-deflection: continuous - B-3-B (2)

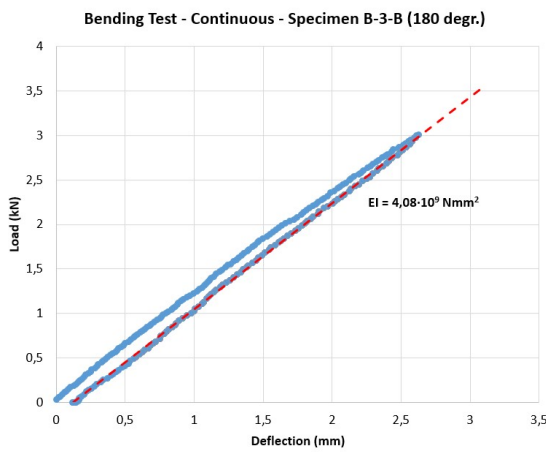


Figure C.28: Load-deflection: continuous - B-3-B (3)

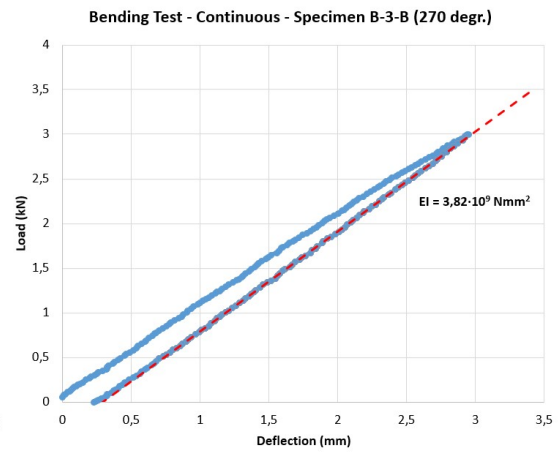


Figure C.29: Load-deflection: continuous - B-3-B (4)

C.2.2. Buckling Tests

In this appendix the load - lateral deflection curves obtained from buckling tests are presented. The European buckling curve for welded hollow sections is used to deduct reference values for the buckling load [48].

Dot-by-dot, L = 1250 mm

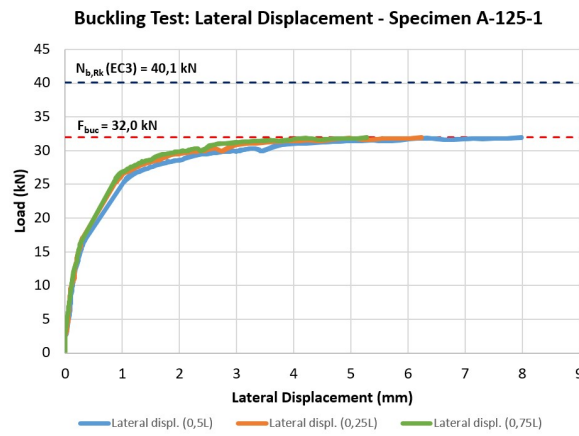


Figure C.30: Lateral displacements dot-by-dot - A-125-1

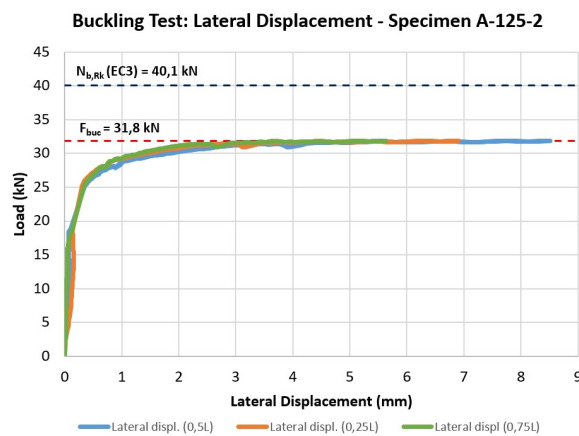


Figure C.31: Lateral displacements dot-by-dot - A-125-2

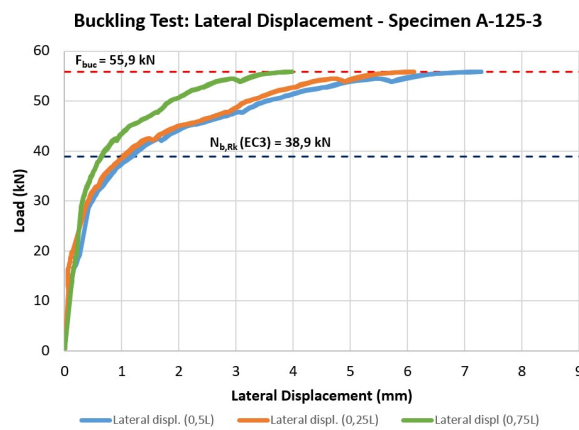


Figure C.32: Lateral displacements dot-by-dot - A-125-3

Dot-by-dot, L = 850 mm

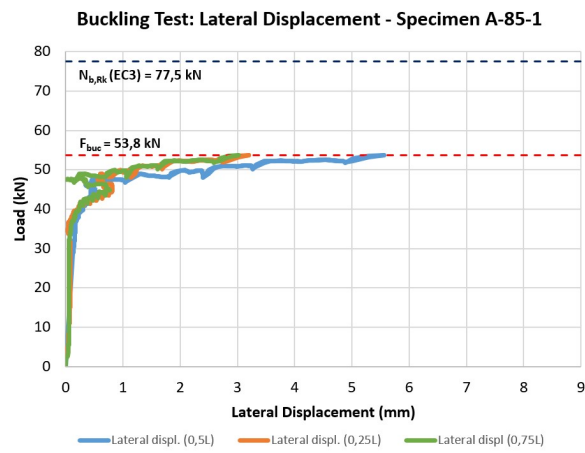


Figure C.33: Lateral displacements dot-by-dot - A-85-1

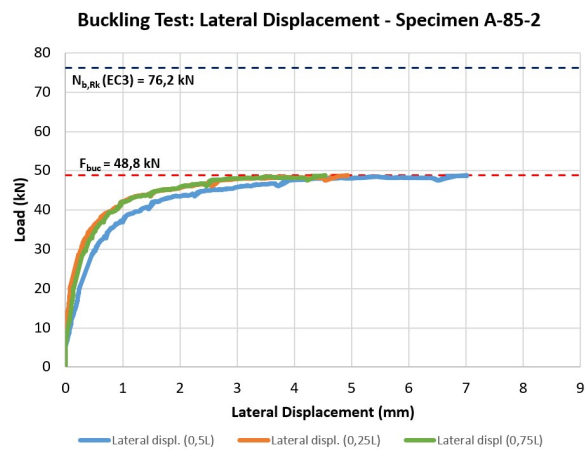


Figure C.34: Lateral displacements dot-by-dot - A-85-2

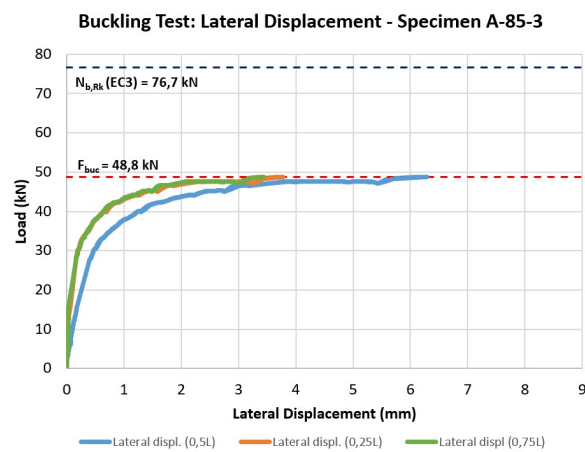


Figure C.35: Lateral displacements dot-by-dot - A-85-3

Dot-by-dot, L = 650 mm

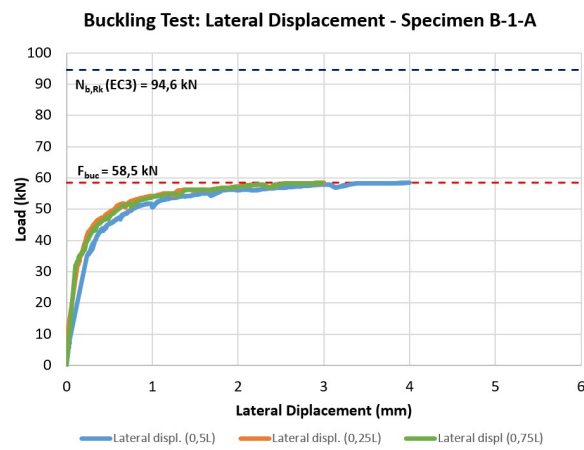


Figure C.36: Lateral displacements dot-by-dot - B-1-A

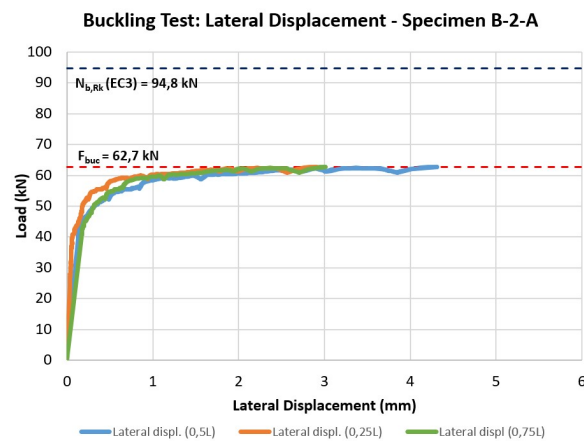


Figure C.37: Lateral displacements dot-by-dot - B-2-A

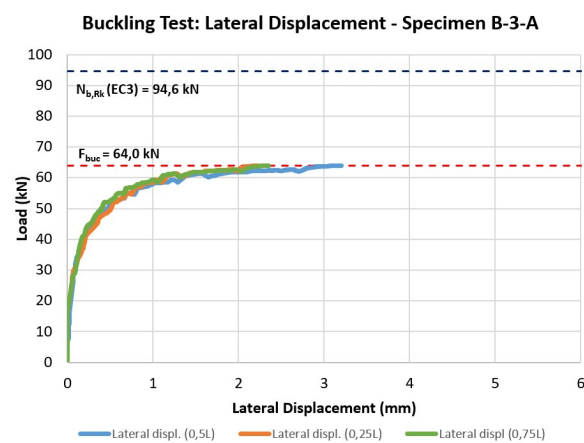


Figure C.38: Lateral displacements dot-by-dot - B-3-A

Dot-by-dot, L = 480 mm

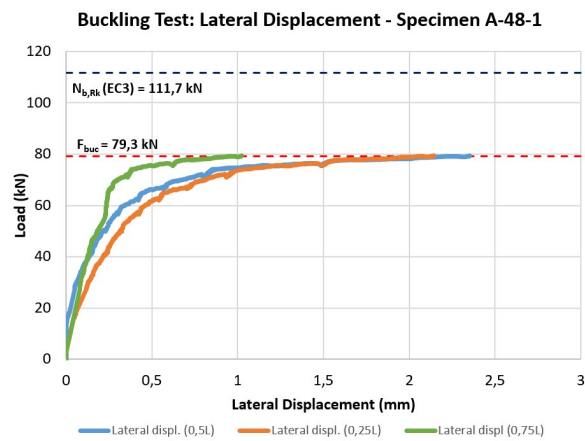


Figure C.39: Lateral displacements dot-by-dot - A-48-1

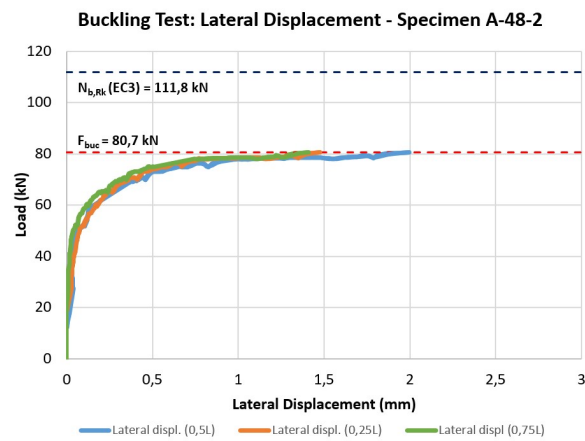


Figure C.40: Lateral displacements dot-by-dot - A-48-2

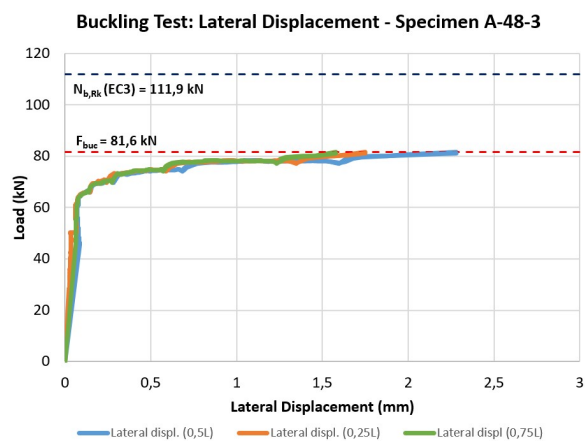


Figure C.41: Lateral displacements dot-by-dot - A-48-3

Continuous, L = 650 mm

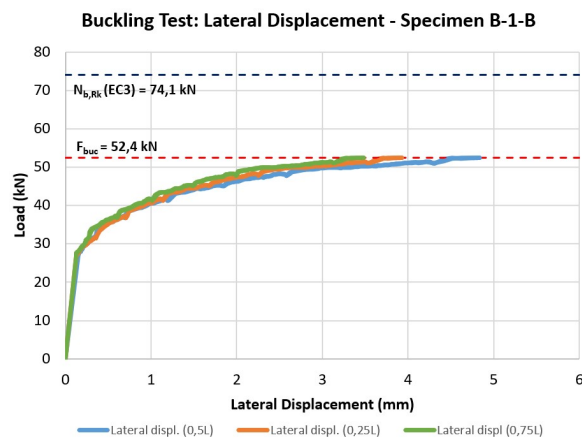


Figure C.42: Lateral displacements continuous - B-1-B

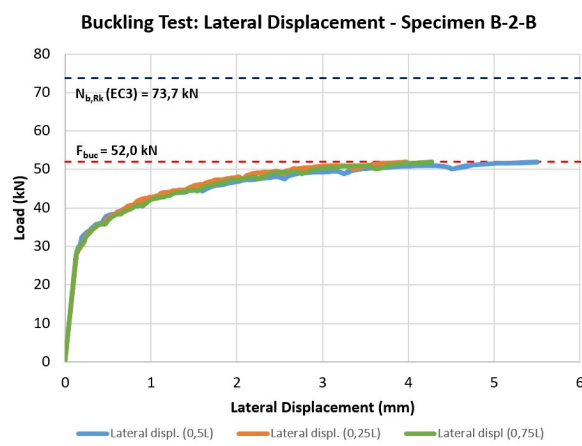


Figure C.43: Lateral displacements continuous - B-2-B

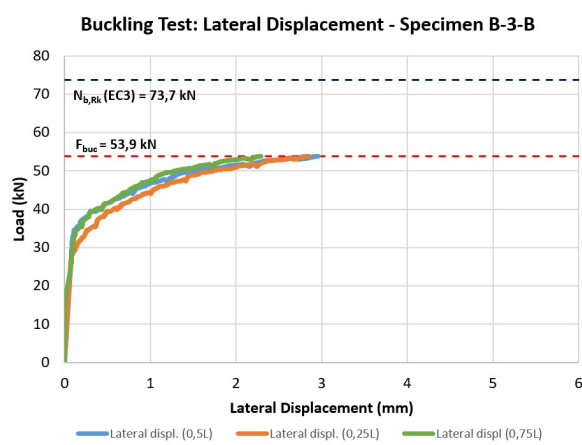


Figure C.44: Lateral displacements continuous - B-3-B

C.2.3. Tensile Tests

In the following figures the stress-strain relations are depicted of milled 308L stainless steel specimens deduced from tensile tests performed by OCAS. First the results of dot-by-dot printed specimens tested in their print (longitudinal) and perpendicular to their print (transversal) direction will be presented. This is done similarly for continuously printed specimens. The figures at the right depict the entire stress-strain relation, whereas the left figures focus on the elastic phase.

Dot-by-dot - Print Direction (Longitudinal)

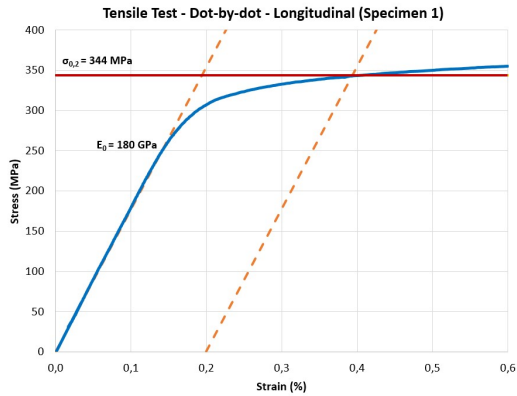


Figure C.45: Stress-strain: dot-by-dot - longitudinal (1)

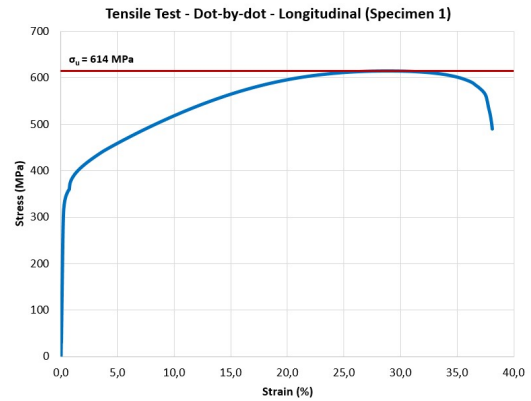


Figure C.46: Stress-strain: dot-by-dot - longitudinal (1)

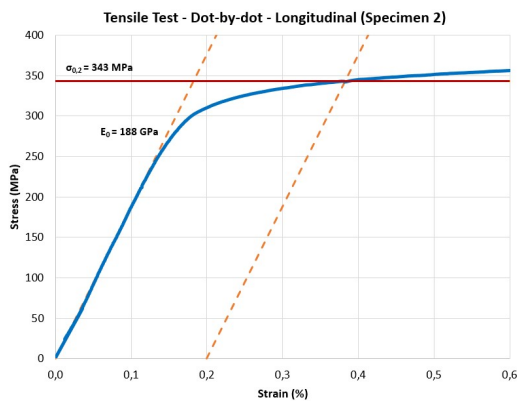


Figure C.47: Stress-strain: dot-by-dot - longitudinal (2)

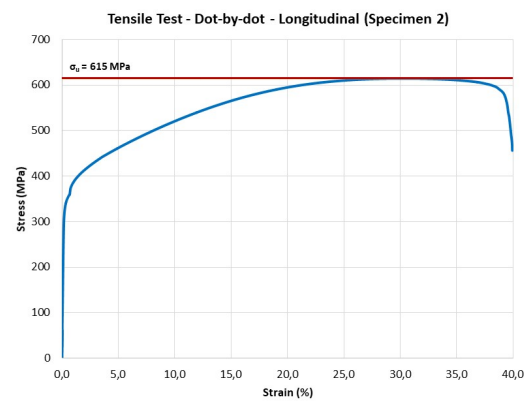


Figure C.48: Stress-strain: dot-by-dot - longitudinal (2)

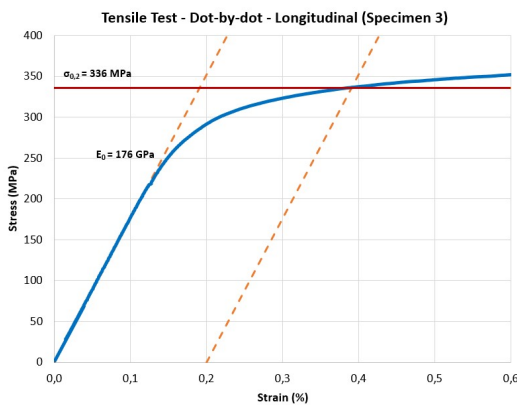


Figure C.49: Stress-strain: dot-by-dot - longitudinal (3)

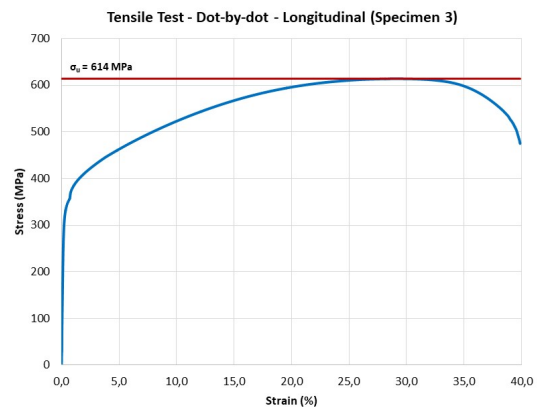


Figure C.50: Stress-strain: dot-by-dot - longitudinal (3)

Dot-by-dot - Perpendicular to Print Direction (Transversal)

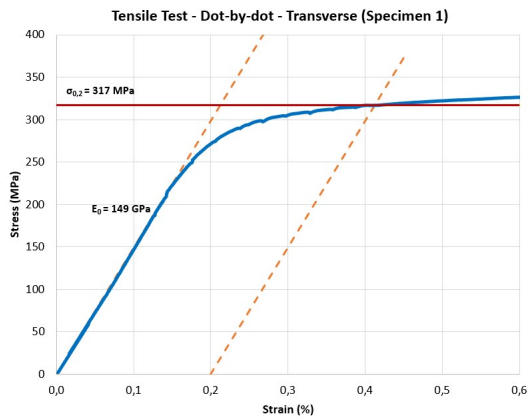


Figure C.51: Stress-strain: dot-by-dot - transversal (1)

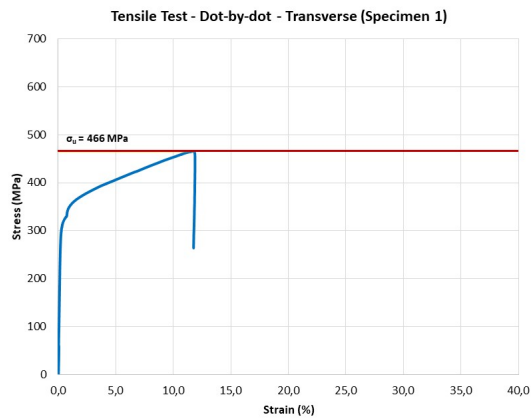


Figure C.52: Stress-strain: dot-by-dot - transversal (1)

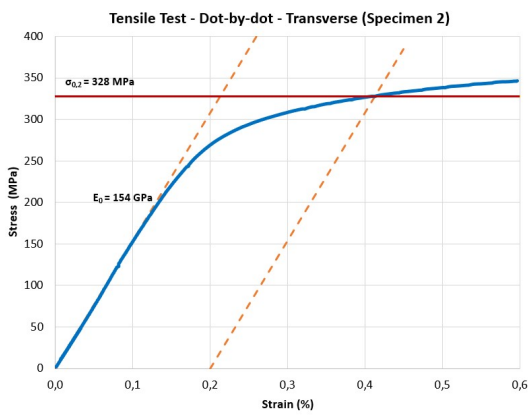


Figure C.53: Stress-strain: dot-by-dot - transversal (2)

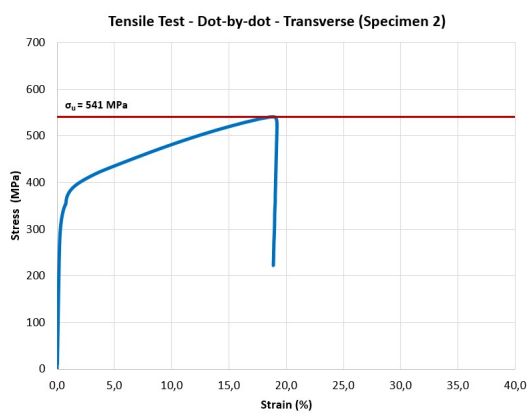


Figure C.54: Stress-strain: dot-by-dot - transversal (2)

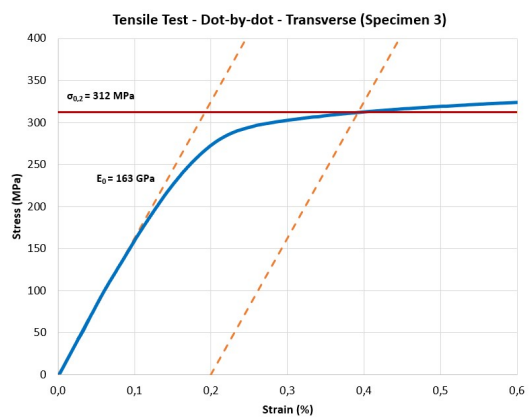


Figure C.55: Stress-strain: dot-by-dot - transversal (3)

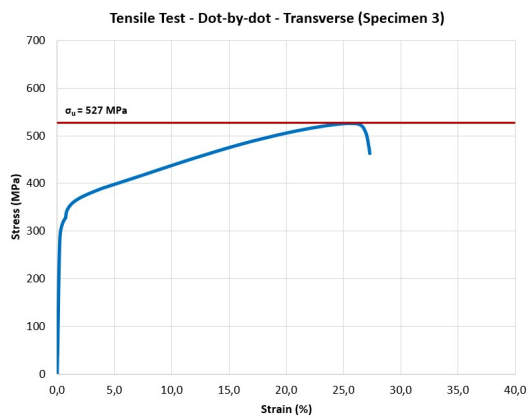


Figure C.56: Stress-strain: dot-by-dot - transversal (3)

Continuous - Print Direction (Longitudinal)

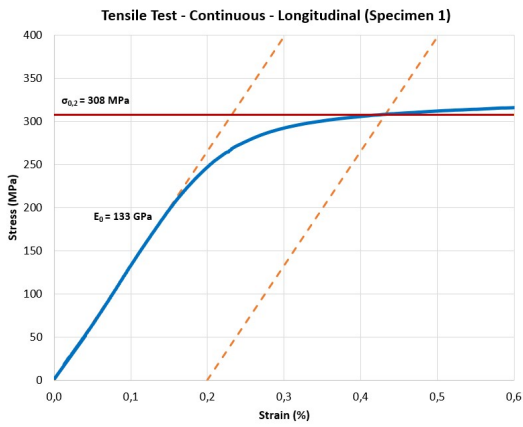


Figure C.57: Stress-strain: continuous - longitudinal (1)

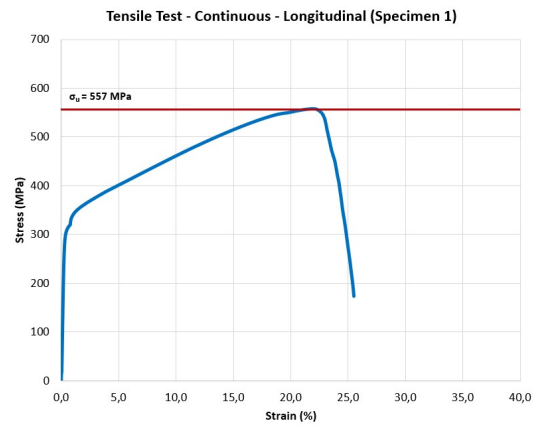


Figure C.58: Stress-strain: continuous - longitudinal (1)

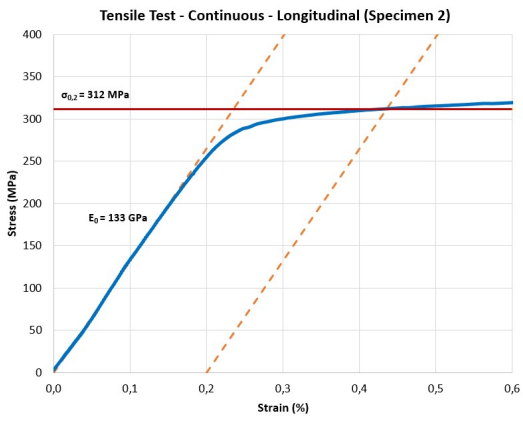


Figure C.59: Stress-strain: continuous - longitudinal (2)



Figure C.60: Stress-strain: continuous - longitudinal (2)

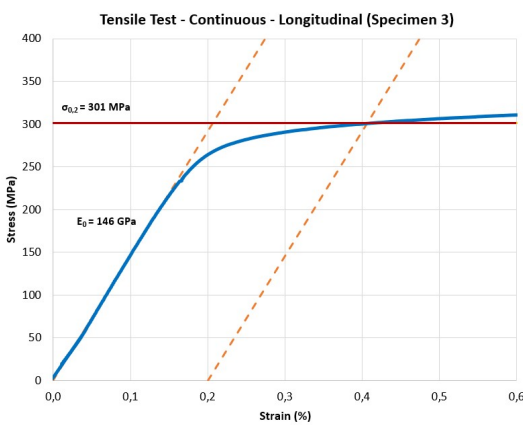


Figure C.61: Stress-strain: continuous - longitudinal (3)

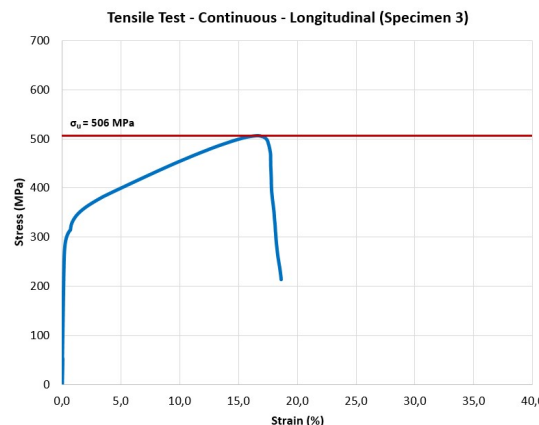


Figure C.62: Stress-strain: continuous - longitudinal (3)

Continuous - Perpendicular to Print Direction (Transversal)

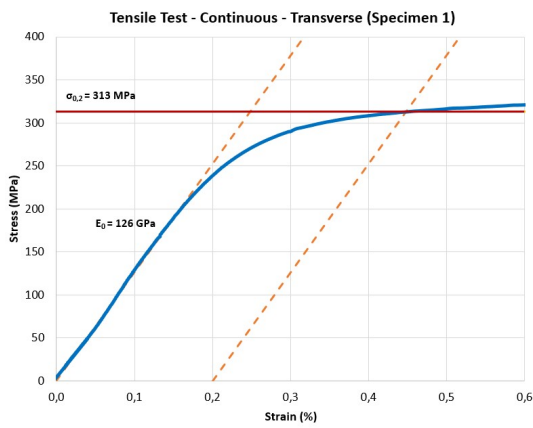


Figure C.63: Stress-strain: continuous - transversal (1)

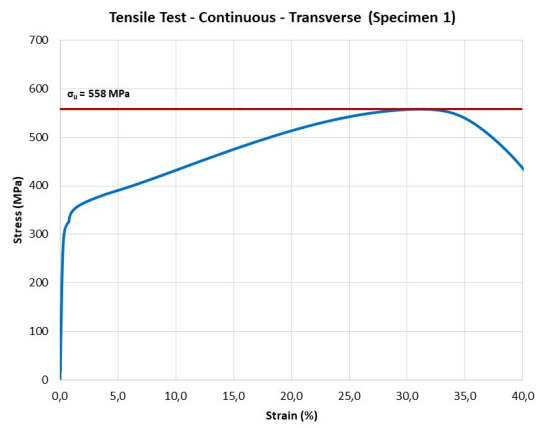


Figure C.64: Stress-strain: continuous - transversal (1)

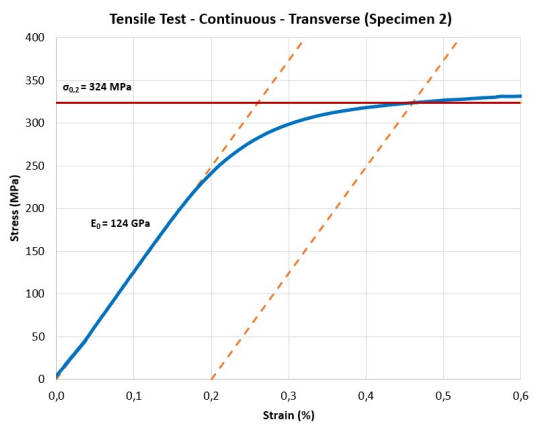


Figure C.65: Stress-strain: continuous - transversal (2)

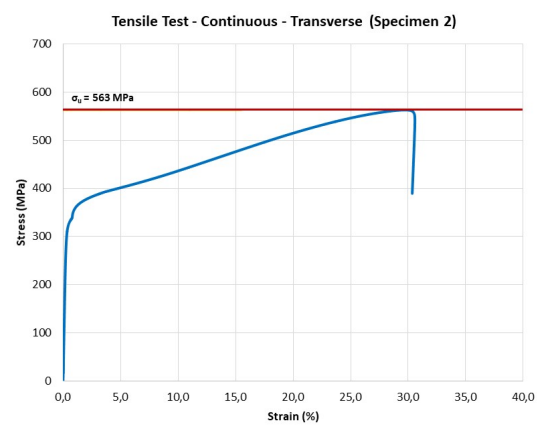


Figure C.66: Stress-strain: continuous - transversal (2)

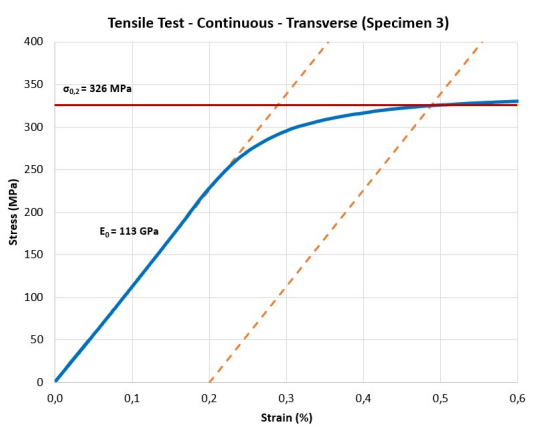


Figure C.67: Stress-strain: continuous - transversal (3)

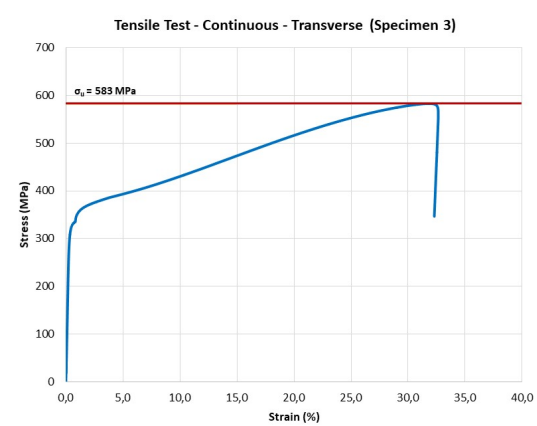


Figure C.68: Stress-strain: continuous - transversal (3)

C.2.4. Hardness Tests

Vickers hardness tests have been performed as explained in section 3.4.5. Line-measurements have been performed to longitudinal and transverse column sections of both dot-by-dot and continuously printed specimens using a load of 3 kgf (HV3). The measurement numbers on the horizontal axis indicate the location of measurements along a specified line (1 = outside and 5 = inside column wall). The results are presented here.

Dot-by-dot - Longitudinal

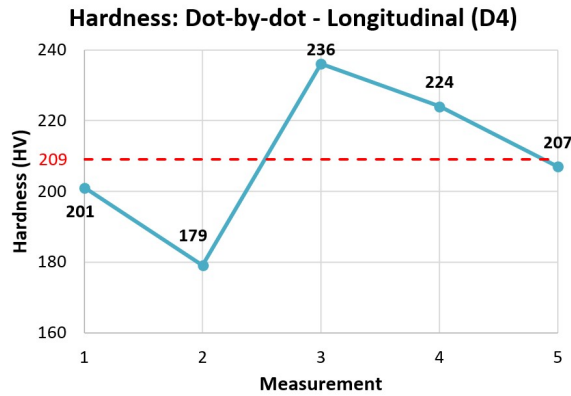


Figure C.69: Vickers hardness: dot-by-dot - longitudinal section - specimen D4

Dot-by-dot - Transversal

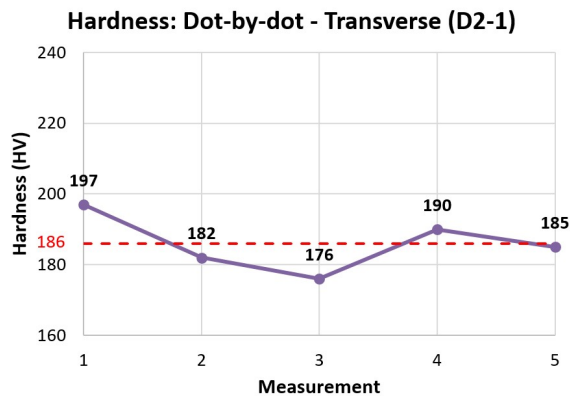


Figure C.70: Vickers hardness: dot-by-dot - transversal section - specimen D2 (1)

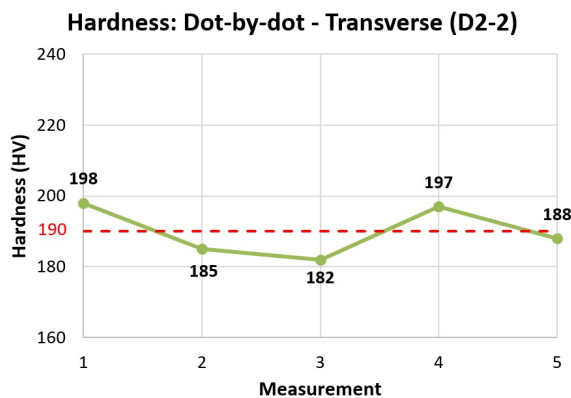


Figure C.71: Vickers hardness: dot-by-dot - transversal section - specimen D2 (2)

Continuous - Longitudinal

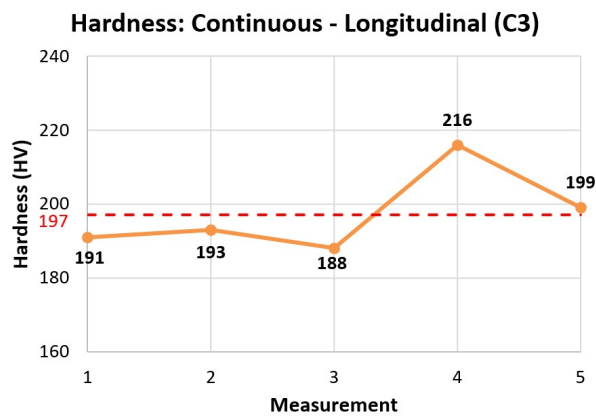


Figure C.72: Vickers hardness: continuous - longitudinal section - specimen C3

Continuous - Transversal

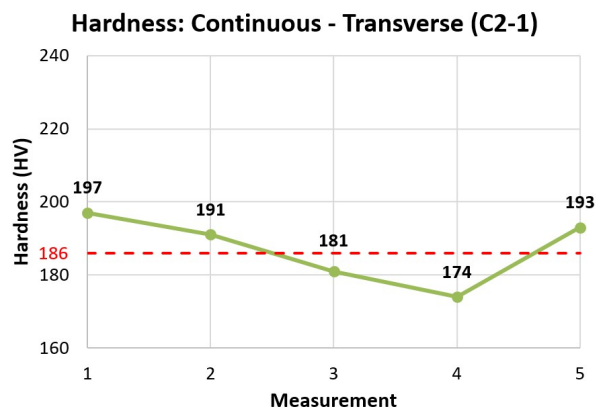


Figure C.73: Vickers hardness: continuous - transversal section - specimen C2 (1)

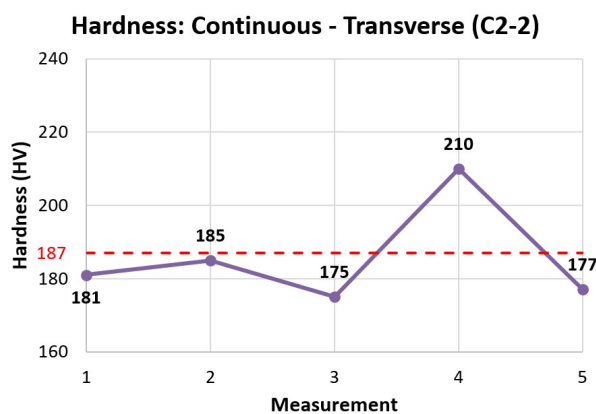


Figure C.74: Vickers hardness: continuous - transversal section - specimen C2 (2)

C.3. Metallography Results

C.3.1. Scanning Electron Microscopy

In this appendix the obtained results of scanning electron microscopy are presented. The chemical composition of selected points of interest has been investigated to analyse impurities in the specimen.

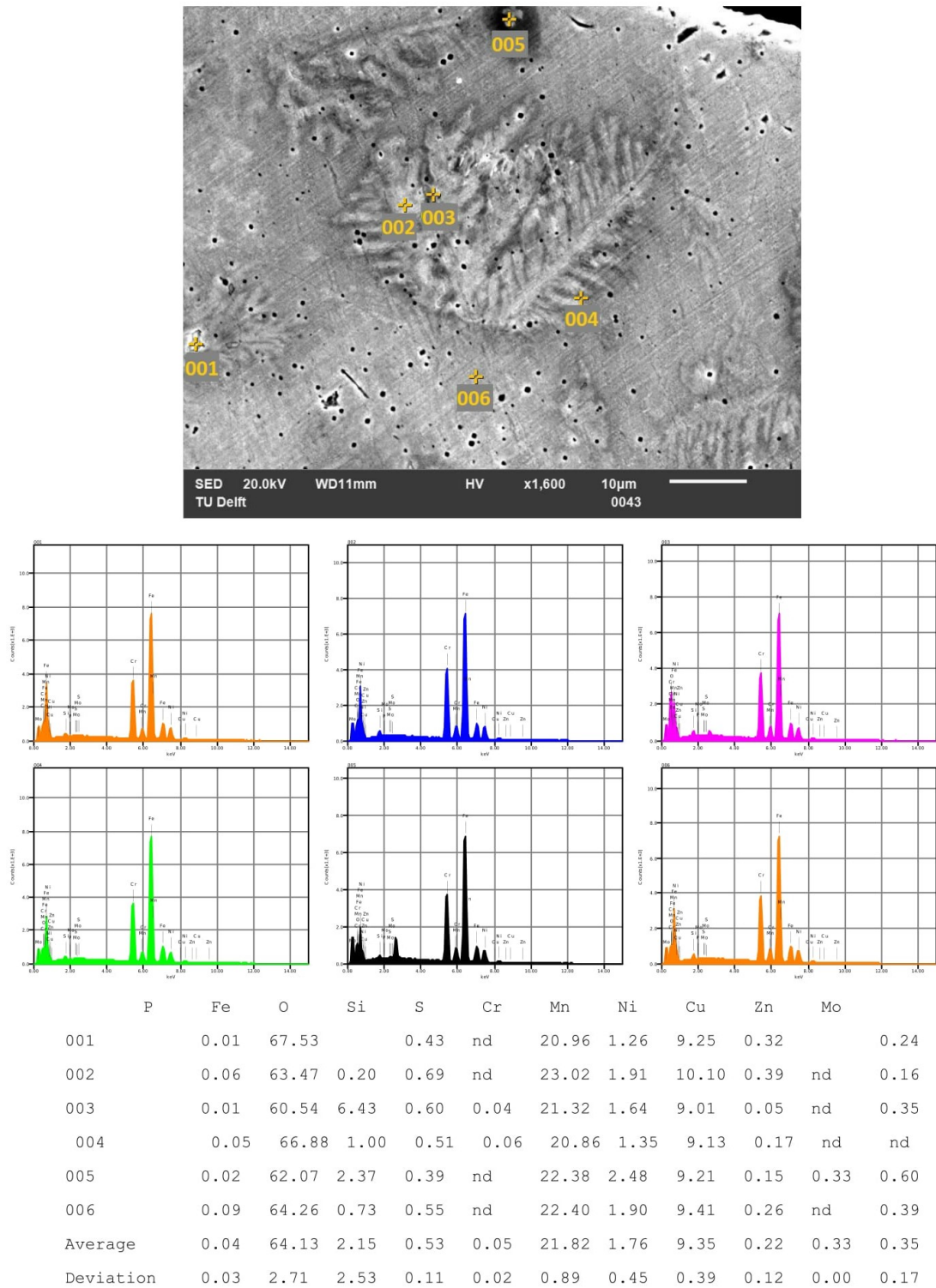
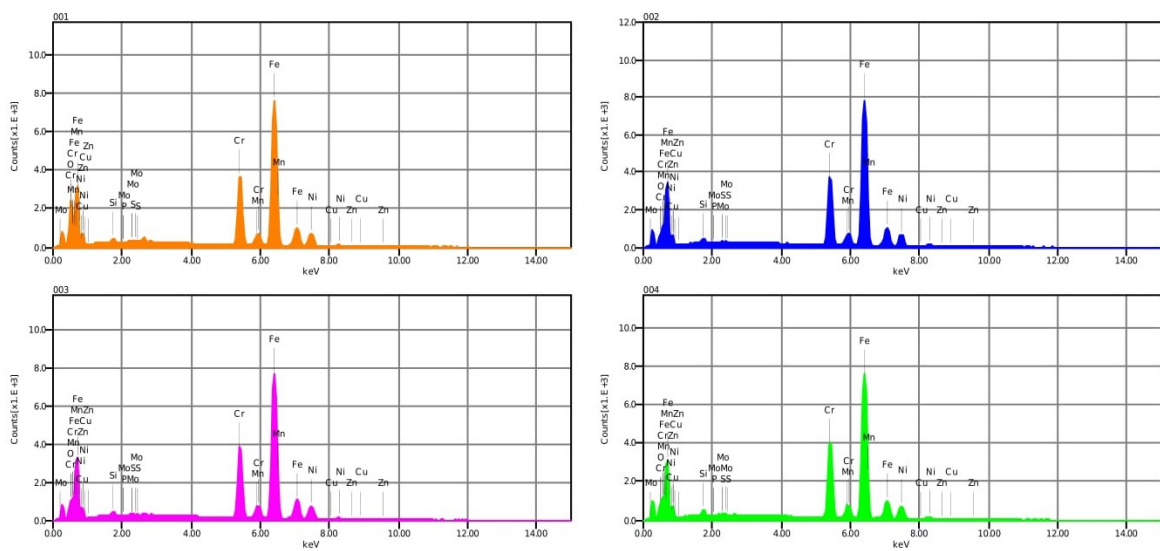
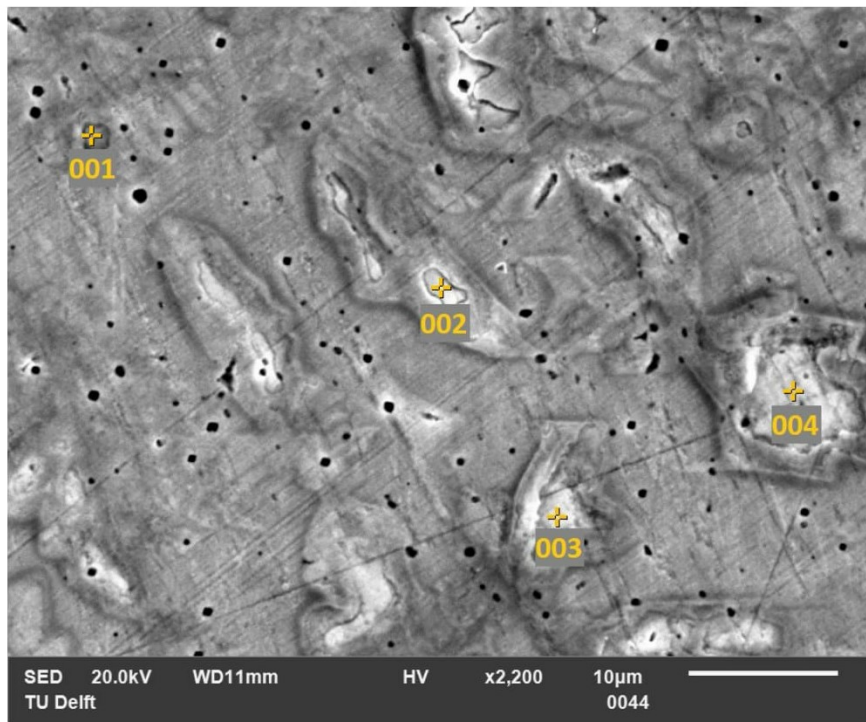
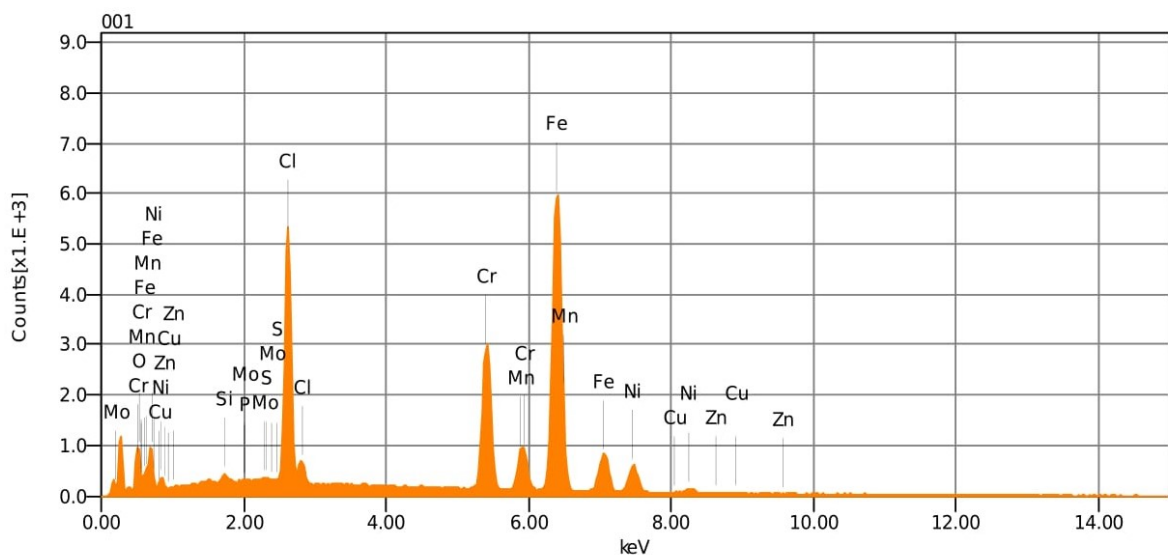
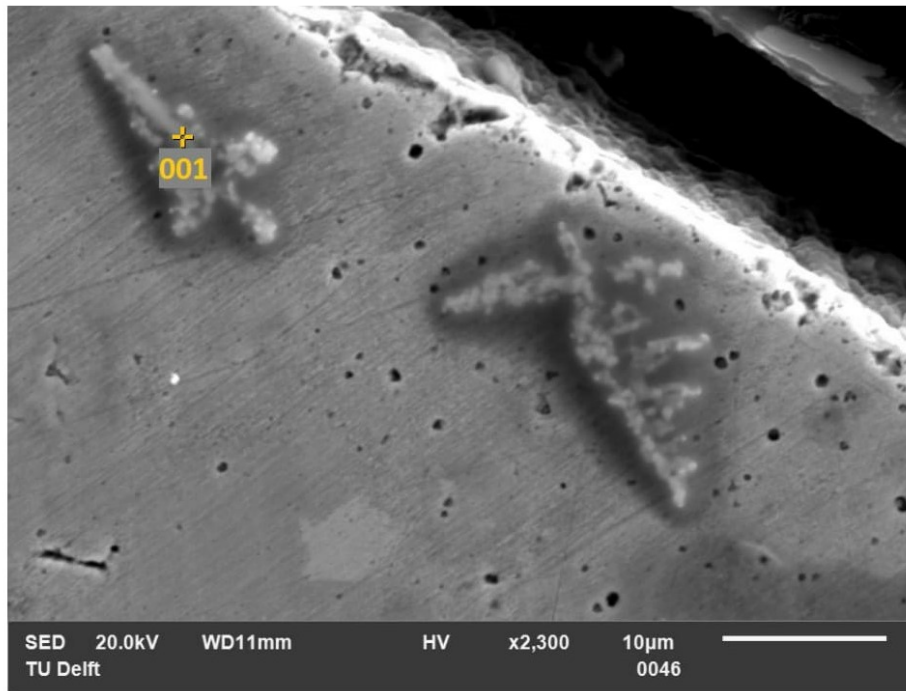


Figure C.75: Results of scanning electron microscopy with observation of silicon oxide inclusions (1)



	P	Fe	O	Si	S	Cr	Mn	Ni	Cu	Zn	Mo
001		nd	63.65	5.39	0.53	0.05	20.15	1.45	8.58	0.08	0.12
002		0.03	67.82	0.13	0.43	nd	20.63	1.26	9.05	0.33	0.14
003		nd	66.69	0.98	0.50	0.02	21.08	1.56	8.78	0.19	0.03
004		0.08	65.13	0.38	0.64	0.04	22.37	1.72	9.43	0.21	nd
Average		0.05	65.82	1.72	0.53	0.03	21.06	1.50	8.96	0.20	0.08
Deviation		0.04	1.82	2.48	0.09	0.01	0.96	0.19	0.37	0.10	0.08

Figure C.76: Results of scanning electron microscopy with observation of silicon oxide inclusions (2)



Formula	mass%	Atom%	Sigma	Net	K ratio	Line
O*	3.61	10.75	0.02	23919	0.0137867	K
Si*	0.31	0.53	0.02	5043	0.0008763	K
P*	0.09	0.14	0.01	1550	0.0003324	K
S*	0.07	0.10	0.01	1285	0.0002639	K
Cl*	11.90	15.99	0.03	242439	0.0529794	K
Cr*	17.65	16.17	0.06	192385	0.0823512	K
Mn*	4.52	3.92	0.05	38670	0.0207519	K
Fe*	54.05	46.11	0.09	425253	0.2527679	K
Ni*	7.42	6.02	0.06	40726	0.0344527	K
Cu*	0.25	0.19	0.04	1067	0.0010440	K
Zn*	0.13	0.10	0.05	482	0.0005627	K
Mo	nd	nd				L

Figure C.77: Results of scanning electron microscopy with observation of oxide inclusions (3)

Bibliography

Cover Image: Adriaan de Groot (MX3D)

- [1] S. Galjaard, S. Hofman, N. Perry, and S. Ren. Optimizing Structural Building Elements in Metal by using Additive Manufacturing. *International Association for Shell and Spatial Structures*, (August), 2015.
- [2] S. Galjaard, S. Hofman, and S. Ren. New Opportunities to Optimize Structural Designs in Metal by Using Additive Manufacturing. *Advances in Architectural Geometry 2014*, pages 79–93, aug 2015. ISSN 00143820. doi: 10.1007/978-3-319-11418-7_6. URL http://www.amazon.com/Advances-Architectural-Geometry-Cristiano-Ceccato/dp/3709103088https://doi.org/10.1007/978-3-319-11418-7_{_}6.
- [3] F Scapolo, A. Geyer, and M. Boden. The Future of Manufacturing in Europe 2015-2020 - The Challenge for Sustainability Europe 2015-2020. Technical report, European Commission Joint Research Centre and Institute for Prospective Technological Studies, 2003.
- [4] S. Zistl. 3D Printing: Facts and Forecasts, 2014. URL <https://www.siemens.com/innovation/en/home/pictures-of-the-future/industry-and-automation/Additive-manufacturing-facts-and-forecasts.html>.
- [5] S.K. Joosten. *Printing a Stainless Steel Bridge: An exploration of structural properties of stainless steel additive manufactures for civil engineering purposes*. Master's thesis, Delft University of Technology, 2015. URL <https://repository.tudelft.nl/islandora/object/uuid{%}3Ab4286867-9c1c-40c1-a738-cf28dd7b6de5?collection=education>.
- [6] ASTM International. Standard Terminology for Additive Manufacturing Technologies. (ASTM F2792-12a).
- [7] R. Baker. Method of Making Decorative Articles. US Patent 1533300A, 1920.
- [8] T. Wohlers and T. Gornet. History of Additive Manufacturing. *Wohlers Report 2014 - 3D Printing and Additive Manufacturing State of the Industry*, pages 1–34, 2014. ISSN 1098-6596. doi: 10.1017/CBO9781107415324.004.
- [9] P.M.S. Almeida. *Process Control and Development in Wire and Arc Additive Manufacturing*. Doctoral dissertation, Cranfield University, 2012. URL <https://dspace.lib.cranfield.ac.uk/handle/1826/7845>.
- [10] D. Brackett, I. Ashcroft, and R. Hague. Topology optimization for additive manufacturing. In *22nd Annual international solid freeform fabrication symposium*, pages 348–362, 2011.
- [11] L.P.L. Van der Linden. *Innovative Joints for Gridshells: Joints Designed by Topology Optimisation and to be Produced by Additive Manufacturing*. Master's thesis, Delft University of Technology, 2015. URL <https://doi.org/10.1017/CBO9781107415324.004>.
- [12] M. Attaran. The Rise of 3D-Printing: The Advantages of Additive Manufacturing over Traditional Manufacturing. *Business Horizons*, 60(5):677–688, 2017. ISSN 00076813. doi: 10.1016/j.bushor.2017.05.011.
- [13] R. Beardmore. Metal Costs, 2014. URL <http://www.roytech.co.uk/Useful{ }Tables/Matter/ Costs.html>.
- [14] M. Megahed, H.W. Mindt, N. N'Dri, H. Duan, and O. Desmaison. *Metal additive-manufacturing process and residual stress modeling*, volume 5. Integrating Materials and Manufacturing Innovation, 2016. ISBN 4019201600472. doi: 10.1186/s40192-016-0047-2. URL <http://link.springer.com/10.1186/s40192-016-0047-2>.

- [15] H. Strauss. *AM Envelope. The potential of Additive Manufacturing for facade constructions*, volume 3. 2013. ISBN 9781481214339. doi: 10.7480/abe.2013.1.
- [16] B. Vayre, F. Vignat, and F. Villeneuve. Metallic additive manufacturing: state-of-the-art review and prospects. *Mechanics & Industry*, 13(2):89–96, 2012. ISSN 2257-7777. doi: 10.1051/meca/2012003. URL <http://www.mechanics-industry.org/10.1051/meca/2012003>.
- [17] D. Ding, Z. Pan, D. Cuiuri, and H. Li. Wire-feed additive manufacturing of metal components: technologies, developments and future interests. *International Journal of Advanced Manufacturing Technology*, 81(1-4):465–481, 2015. ISSN 14333015. doi: 10.1007/s00170-015-7077-3.
- [18] F. Wang. Microstructure and mechanical properties of wire and arc additive manufactured Ti-6Al-4V. *Metallurgical and Materials Transactions A: Physical Metallurgy and Materials Science*, (44(2)):968–977, 2013.
- [19] J. R. Hönnige. Control of Residual Stress in Large Scale Metal AM. In *ENGIN-X user meeting at ISIS*. Cranfield University, 2017. URL <https://waammat.com/documents/control-of-residual-stress-in-large-scale-metal-am>.
- [20] F. Martina. Recent Developments in Large-Scale Wire+Arc Additive Manufacturing. In *Additive Manufacturing in Aerospace Conference*. Cranfield University, 2016. URL <https://waammat.com/documents/ila-berlin-2016>.
- [21] Wohler's. Wohlers Report 2015: 3D Printing and Additive Manufacturing State of the Industry Annual Worldwide Progress Report. Technical report, Wohler's Associates, Fort Collins, Colo, USA, 2015.
- [22] A.C.M. Bekker and J.C. Verlinden. A Life Cycle Assessment of Wire+Arc Additive Manufacturing Compared to Green Sand Casting and CNC Milling in Stainless Steel. 2017.
- [23] S. Williams. Large Scale Metal Wire + Arc Additive Manufacturing of Structural Engineering Parts. In *69th IIW Annual Assembly and International Conference*. Cranfield University, 2016.
- [24] T. E. Norgate, S. Jahanshahi, and W. J. Rankin. Assessing the Environmental Impact of Metal Production Processes. *Journal of Cleaner Production*, 15(8-9):838–848, 2007. ISSN 09596526. doi: 10.1016/j.jclepro.2006.06.018.
- [25] A. Adebayo. *Characterisation of Integrated WAAM and Machining Processes*. Doctoral dissertation, Cranfield University, 2013.
- [26] J. Mehnen, J. Ding, H. Locket, and P. Kazanas. Design for wire and arc additive layer manufacture. *International Journal of Product Development*, (19(1/2/3)):2–20, 2010. URL <http://www.inderscience.com/link.php?id=60028>
http://dx.doi.org/10.1007/978-3-642-15973-2_{_}73.
- [27] J. A. Choren, S. M. Heinrich, and M. B. Silver-Thorn. Young's modulus and volume porosity relationships for additive manufacturing applications. *Journal of Materials Science*, 48(15):5103–5112, 2013. ISSN 00222461. doi: 10.1007/s10853-013-7237-5.
- [28] F. Petzholdt and C. Aumund-Kopp. Standards for Metal Additive Manufacturing: a Global Perspective. *Metal Additive Manufacturing, vol.2 no.2*, 2016.
- [29] G. Mathers. Welding of Austenitic Stainless Steel - Job Knowledge 103, 2014. URL <http://www.twi-global.com/technical-knowledge/job-knowledge/welding-of-austenitic-stainless-steel-103/>.
- [30] A.C. Reardon. *Metallurgy for the Non-Metallurgist*. ASM International, Materials Park, OH 44073-0002, second edition, 2011. ISBN 978-1-61503-821-3.
- [31] ESDEP. European Steel Design Educational Programme: Lecture Notes [WG18], 2014. URL <http://fgg-web.fgg.uni-lj.si/~pmoze/ESDEP/master/wg18/toc.htm>.
- [32] A. Nickel. *Analysis of Thermal Stresses in Shape Deposition Manufacturing of Metal Parts*. Doctoral dissertation, Stanford University, 1999.

- [33] ESDEP. European Steel Design Educational Programme: Lecture Notes [WG2], 2014. URL <http://fgg-web.fgg.uni-lj.si/~pmoze/ESDEP/master/wg02/toc.htm>.
- [34] D. Hull and D.J. Bacon. *Introduction to Dislocations*. Elsevier Ltd, 4th ed. edition, 2003. ISBN 978-0-7506-4681-9.
- [35] D.L. Olson. Prediction of Austenitic Weld Metal Microstructure and Properties. *AWS 65th Annual Meeting*, pages 280–295, 1984. ISSN 00432296. doi: 10.1017/CBO9781107415324.004. URL http://www.aws.org/wj/supplement/WJ_{ }1985_{ }10_{ }s281.pdf.
- [36] G.F. VanderVoort, editor. *ASM Handbook: Metallography and Microstructures*. ASM International, volume 9 edition, 2004. ISBN 978-0-87170-706-2.
- [37] E.O. Hall. The Deformation and Ageing of Mild Steel: III Discussion of Results. *Proceedings of the Physical Society. Section B*, 64(9):747–753, 1951. ISSN 0370-1301. doi: 10.1088/0370-1301/64/9/303. URL <http://stacks.iop.org/0370-1301/64/i=9/a=303?key=crossref.4407b3b2b9fb54a7b0f006cb2475b0ef>.
- [38] N.J. Petch. The Cleavage Strength of Polycrystals. *Journal of the Iron and Steel Institute*, Vol.174:25–28, 1953.
- [39] R.E. Smallman and R.J. Bishop. *Modern Physical Metallurgy and Materials Engineering*. *Modern Physical Metallurgy and Materials Engineering*, 1999. ISSN 1098-6596. doi: 10.1016/B978-075064564-5/50010-0. URL <http://www.sciencedirect.com/science/article/pii/B9780750645645500100>.
- [40] J. Moysan, A. Apfel, G. Corneloup, and B. Chassignole. Modelling the grain orientation of austenitic stainless steel multipass welds to improve ultrasonic assessment of structural integrity. *International Journal of Pressure Vessels and Piping*, 80(2):77–85, 2003. ISSN 03080161. doi: 10.1016/S0308-0161(03)00024-3.
- [41] S. Lampman. *Weld Integrity and Performance: A Source Book Adapted from ASM International Handbooks, Conference Proceedings, and Technical Books*. ASM International, 1997. ISBN 0871706008, 9780871706003.
- [42] J.M. Vitek, A. Desgupta, and S.A. Davis. Microstructural Modification of Austenitic Stainless Steels By Rapid Solidification. *Metallurgical and materials transactions. A, Physical metallurgy and materials science*, 14A(9):1833–1841, 1983. ISSN 0360-2133. doi: 10.1007/BF02645553.
- [43] S.A. David, J.M. Vitek, and T.L. Hebble. Effect of Rapid Solidification on Stainless Steel Weld Metal Microstructures and Its Implications on the Schaeffler Diagram. *Welding Journal*, (October):289–300, 1987.
- [44] J.W. Elmer, S.M. Allen, and T.W. Eagar. Microstructural development during solidification of stainless steel alloys. *Metallurgical Transactions A*, 20(10):2117–2131, 1989. ISSN 03602133. doi: 10.1007/BF02650298.
- [45] BSSA British Stainless Steel Association. Comparison of Structural Design in Stainless Steel and Carbon Steel, 2014. URL <http://www.bssa.org.uk/topics.php?article=125>.
- [46] A.L. Schaeffler. Constitution Diagram for Stainless Steel Weld Metal. *Metal Progress*, pages 56(11):680–680B, 1949.
- [47] Oerlikon. Inertfil 308LSi Datasheet. URL http://www.oerlikon-online.de/Handbuch/pdf/MD/korrosionsbestaendig/Seite_{ }179_{ }INERTFIL_{ }308LSi.pdf.
- [48] NEN. *Eurocode 3 - Design of Steel Structures - Part 1-4: General Rules - Supplementary Rules for Stainless Steel*. Nederlands Normalisatie Instituut, Delft, The Netherlands, 2006.
- [49] A. Almubarak, W. Abuhaimeed, and A. Almazrouee. Corrosion Behavior of the Stressed Sensitized Austenitic Stainless Steels of High Nitrogen Content in Seawater. *International Journal of Electrochemistry*, Vol.2013, 2013. doi: 10.1155/2013/970835. URL <http://dx.doi.org/10.1155/2013/970835>.

- [50] TWI. Effect of Intermetallic Content on Pitting Resistance of Ferritic-Austenitic Stainless Steels, 2014. URL <http://www.twi-global.com/technical-knowledge/published-papers/effect-of-intermetallic-content-on-pitting-resistance-of-ferritic-austenitic-stainless-steel>
- [51] SCI: Steel Construction Institute. *Design Manual For Structural Stainless Steel*. Euro Inox and Steel Construction Institute., Brussels, third ed. edition, 2006. ISBN 2-87997-20.
- [52] TWI. What is Hot Cracking (Solidification Cracking)?, . URL <http://www.twi-global.com/technical-knowledge/faqs/faq-what-is-hot-cracking-solidification-cracking/>.
- [53] TWI. What is Porosity and how can it be Prevented?, . URL <http://www.twi-global.com/technical-knowledge/faqs/faq-what-is-porosity-and-how-can-it-be-prevented/>.
- [54] N. R. Baddoo. Stainless Steel in Construction: A Review of Research, Applications, Challenges and Opportunities. *Journal of Constructional Steel Research*, 64(11):1199–1206, 2008. ISSN 0143974X. doi: 10.1016/j.jcsr.2008.07.011.
- [55] S.H. Lin, W.W. Yu, T.V. Galambos, and E. Wang. Revised ASCE Specification for the Design of Cold-Formed Stainless Steel Structural Members. *Engineering Structures*, 27(9):1365–1372, 2005. ISSN 01410296. doi: 10.1016/j.engstruct.2005.03.007.
- [56] NEN. *Eurocode 3 - Design of Steel Structures Part 1-1: General Rules and Rules for Buildings*. Nederlands Normalisatie Instituut, Delft, The Netherlands, 2011.
- [57] P. Hradil, A. Talja, E. Real, and E. Mirambell. Structural Applications of Ferritic Stainless Steels (SAFSS) WP2: Structural Performance of Steel Members. Technical report, VTT, 2014.
- [58] W. Ramberg and W. Osgood. Determination of Stress-Strain Curves by three Parameters., 1941.
- [59] K.J.R. Rasmussen. Full-Range Stress-Strain Curves for Stainless Steel Alloys. *Journal of Constructional Steel Research*, 59(1):47–61, 2003. ISSN 0143974X. doi: 10.1016/S0143-974X(02)00018-4.
- [60] TWI. What is Charpy Testing?, . URL <http://www.twi-global.com/technical-knowledge/faqs/faq-what-is-charpy-testing/>.
- [61] O. Takakuwa, Y. Kawaragi, and H. Soyama. Estimation of the Yield Stress of Stainless Steel from the Vickers Hardness Taking Account of the Residual Stress. *Journal of surface engineered materials and advanced technology*, 3(October):262–268, 2013. ISSN 2161-4881. doi: 10.4236/jsemat.2013.34035.
- [62] I.S. Kim, K.J. Son, Y.S. Yang, and P.K.D.V. Yaragada. Sensitivity analysis for process parameters in GMA welding processes using a factorial design method. *International Journal of Machine Tools and Manufacture*, 43(8):763–769, 2003. ISSN 08906955. doi: 10.1016/S0890-6955(03)00054-3.
- [63] TWI. Why is There no Amperage Control on a MIG Welding Power Source?, . URL <http://www.twi-global.com/technical-knowledge/faqs/process-faqs/faq-why-is-there-no-amperage-control-on-a-mig-welding-powersource/>.
- [64] R.S. Funderburk. Key Concepts in Welding Engineering: A Look at Heat Input. *Welding Innovation*, XVI (1), 1999. URL <http://www.jflf.org/pdfs/papers/keyconcepts2.pdf>.
- [65] N.W Klingbeil, J.L. Beuth, R.K. Chin, and C. Amon. Residual Stress-Induced Warping in Direct Metal Solid Freeform Fabrication. *International Journal of Mechanical Sciences*, (44):57–77, 2002.
- [66] M.P. Mughal, H. Fawad, R.A. Mufti, and M. Siddique. Deformation Modelling in Layered Manufacturing of Metallic Parts Using Gas Metal Arc Welding: Effect of Process Parameters. *Modelling and Simulation in Materials Science and Engineering*, 13(7):1187–1204, 2005. ISSN 0965-0393. doi: 10.1088/0965-0393/13/7/013. URL <http://stacks.iop.org/0965-0393/13/i=7/a=013?key=crossref.b819af73538298a2a9cd7f5473d02946>.
- [67] M. Alimardani, E. Toyserkani, and J.P. Huissoon. A 3D Dynamic Numerical Approach for Temperature and Thermal Stress Distributions in Multilayer Laser Solid Freeform Fabrication Process. *Optics and Lasers in Engineering*, 45(12):1115–1130, 2007. ISSN 01438166. doi: 10.1016/j.optlaseng.2007.06.010.

- [68] D. Ding. *Process Planning for Robotic Wire Arc Additive Manufacturing*. Doctoral dissertation, University of Wollongong, 2015.
- [69] J. Ding, P. Colegrove, J. Mehnen, S. Ganguly, P.M. Sequeira Almeida, F. Wang, and S. Williams. Thermo-Mechanical Analysis of Wire and Arc Additive Layer Manufacturing Process on Large Multi-Layer Parts. *Computational Materials Science*, 50(December):3315–3322, 2011.
- [70] A.H. Nickel, D.M. Barnett, and F.B. Prinz. Thermal Stresses and Deposition Patterns in Layered Manufacturing. 317:59–64, 2001.
- [71] N. Murugan and R.S. Parmar. Effects of MIG Process Parameters on the Geometry and Dilution of the Bead in the Automatic Surfacing. *Journal of Materials Processing Technology*, 41:381–398, 1994. ISSN 12129151. doi: 10.1016/0924-0136(94)90003-5.
- [72] S. Chandel, S.R. Bala. Relationship Between Submerged Arc Welding Parameters and Weld Bead Size. *Schweissen Schneiden*, 40:28–31, 1988.
- [73] F. Martina. *Additive Manufacturing for Advance Welding Processes [Lecture 4.13]*. PhD thesis, Cranfield University, 2015.
- [74] ESDEP. European Steel Design Educational Programme: Lecture Notes [WG7], 2014. URL <http://fgg-web.fgg.uni-lj.si/~pmoze/ESDEP/master/wg07/toc.htm>.
- [75] L. Euler. *Methodus Inveniendi Lineas Curvas Maximi Minimive Proprietate Gaudentes, sive Solutio Problematis Isoperometrici Latissimo Sensu Accepti*. Lausanne and Geneva: Marc-Michel Bousquet, 1744.
- [76] F. Engesser. Über die Knickfestigkeit Geradu Sträbe. *Z.Architek.Ing.*, 35:455, 1889.
- [77] Bruce G. Johnston. Column Buckling Theory: Historic Highlights. *Journal of Structural Engineering*, 109(9):2086–2096, 1983. ISSN 0733-9445. doi: 10.1061/(ASCE)0733-9445(1983)109:9(2086). URL [http://ascelibrary.org/doi/10.1061/\(ASCE\)0733-9445\(1983\)109:9\(2086\)](http://ascelibrary.org/doi/10.1061/(ASCE)0733-9445(1983)109:9(2086)).
- [78] R.D. Ziemian, editor. *Guide to Stability Design Criteria for Metal Structures*. John Wiley & Sons, sixth edition, 2010. ISBN 978-0-470-08525-7.
- [79] ESDEP. European Steel Design Educational Programme: Lecture Notes [WG6], 2014. URL <http://fgg-web.fgg.uni-lj.si/~pmoze/ESDEP/master/wg06/toc.htm>.
- [80] R.H. Batterman and B.G. Johnston. Behavior and Maximum Strength of Metal Columns. *ASCE Journal of the Structural Division*, Vol.93(ST2):205–230, 1967.
- [81] R. Bjorhovde. *Deterministic and Probabilistic Approaches to the Strength of Steel Columns*. Doctoral dissertation, Lehigh University, 1972.
- [82] AISC. *Steel Construction Manual*. American Institute of Steel Construction, fourteenth edition, 2011.
- [83] ECCS. *Manual on Stability of Steel Structures*. European Convention For Constructional Steelwork: Committee 8 - Stability, second edition, 1976.
- [84] W.E. Ayrton and J. Perry. On Struts. *The Engineer*, Vol.62:464, 1886.
- [85] G. Beer and H. Schulz. The European Column Curves. In *International Colloquium on Column Strength*, Paris, 1972. IABSE.
- [86] K.J.R. Rasmussen and J. Rondal. Strength curves for metal columns. *Journal of Structural Engineering ASCE*, 123(6):721–728, 1997. ISSN 07339445 (ISSN). doi: 10.1061/(ASCE)0733-9445(1997)123:6(721). URL <http://www.scopus.com/inward/record.url?eid=2-s2.0-0031169012&partnerID=40&md5=c1a9a9257bdc560f35782b442d9dbec7>.
- [87] A.L. Johnson and G. Winter. Behavior of Stainless Steel Columns and Beams. *ASCE Journal of the Structural Division*, Vol.92(ST5):97–118, 1966.

- [88] B.A. Burgan, N.R. Baddoo, and K.A. Gilsean. Structural Design of Stainless Steel Members—Comparison between Eurocode 3, Part 1.4 and Test Results. *Journal of Constructional Steel Research*, Vol.54(1):51–73, 2000.
- [89] Sadev. Austinox Material Safety Data Sheet Stainless Steel, 2010. URL <http://sadev-stainless-steel.com/wp-content/uploads/MSDS-St.Steels-English-2014.pdf>.
- [90] Ugitech. Ugiweld 308LM Datasheet. URL http://www.ugitech.com/uploads/ugitransfer/docs/GED_{_}2289.pdf.
- [91] R.F. Egerton. *Physical Principles of Electron Microscopy*, volume 8. 2005. ISBN 2005924717. doi: 10.1016/S1369-7021(05)71232-3. URL <http://linkinghub.elsevier.com/retrieve/pii/S1369702105712323>.
- [92] S. Suryakumar, K.P. Karunakaran, U. Chandrasekhar, and M.A. Somashekara. A Study of the Mechanical Properties of Objects Built Through Weld-Deposition. *Proceedings of the Institution of Mechanical Engineers, Part B: Journal of Engineering Manufacture*, 227(8):1138–1147, 2013. ISSN 0954-4054. doi: 10.1177/0954405413482122. URL <http://journals.sagepub.com/doi/10.1177/0954405413482122>.

